universität wien

DISSERTATION

Titel der Dissertation

The Interaction of Rare Earth Elements with Cadmium:

The systems Cd-Gd and Cd-Pr

Verfasser

Mag. Thomas L. Reichmann

angestrebter akademischer Grad

Doktor der Naturwissenschaften (Dr.rer.nat.)

Wien, August 2014

Studienkennzahl lt. Studienblatt:	A 796 605 419
Dissertationsgebiet lt. Studienblatt:	Chemie
Betreuerin / Betreuer:	O. Univ.-Prof. Dr. Herbert Ipser

Acknowledgments

I would like to express my sincere gratitude to my supervisor

O. Univ.-Prof. Dr. Herbert Ipser

who was always there with a sympathetic ear. His expertise in thermodynamic characterisation of alloys and phase diagram evaluation was of great help to me

A special thank you also to our project collaborators

Dr. Rajesh Ganesan and **Dr. Raghavachary Sridharan,**

from the Indira Gandhi Centre for Atomic Research (IGCAR), who enabled a research stay and supported this study with their huge experience in experimental thermodynamics

I would like to thank

Ao. Univ.-Prof. Dr. Klaus W. Richter and **Ao. Univ.-Prof. Mag. Dr. Hans Flandorfer**

for their excellent scientific support in exploring specific questions,

Dr. Stephan Puchegger

who always offered time for SEM measurements,

and

Ao. Univ.-Prof. Dr. Herta S. Effenberger

for her excellent support with single crystal XRD measurements

Thank you to all my

colleagues at the **Department of Inorganic Chemistry (Materials Chemistry)**

for creating a pleasant working environment

Particular thanks go to

Dolores and my **Family** as well as to **all my Friends,**

who always have been there for me

Table of contents

I. Introduction

Energy consumption is rising across the globe. Therefore scientific work is done in a range of areas to increase the efficiency and output of current energy sources. Nowadays it is customary that economic growth and global competitiveness go hand in hand with an efficient energy situation - especially emerging and developing countries are inevitably dependent on steadily delivered energy. To satisfy the demand of energy and bolster national economic growth, many countries are turning to nuclear energy. However, that comes at a price – the process of nuclear energy production creates radioactive waste and as yet there is no acceptable strategy for its disposal.

Under the current system a few thousand tons of nuclear waste accumulate annually and, instead of being disposed of properly, low-level and intermediate-level radioactive waste is temporarily stored in interim storage facilities or deposited in large geological repositories. Although proper concepts for the disposal of so-called high-level radioactive waste are already in the planning stages, the only appropriate solution currently available is to store this waste on-site.

However, by utilising nuclear reprocessing, the amount of radioactive waste could be drastically decreased as all fission products are separated into fractions. While some of these fractions can re-enter the nuclear fuel cycle through further treatment [1], especially long-lived radioactive actinides can be transmuted into shorter-lived nuclides through a process of particle- or light-induced spallation in accelerator driven systems [2-4].

Conventionally, nuclear waste is reprocessed using the hydrometallurgical technique or aqueous reprocessing [1]. Large-scale operations are currently underway in la Hague (France), Sellafield (UK) and Rokkasho (Japan), which have a combined capacity of about 4000 tons/year [5]. All commercial reprocessing plants exclusively utilise the PUREX process (Plutonium and Uranium Recovery by Extraction) [6-7], which was initially established in the late 1950s for the recovery of weapon-grade Pu in the course of the "Manhattan project". As today most nations are members of the "Treaty on the Non-Proliferation of Nuclear Weapons", nuclear waste is reprocessed exclusively for economical and ecological purposes.

Generally speaking all hydrometallurgical techniques are based on a process of solvent extraction and a subsequent partitioning of the extracts. Commonly, tributyl phosphate (TBP) is used to selectively extract U and Pu from dissolution of spent nuclear fuels in nitric acid [1]. Through chemical reduction, Pu is separated and returned to the nuclear fuel cycle in the form of mixed oxide fuel (MOX). U (mainly U-238) enters a conversion plant prior to re-enrichment [8]. The remaining radioactive liquid waste is dried and enclosed in suitable formulated glass matrices [9]. This so-called vitrification process is technologically feasible and environmentally safe. However, aqueous reprocessing has a number of disadvantages. Nuclear fuel materials show huge diversity in terms of their applicability. Likewise, chemical digestion can be performed in many different ways, which can create immense costs and require enormous efforts. Most of the solvents used for the selective extraction suffer from radiation and temperature instability. As a consequence, high-level radioactive waste cannot directly enter the reprocessing plant but has to be cooled down for several months in large water pools first. To achieve U and Pu of industrially viable purity, several extraction steps have to be employed creating a huge amount of radioactive liquid waste [1]. To overcome the major disadvantages of these hydro-metallurgical methods it was necessary to investigate another type of reprocessing technique, called pyrometallurgical reprocessing.

In general, pyroprocessing is a term for high-temperature methods which readily allow the reprocessing of high-burnup spent fuels. These methods were established in the early stages of reprocessing technologies and pursue the same objectives as hydrometallurgical methods. Their main advantage compared to the latter methods is that Pu cannot be separated in a pure state, meaning that proliferation of nuclear weapons can be prevented. This issue became more important in the course of demobilisation after the cold war [10]. Hence, extensive research has been carried out to develop various non-aqueous techniques but only a few reached reasonable levels for large-scale application, i.e. fluoride volatility [11], salt cycle process [12] and pyrochemical reprocessing [6]. Of all the methods pyrochemcial reprocessing attracted the most attention as it offers a wide range of applicability. In addition, it is potentially very safe because of the high thermal resistance of the whole assembly.

In principle, pyrochemical reprocessing is based on an electrorefining step carried out in an electro-transportable cell. A schematic view of this cell is shown in Figure 1.

Corresponding chemical and thermodynamic expressions are repeatedly discussed in the literature [1, 13-16].

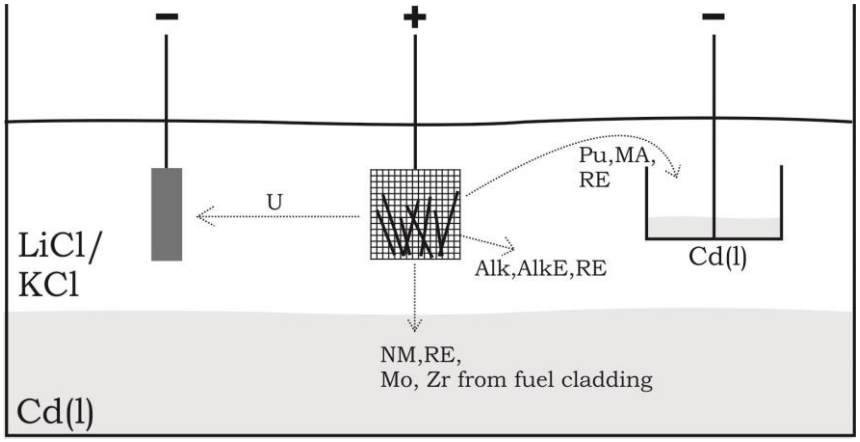

Fig. 1: Electro-transportable cell; abbreviations are explained in the text below

In particular, the cell consists of a massive steel vessel, which is occupied by a low melting metal topped by a eutectic LiCl/KCl salt mixture. Both, the salt and the metal phase become liquid when the operation temperature is achieved. Several low melting metals have been tested, e.g. Al [17], Bi and Cd [18], but among these Cd is the most promising candidate. Cd has a rather high vapour pressure, making it convenient for removal by distillation in a cathode processor [16]. It even forms a series of intermetallic compounds with all actinides and rare earth elements (REs). The cell contains a basket steel anode, where the chopped nuclear fuels are inserted, and at least two cathodes are inserted into the molten salt phase. To obtain different product streams, two types of cathodes are used, i.e. steel cathodes and liquid Cd cathodes. By applying a definite potential most elements are anodically dissolved in the salt phase as their chlorides. The Gibbs free energies of formation of the chlorides allow separating the fission products into three categories: highly stable chlorides formed by alkali and alkaline earth elements (Alk, AlkE); intermediately stable chlorides formed by U, Pu, minor actinides (MA) and rare earth elements (RE); less stable chlorides formed by noble metals (NM) and fuel cladding materials (Mo, Zr) [16]. While Alk and AlkE form highly stable chlorides and accumulate in the electrolyte without being reduced, NM and transition elements from the fuel cladding (e.g. Zr, Mo) settle down below the anode as anodic sludge. However, a sustainable electrotransport can only be achieved by elements

forming intermediately stable chlorides with a significant concentration in the electrolyte. The concentration is determined by the oxidation state of the electrorefiner, which can be altered by adding a reductive or oxidising substance [15]. The potential is applied in such a way that especially U, Pu and MA are transportable [1,16], i.e. Gibbs free energies of their corresponding chlorides are in a certain range, which allows electrotransport to happen. In fact, RE-chlorides are slightly more stable and accumulate in the electrolyte. While U is exclusively deposited onto the iron cathode, Pu and MA form intermetallic compounds with Cd at the liquid Cd cathode. The formation of intermetallic compounds lowers the thermodynamic activities of these transuranic elements extensively [19]. Hence, these elements are caught by the Cd cathode and are not re-dissolved into the electrolyte. One of the key problems of the pure separation of the transuranic elements is that accumulating RE co-deposit at the liquid Cd cathode by forming intermetallic compounds.

A proposed method for pyrometallurgical separation of RE is the reductive extraction in the chloride salt/liquid metal system [18]. The extraction behaviour in this arrangement strongly depends on the standard free energy of formation of the corresponding chlorides, as well as on the activity coefficients of the extracted metals in the respective intermetallic compounds [15,20]. Hence, a thorough knowledge of the existence and stability of intermetallic compounds in various binary Cd-RE phase diagrams is essential. From experimentally obtained distribution coefficients, separation factors were derived for several actinides and RE [21-23] pairs. For each pair a so-called exchange reaction can be deployed to evaluate the distribution behaviours and to control the extractability of different elements. As an alternative, separation factors can be calculated from thermodynamic properties [18], but most of the corresponding data are currently not available from literature.

It was the aim of the current project to provide a detailed knowledge of thermodynamic properties as well as phase diagrams in several Cd-RE systems, i.e. RE = Ce, Pr, Nd, Gd. The complete phase diagrams have been accurately investigated using conventional isothermal and dynamic methods; *cf. Refs.* [24-27]. An isopiestic vapour pressure method was applied to obtain thermodynamic activities and integral Gibbs energies in all of these systems [28-31]. Moreover, standard enthalpies of formation of Cd-Pr alloys were derived from calorimetric measurements, which served as input data into a CALPHAD-type (Computer Coupling of

Phase Diagrams and Thermochemistry) optimisation [32]. The research papers [24,25,28,29,32], presented in the *Results and Discussion* section, comprise all results dedicated to the present cumulative dissertation.

Phase diagrams – a useful tool for materials science

As indicated above, whenever phase formation occurs within a certain materials system, knowledge of the existence and stability of corresponding compounds and phases is of great importance. Especially for metallic systems, phase diagrams, also known as equilibrium diagrams, are used to graphically represent all corresponding intermetallic phases and phase equilibria among them. Hence, phase diagrams are an indispensable tool for materials science and engineering, describing the state of a materials system in thermodynamic equilibrium as a function of the intensive variables temperature, pressure and composition.

A commonly known phase diagram is the unary T/p diagram of water, which presents the state of matter of water at any given condition [33], i.e. temperature and pressure. If a system becomes more complex, e.g. diversity of alloying elements in steel, the respective phase diagram becomes of a higher order. For applications in materials science, pressure is often assumed to be constant at atmospheric pressure and corresponding multi-component systems are specified in terms of x/T diagrams. These so-called condensed diagrams represent phase formations and corresponding transition reactions as a function of temperature and composition.

From the thermodynamic point of view, an equilibrium phase diagram comprises all phases that are stable at given conditions. Any phase in a multi component system can be described by the Gibbs free energy as a function of composition and temperature (p = const.). Basically, the equilibrium state of an individual phase is determined by the minimum in its G/x_i curve at any given condition. In a multi-phase system, the minimum over all individual G/x_i curves represents the equilibrium state of the system at one well defined temperature (p = const.). This so-called integral Gibbs energy, which represents the overall minimum at particular compositions, can be determined through the tangent method [34]. From a set of integral Gibbs energy curves at different temperatures, the complete equilibrium diagram can be drawn with respect to some distinct thermodynamic rules [34].

Phase transitions are typically specified according to the Ehrenfest classification [35] to be first or second order. First order transitions mostly involve congruent phase melting or invariant phase reactions. These type of transition reactions exhibit discontinuities in the first derivatives of the Gibbs free energy [36]. Consequently, their reaction temperatures are well defined. In contrast, second order transition reactions, e.g. some solid-solid transformations or magnetic transformations, are continuous in respect to the first derivation but discontinuous in the second derivation of the Gibbs free energy, i.e. heat capacity. Such phase reactions are observed over a certain temperature range.

Literature overview

In the following, a complete literature overview comprising all available data of the Cd-Gd and Cd-Pr systems is given. This overview includes phase diagram and thermodynamic data as well as a complete survey of all intermetallic compounds present in these systems.

Due to the cumulative character of the present dissertation, the literature overview is based on the research papers [24,25,28,29,32] shown in the *Results and Discussion* section and might therefore cover repeated information and word order.

The Cd-Gd phase diagram

Initial data related to the Cd-Gd phase diagram were available from Johnson [37] who determined the solubility of Gd in liquid Cd by chemical analysis of filtered samples between 324 and 500 °C. The corresponding solubilities within this temperature range were given between 0.17 and 1.45 at.% Gd, respectively.

In a subsequent study by Bruzzone et al. [38], the Cd-Gd phase diagram was investigated by a combination of differential thermal analysis and chemical-, metallographic- and X-ray studies. Their corresponding phase diagram is shown in Figure 2. Phase equilibria and melting behaviour were determined in the complete composition range and altogether six intermetallic compounds were obtained. No detectable range of solid solubility was observed for any of the phases except for the high-temperature allotropic modification of Gd. By addition of Cd, β-Gd could be stabilised down to 725 °C where it decomposed in terms of a eutectoid reaction at 16 at.% Cd. β-Gd participates in a eutectic reaction $L \rightleftarrows$ β-Gd+CdGd at 27 at.% Cd and 920 °C, a temperature where 22 at.% Cd are dissolved. The compound richest in Gd is CdGd which melts congruently at 1170 °C. From this relatively high melting point, the liquidus is continuously decreasing, ending up in a eutectic reaction at 316 °C. All compounds except CdGd are formed incongruently along a cascade of peritectic reactions, i.e. Cd_2Gd (1010 °C), Cd_3Gd (815 °C), $Cd_{4-}Gd$ (806 °C), $Cd_{4.5-}Gd$ (803 °C), and Cd_6Gd (716 °C).

Moreover, a polymorphic transformation of Cd_2Gd into a high-temperature modification β-Cd_2Gd was indicated by Bruzzone et al. [38]. Since the range of stability of β-Cd_2Gd is

limited to a rather narrow temperature region, all attempts to obtain β-Cd_2Gd were unsuccessful.

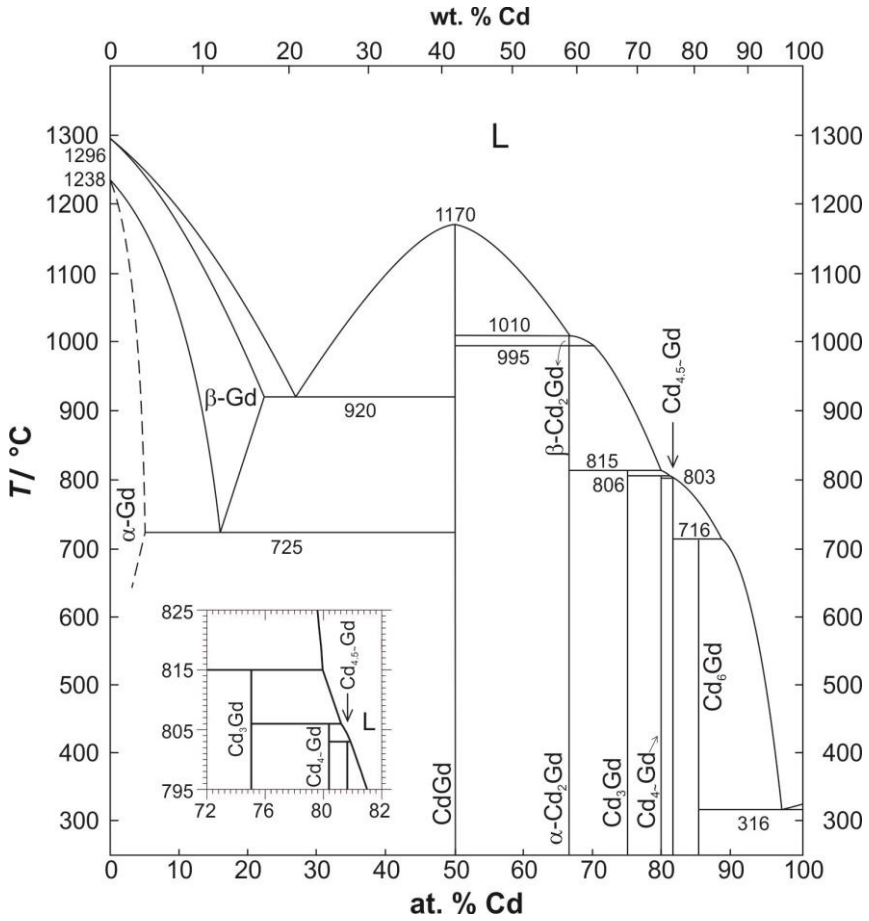

Fig. 2: Cd-Gd phase diagram according to Bruzzone et al. [38]

As indicated above, the liquidus line has its minimum at 316 °C and 97.5 at. % Cd which corresponds to the eutectic reaction L ⇄ Cd_6Gd+Cd. The solubility of Gd in liquid Cd was extrapolated from DTA results. Actually, the solubility up to 500 °C did not correspond to the data presented by Johnson [37] but was considerably higher. Subsequently, Roshchina and Bayanov [39] employed an emf method to determine activities of Gd in liquid Cd. From the kinks in their emf curves (*cf.* Fig. 3) the solubility of Gd in liquid Cd could be estimated between 390 and 528 °C. The values given within 2.4 and 3.5 at.% Gd are in good agreement with the corresponding phase boundary evaluated by Bruzzone et al. [38].

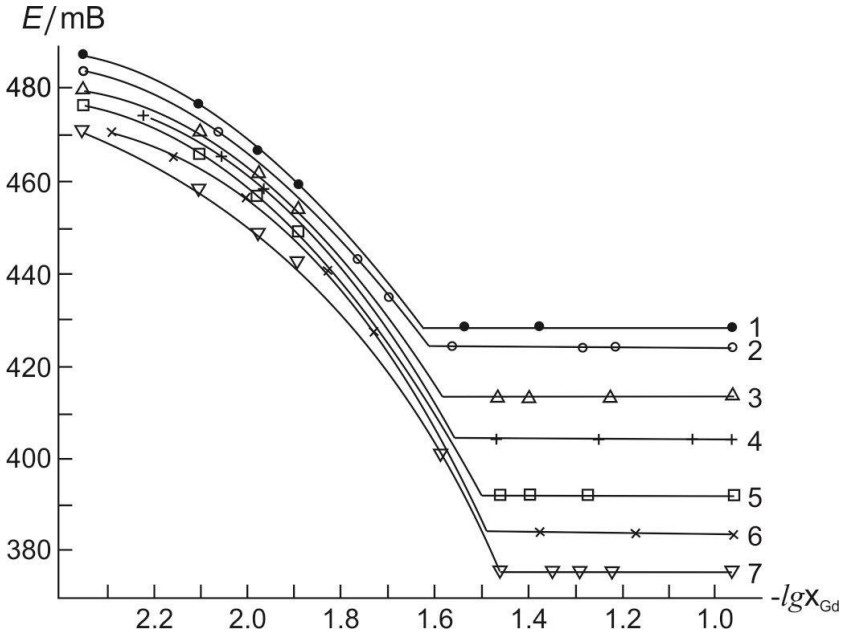

Fig. 3: emf results at different temperatures from Roshchina and Bayanov [39];
curve – T(K): 1 – 663.15, 2 – 675.15, 3 – 700.15, 4 – 723.65, 5 – 753.65, 6 – 775.15, 7 – 801.15

Based on the results of Bruzzone et al. [38], Gschneidner and Calderwood [40] presented an assessment of the Cd-Gd phase diagram. The latter authors described the compounds $Cd_{4\sim}Gd$ and $Cd_{4.5\sim}Gd$ with the consistent notation $Cd_{45}Gd_{11}$ and $Cd_{58}Gd_{13}$, which is also commonly used in other Cd-RE systems, see chapter *Intermetallic compounds in Cd-RE systems*. In addition, Gschneidner and Calderwood used slightly different temperatures for the allotropic transition and melting of Gd [41]. To maintain a temperature difference of 376 °C to their accepted melting point of Gd (1313 °C), the authors raised the isothermal reaction temperature of the eutectic reaction L⇄β-Gd+CdGd from 920 to 937 °C.

More recently, Tang and Gschneidner [42] performed DTA measurements of rapidly cooled as-cast alloys within the primary crystallisation field of β-Gd. They determined the isothermal reaction temperature of the eutectoid β-Gd ⇄ α-Gd+CdGd at 738 °C, i.e. 13 °C higher than the value given by Bruzzone et al. [38]. Moreover, they employed powder-XRD of alloys within the homogeneity range of the solid solution of Cd in β-Gd and derived a lattice parameter of pure β-Gd by extrapolation, given as 3.99±0.04 Å.

Actually, relevant phase diagram data were at first presented by Veleckis and Van Deventer [43] who listed isothermal reaction temperatures for eutectic reactions between REs and the respective compound richest in RE. As indicated by Gschneidner and Calderwood [44] these eutectic temperatures do not fit at all with subsequently reported values. Curiously, the values from Veleckis and Van Deventer agree reasonably with the isothermal reaction temperature values of the eutectoid reactions. Hence, it has to be assumed that the authors did not consider the high-temperature allotropic modifications of the respective RE. Indeed, their reported value for the eutectic reaction $L \rightleftarrows Gd+CdGd$ was 719 °C, a temperature which is considerably close to the isothermal reaction temperature of the eutectoid reaction $\beta\text{-}Gd \rightleftarrows \alpha\text{-}Gd+CdGd$ reported by Bruzzone et al. [38].

The Cd-Pr phase diagram

Compared to Cd-Gd, only limited information about the phase diagram Cd-Pr was available from literature. In a compilation of structural data of all intermetallic compounds present in the Cd-Pr equilibrium diagram (see below), Gschneidner and Calderwood [45] presented a partial phase diagram (Fig. 4). This version includes liquidus data reported previously by Johnson et al. [46]. The latter authors determined the solubility of Pr in liquid Cd by chemical analysis of filtered samples in the temperature range 350-534 °C. In addition, Johnson et al. performed differential thermal analysis and determined at least two invariant reactions, i.e. a degenerate eutectic between Cd and $Cd_{11}Pr$ and a peritectic decomposition of $Cd_{11}Pr$ at 570 °C. At this temperature a solubility of 3.5 at.% Pr was extrapolated from the data of Johnson et al. [46].

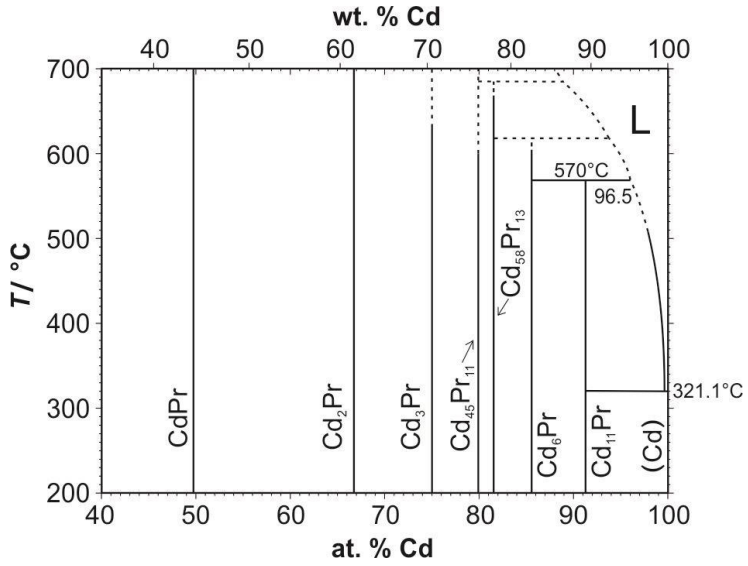

Fig. 4: Partial phase diagram of Cd-Pr according to [45]

Altogether, seven intermetallic compounds were indicated at the exact stoichiometric compositions of CdPr, Cd_2Pr, Cd_3Pr, $Cd_{45}Pr_{11}$, $Cd_{58}Pr_{13}$, Cd_6Pr and $Cd_{11}Pr$. Compared to the Cd-Gd phase diagram the compound richest in Cd has the stoichiometric composition $Cd_{11}RE$. Moreover, Veleckis and Van Deventer [43] determined experimentally an isothermal reaction temperature for a eutectic reaction between Pr and CdPr, given as 435 °C.

Intermetallic compounds in Cd-RE systems

As indicated in a previous review by Iandelli and Palenzona [47], only some of the Cd-RE phase diagrams have been investigated in detail, i.e. Cd-Y [48], Cd-La [49], Cd-Sm [50], Cd-Eu [51], Cd-Gd [38] and Cd-Yb [52]. More recently, Palenzona and Manfrinetti [52] and Canepa at al. [53] presented investigations in the systems Cd-Sc and Cd-Ce, respectively. However, less information was available about Cd-RE (RE...Pr, Nd, Tb, Dy, Ho, Er, Tm, Lu).

Although phase equilibria and melting behaviour of several systems are not known, almost all equilibrium phases were still determined and discussed extensively in literature. Curiously, all Cd-RE phase diagrams indicate that numerous intermetallic compounds are isotypic or even isostructural. Hence, structural data of these compounds were often investigated in a course of study; *cf. Refs.* [55-57]. A compilation of all stoichiometric compounds between Cd and REs with the exception of Pm is shown in Figure 5.

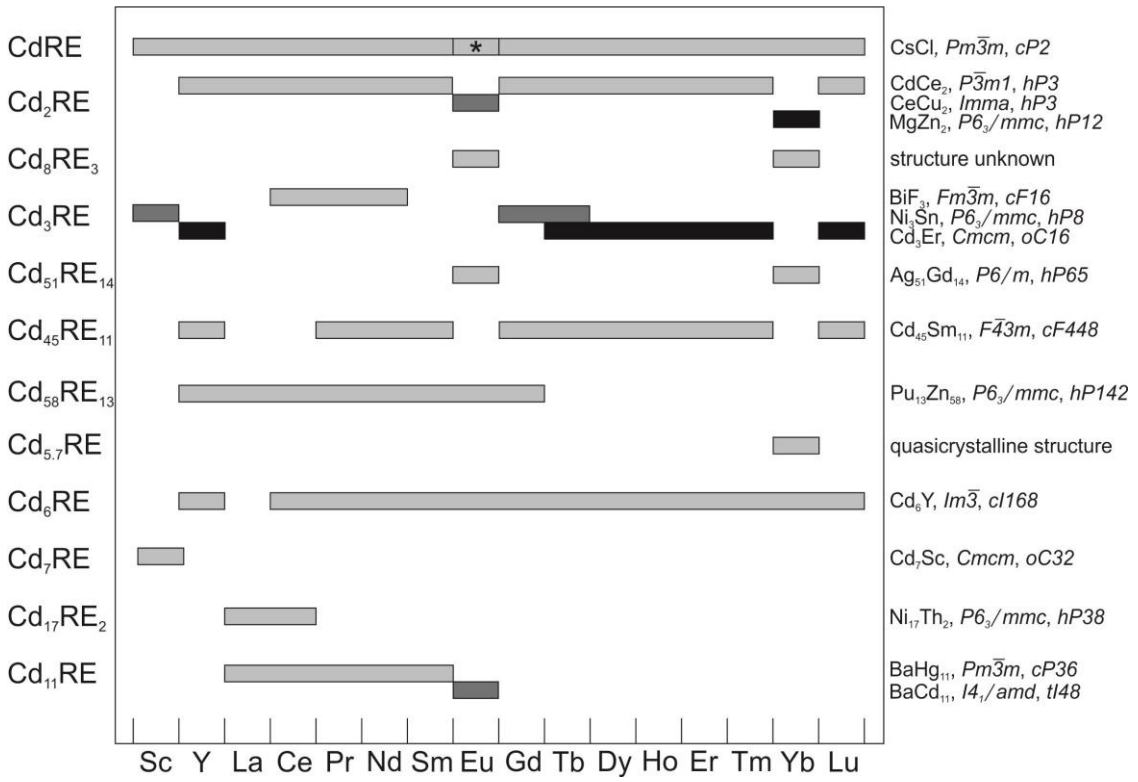

Fig. 5: Compilation of all intermetallic compounds between Cd and REs except Pm [44,48,53,54,59]

It is noticeable that with the exception of Cd_5Eu_6, which adopts a defect structure of the CsCl type [51], no intermetallic compounds are formed below 50 at.% Cd. Up to now, no information was given concerning homogeneity ranges and all compounds were described as line-compounds, i.e. no solid solubility of both Cd and RE was indicated. It can be observed that with increasing Cd content the crystal structures become more complicated and the existence of extensive order/disorder phenomena especially for structures with relatively high amounts of atoms per unit cell is assumed. In fact, Piao et al. [58] discussed for $Cd_{58}Ce_{13}$ a metrically commensurable representative $Cd_{58.68}Ce_{12.60}$, which is obviously a lock-in phase.

Previously, Palenzona [52] reported investigations in the Cd-Yb system and presented the complete phase diagram. A congruently melting compound with the stoichiometric composition $Cd_{5.7}Yb$ was indicated but no accurate structural information was given. From a recent examination of Tsai et al. [59], this phase was discovered to be a binary quasicrystal.

A compilation of all intermetallic compounds together with respective structure data and references relevant for the present studies is given in Table 1. The corresponding crystal structures are discussed in detail below.

Table 1: Crystal structure data of binary compounds in the Cd-Gd and Cd-Pr system

Stoich. comp.	RE	Lattice parameter (Å)	Pearson symbol	Space group	Strukturber. designation	Struct. type	Refs.
CdRE	Gd	a = 3.750	*cP*2	$Pm\bar{3}m$	*B*2	CsCl	[38]
	Pr	a = 3.822					[60]
α-Cd_2RE	Gd	a = 4.941, c = 3.467	*hP*3	$P\bar{3}m1$	*C*6	Cd_2Ce	[38]
	Pr	a = 5.025, c = 3.459					[61]
β-Cd_2RE	Gd	structure unknown					[38]
Cd_3RE	Gd	a = 6.621, c = 4.933	*hP*8	$P6_3/mmc$	$D0_{19}$	Ni_3Sn	[38]
	Pr	a = 7.186	*cF*16	$Fm\bar{3}m$	$D0_3$	BiF_3	[60]
$Cd_{45}RE_{11}$	Gd	a = 21.603	*cF*448	$F\bar{4}3m$	–	$Cd_{45}Sm_{11}$	[38]
	Pr	a = 21.842					[57]
$Cd_{58}RE_{13}$	Gd	a = 15.40, c = 15.28	*hP*142	$P6_3/mmc$	–	$Pu_{13}Zn_{58}$	[38]
	Pr	a = 15.71, c = 15.52					[57]
Cd_6RE	Gd	a = 15.441	*cI*168	$Im\bar{3}$	–	Cd_6Y	[62]
	Pr	a = 15.689					[63]
Cd_{11}RE	Pr	a = 9.287	*cP*36	$Pm\bar{3}m$	$D2_e$	$BaHg_{11}$	[60]

CdRE

Compounds with the stoichiometry CdRE are stable in all Cd-RE systems, and with no exception the crystal structure is of the CsCl-structure type [48,53,64]. However, the CsCl structure is in close relation to the *bcc* W-structure type (*A*2 type), which corresponds to the high-temperature allotropic modification of most REs [65]. From respective phase diagram data [38,49,50,54], rather high solid solubilities of Cd in high-temperature phases of REs are observed whenever the corresponding high-temperature phase adopts the *bcc* W-structure type. Certainly, the CsCl structure is an ordered variety of this solid solution. At the stoichiometric composition of CdRE, half of the RE sites in the *bcc* structure are substituted by Cd atoms. From the evaluation of single-phase alloys of the solid solution of Cd in β-Gd, Tang and Gschneidner [42] determined the lattice parameter of pure β-Gd by extrapolation. A linear decrease of the lattice parameter *a* with increasing Cd content was observed according to Vegard's rule. Regarding to the difference in covalent radii, this is exactly what is expected when Cd atoms systematically occupy Gd sites. However, a continuous solid solution does not exist in any of the Cd-RE phase diagrams between these related structures.

Cd_2RE

Except for Cd-Sc [53], compounds with the composition ratio 2:1 were found to exist in all Cd-RE systems [48,61]. Compounds at this stoichiometry were investigated extensively and at least three different structure types were found to exist; *cf.* Figure 5. Although most Cd_2RE compounds were described to adopt the Cd_2Ce-type some disagreement concerning the space group was observed in literature. They crystallise either in space group $P6/mmm$ [60-61] or $P\bar{3}m1$ [66-68]. Compounds with space-group symmetry $P6/mmm$ adopt the simple AlB_2-structure type with the site positions (⅓⅔½) and (000). This structure is characterised by a planar arrangement of Cd atoms with equidistant spacing to all neighbouring RE atoms, see Figure 6. Compounds crystallising with the space group $P\bar{3}m1$ maintain the Pearson code and Wyckoff sequence, the site positions are (⅓⅔ *z*) and (000). The latter structure, also known as the deformed AlB_2-type, is a disordered mixture of the simple AlB_2- and CdI_2-type structures. Hence, the Cd atoms are closer to the RE sites which

is indicated with bonds in Figure 6. Iandelli and Palenzona [61] as well as Mulokozi [69] described both Cd_2Gd and Cd_2Pr to crystallise in the Cd_2Ce-type with z = 0.42.

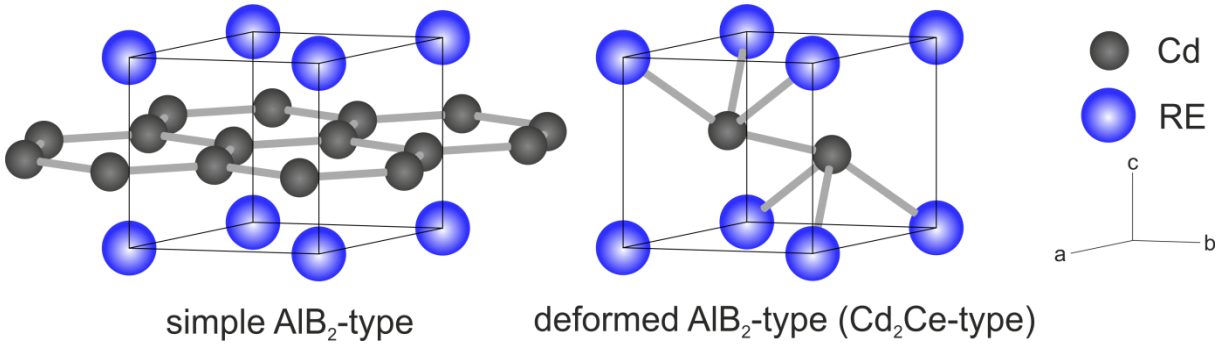

Fig. 6: Comparison of the simple and the deformed AlB_2-type (Cd_2Ce-type) structure

More recently, Bruzzone et al. [38] argued for a polymorphic transformation of the Cd_2Gd structure into a high-temperature modification denoted as β-Cd_2Gd. No information on the crystal structure was given.

Cd_3RE

Three different structure types have been investigated for Cd-RE compounds with the stoichiometric composition Cd_3RE. Corresponding compounds which contain so-called heavy REs (i.e. Tb-Lu) adopt the Cd_3Er-structure type with an orthorhombic crystal structure. Cd_3RE (RE = Ce, Pr, Nd) crystallise with a cubic structure originally known as the α-BiF_3 type [57]. This structure was previously determined by Hund and Fricke [70]. Obviously, α-BiF_3 is a homeotype structure of the *fcc* Cu-structure type (*A*1 type). In the case of Cd_3RE, Cd atoms are occupying all tetrahedral and octahedral holes formed by a virtual *fcc* atomic arrangement of RE atoms. In their study, Hund and Fricke found that atoms which are occupying the tetrahedral holes are slightly distorted referred to the atom in the centre (½½½). This leads to the occurrence of reflections which should be systematically absent according to the extinction rules of a face centred Bravais lattice. In the corresponding data set of Cd_3Pr, no mixed indices were observed and a perfect ordering was assumed.

Cd_3Gd crystallises with the Ni_3Sn-structure type [38]. Interestingly, the high-temperature modification of Ni_3Sn adopts the α-BiF_3 structure; *cf.* Schmetterer et al. [71]. The corresponding crystal structure of Cd_3Gd is characterised by a hexagonal arrangement of Cd atoms which are interconnected with Gd atoms. Both Cd and Gd atoms are coincidently arranged along chains, see Figure 7.

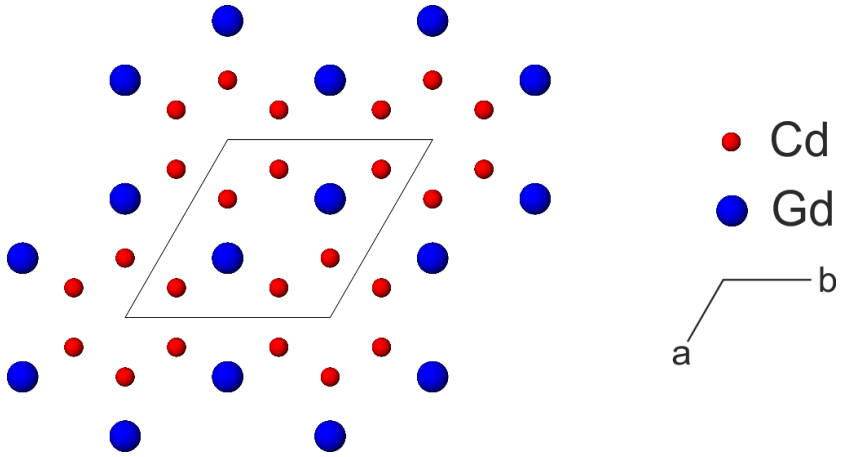

Fig. 7: Ni_3Sn-structured Cd_3Gd along [001] direction

$Cd_{45}RE_{11}$

Compounds with the stoichiometric composition $Cd_{45}RE_{11}$ are stable in almost all Cd-RE systems. According to Bruzzone et al. [57], these compounds are all isotypic and adopt the $Cd_{45}Sm_{11}$ structure with the Pearson symbol *cF*448. The rather complex structure was previously discussed by Fornasini et al. [72]. It can be described by the so-called cluster concept originally adopted by Bradley and Jones [73]. Accordingly, $Cd_{45}RE_{11}$ is an arrangement of 16 clusters of two types which are distributed along a NaTl-type unit cell which corresponds to a 2×2×2 superstructure of the *A*2 type. The two types of clusters which build up the $Cd_{45}Sm_{11}$ structure are also found in $Li_{22}Pb_5$ [74] and α-Mn [75], respectively.

$Cd_{58}RE_{13}$

With a composition close to $Cd_{45}RE_{11}$, a compound $Cd_{58}RE_{13}$ is formed in systems where the respective RE belongs to one of the elements between Y-Gd. Most structural information on the corresponding compounds was derived from powder diffraction methods [57,76]. It was indicated in literature that all $Cd_{58}RE_{13}$ compounds are isomorphous. The rather complex structure adopts the Pearson symbol *hP*142.

In an early study, Roof and Elliott [77] reported $Cd_{58}Ce_{13}$ with a variable composition and indicated that a continuous series of superstructures appear. The authors described this phase as a collection of micro phases which are responsible for various satellite reflections. More recently, an incommensurable modulation of $Cd_{58}Ce_{13}$ was elucidated by Piao et al. [58] and at least one lock-in phase $Cd_{58.68}Ce_{12.60}$ was indicated. Hence, extensive order-disorder phenomena are also assumed to be present in the $Cd_{58}Pr_{13}$ and $Cd_{58}Gd_{13}$ phases which are actually described in literature to adopt the $Pu_{13}Zn_{58}$-structure type.

From a detailed investigation of $RE_{13}Zn_{58}$ (RE...Ce,Pr,Sm,Gd,Tb,Dy) compounds, Piao et al. [78] observed a large variability in local ordering and composition. In fact, only $Ce_{13}Zn_{58}$ and $Pr_{13}Zn_{58}$ adopt the archetype structure $Pu_{13}Zn_{58}$. It has to be assumed that a similar structural diversity is also present for $Cd_{58}RE_{13}$ phases.

Cd_6RE

Investigations in various Cd-RE systems disclosed the existence of an intermetallic compound Cd_6RE. Johnson et al. [63] listed cell parameters for a number of Cd_6RE compounds. No additional structural information was given except that all homologues seem to be isomorphous. Moreover, Larson and Cromer [79] reported that the crystal structure of Cd_6Y is isotypic with $Be_{17}Ru_3$ but with an additional Cd position in a 24-fold position with the site occupation factor 0.33. The respective Cd atoms form a disordered tetrahedron which is located within a pentagonal dodecahedron cavity of Cd atoms.

Recently, Gomez and Lidin [62] employed single crystal X-ray diffraction to elucidate disorder phenomena in MCd_6 (M = Pr, Nd, Sm, Eu, Gd, Dy, Yb, Y and Ca) compounds. In the course of their study they could compare the different types of disorder of the central Cd_4 tetrahedra, which belong to the additional Cd position introduced by Larson and Cromer.

According to Gomez and Lidin, the respective Cd position is somehow split and manifests itself as smeared out electron density.

In a previous work, Gomez and Lidin [80] showed that $Dy_{13}Zn_{57}$ comprises structural building blocks that are also encountered in other $RE_{13}Zn_{58}$ compounds as well as in the related compounds $Cd_{58}RE_{13}$ and Cd_6RE. The structural motifs of the latter compounds differ only in the loss of some capping atoms and their orientation within the structure. The basic building block of Cd_6RE is shown in Figure 8a together with the respective cluster unit (Fig. 8b) which is formed by fusion of two building blocks.

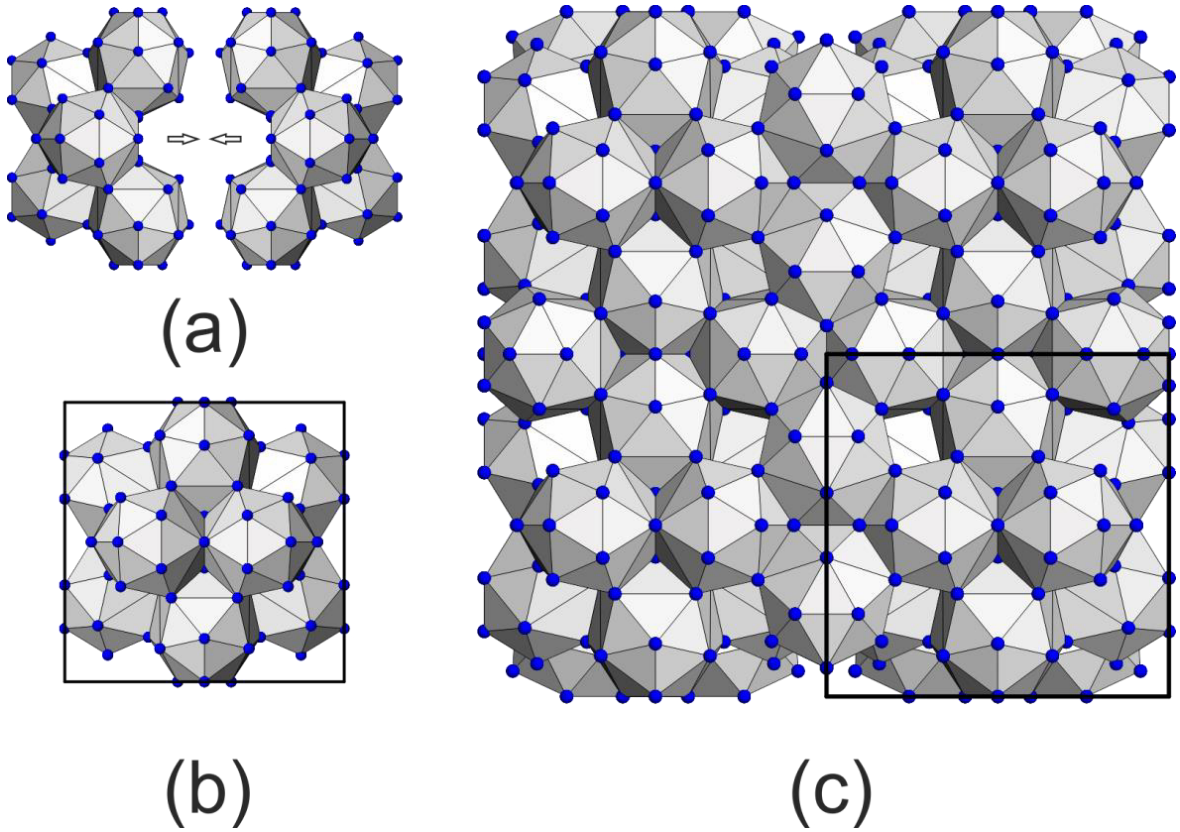

Fig. 8: Basic building block of Cd_6RE (a) and respective cluster unit of 12 MCd_{16} polyhedra (b); the cluster arrangement for the entire structure is shown in (c)

Actually, the cluster unit is built up of 12 MCd_{16} polyhedra forming 8 interstitial Cd_8 cubes. The Cd_8 cubes can be best seen in Figure 8c. The respective central Cd_4 tetrahedra are residing inside a cavity which is formed by the pentagonal basis of each polyhedral; *cf.* Figure 9.

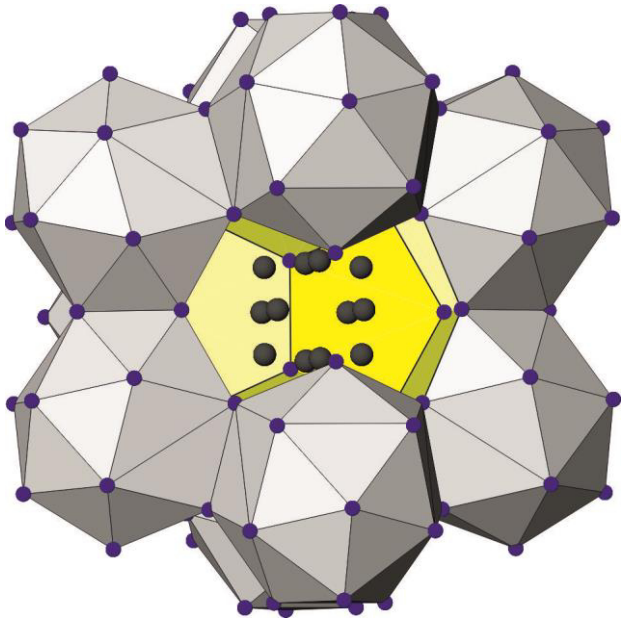

Fig. 9: Look inside the cluster unit; red atoms belong to the 24-fold position (occ. = 0.33); the pentagonal bases of the polyhedra are shown with different yellow nuances

Moreover, Gomez and Lidin [80] indicated that typical structure motifs found in Cd_6RE are also present in $Cd_{5.7}Yb$ which was previously discovered by Tsai et al. [59] to be a quasicrystal. Hence, Cd_6Yb serves as a crystalline approximant to the quasicrystal.

$Cd_{11}RE$

The compound richest in Cd is $Cd_{11}RE$. Compounds with this stoichiometry appear with two different crystal structures. With the exception of Eu all respective compounds adopt the $BaHg_{11}$-structure type with the Pearson Symbol *cP*36. No structural details except lattice parameters were given in literature. The archetype structure was determined by Peyronel [81].

The unit cell of $Cd_{11}RE$ is shown in Figure 10 together with two types of polyhedra which fill up the complete lattice.

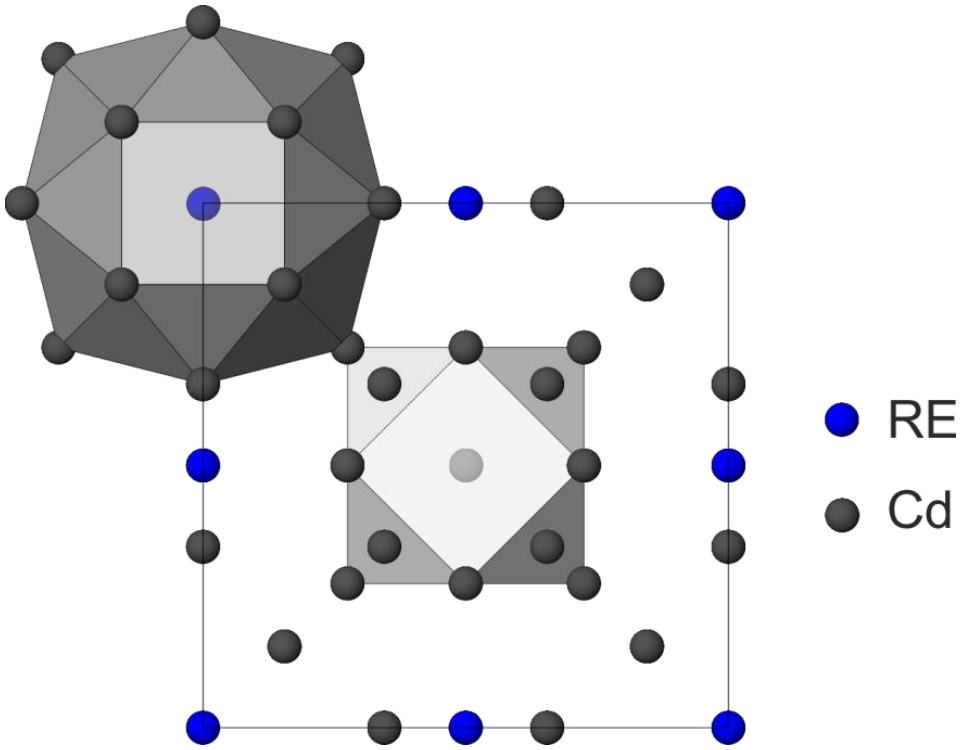

Fig. 10: View along [001] direction of the $Cd_{11}RE$ unit cell

Thermodynamic data in the system Cd-Gd

Compared to the thorough investigation of the equilibrium phase diagram, less information was available from literature regarding thermodynamic data. As indicated above, Roshchina and Bayanov [39] employed an emf method to determine activities of Gd in liquid Cd between 390 and 528 K (Fig. 3). By means of a Gibbs-Duhem integration, the standard Gibbs energy of formation of Cd_6Gd was calculated and given as -20.8±0.6 kJ·mol(at)$^{-1}$, referred to Cd(s) and Gd(s).

More recently Kurata et al. [82] presented an activity coefficient of Gd in liquid Cd at 500 °C, given as $\log\gamma_{Gd}$ = -6.20. Obviously, this value was derived from an evaluation of electrochemical studies of Sakamura et al. [83]. The latter authors listed activity coefficients of several REs in liquid Cd at 450 °C. Their corresponding activity coefficient of Gd at this temperature was given as -6.60.

Based on the phase diagram data of Johnson [37] and Bruzzone et al. [38], Kurata and Sakamura [84] made a CALPHAD-type optimisation of the Cd-Gd system between 0 and 60 at.% Cd, see Figure 11. All intermetallic compounds were modelled as stoichiometric line compounds with temperature dependent Gibbs energies in Joules per mole atoms, i.e. CdGd: -55700+22.5·T, Cd_2Gd: -43000+16.7·T, Cd_3Gd: -37200+16.0·T, $Cd_{45}Gd_{11}$: -33100+15.4·T, $Cd_{58}Gd_{13}$: -31900+15.1·T, Cd_6Gd: -26800+13.3·T.

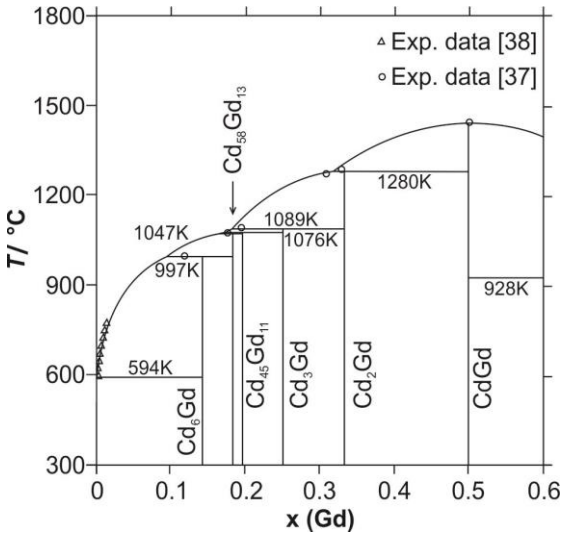

Fig. 11: Calculated Cd-Gd phase diagram according to [84]

Thermodynamic data in the system Cd-Pr

Concerning the system Cd-Pr, only limited information about thermodynamic data was available from literature. In an early study, Johnson and Yonco [85] determined activities of Pr in Cd-Pr alloys by electrochemical techniques. By means of a Gibbs-Duhem integration, the Gibbs energy of formation of $Cd_{11}Pr$ was calculated at 550 °C and given as -11.2 kJ·mol(at)$^{-1}$, referred to Cd(l) and Pr(s).

More recently, Castrillejo et al. [86] derived Gibbs energies of formation of $Cd_{11}Pr$, Cd_6Pr and $Cd_{58}Pr_{13}$ at 550 °C from activity data of their emf measurements. The corresponding values were listed as -11.2±0.1, -18.7±0.1 and -22.9±0.1 kJ·mol(at)$^{-1}$, respectively, for a temperature of 550°C. Furthermore, partial Gibbs energies of Pr in the two-phase fields $Cd_{58}Pr_{13}$+Cd_6Pr, Cd_6Pr+$Cd_{11}Pr$, and $Cd_{11}Pr$+L, were given as -107.6±0.6, -127.4±0.9 and -133.8±1.2 kJ·mol(at)$^{-1}$ at 550 °C.

Based on the results of Johnson and co-workers [46,85], Kurata and Sakamura [84] made a CALPHAD-type optimisation of the Cd-Pr system up to 25 at.% Pr; *cf.* Figure 12. They considered $Cd_{11}Pr$, Cd_6Pr and $Cd_{58}Pr_{13}$ as line compounds and listed following temperature dependent Gibbs energies in Joules per mole atoms: -24100+15.6·T ($Cd_{11}Pr$) and -27700+11.0·T (Cd_6Pr).

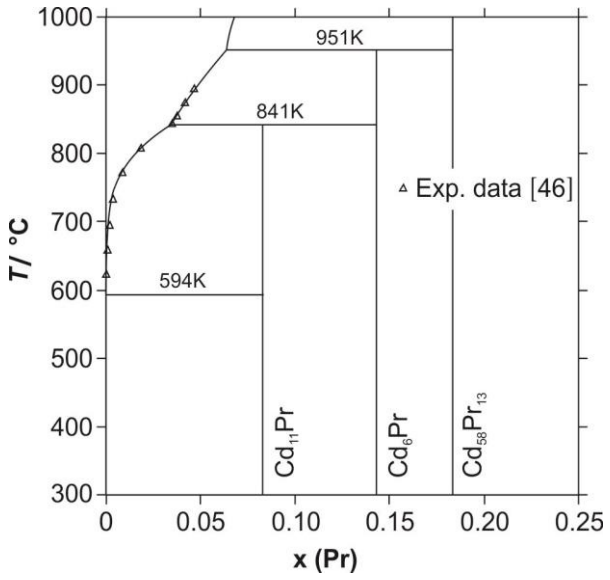

Fig. 12: Calculated Cd-Gd phase diagram according to [84]

References

[1] D. Olander. Nuclear fuels – present and future. *J. Nuclear Mater.* (2009), 389: 1-22.

[2] J. Magill, H. Schwoerer, F. Ewald, J. Galy, R. Schenkel, R. Sauerbrey. Laser transmutation of iodine-129. *Appl. Phys. B* (2003), 77(4): 387-390.

[3] M. Salvatores, G. Palmiotti. Radioactive waste partitioning and transmutation within advanced fuel cycles: Achievements and challenges. *Progr. Part. Nucl. Phys.* (2011), 66: 144-166.

[4] V. Arkhipov. Future nuclear energy systems: Generating electricity, burning wastes. *IAEA Bull.* (1997), 39(2): 30-33.

[5] OECD Nuclear Energy Agency. *Nuclear Energy Data* (2007), p. 56.

[6] D. D. Sood, S. K. Patil. Chemistry of nuclear fuel reprocessing: current status. *J. Radioanal. Nucl. Ch.* (1996), 203(2): 547-573.

[7] G. Choppin, J.-O. Liljenzin, J. Rydberg. Radiochemistry and Nuclear Chemistry, 3rd edition. *Butterworth-Heinemann* (2001), p. 610.

[8] World Nuclear Association. *Processing of Used Nuclear Fuel.* (updated 2013), available at: <http://www.world-nuclear.org/info/Nuclear-Fuel-Cycle/Fuel-Recycling/Processing-of-Used-Nuclear-Fuel/#1,2>.

[9] K. Banerjee, K. Raj, P. K. Wattal. Process Technology for Vitrification of High-level Radioactive waste. *International Conferences on Peaceful Uses of Atomic Energy* (2009), 2: 489-495.

[10] L. W. Gray. From Separations to Reconstitution-A Short History of Plutonium in the US and Russia. *Book of Abst., 217th ACS Nat. Meet., Calif.* (1999).

[11] M. J. Steindler, L. J. Anastasia, L. E. Trevorrow, A. A. Chilenkas. Laboratory development of the fluoride volatility process for oxidic nuclear fuels. *Nucl. Metall.* (1969), 15: p. 177.

[12] K. M. Harmon, G. Jansen. The salt cycle process. *Progr. Nucl. Energy* (1970), 4: p.429.

[13] T. Koyama, R. Fujita, M. Iizuka, Y. Sumida. An Experimental Study of Molten Salt Electro-refining of Uranium Using Solid Iron Cathode and Liquid Cadmium Cathode for Development of Pyrometallurgical Reprocessing. *J. Nucl. Sci. Technol.* (1995), 110: 357-368.

[14] T. Koyama, M. Iizuka, Y. Shoji, R. Fujita, H. Tanaka, T. Kobayashi, M. Tokiwai. An Experimental Study of Molten Salt Electro-refining of Uranium Using Solid Iron Cathode and Liquid Cadmium Cathode for Development of Pyrometallurgical Reprocessing. *J. Nucl. Sci. Technol.* (1997), 34: 384-393.

[15] J. P. Ackerman. Chemical Basis for Pyrochemical Reprocessing of Nuclear-Fuel. *Ind. Eng. Chem.* Res. (1991), 30: 141-145.

[16] J. J. Laidler, J. E. Battles, W. E. Miller, J. P Ackerman, E. L. Carls. Development of Pyroprocessing Technology. *Progr. Nucl. Energy* (1997), 31(1/2): 131-140.

[17] O. Conocar, N. Douyere, J.-P. Glatz, J. Lacquement, R. Malmbeck, J. Serp. Promising pyrochemical actinide/lanthanide separation processes using aluminium. *Nuclear Sci. Eng.* (2006), 153: 253-261.

[18] M. Kurata, Y. Sakamura, T. Hijikata, K. Kinoshita. Distribution behavior of uranium, neptunium, rare-earth elements (Y,La,Ce,Nd,Sm,Eu,Gd) and alkaline-earth metals (Sr,Ba) between molten LiCl-KCl eutectic salt and liquid cadmium or bismuth. *J. Nuclear Mater.* (1995), 227: 110-121.

[19] I. Johnson, M. Chasanov, R. Yonco. Pu-Cd System: Thermodynamics and Partial Phase Diagram. *Trans. Met. Soc. AIME* (1965), 233: 1408-1414.

[20] J. P. Ackerman, J. L. Settle. Partition of lanthanum and neodymium metals and chloride salt between molten cadmium and molten LiCl-KCl eutectic. *J. Alloys Comp.* (1991), 177: 129-141.

[21] T. Koyama, T. R. Johnson, D. F. Fischer. Distribution of actinides in molten chloride salt/cadmium metal systems. *J. Alloys Comp.* (1992), 189: 37-44.

[22] H. Moriyama, S. Seshimo, K. Moritani, Y. Ito, T. Mitsugashira. Reductive Extraction Behavior of Actinide and Lanthanide Elements in Molten-Salt and Liquid- Metal Binary Phase Systems. *J. Alloys Comp.* (1994), 213: 354-359.

[23] H. Moriyama, H. Yamana, S. Nishikawa, S. Shibata, N. Wakayama, Y. Miyashita, K. Moritani, T. Mitsugashira. Thermodynamics of reductive extraction of actinides and lanthanides from molten chloride salt into liquid metal. *J. Alloys Comp.* (1998), 271: 587-591.

[24] T. L. Reichmann, H. S. Effenberger, H. Ipser. Experimental investigation of the Cd-Pr phase diagram. *PlosOne* (2014), 9(4): 1-14.

[25] T. L. Reichmann, H. Ipser. Reinvestigation of the Cd-Gd phase diagram. *J. Alloys Comp.* (2014), in print.

[26] B. Skołyszewska-Kühberger, T. L. Reichmann, H. Ipser. Phase equilibria in the neodymium-cadmium binary system. *J. Alloys Comp.* (2014), 606: 242-248.

[27] B. Skołyszewska-Kühberger, T. L. Reichmann, H. S. Effenberger H. Ipser. A re-investigation of the cerium-cadmium phase diagram and a structural analysis of the high-temperature phase Ce_2Cd_{17}. *Publication in preparation*.

[28] T. L. Reichmann, H. Ipser. Thermochemical Investigations in the System Cadmium-Praseodymium Relevant for Pyrometallurgical Fuel Reprocessing. *Metall. Mater. Trans. A* (2014), 45(3): 1171-1180.

[29] T. L. Reichmann, R. Ganesan, H. Ipser. Thermochemical investigations in the system Cd-Gd. *J. Alloys Comp.* (2014), 610: 676-683.

[30] B. Skołyszewska-Kühberger, T. L. Reichmann, R. Ganesan, H. Ipser. Thermodynamic study of the cerium-cadmium system. *CALPHAD* (2014), 44: 14-20.

[31] B. Skołyszewska-Kühberger, H. Ipser. Thermodynamic study of the neodymium-cadmium system. *Publication in preparation*.

[32] T. L. Reichmann, K. W. Richter, H. Ipser. Enthalpies of formation of Cd-Pr intermetallic compounds and thermodynamic assessment of the Cd-Pr system. *CALPHAD* (2014), 47: 56-62.

[33] F. L. Verwiebe. Water and the different forms of ice. *J. Tennessee Acad. Sc.* (1939), 14: 328-331.

[34] A. Prince. Alloy phase equilibria. *Elsevier publishing company* (1966).

[35] P. Ehrenfest. Phase changes in the ordinary and extended sense classified according to the corresponding singularities of the thermodynamic potential. *Proceedings of the Koninklijke Nederlands Akademie van Wetenschappen* (1933), 36: 153-157.

[36] J. S. Blundell, K. M. Blundell. Concepts in Thermal Physics. *Oxford University Press* (2008).

[37] I. Johnson. Solubility of the Rare-Earth Metals in Liquid Cadmium. *2nd Proc. Conf. Rare Earth Res.* (1962), 125-131.

[38] G. Bruzzone, M. L. Fornasini, F. Merlo. The Gadolinium-Cadmium System. *J. Less-Common Met*. (1971), 25: 295-301.

[39] V. R. Roshchina, A. P. Bayanov. Thermochemistry of gadolinium-cadmium alloy formation. *J. Phys. Chem.* (1981), 55(12): 3017-3020.

[40] K. A. Gschneidner Jr, F. W. Calderwood. The Cd-Gd (Cadmium-Gadolinium) System. *Bull. Alloy Ph. Diagr.* (1988), 9(1): 29-30.

[41] K. A. Gschneidner Jr, F. W. Calderwood. Intra Rare Earth Binary Alloys: Phase Relationships, Lattice Parameters and Systematics. *Handb. Phys. Chem. Rare Earths* (1986).

[42] J. Tang, K. A. Gschneidner Jr. Physical metallurgy and magnetic behaviour of Cd-stabilized b.c.c. β-Gd alloys. *J. Alloys Comp.* (1996), 234: 26-33.

[43] E. Veleckis, E. Van Deventer. ANL-6925, Semi-Annual Report. *Argone National Lab* (1964).

[44] K. A. Gschneidner Jr, F. W. Calderwood. The Cadmium-Rare Earth Systems. *Bull. Alloy Ph. Diagr.* (1988), 9(1): 16-20.

[45] K. A. Gschneidner Jr, F. W. Calderwood. The Cd-Pr system. *Bull. Alloy Phase Diag.* (1988), 9: 130-132.

[46] I. Johnson, K. E. Anderson, R. A. Blomquist. Partial Constitutional Diagrams for Cd-La, Cd-Ce, Cd-Pr, Cd-Nd and Cd-Sm Systems. *Trans. ASM* (1966), 59: 352-355.

[47] A. Iandelli, A. Palenzona. Crystal chemistry of intermetallic compounds. *Hand. Phys. Chem. Rare Earths* (1979), 2: 1-54.

[48] E. Ryba, P. K. Kejriwal, R. Elmendorf. The Partial Yttrium-Cadmium System. *J. Less-Common Met.* (1969), 18(4): 419-422.

[49] G. Bruzzone, F. Merlo. The Lanthanum- Cadmium System. *J. Less-Common Met.* (1973), 30(2): 303-305.

[50] G. Bruzzone, M. L. Fornasini. Contribution to the system samarium-cadmium. *J. Less-Common Met.* (1974), 37: 289-292.

[51] W. Köster, J. Meixner. The constitution of the systems of europium with silver, cadmium, and indium and the cadmium-strontium system. *Z. Metallk.* (1965), 56(10): 695-703.

[52] A. Palenzona. The Ytterbium-Cadmium System. *J. Less-Common Met.* (1971), 25: 367-372.

[53] A. Palenzona, P. Manfrinetti. The phase diagram of the Sc-Cd system. *J. Alloys Comp.* (1996), 237: 121-123.

[54] F. Canepa, G. A. Costa, E. A. Franceschi. The phase diagram of the cerium-cadmium system. *Lan. and Act. Res.* (1985), 1(1): 41-47.

[55] A. Iandelli, E. Botti. The crystal structure of some intermetallic compounds of the rare earths. *Gazz. Chim. Ital.* (1937), 67: 638-644.

[56] A. Iandelli. Intermetallic compounds of the rare earth metals. *Phys. Chem. of Metall. Sol. Intermetall. Comp.* (1960), 1: 367-385.

[57] G. Bruzzone, M. L. Fornasini, F. Merlo. Rare Earth Intermediate Phases with Cadmium. *J. Less-Common Met.* (1973), 30: 361-375.

[58] S. Y. Piao, L. Palatinus, S. Lidin. All the disorder mechanisms in the 13:58 phases come together. Out of the modulated confusion rises the remarkable phase $Ce_{12.60}Cd_{58.68}$. *Inorg. Chem.* (2008), 47: 1079-1086.

[59] A. P. Tsai, J. Q. Guo, E. Abe, H. Takakura, T. J. Sato. A stable binary quasicrystal. Nature (2000), 408: 537-538.

[60] A. Iandelli, R. Ferro. Alloys of Cadmium with Lanthanum, Cerium and Praseodymium. *Gazz. Chim. Ital*. (1954), 84: 463-478.

[61] A. Iandelli, A. Palenzona. On Occurrence of MX_2 Phases of Rare Earths with Ib, IIb and IIIb Group Elements and Their Crystal Structures. *J. Less-Common Met.* (1968), 15: 273-284.

[62] C. P. Gomez, S. Lidin. Comparative structural study of the disordered MCd_6 quasicrystal approximants. *Phys. Rev. B* (2003), 68: 1-9.

[63] I. Johnson, R. V. Schablaske, B. S. Tani, K. Anderson. $CeCd_6$-Type Rare Earth-Cadmium Alloys. *Trans. Met. Soc. AIME* (1964), 230: 1485-1487.

[64] A. Iandelli, A. Palenzona. Atomic size of rare earths in intermetallic compounds. MX compounds of CsCl type. *J. Less-Common Met.* (1965), 9: 1-6.

[65] K. A. Gschneidner. The theory of phase formation in rare earth metal systems. *Archives Metall. Mat.* (2006), 51(4): 519-524.

[66] E. Laube, J. B. Kusma. Über einige Y- und Dy-haltige Legierungsphasen. *Monatsh. Chem.* (1964), 95: 1504-1513.

[67] J. B. Kusma, N. S. Uhryn. Crystal structures of some compounds of rare earth metals with cadmium. *Dopovidi Akademii Nauk Ukrains'koi RSR* (1966), 1025-1027.

[68] R. D. Hoffmann, R. Pöttgen. AlB_2-related intermetallic compounds - a comprehensive view based on group-subgroup relations. *Z. Kristallogr.* (2001), 216: 127-145.

[69] A. M. Mulokozi. Nature of bonding in Rare-Earth compounds RX_2 with AlB_2-type or closely related structures I: Compounds RCd_2 with a deformed AlB_2 structure and influence of F-bonding. *J. Less-Common Met.* (1977), 53: 205-210.

[70] F. Hund, R. Fricke. Der Kristallbau von α-BiF_3. *Z. Anorg. Ch.* (1949), 258: 198-204.

[71] C. Schmetterer, H. Flandorfer, K. W. Richter, U. Saeed, M. Kauffman, P. Roussel, H. Ipser. A new investigation of the system Ni-Sn. *Intermetallics* (2007), 15: 869-884.

[72] M. L. Fornasini, B. Chabot, E. Parthe. The Crystal Structure of $Sm_{11}Cd_{45}$ with γ-Brass and α-Mn Clusters. *Acta Cryst.* (1978), B34: 2093-2099.

[73] A. J. Bradley, P. Jones. An X-ray investigation of the copper-aluminium alloys. *J. Inst. Met.* (1933), 51: 131-162.

[74] A. Zalkin, W. J. Ramsey. Intermetallic Compounds between Lithium and Lead. IV. The Crystal Structure of $Li_{22}Pb_5$. *J. Phys. Chem.* (1958), 62: 689-693.

[75] J. A. Oberteuffer, J. A. Ibers. A refinement of the atomic and thermal parameter of α-manganese from a single crystal. *Acta Cryst.* (1970), B26: 1499-1504.

[76] J. Tang, K. A. Gschneidner Jr. Searching for new heavy fermion materials in cerium intermetallic compounds. *J. Less-Common Met.* (1989), 149: 341-347.

[77] R. B. Roof Jr., G. R. B. Elliot. X-ray diffraction evidence for microphases in $CeCd_{\sim 4.5}$ solid solutions. *Inorg. Chem.* (1965), 4: 691-697.

[78] S. Y. Piao, C. P. Gomez, S. Lidin. Complexity of hexagonal approximants in the $RE_{13}Zn{\sim}58$ system (RE = Ce, Pr, Nd, Sm, Gd, Tb and Dy). *Z. Kristallogr.* (2006), 221: 391-401.

[79] A. C. Larson, D. T. Cromer. Crystal Structure of YCd_6. *Acta Cryst.* (1971), B27: 1875-1879.

[80] C. P. Gomez, S. Lidin. Structure of $Dy_{13}Zn_{57}$ a binary quasicrystal approximant. *Solid State Sci.* (2002), 4: 901-906.

[81] G. Peyronel. Struttura della fase $BaHg_{11}$. *Gazz. Chim. Ital.* (1952), 82: 679-690.

[82] M. Kurata, Y. Sakamura, T. Matsui. Thermodynamic quantities of actinides and rare earth elements in liquid bismuth and cadmium. *J. Alloys Comp.* (1996), 234: 83-92.

[83] Y. Sakamura, T. Inoue, T. S. Storvick, L. F. Grantham. Characterizations of Rare Earths and Actinides in a Molten Salt/Liquid Cadmium System. *26th Symp. on Molten Salt Chem. Sapporo* (1995), p. 101.

[84] M. Kurata, Y. Sakamura. Thermodynamic assessment of systems of actinide or rare earth with Cd. *J. Phase Equilib.* (2001), 22(3): 232-240.

[85] I. Johnson, R.M. Yonco. Thermodynamics of Cadmium- and Zinc-Rich Alloys in the Cd-La, Cd-Ce, Cd-Pr, Zn-La, Zn-Ce and Zn-Pr Systems. *Met. Trans.* (1970), 1: 905-910.

[86] Y. Castrillejo, M. R. Bermejo, P. D. Arocas, A. M. Martínez, E. Barrado. The electrochemical behaviour of the Pr(III)/Pr redox system at Bi and Cd liquid electrodes in molten eutectic LiCl-KCl. *J. Electroanalyt. Chem.* (2005), 579: 343-358.

II. Experimental methods

Sample preparation

The preparation of bulk alloys as required for phase diagram studies and structure determination was strongly dependent on the element combination and thus on the respective RE. Detailed descriptions of thermal treatments and preparation conditions are given in the respective research papers in chapter *Results and Discussion*. The basic preparation strategy is outlined below.

To prevent REs from oxidation, the complete sample preparation was carried out in a glove box with Ar as protective gas. All samples were prepared from pure elements, using Cd shots and RE lumps. Before use, RE metals were filed in order to remove their matte surface layer. Stoichiometric amounts of the metals were weighed into Ta crucibles and enclosed by arc welding (Fig. 13). For further equilibration, the crucibles were sealed into silica glass tubes.

Fig. 13: Ta crucible were enclosed by arc welding

Afterwards, melting and annealing procedures were performed in muffle furnaces. In an initial pre-heating step at a very low heating rate, Cd reacted with the RE rather completely before reaching elevated temperatures. This had a decisive influence on the quality of the final samples because it drastically decreased the Cd vapour pressure inside the crucible: several times it was observed that samples with rather high Cd contents, heated too fast, showed a drastic expansion of the Ta crucibles (see Fig. 14).

Subsequently, samples were homogenised at elevated temperatures, typically above the melting point of the respective alloy. Optionally, an induction furnace as well as a high-temperature Mo-furnace was used to reach temperatures above 1100 °C.

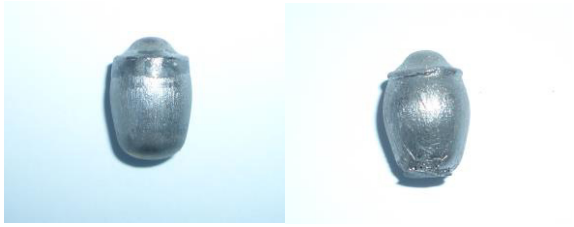

Fig. 14: Expanded Ta-cruciples

After homogenisation, the samples were annealed at defined temperatures allowing respective equilibrium phase formation to occur. Corresponding phase equilibria were preserved by quenching in cold water. In the case of annealing at moderate temperatures it was sometimes useful to powder respective samples and press them into pills before annealing. This allowed for rather short diffusion paths and supported equilibration.

In addition, as-cast alloys were prepared by fast cooling from the liquid state. Their characteristic microstructures served as helpful information for the correct evaluation of reaction types. Cooling from the liquid state was also required to prepare single crystals of various phases for structural investigation, i.e. single crystal X-ray diffraction. In this case, slowly cooling of alloys with a nominal composition within the primary crystallisation field of the respective compound was a very effective method. Suitable single crystals could also be synthesised by annealing the corresponding phase in equilibrium with the liquid. As an alternative “pendulum-annealing”, i.e. slow and repeated cycling over the transformation temperature of the respective phase, was a proper way to achieve single crystals at moderate temperatures.

Experimental evaluation of phase diagrams – strategy

The principal access to experimental phase diagram evaluation is to prepare equilibrated samples comprising distinct phase equilibria at various defined conditions, i.e. temperature, pressure and composition. In metallic systems, homogenisation of the components is primary achieved by alloying at temperatures above the corresponding melting points (e.g. arc melting, induction or levitation melting). After a certain annealing duration, the alloys are usually investigated by isothermal and dynamic methods. Actually, there is no guarantee that an alloy reached thermodynamic equilibrium at the corresponding conditions after annealing and good sample quality mostly depends on the experience of the experimenter. Moreover, different element combinations have to be treated in different ways with respect to the sample preparation. In the current studies, the rather high vapour pressure of Cd even at low-temperatures as well as the high reactivity of REs turned out to be the main challenges which had to be overcome. Details of the experimental procedure used for the current studies are given in the respective research papers in chapter *Results and Discussion*.

An initial sample characterisation is usually done by X-ray powder diffraction (powder-XRD) which allows the identification of phases formed in an alloy. Powder-XRD is best combined with energy- or wavelength-dispersive X-ray spectroscopy (EDS, WDS) as these methods allow a rather exact determination of the phase compositions within a multi-phase sample. A combination of powder-XRD and X-ray spectroscopy is usually used to determine equilibria between well identified phases. In the case of non-stoichiometric compounds or extended solid solutions, cell dimensions usually show distinct variation as a function of composition. From the variation of the lattice parameters with composition, defect mechanism of certain phases can be elucidated.

Corresponding phase transitions and melting temperatures are measured using dynamic methods, e.g. differential thermal analysis (DTA). With a combination of isothermal and dynamic methods a complete phase diagram can be constructed. To realise a proper description of a phase diagram as well as a complete structural characterisation of all intermetallic compounds, several experiments may be used for combination (e.g. high-temperature powder XRD, single crystal X-ray diffraction).

Light optical microscopy (LOM)

Light optical microscopy is often the first method applied to check if a sample is well homogenised and if the amount of present phases corresponds to the equilibrium state. The instrument used for the present study was a binocular reflected-light microscope (Zeiss Axiotech 100) equipped with a bi-refringent prism for differential interference contrast (DIC) mode.

For imaging, a representative piece of the bulk sample was embedded in hot mounting resin and then ground and polished. Most frequently, bright field imaging was used to distinguish different phases according to their reflectance. Additional information concerning surface consistency is obtained by dark field imaging where the beam passes a dark channel system before it enters the surface at low angle. The contrast in this mode is exclusively due to scratches, holes and cracks which arise during pre-treatment of the samples. Edges at the grain boundaries provide information about size and shape of different grains.

In the polarised imaging mode, a polarised beam is modified according to the optical properties of the respective phases. Usually, phases with low cell symmetry affect the polarised light more than phases with high symmetry. The polarisation imaging mode is a helpful tool to identify single crystals which make themselves appear with a unique crystallographic orientation.

When the polarised beam passes a bi-refringent prism before it enters the sample one is operating in the DIC imaging mode. This method allows observing a relief in the microstructure which may appear during polishing of the samples. The effect is due to different abrasive rates originated from different mechanical properties of the respective phases in the sample.

In fact, the combination of LOM with backscattering electron imaging (BSE) used in scanning electron microscopy (SEM) is often essential for the unambiguous identification of phases. As the thermal history of a sample is directly displayed from its microstructure, an accurate investigation with LOM is often inevitable to gain information about the crystallisation sequence and type of reactions.

Scanning electron microscopy (SEM)

Scanning electron microscopy (SEM) in combination with EDS analysis is conventionally applied to determine homogeneity ranges and limiting solid solubilities of the phases. In combination with a backscattering electron (BSE) as well as a secondary electron (SE) detector, the microstructure and topography of the surface is displayed with high resolution.

Representative pieces of the bulk samples are embedded into conducting resin before they are ground and polished. In the current studies an environmental SEM (Zeiss Supra 55 VP ESEM) was used. Pure elements were employed for the calibration at the characteristic X-ray lines. As an alternative an internal standard was used. ZAF matrix correction was used to determine the composition from the measured X-ray intensities. The composition of a certain phase was measured at ten or more spots in order to minimise statistical errors.

Actually, a thorough EDS investigation comprises the search for compositional variability within the corresponding phases as it may be present especially within large grains. These so-called coring effects often occur within non-stoichiometric phases which exhibit significant changes of the composition range with temperature. Accordingly, line scans with a fine raster of measured points are performed. By the way, this method exposes small inclusions which may be dedicated to unreacted material or result from secondary precipitation. In addition, surface scans with a two-dimensional raster of measured points are used to determine the overall composition of a sample. However, this may be only valuable if the microstructure does not expose holes or scratches.

The visual distinction of phases with BSE is often not unambiguous because of the weak contrast which is primarily due to differences of the electron densities of the phases. It turned out that especially Cd-RE phases show unexpected backscatter coefficients due to differences in packing density. Although $Cd_{45}RE_{11}$ has a higher average atomic number than $Cd_{58}RE_{13}$, the latter phase appears brighter in the BSE imaging mode. A proper distinction of both phases with stoichiometric compositions rather close to each other is only realised in combination with LOM. For a clear identification of phases another method has to be taken into account, the powder X-ray diffraction.

Powder X-ray diffraction (powder-XRD)

Powder-XRD is one of the most frequently applied methods for the identification of crystalline substances. This method uses approximately monochromatic X-ray radiation for diffraction on hypothetical lattice planes according to the Bragg approach. The appearance of interferences is exclusively dependent on the cell content of the crystal structure which is unique for each crystalline substance.

Phase identification and precise lattice parameters were obtained using a Bruker D8 Discover Series 2 powder diffractometer equipped with a LynxEye silicon strip detector and a Guinier-Huber camera 670 operating with Cu-$K_{\alpha 1}$ radiation and an image plate detector. As an alternative a solid state detector was used in combination with Bragg-Brentano pseudo-focussing geometry. High purity standard materials (Si, Ge) were taken as internal standards to precisely determine lattice parameters.

For structural refinement, a least square algorithm according to the Rietveld Method [1,2] was applied using the software DIFFRAC^{plus}TOPAS [3]. This semi-empirical method is used to adapt a theoretical line profile to the observed line profile. The calculated pattern is based on structure-, profile- and instrument-related parameters. Depending on the quality of the data set different refinement parameters can be varied in order to minimise the residual values which express the quality of the refinement. All initial structural data for the refinement are taken from literature (e.g. [4]) or have to be determined with single crystal methods (e.g. single crystal XRD). Diffraction peaks, which are usually subjected to peak broadening, were modelled according to the *fundamental parameter Ansatz* [5-7]. This approach exclusively uses instrumental parameters to describe the shape of the peaks and no experimental parameters are taken into account.

Powder-XRD measurements of Cd-RE alloys turned out to be challenging due to the high sensitivity of REs against oxygen and moisture. During diffraction experiments sample holders with X-ray transparent lids were used to prevent the sample powders from oxidation. Unfortunately, measured intensities were drastically lowered due to scattering effects of the X-rays on the surface of the respective lids. This was accompanied by quite high absorption effects of the REs itself.

Differential thermal analysis (DTA)

Thermal analyses (TA) are standard dynamic techniques used for measuring physical properties of a substance as a function of temperature, using a controlled temperature program. Differential thermal analysis (DTA), however, is especially applied to determine thermal reaction temperatures. The use of DTA in combination with the above mentioned isothermal methods is inevitable for the determination of transition reactions and the interpretation of the reaction sequence.

In the current studies, three different instruments were used for DTA, a Netzsch 404S DTA, a Setaram multi HT Calorimeter and a Netzsch DSC 404 F1 Pegasus. Representative sample pieces were enclosed in Ta crucibles (Fig. 15) with flat bottoms by arc welding. Sapphire was taken as a reference material and the temperature was measured with type-S (Pt/Pt10%Rh) thermocouples which were calibrated at the melting points of high purity Sn, Zn, Ag and Cu. Evaluation of the DTA curves was done with Netzsch Proteus Software.

In principle, sample and reference are placed in a symmetrical furnace chamber which provides an equal geometrical surrounding of both positions. The temperature is recorded at the sample and reference position while both undergo the same heat treatment. During different heating and cooling cycles, thermal effects exclusively occur within the sample material. Corresponding temperature differences are recorded and serve for the evaluation of transition temperatures.

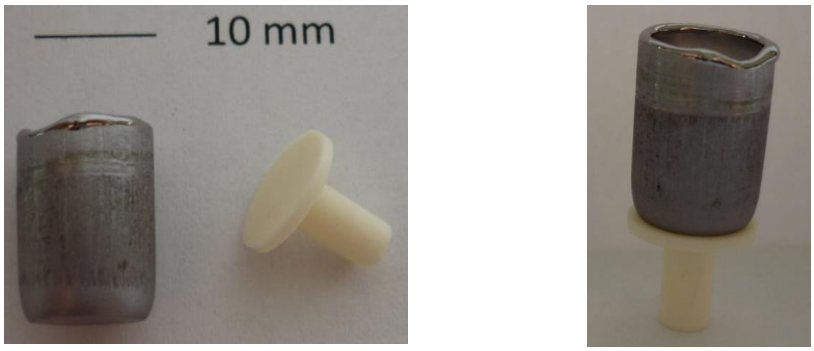

Fig. 15: Ta crucibles used for DTA measurements

Determination of thermodynamic properties

For a proper description of a phase diagram, phase equilibria and transition temperatures have to be determined at given conditions. Nevertheless, phase diagram data exclusively originate from thermodynamic properties as a function of temperature, pressure and composition. The knowledge of thermodynamic data is inevitable as these data may allow the prediction of diffusion behaviours and phase formations in multi-component systems.

Partial thermodynamic data can be gained performing vapour pressure measurements or electrochemical methods. From the partial values, integral data can be obtained by mathematical approaches (e.g. Gibbs-Duhem integration). Calorimetric methods are usually employed to determine integral enthalpies of mixing of liquid alloys as well as enthalpies of formation at well defined compositions. With the use of differential scanning calorimetry (DSC), heat capacities or heats of transition are obtained. Although several thermochemical and thermodynamic measurement techniques exist, it depends on the behaviour of the material which methods are applicable. In the case of Cd-RE alloys, the rather high vapour pressure of Cd even at low-temperatures together with the sensitivity of REs against oxygen and moisture, excluded some of the conventional methods. However, the high vapour pressure of Cd was favourable for the use of a rather exotic vapour pressure measurement, the non-isothermal isopiestic method.

In the course of a thermodynamic optimisation of a multi-component system according to the CALPHAD (Computer Coupling of Phase Diagrams and Thermochemistry) approach, phase diagram and thermodynamic data are critically evaluated. The CALPHAD approach is a semi-empirical method which is usually used to describe multi-component systems on the basis of a consistent set of thermodynamic data. A reliable data set of Gibbs energies of all stable or metastable phases is used to calculate phase diagrams and thermodynamic property diagrams. Proper thermodynamic descriptions of sub-systems also allow extrapolation of phase diagrams and thermodynamic properties into complex higher-order systems whose investigations are often time-consuming and expensive.

Isopiestic vapour pressure measurement

The basic setup of the non-isothermal isopiestic method used in the current studies was described in detail by Ipser et al. [8]. Actually, the isopiestic method was originally performed in an isothermal way to determine vapour pressures of aqueous solutions. Accordingly, aqueous solutions were equilibrated with standard solutions with a well known water vapour pressure. Corresponding measurements were described by Sinclair and co-workers [9,10].

This method became much more applicable when experimenters started to use pure volatile substances with well known vapour pressures at various temperatures. Hence, a non-isothermal isopiestic method was devised which was even interesting for metallic systems. For the first time, Herasymenko [11] placed a certain number of Ag-Cd alloys in a temperature gradient to equilibrate them with Cd vapour from a reservoir. Subsequently, this method was applied by several authors [12-15] for the thermodynamic description of various binary and ternary metallic systems. More recently, Richter et al. [16] demonstrated the applicability of the non-isothermal isopiestic method in Cd-RE systems. The authors determined Cd vapour pressures over Cd-La alloys in a series of experiments.

The determination of Cd vapour pressures in the systems Cd-Gd and Cd-Pr were part of the present doctoral studies. The corresponding procedure and evaluation of the isopiestic experiments is presented in research papers [17,18] as well as in chapter *Results and Discussion*. In the following a short description of the non-isothermal isopiestic method is given and basic questions are discussed.

In principle, a non volatile sample (pure metal A or master alloy $A_{1-x}B_x$) at a certain sample temperature is equilibrated in a closed system with vapour from a volatile component B. To obtain more results within a single run, a certain number of samples is arranged along a temperature gradient and simultaneously equilibrated; *cf.* Figure 16. The temperature minimum is at the reservoir which contains the volatile component and is located at the bottom of the reaction tube. The main conditions are that the vapour pressures of component A and B differ by at least three orders of magnitude and the vapour pressure of component A is low enough to be neglected altogether.

After a certain time of equilibration the volatile component has reacted with the sample in such a way, that an alloy has been formed with a composition for which the partial pressure of

B over the sample at the respective sample temperature is equal to the vapour pressure of B over pure B at the reservoir temperature.

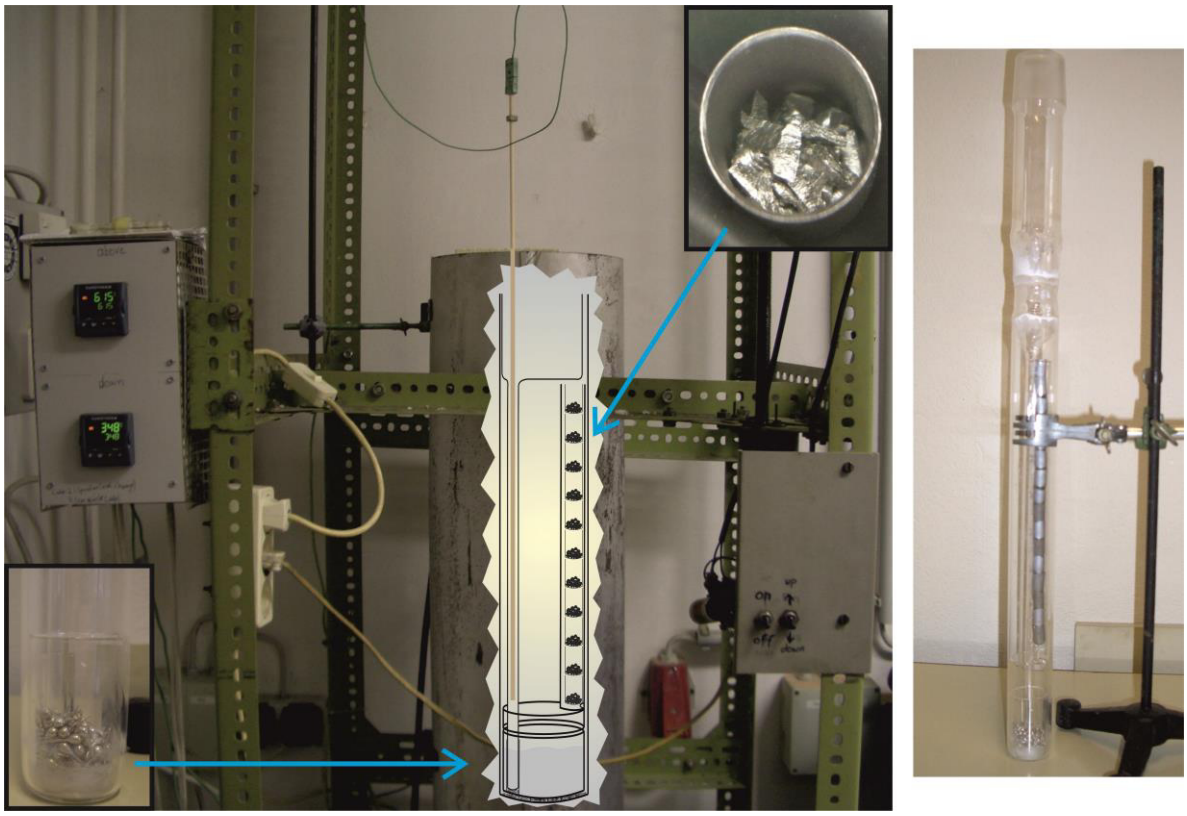

Fig. 16: Non-isothermal isopiestic method used in the present studies

However, the time necessary to reach thermodynamic equilibrium within a non-isothermal isopiestic experiment is strongly dependent on several experimental and preparative conditions. A decisive influence on the reaction rate between the gaseous component and the solid sample comes from the temperature at the reservoir and thus the corresponding vapour pressure. The non-isothermal isopiestic method is usually performed within a relatively high pressure range where the conditions do not correspond to that of the Knudsen regime. This means that the mean free path is very small compared to the dimension of the reaction tube and gas species collide frequently enough with each other. Hence, a continuous exchange of momentum is warranted and the pressure is assumed to be the same

over the whole tube. Indeed, the dimension of the reaction tube should be limited and an equal diameter along the whole tube is advantageous.

Of course, the reaction rate is strongly dependent on diffusivity and equilibrium phase formation within the sample. Elevated sample temperatures are usually inevitable if a pure metal with a rather high melting point is used as sample material. Unfortunately, the limitation of sample temperatures to a certain range also limits the data accessible in the respective isopiestic experiment. In such a case it is helpful to use metal powder of the respective high melting metal as it provides a large surface and rather short diffusion paths. As an alternative, a master alloy $A_{1-x}B_x$ may be synthesised and used as sample material, *cf.* [18].

From the obtained vapour pressures, thermodynamic activities of B in the samples at the respective sample temperatures can be calculated. Therefore, the temperature dependence of the vapour pressure of pure component B has to be known. A rather accurate measurement of the temperature gradient is required for a precise determination of sample and reservoir temperatures. Moreover, sample compositions have to be determined in an accurate manner, either simply by weighing or by chemical analysis. The accuracy of isopiestic measurements is dependent on a number of statistical and systematic errors which are listed and discussed in detail by Ipser et al. [8].

Calorimetry

Standard enthalpies of formation of intermetallic compounds were determined by calorimetric measurements. The corresponding data served as input data into a CALPHAD-type optimisation [19], see *Results and Discussion*.

Solution calorimetry was performed using a Tian-Calvet twin calorimeter with isoperibolic environment. In principle, the enthalpy of formation of a certain alloy $A_{1-x}B_x$ is determined indirectly by dropping pure components and pieces of the respective alloy into a liquid solvent (e.g. Sn). The corresponding heat signals are recorded over time. Through calibration with a substance whose heat capacity is well known (e.g. NIST sapphire), the respective heat signals can be evaluated. From extrapolation of the heat signals, limiting partial molar enthalpies of solution $\Delta_{sol}\overline{H}_i^0$ are derived for the pure components and the respective alloy. According to equation (1), the molar enthalpy of formation is calculated for the alloy at the drop temperature T_d.

$$\Delta_f H_{A_{1-x}B_x}^{T_d} = (1-x)\cdot\Delta_{sol}\overline{H}_A^0 + x\cdot\Delta_{sol}\overline{H}_B^0 - \Delta_{sol}\overline{H}_{A_{1-x}B_x}^0 \qquad (1)$$

Furthermore, reaction calorimetry was carried out in collaboration with colleagues from Genova. Corresponding measurements were done in an isoperibolic high-temperature calorimeter designed by Borzone et al. [20]. Accordingly, a sample, in terms of a pressed pill, is prepared from powders of the pure components with an exact stoichiometric composition. The sample is thrown twice into the calorimeter. In the first run, the so-called reaction run, the two components are reacting by forming the respective alloy. The measured heat signal ΔH_1 is corrected by the heat signal ΔH_1 derived from the second run, the reference run. The difference from the heat effects corresponds to the enthalpy of formation of the alloy at the drop temperature T_d:

$$\Delta H_1 - \Delta H_2 = \Delta_f H_{A_{1-x}B_x}^{T_d} \qquad (2)$$

Thermodynamic assessment – The CALPHAD approach

The use of the CALPHAD (Computer Coupling of Phase Diagrams and Thermochemistry) approach has attracted much attention for modelling of thermodynamic properties and phase diagrams of multi-component systems. The method and its applicability have been described repeatedly in literature [21-24]. In principle, it is a semi-empirical method which is usually used to model thermodynamic properties based on a consistent set of thermodynamic data. The modelling of a certain multi-component system requires a reliable set of experimentally determined data for the calculation of Gibbs energies of all phases and constituents. The theoretical background of the CALPHAD approach is described in detail in research paper [19], see *Research and Discussion*.

Each modelling starts from reliable descriptions of the Gibbs energies of the pure elements. The temperature dependent Gibbs energies of pure elements in their stable and metastable modifications are listed in the unary thermodynamic databases created by Dinsdale [25,26].

For the description of Gibbs energies of stoichiometric and non-stoichiometric phases, the knowledge of experimental thermodynamic and phase diagram data is important. Accordingly, calorimetric measurements can be employed to gain enthalpies of formation of intermetallic compounds and enthalpies of mixing of liquid alloys. These data can be directly used as input data into a thermodynamic model.

Usually, non-stoichiometric compounds are modelled using sublattices due to the compound energy formalism [22]. Accordingly, a set of Gibbs energy terms is defined for a number of hypothetical ordered compounds for all possible arrangements on a sublattice. These so-called end members have to be defined in a crystallographically accurate manner. Each end member is modelled like a stoichiometric compound with a distinct Gibbs energy. Since in reality only a few of these end members are stable, respective Gibbs energies are usually estimated or derived from *ab initio* calculations [27]. Corresponding structural and solubility data have to be obtained in the course of phase diagram studies, to define defect mechanisms and solubility limits of corresponding phases.

An accurate selection of the input data is initially performed in terms of a critical assessment of all available data. This is probably the most important step to achieve a proper

and reliable model in the subsequent iterative process according to the CALPHAD approach (Fig. 17). On the basis of the deployed database, phase diagrams and property diagrams are calculated according to the Gibbs energy minimisation technique [22]. Error minimisation procedures using non-linear least squares regression are typically very helpful for a consistent description of all input data. Subsequently, calculated output data have to be compared to the input data and reliable data for comparison selected in the course of the previous assessment.

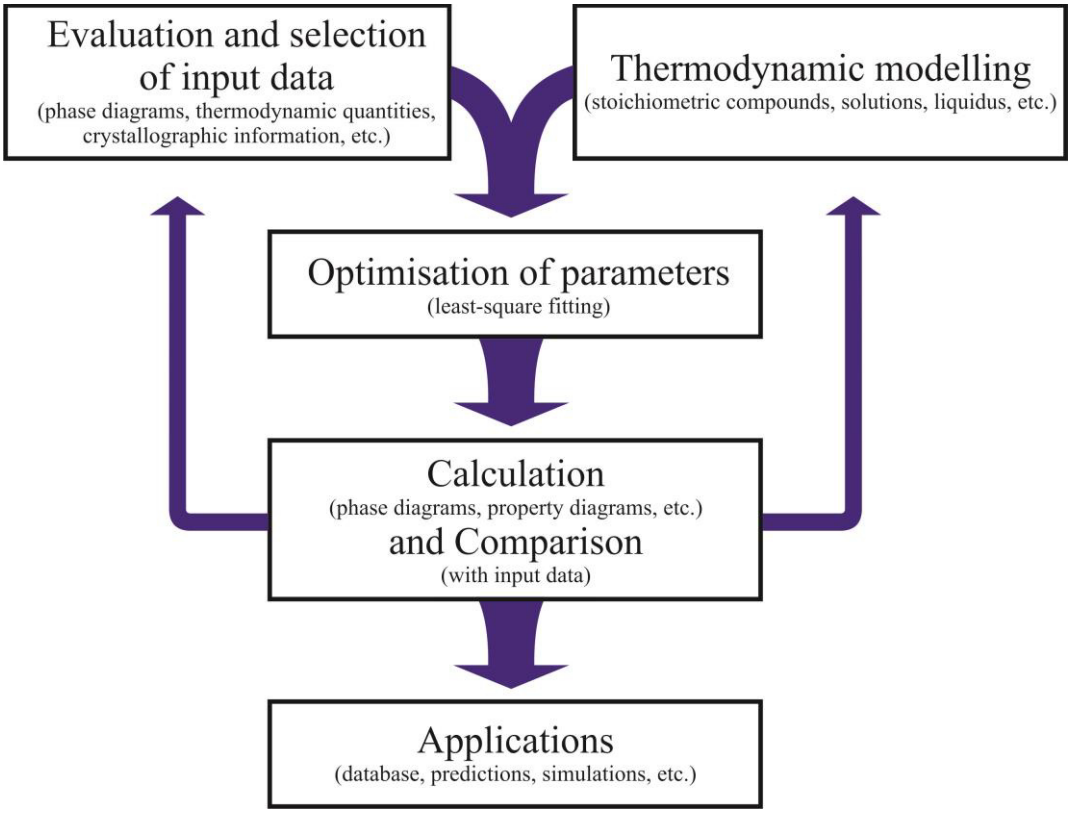

Fig. 17: The CALPHAD approach

Data for comparison are usually based on phase diagram features (phase equilibria, transition reaction temperatures, liquidus temperatures) and additional thermodynamic properties (vapour pressures, thermodynamic activities, heat capacities) gained from vapour pressure methods, electrochemical techniques and dynamic methods. In this kind of an optimisation process, a satisfactory model should be obtained which describes all data in a mutually consistent manner.

The CALPHAD approach is currently the most advanced method for modelling of complex heterogeneous systems with strongly non-stoichiometric phases. It uses many different databases, provided by e.g. the SGTE organisation or the CALPHAD community [28], and is usually oriented towards specific groups of materials, such as steels, Ni-based superalloys or solder materials. Beside the use in fundamental research, the CALPHAD approach has become more and more attractive as it serves as a source of data for simulations of phase transformations in multi-component systems, e.g. diffusion controlled transformations, microstructure evolutions, nucleation and grain growth.

References

[1] H. M. Rietveld. Line profiles of neutron powder-diffraction peaks for structure refinement. *Acta Cryst.* (1967), 22: 151-152.

[2] H. M. Rietveld. Profile refinement method for nuclear and magnetic structures. *J. Appl. Cryst.* (1969), 2: 65-71.

[3] AXS Bruker, TOPAS V3. General profile and structure analysis software for powder diffraction data. *Users Manual*, Bruker AXS, Germ. (2005).

[4] P. Villars, L. D. Calvert. Pearson's Handbook of Crystallographic Data for Intermetallic Phases, 2nd edition. *ASM International* (1991).

[5] R. W. Cheary, A. A. Coelho. A fundamental parameters approach to X-ray line-profile fitting. *J. Appl. Cryst.* (1992), 25: 109-121.

[6] R. W. Cheary, A. A. Coelho, J. P. Cline. Fundamental Parameters Line Profile Fitting in Laboratory Diffractometers. *J. Res. Natl. Inst. Stan.* (2004), 109: 1-25.

[7] A. Kern, A. A. Coelho, R. W. Cheary. Convolution based profile fitting, Diffraction Analysis of the Microstructure of Materials. E. J. Mittermeijer, P. Scardi (Eds.), *Materials Science Springer* (2004), II(2): 17-49.

[8] H. Ipser, R. Krachler, K. L. Komarek. The isopiestic method and its application to a thermodynamic study of the Au-Zn system. H. Brodowsky, H.-J. Schaller (Eds.), *Thermochemistry of Alloys* (1989), 286: 293-306.

[9] D. A. Sinclair. A Simple Method for Accurate Determinations of Vapor Pressures of Solutions. *J. Phys. Chem.* (1933), 37: 495-504.

[10] R. A. Robinson, D. A. Sinclair. Activity coefficients of the alkali chlorides and lithium iodide in aqueous solution from vapor pressure measurements. *J. Amer. Chem. Soc.* (1934), 56: 1830-1835.

[11] P. Herasymenko. Thermodynamic properties of solid solutions. I. Vapor pressures of cadmium over alpha silver-cadmium alloys. *Acta Metall.* (1956), 4(1): 1-6.

[12] L. J. Bartha, W. A. Alexander. The thermodynamic properties and phase diagram of the Gold-Cadmium system by the isopiestic method. *Can. J. Chem.* (1965), 43: 2319- 2327.

[13] K. W. Richter, K. Micke, H. Ipser. Antimony activities in the ternary NiAs-phase of the In-Ni-Sb system. *Thermoc. Acta* (1998), 314: 137-144.

[14] Y. Huang, K. W. Richter, W. Yuan, Z. Qiao, H. Ipser. Thermodynamic properties and phase relations of Zn-rich alloys in the system Pt-Zn. *Int. J. Mat. Res.* (2006), 97: 429-433.

[15] R. Ganesan, A. T. Dinsdale, H. Ipser. Thermochemistry of the nickel-phosphorus system. *Intermetallics* (2011), 19: 927-933.

[16] K. W. Richter, S. Besana, G. Borzone, H. Ipser. Thermodynamic investigations in the lanthanum-cadmium system. *J. Alloys Comp.* (2004), 365: 181-187.

[17] T. L. Reichmann, H. Ipser. Thermochemical Investigations in the System Cadmium-Praseodymium Relevant for Pyrometallurgical Fuel Reprocessing. *Metall. Mater. Trans. A* (2014), 45(3): 1171-1180.

[18] T. L. Reichmann, R. Ganesan, H. Ipser. Thermochemical investigations in the system Cd-Gd. *J. Alloys Comp.* (2014), 610: 676-683.

[19] T. L. Reichmann, K. W. Richter, H. Ipser. Enthalpies of formation of Cd-Pr intermetallic compounds and thermodynamic assessment of the Cd-Pr system. *CALPHAD* (2014), 47: 56-62.

[20] G. Borzone, R. Raggio, R. Ferro. Remarks on the role of thermochemical data in intermetallic crystallochemistry. *J. Alloys Compd.* (2004), 367: 89-102.

[21] L. Kaufman, H. Bernstein. Computer Calculation of Phase Diagrams. *Academic Press*, New York (1970).

[22] H. L. Lukas, S. G. Fries, B. Sundman. Computational Thermodynamics – The Calphad method. *Cambridge University Press* (2007).

[23] P. J. Spencer. A brief history of CALPHAD. *CALPHAD* (2008), 32(1): 1-8.

[24] A. Kroupa. Modelling of phase diagrams and thermodynamic properties using Calphad method – Development of thermodynamic databases. *Comp. Mat. Sc.* (2013), 66: 3-13.

[25] A. T. Dinsdale. SGTE data for pure elements. *CALPHAD* (1991), 15(4): 317-425.

[26] A. T. Dinsdale. SGTE unary Database. Version 5.0 (updated 2009), available at: <http://www.sgte.org>.

[27] M. Sob, A. Kroupa, J. Pavlu, J. Vrestal. Application of Ab Initio Electronic Structure Calculations in Construction of Phase Diagrams of Metallic Systems with Complex Phases. *Solid St. Phen.* (2009), 150: 1-28.

[28] Thermo-Calc Software – User's Guide. P. Shi, B. Sundman (Eds.), Thermo-Calc software AB (2010).

III. Results and Discussion

It was the aim of the current study to provide a detailed knowledge of thermodynamic properties as well as phase diagrams in the systems Cd-Gd and Cd-Pr. The complete phase diagrams have been accurately investigated using conventional isothermal and dynamic methods. An isopiestic vapour pressure method was applied to obtain thermodynamic activities and integral Gibbs energies in both systems. Moreover, standard enthalpies of formation of Cd-Pr alloys were derived from calorimetric measurements, which served as input data into a CALPHAD-type (Computer Coupling of Phase Diagrams and Thermochemistry) optimisation. The present cumulative doctoral thesis covers all results and is mainly based on the following publications:

- T. L. Reichmann, H. Ipser. Thermochemical Investigations in the System Cadmium-Praseodymium Relevant for Pyrometallurgical Fuel Reprocessing. *Metall. Mater. Trans. A* (2014), 45(3): 1171-1180.

- T. L. Reichmann, H. S. Effenberger, H. Ipser. Experimental investigation of the Cd-Pr phase diagram. *PlosOne* (2014), 9(4): 1-14.

- T. L. Reichmann, K. W. Richter, H. Ipser. Enthalpies of formation of Cd-Pr intermetallic compounds and thermodynamic assessment of the Cd-Pr system. *CALPHAD* (2014), 47: 56-62.

- T. L. Reichmann, R. Ganesan, H. Ipser. Thermochemical investigations in the system Cd-Gd. *J. Alloys Comp.* (2014), 610: 676-683.

- T. L. Reichmann, H. Ipser. Reinvestigation of the Cd-Gd phase diagram. *J. Alloys Comp.* (2014), in print.

Publication 1

Thomas L. Reichmann and Herbert Ipser

Thermochemical investigations in the system cadmium-praseodymium relevant for pyro-metallurgical fuel reprocessing

Metall. Mater. Trans. A (2014), 45(3): 1171-1180

Contributions to this paper:

T.L. Reichmann: performance of experiments, analysis and evaluation, writing of the paper

H. Ipser: introduction into isopiestic measurements, general advice and helpful comments, proofreading of the manuscript

Contribution of T. L. Reichmann to this paper: 70 %

Thermochemical Investigations in the System Cadmium-Praseodymium Relevant for Pyrometallurgical Fuel Reprocessing

THOMAS L. REICHMANN and HERBERT IPSER

Vapor pressure measurements, in terms of a (non-)isothermal isopiestic method, were carried out in the system Cd-Pr between 749 K and 1067 K (476 °C and 794 °C). Thermodynamic activities of cadmium as a function of temperature were obtained directly for the composition ranging from 50.0 to 85.7 at. pct Cd. From these results, partial molar enthalpies of mixing of Cd were derived for the corresponding composition range. The activity values of Cd were converted to an average sample temperature of 823 K (550 °C) by applying an integrated form of the Gibbs–Helmholtz equation. These data indicate that Cd_2Pr and $Cd_{58}Pr_{13}$ are probably the most stable intermetallic compounds in this system. Using an activity value of Pr from the literature as integration constant, Gibbs–Duhem integration was performed, and integral Gibbs energies are presented at 823 K (550 °C), referred to Cd(l) and α-Pr(s). Gibbs energies of formation at the stoichiometric compositions of the phases Cd_6Pr, $Cd_{58}Pr_{13}$, $Cd_{45}Pr_{11}$, Cd_3Pr, and Cd_2Pr were determined to be about −18.8, −23.5, −24.8, −28.7, and −33.8 kJ g-atom^{-1} at 823 K (550 °C), respectively.

DOI: 10.1007/s11661-013-2065-4

I. INTRODUCTION

NOWADAYS several countries in the world strive for strong nuclear power programs to satisfy their demands of energy. As a consequence, according to the World Nuclear Association* around 12,000 tons of high-level nuclear waste is produced annually. Currently, a considerable amount is stored intermediately in on-site water pools, waiting for long-term deposition in geological repositories. For an adequate and economic utilization of nuclear fuels, reprocessing of spent nuclear fuels is an option which is currently adopted only in a few countries. Conventionally, reprocessing is practiced by means of solvent extraction of actinides using tributyl phosphate (TBP), known as hydrometallurgical technique or aqueous reprocessing. Unfortunately, this technique has to deal with several problems like radiation and temperature instability of the various solvents used in the process. In addition, a huge amount of liquid waste is produced by this method. This problem makes it reasonable to investigate another type of reprocessing technique, called the pyrometallurgical technique. Pyrometallurgical reprocessing overcomes some of the major problems of aqueous reprocessing, as described by Olander.[1]

*http://world-nuclear.org/.

The central part of pyrometallurgical reprocessing is the electrorefining step, which is carried out in an "electrotransporter" cell. The theoretical feasibility has been described repeatedly in the literature, see *e.g.*, References 2 through 5. In particular, electrotransport and reductive extraction are applied to separate actinides and lanthanides from high level radioactive waste (HLW). The respective electrochemical vessel contains a liquid metal pool at the bottom, covered by a molten salt solution serving as electrolyte. One basket of anode, containing chopped nuclear fuels, and at least two cathodes are inserted into the liquid salt. During this process, especially uranium, plutonium, and minor actinides are transported whereas rare-earth (RE) elements, alkaline, and alkaline earth elements remain in the liquid salt. Additional reductive agents are added to the salt which promotes the extractability of RE elements into the liquid metal pool at the bottom by forming intermetallic compounds. Moriyama *et al.*[6,7] determined that the separation factors, which are an indicator for extractability, are quite different between actinides and lanthanides. In principle, actinides have the higher affinity for extraction into a metal phase, a fact that is preferable, considering the chemical similarity to lanthanides. The extraction behaviors of different elements between a molten chloride salt phase and a liquid metal strongly depend on the standard free energy of formation of the corresponding chlorides, as well as on the activity coefficients of the extracted metals in the respective intermetallic compounds. Thus, the separation factors differ noticeably when using different liquid metals. Several low melting metals have been tested,

THOMAS L. REICHMANN, Project Worker, and HERBERT IPSER, Professor, are with the Department of Inorganic Chemistry (Materials Chemistry), University of Vienna, 1090 Wien, Austria. Contact e-mail: Thomas.Reichmann@univie.ac.at
Manuscript submitted May 6, 2013.
Article published online October 18, 2013

such as Al,[8] Bi,[9] and Cd.[9] Among these elements, Cd is the most promising metal because it has a rather high vapor pressure, making it convenient for removal by distillation, and it forms a series of rather stable intermetallic compounds with all RE elements. Therefore, a detailed knowledge of the respective Cd-RE phase diagrams as well as of the thermodynamic stabilities of the corresponding intermetallic compounds is of great importance. This was the reason behind our initiating a series of thermodynamic and phase diagram studies of different Cd-RE systems in our laboratory.[10]

Concerning the system Cd-Pr, only limited information about phase diagram and thermodynamic data was found in the literature. Although no complete phase diagram information is available, seven intermetallic compounds were reported which seem to have been well investigated.[11] The most Cd-rich intermetallic compound in this system is $Cd_{11}Pr$ which decomposes incongruently at 843 K (570 °C). At this temperature, 3.5 at. pct Pr is soluble in liquid Cd according to Johnson *et al.*[12] The latter authors reported also liquidus data in the composition range of up to 1.83 at. pct Pr, as determined by chemical analysis of filtered samples of the corresponding equilibrium liquid phases.

In a subsequent study, Johnson and Yonco[13] determined the Gibbs energy of formation of $Cd_{11}Pr$ by means of Gibbs–Duhem integration, using thermodynamic activity values of Pr from their own emf measurements. The value, given as -11.2 kJ g-atom^{-1} at 823 K (550 °C), served as an integration constant for the current calculations. In an early study of Castrillejo *et al.*,[14] Gibbs energies of formation of the three intermetallic compounds $Cd_{11}Pr$, Cd_6Pr, and $Cd_{58}Pr_{13}$ were examined by electrochemical techniques. These values were determined to be -11.2 ± 0.1, -18.7 ± 0.1, and -22.9 ± 0.1 kJ g-atom^{-1}, respectively, for a temperature of 823 K (550 °C). The authors presented also partial Gibbs energies of Pr in the two-phase fields $Cd_{58}Pr_{13} + Cd_6Pr$, $Cd_6Pr + Cd_{11}Pr$, and $Cd_{11}Pr + L$, given as -107.6 ± 0.6, -127.4 ± 0.9, and -133.8 ± 1.2 kJ mol(Pr)$^{-1}$, respectively, for 823 K (550 °C).

Due to the limited information from the literature, the aim of the current study was to provide an experimental thermodynamic description of the Cd-Pr system. Vapor pressure measurements were carried out, and thermodynamic activities of Cd and Pr as well as integral Gibbs energies were determined for the composition ranging from 50 to 100 at. pct Cd. These data can serve as input into a CALPHAD-type optimization and will subsequently support understanding the distribution behavior of Pr in the electrorefining cell.

II. EXPERIMENTAL

A (non-)isothermal isopiestic method was applied to determine Cd activities in Cd-Pr alloys. This method was previously described by Ipser *et al.*[15] The corresponding experimental arrangement is shown schematically in Figure 1. The entire setup is made of fused silica glass and consists of four parts. A silica glass crucible, where the volatile metal is held (the reservoir), is placed at the bottom of the outer tube. On top of this crucible, a glass spacer connected to a sample holder tube is located in which tantalum crucibles are stacked, with one on top of the other. The defined distance from the bottom of the reservoir to the uppermost crucible is around 350 mm. Another inner tube with its upper end widened, is used as a thermocouple well. This widened part is sealed with the outer tube under dynamic vacuum.

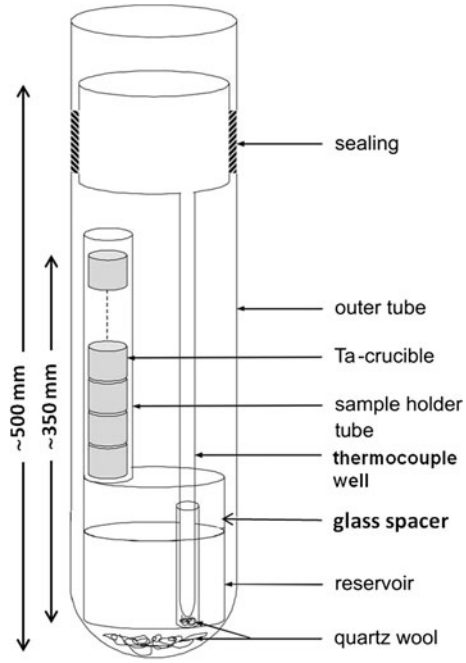

Fig. 1—Isopiestic quartz glass apparatus used in the current study.

Before use, the entire apparatus is cleaned with an acid mixture ($HF/HNO_3/H_2O$), rinsed with distilled water and dried. Afterward, the completely assembled setup, including the empty Ta crucibles (~20), is degassed under dynamic vacuum (10^{-3} mbar) at 1173 K (900 °C) for 5 hours. The subsequent sample preparation is carried out in a glove box, filled with Ar, to prevent the pure Pr samples from oxidation. Depending on the experimental temperatures, the reservoir is filled with weights ranging between 25 and 35 g of Cd (99.9999 pct Alfa AESAR, Karlsruhe, Germany), and between 160 and 220 mg of pure Pr (99.9 pct Alfa AESAR, Karlsruhe, Germany, and smart-elements, Vienna, Austria) is weighed into each Ta crucible (10 mm o.d., 12 mm height) with an accuracy of ±0.1 mg. Thereafter, the assembled setup is securely closed with a glass stopper and shuttled out of the glove box. It is connected to a vacuum pump, evacuated, and sealed under a dynamic vacuum of better than 10^{-4} mbar.

Afterward, the isopiestic experiments are heated in different temperature gradients, as applicable in conventional two-zone furnaces. A total number of seven runs were performed with different reservoir (T_R) and sample temperatures (T_S). The respective temperature gradients were recorded by raising a Pt/Pt10 pct Rh thermocouple inside the thermocouple well. Each experiment lasted for about 3 to 5 weeks, depending on the

reservoir temperature. After equilibration, the isopiestic apparatus was quenched in cold water and cut open by a diamond saw. The Cd-Pr alloys which had formed within the Ta crucibles during equilibration with the Cd vapor were weighed back and their compositions calculated from the difference in weight, which was attributed to the uptake of Cd.

Representative samples were characterized by powder X-ray diffraction (XRD) with Cu-Kα radiation using a Bruker D8 Advance Diffractometer with Bragg–Brentano geometry. The corresponding XRD patterns were analyzed and refined by means of the TOPAS 3 software, applying the fundamental parameter approach for peak profile modeling. To protect the powdered alloys from oxidation, a special XRD sample holder with an X-ray transparent lid was used.

Quantitative and optical examinations of the microstructures were performed on a Zeiss Supra 55 VP environmental scanning electron microscope using pure elements as standard materials and Co for an energy calibration of the energy-dispersive X-ray detector signal. A 120 μm aperture was used, and an acceleration voltage of 20 kV was applied. For imaging of the microstructures, a backscatter detector was employed. The composition of each phase was measured at three or more spots to minimize statistical errors and to obtain more reliable results. A maximum error of about $\pm$0.5 at. pct is assumed for the final results.

III. RESULTS AND DISCUSSION

A. *(Non-)isothermal Isopiestic Measurements*

Seven isopiestic runs in total were carried out at different temperature conditions, to obtain a complete description of thermodynamic activity data in the Cd-Pr system. The corresponding reservoir temperatures were chosen between 729 K and 869 K (456 °C and 596 °C), with the corresponding Cd vapor pressures being between 7 and 101 mbar, respectively. Sample temperatures were located between 749 K and 1067 K (476 °C and 794 °C). The vapor pressure values of pure Cd as a function of temperature were taken from Binnewies and Milke[16]:

$$\log\left(\frac{p^0_{\mathrm{Cd}}}{\mathrm{bar}}\right) = 8.7 - 5690 \cdot \frac{\mathrm{K}}{T} - 1.07 \cdot \log\frac{T}{\mathrm{K}} \qquad [1]$$

Since the melting point of Cd is rather low and it has indeed a much higher vapor pressure than Pr at the respective reservoir temperatures, the total pressure in the system is determined only by the temperature of the Cd reservoir (T_{R}). Equilibrium within the system is reached when the Cd vapor pressure over each sample, at its sample temperature T_{S}, is equal to the vapor pressure of pure Cd at the reservoir temperature T_{R}:

$$p_{\mathrm{Cd}}(T_{\mathrm{S}}) = p^0_{\mathrm{Cd}}(T_{\mathrm{R}}) \qquad [2]$$

Thus, the thermodynamic activity of Cd for each sample can be obtained by combining Eqs. [1] and [2] based on the conventional definition for the activity:

$$a_{\mathrm{Cd}}(T_{\mathrm{S}}) = \frac{p_{\mathrm{Cd}}(T_{\mathrm{S}})}{p^0_{\mathrm{Cd}}(T_{\mathrm{S}})} = \frac{p^0_{\mathrm{Cd}}(T_{\mathrm{R}})}{p^0_{\mathrm{Cd}}(T_{\mathrm{S}})} \qquad [3]$$

All results, including sample temperatures and compositions, sample identifications, Cd activities, and partial enthalpy values, are listed in Table I. The compositions were calculated from the mass change during the experiment as described above. All samples were ascribed to one- or two-phase fields in the phase diagram, which was confirmed by powder XRD. Sample compositions were partially controlled by SEM, and both sets of results were found to be in good agreement. The relative uncertainty in the compositions due to experimental errors is estimated to be less than 0.5 at. pct, and the temperatures are assumed to be accurate within $\pm$2 K (A more detailed discussion on possible error sources in this type of isopiestic experiments can be found in Reference 15).

Although the results were consistent in general, some discrepancies were found, predominantly for isopiestic runs with higher reservoir temperatures. Accordingly, the homogeneity ranges of all phases in the Cd-Pr system were separately determined by SEM. For this purpose, isopiestic samples within two-phase fields were annealed at different temperatures. The resulting solubilities for 823 K (550 °C) are shown in Table II. Although $Cd_{11}Pr$ and Cd_6Pr were exclusively determined as line compounds, noticeable homogeneity ranges were found for the other compounds. All isopiestic samples, except those from run 7, covered the experimentally found homogeneity ranges of the different phases. Most of the calculated compositions of run 7 appeared, in contrast to the other runs, to be located in two-phase fields as well as systematically shifted toward Pr-rich compositions. The corresponding SEM investigations suggested that, during quenching from 869 K (596 °C), some Cd was lost from the surface of the particles in all the samples of run 7, as can be seen in the example of sample 11 in Figure 2(a). This loss is caused by the rather significant Cd partial pressure at this high reservoir temperature and by the finite quenching rate of the evacuated isopiestic tubes. Although the overall composition could not be measured reliably because of porosity, powder XRD pointed to $Cd_{58}Pr_{13}$ as the bulk phase (*cf.* Figure 3). Therefore, it is strongly assumed that sample 11 was located within the homogeneity range of $Cd_{58}Pr_{13}$ while being equilibrated and was shifted in composition only during quenching.

Another possible explanation as to why these calculated compositions were shifted could be that a continuous solid solution exists between the two phases $Cd_{58}Pr_{13}$ and $Cd_{45}Pr_{11}$ at elevated temperatures, especially at 823 K (550 °C). However, due to pronounced differences in the crystal structures and because both phases were found in thermodynamic equilibrium at 873 K (600 °C), as seen in Figure 2(b), such a continuous solid solubility is very unlikely. Therefore, all sample compositions of run 7 were shifted systematically 0.35 at. pct toward the Cd-rich side.

By plotting sample compositions against sample temperatures T_{S} for one particular run, the so-called equilibrium curve can be drawn connecting the individ-

Table I. Experimental Results of Isopiestic Experiments, Standard State: Cd(l)

Sample No.	Cd (at. pct)	T_S/K	ln a_{Cd} (T_S)	Phases	$\Delta\overline{H}_{Cd}$/kJ g-atom^{-1}	ln a_{Cd} [823 K (550 °C)]
Run 1: T_R = 841 K (568 °C), 41 days						
1	84.88	850	−0.16	$Cd_{58}Pr_{13}$ + Cd_6Pr	−20.5	−0.29
2	81.49	856	−0.25	$Cd_{58}Pr_{13}$	−23.9	−0.39
3	81.24	864	−0.39	$Cd_{58}Pr_{13}$	−28.7	−0.59
4	80.94	875	−0.56	$Cd_{58}Pr_{13}$	−40.9	−0.92
5	80.83	890	−0.79	$Cd_{58}Pr_{13}$	−45.5	−1.29
6	79.89	908	−1.06	Cd_3Pr + $Cd_{45}Pr_{11}$	−30.2	−1.48
7	73.77	926	−1.33	Cd_2Pr + Cd_3Pr	−39.3	−1.97
8	66.61	950	−1.66	Cd_2Pr	−8.70	−1.83
9	66.47	969	−1.91	Cd_2Pr	−1.80	−1.95
10	66.43	992	−2.19	Cd_2Pr	−0.55	−2.21
11	65.59	1012	−2.44	CdPr + Cd_2Pr	−66.0	−4.24
Run 2: T_R = 818 K (545 °C), 49 days						
1	79.44	872	−0.92	Cd_3Pr + $Cd_{45}Pr_{11}$	−30.2	−1.17
2	73.89	885	−1.12	Cd_2Pr + Cd_3Pr	−39.3	−1.53
3	66.79	899	−1.34	Cd_2Pr + Cd_3Pr	−39.3	−1.87
4	66.64	913	−1.55	Cd_2Pr	−10.2	−1.70
5	66.50	929	−1.78	Cd_2Pr	−3.33	−1.84
6	66.48	942	−1.96	Cd_2Pr	−2.29	−2.00
7	66.41	957	−2.16	Cd_2Pr	0.12	−2.16
8	66.19	974	−2.38	Cd_2Pr	3.51	−2.30
9	65.43	995	−2.64	CdPr + Cd_2Pr	−66.0	−4.31
10	57.62	1018	−2.91	CdPr + Cd_2Pr	−66.0	−4.74
Run 3: T_R = 802 K (529 °C), 35 days						
1	81.22	825	−0.43	$Cd_{58}Pr_{13}$	−29.5	−0.44
2	81.10	831	−0.54	$Cd_{58}Pr_{13}$	−34.2	−0.59
3	80.98	837	−0.64	$Cd_{58}Pr_{13}$	−39.4	−0.74
4	80.78	843	−0.75	$Cd_{58}Pr_{13}$	−47.6	−0.92
5	80.73	850	−0.86	$Cd_{58}Pr_{13}$	−49.0	−1.08
6	80.70	858	−0.99	$Cd_{58}Pr_{13}$	−49.9	−1.28
7	80.53	865	−1.10	$Cd_{45}Pr_{11}$ + $Cd_{58}Pr_{13}$	−38.1	−1.38
8	79.61	872	−1.22	Cd_3Pr + $Cd_{45}Pr_{11}$	−30.2	−1.47
9	77.02	881	−1.36	Cd_3Pr + $Cd_{45}Pr_{11}$	−30.2	−1.66
10	69.47	892	−1.53	Cd_2Pr + Cd_3Pr	−39.3	−1.96
11	66.54	906	−1.74	Cd_2Pr	−4.78	−1.53
12	66.35	920	−1.94	Cd_2Pr	1.70	−2.01
13	66.32	937	−2.19	Cd_2Pr	2.23	−2.26
14	66.30	855	−2.43	Cd_2Pr	2.56	−2.51
15	66.18	973	−2.66	Cd_2Pr	3.52	−2.76
16	66.01	990	−2.88	Cd_2Pr	1.54	−2.91
17	65.82	1005	−3.06	CdPr + Cd_2Pr	−66.0	−4.81
18	60.72	1017	−3.20	CdPr + Cd_2Pr	−66.0	−5.04
Run 4: T_R = 780 K (507 °C), 42 days						
1	84.54	800	−0.40	$Cd_{58}Pr_{13}$ + Cd_6Pr	−20.5	−0.35
2	83.55	804	−0.47	$Cd_{58}Pr_{13}$ + Cd_6Pr	−20.5	−0.35
3	81.27	808	−0.54	$Cd_{58}Pr_{13}$	−27.9	−0.47
4	81.16	811	−0.61	$Cd_{58}Pr_{13}$	−31.8	−0.54
5	81.09	814	−0.66	$Cd_{58}Pr_{13}$	−34.3	−0.60
6	81.03	817	−0.72	$Cd_{58}Pr_{13}$	−37.1	−0.68
7	81.06	820	−0.76	$Cd_{58}Pr_{13}$	−35.9	−0.75
8	80.98	822	−0.81	$Cd_{58}Pr_{13}$	−39.5	−0.80
9	80.92	825	−0.86	$Cd_{58}Pr_{13}$	−41.9	−0.87
10	80.92	828	−0.91	$Cd_{58}Pr_{13}$	−41.9	−0.94
11	81.00	832	−0.98	$Cd_{58}Pr_{13}$	−38.5	−1.04
12	80.97	837	−1.07	$Cd_{58}Pr_{13}$	−39.9	−1.17
13	80.41	847	−1.24	$Cd_{45}Pr_{11}$ + $Cd_{58}Pr_{13}$	−38.1	−1.40
14	78.86	858	−1.42	Cd_3Pr + $Cd_{45}Pr_{11}$	−30.2	−1.58
15	69.47	871	−1.63	Cd_2Pr + Cd_3Pr	−39.3	−1.95
16	66.57	882	−1.82	Cd_2Pr	−6.56	−1.88
17	66.48	894	−1.99	Cd_2Pr	−2.46	−2.02
18	66.43	904	−2.14	Cd_2Pr	−0.60	−2.15
19	66.42	914	−2.30	Cd_2Pr	−0.35	−2.30
20	66.41	922	−2.41	Cd_2Pr	0.18	−2.41
21	66.30	930	−2.52	Cd_2Pr	2.64	−2.48

Table I. continued

Sample No.	Cd (at. pct)	T_S/K	ln a_{Cd} (T_S)	Phases	$\Delta\overline{H}_{Cd}$/kJ g-atom^{-1}	ln a_{Cd} [823 K (550 °C)]
Run 5: T_R = 795 K (522 °C), 45 days						
1	81.22	808	−0.25	$Cd_{58}Pr_{13}$	−29.4	−0.18
2	81.02	818	−0.44	$Cd_{58}Pr_{13}$	−37.6	−0.41
3	80.89	827	−0.60	$Cd_{58}Pr_{13}$	−43.1	−0.63
4	80.74	837	−0.78	$Cd_{58}Pr_{13}$	−48.6	−1.90
5	80.66	845	−0.91	$Cd_{58}Pr_{13}$	−51.0	−1.11*
6	80.56	854	−1.06	$Cd_{58}Pr_{13}$	−52.7	−1.33*
7	80.54	861	−1.17	$Cd_{45}Pr_{11}$ + $Cd_{58}Pr_{13}$	−38.1	−1.42
8	79.53	867	−1.27	Cd_3Pr + $Cd_{45}Pr_{11}$	−30.2	−1.50
9	73.16	873	−1.38	Cd_2Pr + Cd_3Pr	−39.3	−1.70
10	72.77	880	−1.48	Cd_2Pr + Cd_3Pr	−39.3	−1.86
11	66.54	884	−1.55	Cd_2Pr	−5.08	−1.61
12	66.63	889	−1.63	Cd_2Pr	−9.59	−1.73
13	66.69	894	−1.69	Cd_2Pr	−13.2	−1.85
Run 6: T_R = 729 K (456 °C), 49 days						
1	85.53	749	−0.45	$Cd_{58}Pr_{13}$ + Cd_6Pr	−20.5	−0.16
2	85.30	753	−0.55	$Cd_{58}Pr_{13}$ + Cd_6Pr	−20.5	−0.26
3	82.11	756	−0.61	$Cd_{58}Pr_{13}$ + Cd_6Pr	−20.5	−0.34
4	81.59	759	−0.67	$Cd_{58}Pr_{13}$	−24.8	−0.37
5	81.48	761	−0.72	$Cd_{58}Pr_{13}$	−24.0	−0.44
6	81.40	763	−0.76	$Cd_{58}Pr_{13}$	−24.8	−0.48
7	81.34	765	−0.80	$Cd_{58}Pr_{13}$	−25.9	−0.51
8	81.29	766	−0.82	$Cd_{58}Pr_{13}$	−27.3	−0.53
9	81.29	767	−0.84	$Cd_{58}Pr_{13}$	−27.0	−0.55
10	81.24	768	−0.86	$Cd_{58}Pr_{13}$	−28.8	−0.56
11	81.15	771	−0.91	$Cd_{58}Pr_{13}$	−32.0	−0.59
12	81.15	775	−0.99	$Cd_{58}Pr_{13}$	−31.9	−0.70
13	81.04	781	−1.13	$Cd_{58}Pr_{13}$	36.8	−0.84
14	80.97	791	−1.32	$Cd_{58}Pr_{13}$	−39.8	−1.08
15	80.88	801	−1.52	$Cd_{58}Pr_{13}$	−43.7	−1.34
16	78.79	810	−1.68	Cd_3Pr + $Cd_{45}Pr_{11}$	−30.2	−1.59
17	66.53	828	−2.00	Cd_2Pr + Cd_3Pr	−39.3	−2.02
18	65.96	834	−2.12	Cd_2Pr	0.29	−2.12
19	65.76	842	−2.25	Cd_2Pr	−7.97	−2.28
Run 7: T_R = 869 K (596 °C), 42 days						
1	81.32	888	−0.30	$Cd_{58}Pr_{13}$	−26.3	−0.58
2	81.09	893	−0.38	$Cd_{58}Pr_{13}$	−34.3	−0.77
3	81.00	897	−0.44	$Cd_{58}Pr_{13}$	−38.5	−0.90
4	80.90	902	−0.51	$Cd_{58}Pr_{13}$	−42.9	−1.05
5	80.88	906	−0.58	$Cd_{58}Pr_{13}$	−43.5	−1.16
6	80.72	911	−0.65	$Cd_{58}Pr_{13}$	−49.4	−1.35
7	80.58	916	−0.72	$Cd_{58}Pr_{13}$	−52.3	−1.50
8	80.55	922	−0.80	$Cd_{45}Pr_{11}$ + $Cd_{58}Pr_{13}$	−38.1	−1.40
9	80.34	927	−0.87	$Cd_{45}Pr_{11}$	−36.7	−1.47
10	80.26	933	−0.96	$Cd_{45}Pr_{11}$	−36.1	−1.58
11	79.43	942	−1.08	Cd_3Pr + $Cd_{45}Pr_{11}$	−30.2	−1.64
12	75.05	954	−1.24	Cd_2Pr + Cd_3Pr	−39.3	−2.03
13	66.28	967	−1.42	Cd_2Pr	2.89	−1.36
14	66.27	984	−1.63	Cd_2Pr	3.01	−1.56
15	66.07	1001	−1.83	Cd_2Pr	2.72	−1.76
16	66.22	1015	−2.01	Cd_2Pr	3.43	−1.91
17	66.17	1028	−2.16	Cd_2Pr	3.52	−2.05
18	66.02	1039	−2.27	Cd_2Pr	1.83	−2.22
19	65.75	1050	−2.40	Cd_2Pr	−8.62	−2.67
20	65.78	1059	−2.50	Cd_2Pr	−6.99	−2.73
21	65.84	1067	−2.58	CdPr + Cd_2Pr	−66.0	−4.78

*Samples are not located within the currently defined homogeneity range of $Cd_{58}Pr_{13}$ but were treated as single-phase samples of $Cd_{58}Pr_{13}$, confirmed by powder-XRD (compare 3.1.).

ual data points. Figure 4 shows these equilibrium curves for all runs, superimposed on the actual version of the Cd-Pr phase diagram, adapted from Gschneidner and Calderwood.[17] As can be seen, all samples are located between 57 and 86 at. pct Cd. Most of the samples are single-phase samples, consisting of pure Cd_2Pr and

$Cd_{58}Pr_{13}$, suggesting that these phases are among the most stable ones in the Cd-Pr system. On the other hand, no samples were obtained in the phase Cd_3Pr suggesting that Cd_3Pr is only slightly more stable than a two-phase mixture of its neighboring compounds. This phenomenon was actually also observed earlier in the Cd-Ce system where likewise no samples were formed in the Cd_3Ce phase.[10]

Table II. Homogeneity Ranges of the Intermetallic Compounds at 823 K (550 °C) as Determined by SEM

Phase	Phase Boundaries (at. pct Cd)	Remarks
CdPr	47.07 to 50.00	
Cd_2Pr	65.80 to 66.67	
Cd_3Pr	75.00 to 76.19	
$Cd_{45}Pr_{11}$	79.98 to 80.36	
$Cd_{58}Pr_{13}$	80.76 to 81.79	
Cd_6Pr	85.71	line compound
$Cd_{11}Pr$	91.67	line compound

In addition, some of the samples formed in the isopiestic runs were obtained in various two-phase fields after equilibration. This is probably caused by slight variations of the sample temperatures. Nevertheless, these samples allow us to calculate Cd activities for the respective two-phase fields at the corresponding sample temperatures T_S.

B. *Partial Enthalpy of Mixing of Cd in Two-Phase Fields*

As indicated above, Cd vapor pressures were used to calculate activities in different two-phase fields at the respective sample temperatures T_S (see Table I). Natural logarithms of these activity values were plotted against reciprocal temperatures for almost all two-phase fields, *i.e.*,: CdPr + Cd_2Pr, Cd_2Pr + Cd_3Pr, Cd_3Pr + $Cd_{45}Pr_{11}$, $Cd_{45}Pr_{11}$ + $Cd_{58}Pr_{13}$, and $Cd_{58}Pr_{13}$ + Cd_6Pr (see Figure 5). According to an adapted Gibbs–Helmholtz equation [4], partial enthalpy values of mixing of Cd were directly calculated from the slopes:

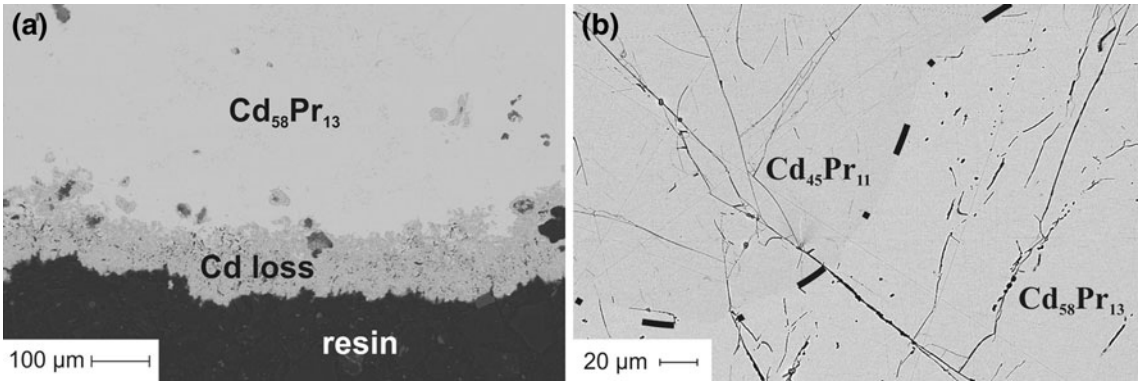

Fig. 2—BSE image of sample 11 from isopiestic run 7 (*a*) and of a sample annealed in the two-phase field $Cd_{58}Pr_{13}$ + $Cd_{45}Pr_{11}$ at 873 K (600 °C) (*b*).

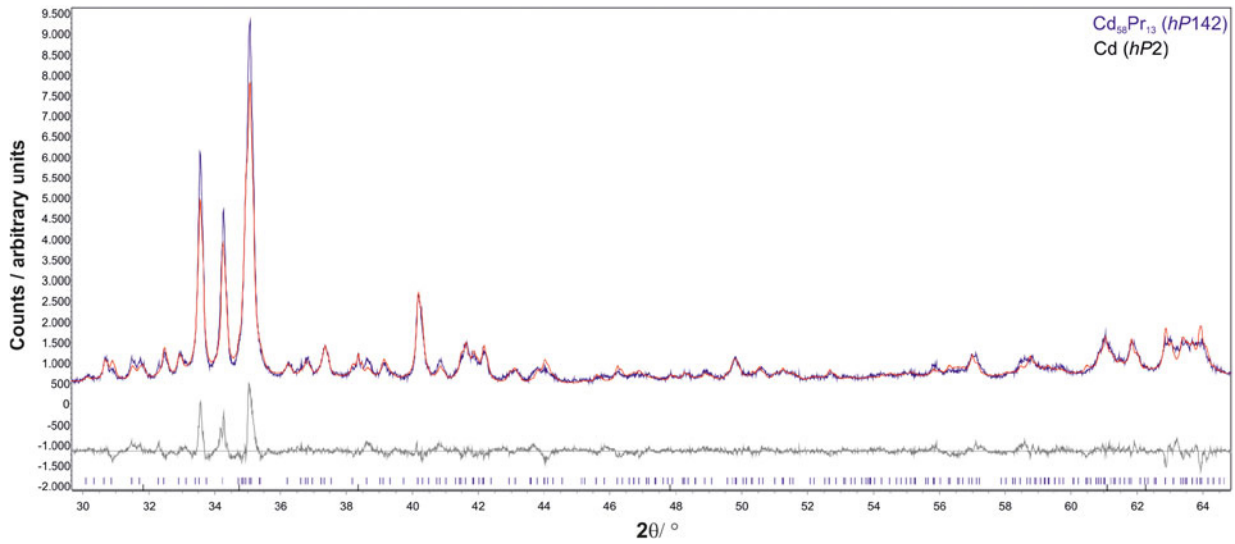

Fig. 3—Powder XRD pattern of sample 11 from isopiestic run 7. Blue curve: observed pattern; red curve: calculated pattern; gray curve: difference pattern (Color figure online).

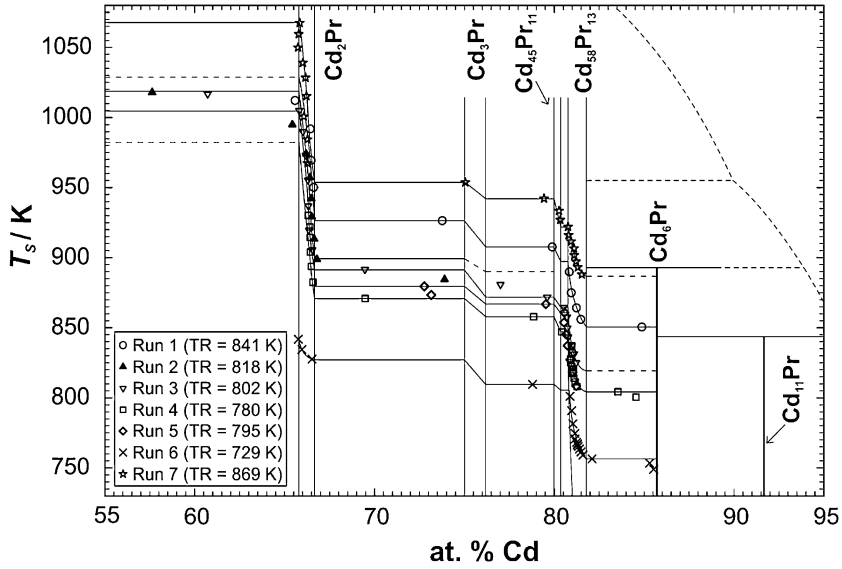

Fig. 4—Sample temperature against sample composition superimposed on the partial Cd-Pr phase diagram.

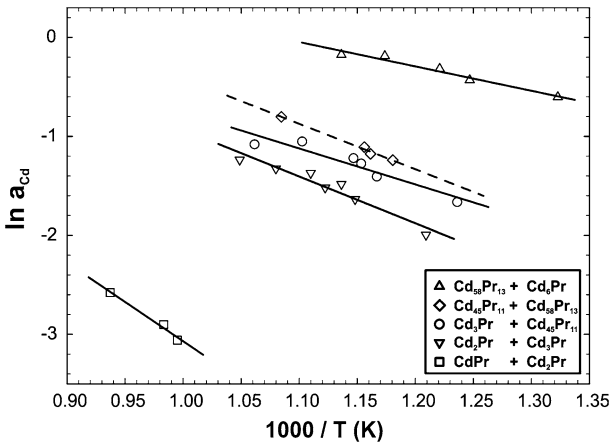

Fig. 5—Natural logarithm of the Cd activity against reciprocal temperature for different two-phase fields.

$$\frac{\partial \ln a_{Cd}}{\partial (1/T)} = \frac{\Delta \overline{H}_{Cd}}{R}, \qquad [4]$$

where the temperature is in K, R is the gas constant in J (mol K)$^{-1}$, and the partial enthalpy of Cd is in J mol(Cd)$^{-1}$. For this approach, straight phase boundaries, *i.e.*, no variation of solid solubilities with temperature, of the different compounds were assumed. Although it is obvious that the solubilities will be temperature dependent in the examined temperature range, this is still a useful approach to obtain information on the corresponding partial enthalpy values in a certain temperature range (*cf.* Table I). On comparing the slopes in Figure 5, an exothermic behavior is observed in the corresponding composition ranging from 50 to 86 at. pct Cd. One can see that, with decreasing Cd concentration, the partial molar enthalpy of mixing of Cd becomes increasingly negative. $\Delta \overline{H}_{Cd}$-values for $Cd_{45}Pr_{11}$ + $Cd_{58}Pr_{13}$ are probably less accurate because of the very narrow two-phase field and because of some variation of the solubility of $Cd_{58}Pr_{13}$ with temperature, as determined by SEM and included in Figure 4. Therefore, the corresponding straight line in Figure 5 is shown as a dashed line.

C. *Partial Enthalpy of Mixing of Cd in Single-Phase Fields*

Partial enthalpies of mixing of Cd were determined in the homogeneity ranges of Cd_2Pr and $Cd_{58}Pr_{13}$ in the same manner as described above. For instance, for the evaluation of $Cd_{58}Pr_{13}$ sample temperatures for selected compositions were obtained along the entire homogeneity range by interpolation from the equilibrium curves in Figure 4. From these hypothetical samples, Cd activities were calculated according to Eqs. [1] and [3]. Natural logarithms of these activities were plotted as a function of reciprocal temperature in Figure 6. Applying the adapted Gibbs–Helmholtz equation [4], a linear regression was applied for data points of each selected composition in the entire homogeneity range of $Cd_{58}Pr_{13}$. It can be seen that there is some noticeable scatter, especially in the central part of the phase. However, it should be kept in mind that the data points are spaced in very narrow composition steps, and that small errors in composition and/or temperature in the equilibrium curves in Figure 4 may lead to a noticeable shift in the ln a_{Cd} *vs.* $1/T$ data points.

Values of $\Delta \overline{H}_{Cd}$ were directly calculated from the slopes of the straight lines in Figure 6 and plotted against composition in Figure 7. As can be seen, the partial enthalpy values vary over an extended range from −24 at the Cd-rich side to −50 kJ mol(Cd)$^{-1}$ at the Pr-rich border of the homogeneity range, pointing again to the considerable stability of this phase.

An analogous evaluation was carried out for the Cd_2Pr phase. The corresponding values are included in Table I. Although the partial enthalpy values in the two-

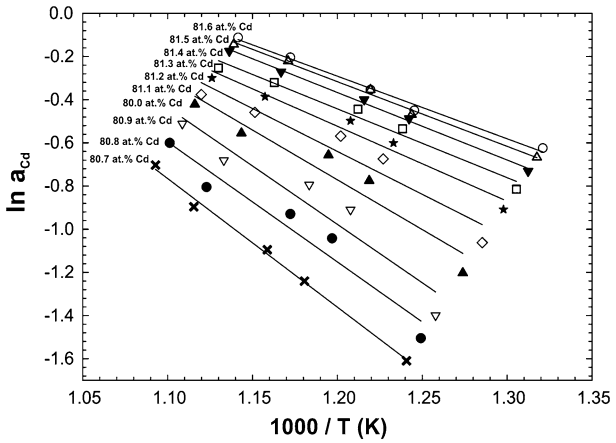

Fig. 6—Natural logarithm of the Cd activity against reciprocal temperature for selected compositions in the $Cd_{58}Pr_{13}$ phase.

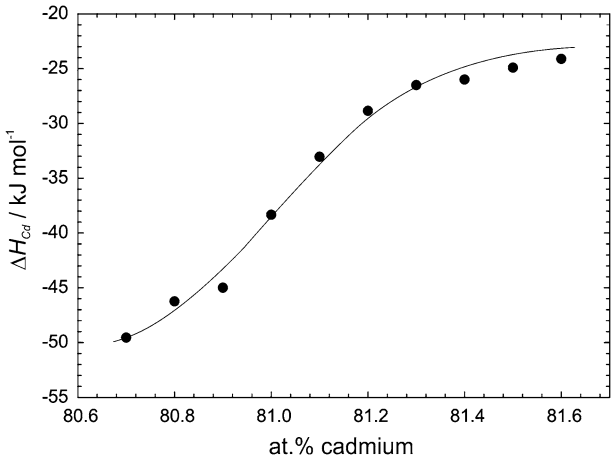

Fig. 7—Partial molar enthalpy of Cd in the homogeneity range of $Cd_{58}Pr_{13}$; standard state: Cd (l).

phase fields become increasingly more negative with increasing Pr content (see Figure 5), the evaluation for Cd_2Pr resulted in surprisingly small negative or even slightly positive values for $\Delta\overline{H}_{Cd}$,which would indicate a somewhat unusual shape of the integral enthalpy of formation curve for this phase. At the moment, the reason for this behavior is not clear; nevertheless, these values were used for the conversion of the Cd activities to a common temperature of 823 K (550 °C) (see below), resulting in activity values consistent with those of the neighboring phases.

Partial enthalpy values for $Cd_{45}Pr_{11}$ could not be derived in the described way, but were estimated from the neighboring two-phase fields assuming a linear behavior with composition between the values of the two-phase fields. The same procedure was employed for the Cd_3Pr phase where no samples were available from the experiment (*cf.* Table I).

D. *Thermodynamic Activity of Cd at 823 K (550 °C)*

To derive thermodynamic activities of Cd for the respective single- and two-phase fields, an integrated

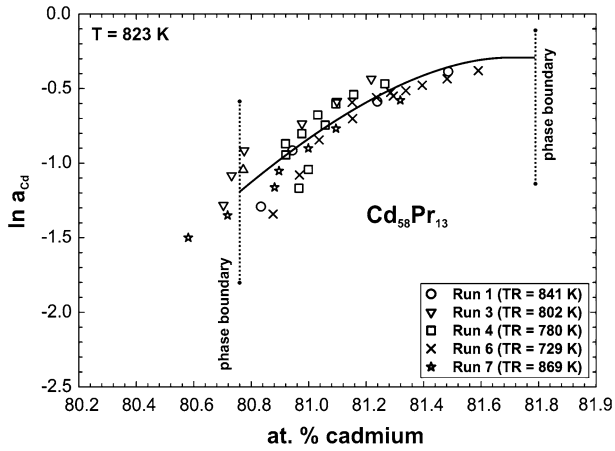

Fig. 8—Natural logarithm of the Cd activity for $Cd_{58}Pr_{13}$ at 823 K (550 °C); standard state: Cd(l). The symbols are same as in Fig. 4.

form of the adapted Gibbs–Helmholtz equation was applied:

$$\ln a_{Cd}[823\,K\,(550\,^{\circ}C)] - \ln a_{Cd}(T_S) = \frac{\Delta\overline{H}_{Cd}}{R}\cdot\left(\frac{1}{823} - \frac{1}{T_S}\right) \quad [5]$$

with the temperature in K and the partial enthalpy of cadmium in J mol(Cd)$^{-1}$. Accordingly, the activity values of all samples, at the respective sample temperatures T_S, were converted to an average temperature of 823 K (550 °C) (see Table I). The required enthalpy values in the respective single- and two-phase fields (Cd_2Pr, $Cd_2Pr + Cd_3Pr$, Cd_3Pr, $Cd_3Pr + Cd_{45}Pr_{11}$, $Cd_{45}Pr_{11}$, $Cd_{45}Pr_{11} + Cd_{58}Pr_{13}$, $Cd_{58}Pr_{13}$, $Cd_{58}Pr_{13} + Cd_6Pr$) were obtained from the current results.

As an example, ln a_{Cd} for $Cd_{58}Pr_{13}$ is shown in Figure 8 as a function of composition at 823 K (550 °C). The corresponding phase boundaries at this temperature were taken from Table II, as obtained from SEM measurements. The data points were fitted with a polynomial function, leading to the best compatibility with the activity values in the adjacent two-phase fields.

As mentioned previously, numerous samples were located in the homogeneity range of Cd_2Pr, making this phase useful to perform the same evaluation as was done for $Cd_{58}Pr_{13}$. The homogeneity range was estimated to be between 65.8 and 66.6 at. pct Cd at 823 K (550 °C). The corresponding activity values of samples located in Cd_2Pr were converted to 823 K (550 °C), using an empirical fit of the respective enthalpy values within this composition range.

Thermodynamic activity values at 823 K (550 °C) for the phases Cd_3Pr and $Cd_{45}Pr_{11}$ which are given in Table I had to be converted from their corresponding sample temperatures with enthalpy values estimated by a linear interpolation between the values in the neighboring two-phase fields, as discussed above.

Activity values in the two-phase fields $Cd_{11}Pr + L$ and $Cd_6Pr + Cd_{11}Pr$ could not be obtained from the current results but were taken from Johnson and Yonco[13] and Castrillejo *et al.*,[14] respectively, based on their experimental values of the Pr activity and their

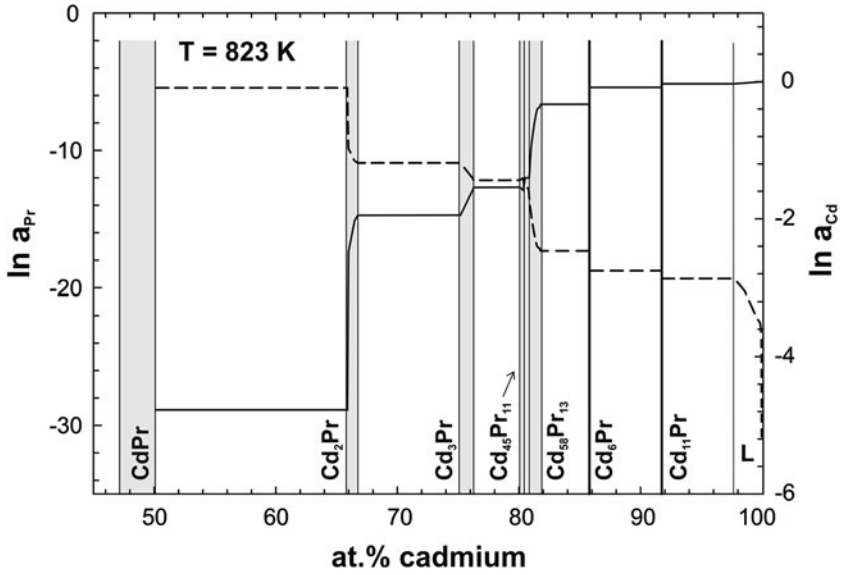

Fig. 9—Natural logarithm of Cd and Pr activities against composition at 823 K (550 °C); standard states: α-Pr(s) and Cd(l).

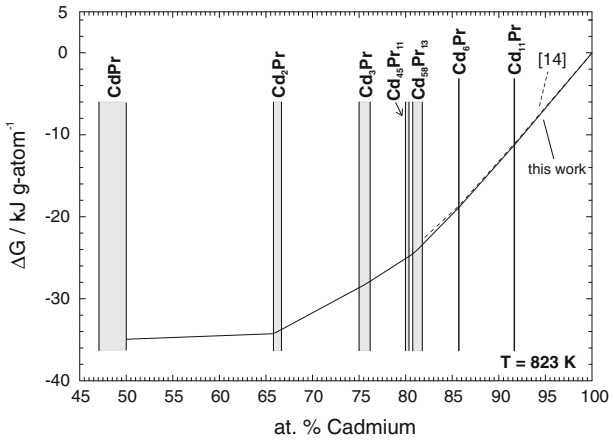

Fig. 10—Integral Gibbs energy of formation against composition at 823 K (550 °C); standard states: α-Pr(s) and Cd(l). Dashed lines refer to Castrillejo *et al.*[14]

integral Gibbs energies of formation of the compounds Cd_6Pr and $Cd_{11}Pr$. They were used for the current Gibbs–Duhem integration as described below. According to Castrillejo *et al.*,[14] a value of ln $a_{Cd} = -0.574$ could be calculated for the two-phase field $Cd_6Pr + Cd_{58}Pr_{13}$, which compares reasonably well with the value of about −0.33 obtained in the current study.

E. *Integral Gibbs Energy*

As outlined above, Johnson and Yonco[13] determined thermodynamic activities of Pr in the liquid phase between 635 and 809 K (362 °C and 536 °C) by means of emf measurements. They calculated partial excess Gibbs energies of Pr, based on solubility data of Pr in liquid Cd from an earlier examination of the Cd-rich part of the phase diagram by Johnson *et al.*[12] An overall fit of the complete data was given, which was used to calculate an activity coefficient of Pr at 823 K (550 °C) for the current study:

$$\Delta\overline{G}^{xs}_{Pr} = x^2_{Cd}(a_1 + a_2T + Bx_{Pr}) \quad [6]$$

with the temperature in K and the partial excess Gibbs energy of Pr in J mol(Pr)$^{-1}$. The respective coefficients, obtained from the emf measurements, were listed as follows:$a_1 = -182.25$ J mol^{-1}, $a_2 = 87.50$ J (mol K)$^{-1}$, and $B = -86.67 \times 10^3$ J mol^{-1}. From the calculated excess partial Gibbs energy of Pr at 823 K (550 °C), a value for the thermodynamic activity of Pr could be obtained for the two-phase field $Cd_{11}Pr + L$, namely, ln $a_{Pr} = -19.34$, which agrees perfectly with the activity value of Castrillejo *et al.*,[14] given as −19.55. The activity value ln $a_{Pr} = -19.34$, calculated from the empirical function of Johnson and Yonco, served as an integration constant for Gibbs–Duhem integration performed in the current study. The corresponding activity values of Cd and Pr in the composition ranging from 50 to 100 at. pct Cd are plotted as natural logarithms in Figure 9.

Again, the figure indicates that the intermetallic compounds Cd_2Pr and $Cd_{58}Pr_{13}$ have to be very stable, because of the marked difference of the activities between their adjacent two-phase fields. Incidentally, it was observed in the Cd-La system[18] that the two phases Cd_2La and $Cd_{58}La_{13}$ with the same crystal structures show congruent melting points, and a similar marked activity change was also observed for the compound $Cd_{58}La_{13}$ by Richter *et al.*[19] Thus, the results for the Cd-Pr system are taken as a strong indication that Cd_2Pr and $Cd_{58}Pr_{13}$ might also exhibit congruent melting behavior.

From the activity data for Cd and Pr, integral Gibbs energies were calculated for the respective composition ranges at 823 K (550 °C) and are plotted in Figure 10, referred to Cd(l) and α-Pr(s) as standard states. Gibbs energies of formation at the exact stoichiometric compositions of the phases Cd_6Pr, $Cd_{58}Pr_{13}$, $Cd_{45}Pr_{11}$,

Cd_3Pr, and Cd_2Pr were obtained to be about −18.8, −23.5, −24.8, −28.7, and −33.8 kJ g-atom^{-1} at 823 K (550 °C), respectively. Comparing with previous data of Castrillejo *et al.*[14] (see Figure 10) who presented a Gibbs energy of formation for $Cd_{58}Pr_{13}$ as −23.7 kJ g-atom^{-1} [at 823 K (550 °C)], the agreement is considered very good. In a thermodynamic assessment, Kurata and Sakamura[20] listed optimized parameters for the Gibbs energy of formation of Cd_6Pr. Using their parameters, a value of about −18.7 kJ g-atom^{-1} was calculated for 823 K (550 °C), referred to Cd(l) and α-Pr(s). This similarity of good agreement confirms the validity of the assumptions made for the Gibbs–Duhem integration performed in the current study.

IV. SUMMARY

Seven successful vapor pressure runs were carried out, using a (non-)isothermal isopiestic method. Liquid Cd served as the volatile component and was equilibrated with pure Pr samples between 749 K and 1067 K (476 °C and 794 °C). From the primary results, equilibrium curves were drawn and thermodynamic activity values of Cd were derived in the composition ranging from 50 to 85 at. pct Cd. An adapted Gibbs–Helmholtz equation was applied to convert thermodynamic activity values of Cd to an average sample temperature of 823 K (550 °C). With additional information from the literature concerning a value for the activity of Pr in the two-phase field $Cd_{11}Pr$ + L, a Gibbs–Duhem integration was performed in the current study. Activity values of Cd and Pr are thus presented in the composition ranging from 50 to 100 at. pct Cd. Moreover, integral Gibbs energies could be derived and are shown for the respective composition ranges. The agreement of Gibbs energies of formation with the available literature data is good.

ACKNOWLEDGMENTS

The authors wish to thank the Austrian Science Fund (FWF) for financial support of this study under Project No. P 23270-N19, and the Scientific-Technical Cooperation between Austria and India (Project No. IN 05/2011). Moreover, the Faculty of Physics of the University of Vienna and especially Dr. Stephan Puchegger are thanked for the help extended to the authors during the SEM measurements.

REFERENCES

1. D. Olander: *J. Nucl. Mater.*, 2009, vol. 389, pp. 1–22.
2. I. Johnson: *J. Nucl. Mater.*, 1988, vol. 154, pp. 169–80.
3. J.P. Ackerman: *Ind. Eng. Chem. Res.*, 1991, vol. 30, pp. 141–45.
4. J.J. Laidler, J.E. Battles, W.E. Miller, J.P. Ackerman, and E.L. Carls: *Prog. Nucl. Energy*, 1997, vol. 31, pp. 131–40.
5. H. Yamana, N. Wakayama, N. Souda, and H. Moriyama: *J. Nucl. Mater.*, 2000, vol. 278, pp. 37–47.
6. H. Moriyama, S. Seshimo, K. Moritani, Y. Ito, and T. Mitsugashira: *J. Alloys Compd.*, 1994, vols. 213–214, pp. 354–59.
7. H. Moriyama, H. Yamana, S. Nishikawa, S. Shibata, N. Wakayama, Y. Miyashita, K. Moritani, and T. Mitsugashira: *J. Alloys Compd.*, 1998, vols. 271–273, pp. 587–91.
8. O. Conocar, N. Douyere, J.-P. Glatz, J. Lacquement, R. Malmbeck, and J. Serp: *Nucl. Sci. Eng.*, 2006, vol. 153, pp. 253–61.
9. M. Kurata, Y. Sakamura, T. Hijikata, and K. Kinoshita: *J. Nucl. Mater.*, 1995, vol. 227, pp. 110–21.
10. B. Skołyszewska-Kühberger, T.L. Reichmann, R. Ganesan, and H. Ipser: *CALPHAD*, 2013. DOI:10.2016/j.calphad.2013.07.005.
11. K.A. Gschneidner, Jr. and F.W. Calderwood: *Bull. Alloy Phase Diagr.*, 1988, vol. 9, pp. 130–32.
12. I. Johnson, K.E. Anderson, and R.A. Blomquist: *Trans. ASM*, 1966, vol. 59, pp. 352–55.
13. I. Johnson and R.M. Yonco: *Metall. Trans.*, 1970, vol. 1, pp. 905–10.
14. Y. Castrillejo, M.R. Bermejo, P.D. Arocas, A.M. Martínez, and E. Barrado: *J. Electroanal. Chem.*, 2005, vol. 579, pp. 343–58.
15. H. Ipser, R. Krachler and K.L. Komarek: in *Thermochemistry of Alloys*, H. Brodowsky and H.-J. Schaller, eds., Kluwer Academic Publishers, Dordrecht, 1989, pp. 293–306.
16. M. Binnewies and E. Milke: *Thermochemical Data of Elements and Compounds*, WileyVCH, Weinheim, 1999, p. 295.
17. K.A. Gschneidner, Jr. and F.W. Calderwood: *Bull. Alloy Phase Diagr.*, 1988, vol. 9, pp. 130–31.
18. K.A. Gschneidner, Jr. and F.W. Calderwood: *Bull. Alloy Phase Diagr.*, 1988, vol. 9, pp. 32–34.
19. K. Richter, S. Besana, G. Borzone, and H. Ipser: *J. Alloys Compd.*, 2004, vol. 365, pp. 181–87.
20. M. Kurata and Y. Sakamura: *J. Phase Equilib.*, 2001, vol. 22, pp. 232–40.

Publication 2

Thomas L. Reichmann, Herta S. Effenberger and Herbert Ipser

Experimental investigation of the Cd-Pr phase diagram

PlosOne (2014), 9(4): 1-14

Contributions to this paper:

T.L. Reichmann:	sample preparation, SEM-, powder XRD-, and DTA-experiments, analysis and interpretation of results, writing of the paper
H.S. Effenberger:	performance of single-crystal XRD measurements and interpretation
H. Ipser:	general advice and helpful comments, interpretation of results, proofreading of the manuscript

Contribution of T. L. Reichmann to this paper: 70 %

OPEN ACCESS Freely available online

PLOS ONE

Experimental Investigation of the Cd-Pr Phase Diagram

Thomas L. Reichmann[1]*, Herta S. Effenberger[2], Herbert Ipser[1]

1 Department of Inorganic Chemistry (Materials Chemistry), University of Vienna, Wien, Austria, **2** Department of Mineralogy and Crystallography, University of Vienna, Wien, Austria

Abstract

The complete Cd-Pr equilibrium phase diagram was investigated with a combination of powder-XRD, SEM and DTA. All intermetallic compounds within this system, already reported in literature, could be confirmed: CdPr, Cd_2Pr, Cd_3Pr, $Cd_{45}Pr_{11}$, $Cd_{58}Pr_{13}$, Cd_6Pr and $Cd_{11}Pr$. The corresponding phase boundaries were determined at distinct temperatures. The homogeneity range of the high-temperature allotropic modification of Pr could be determined precisely and a limited solubility of 22.1 at.% Cd was derived. Additionally, single-crystal X-ray diffraction was employed to investigate structural details of Cd_2Pr; it is isotypic to the AlB_2-type structure with a *z* value of the Cd site of 0.5. DTA results of alloys located in the adjacent two-phase fields of Cd_2Pr suggested a phase transformation between 893 and 930°C. For the phase Cd_3Pr it was found that the lattice parameter *a* changes linearly with increasing Cd content, following Vegard's rule. The corresponding defect mechanism could be evaluated from structural data collected with single-crystal XRD. Introduction of a significant amount of vacancies on the Pr site and the reduction in symmetry of one Cd position (8*c* to 32*f*) resulted in a noticeable decrease of all R-values.

Citation: Reichmann TL, Effenberger HS, Ipser H (2014) Experimental Investigation of the Cd-Pr Phase Diagram. PLoS ONE 9(4): e94025. doi:10.1371/journal.pone.0094025

Editor: Andreas Hofmann, Griffith University, Australia

Received October 28, 2013; **Accepted** March 11, 2014; **Published** April 9, 2014

Funding: This work was supported by the Austrian Science Fund (FWF) under Project No. P 23270-N19 (www.fwf.ac.at). The funders had no role in study design, data collection and analysis, decision to publish, or preparation of the manuscript.

Competing Interests: The authors have declared that no competing interests exist.

* E-mail: Thomas.Reichmann@univie.ac.at

Introduction

An ever increasing demand of energy, especially in developing countries with high economic growth, makes the utilization of nuclear energy sometimes inevitable. On the back-end of the nuclear fuel cycle an immense amount of nuclear waste is being produced which has to be overcome. Indeed, low-level and intermediate-level radioactive waste is currently stored in interim storage facilities or deposited in geological repositories. Solutions for high-level waste are currently still in a planning stage and thus this waste is actually stored on-site. For an efficient utilization of nuclear fuels as well as to decimate the amount and radioactivity of nuclear waste, reprocessing techniques have been established.

Focusing onto reprocessing of nuclear waste, this is currently practiced by means of solvent extraction of actinides. Aqueous extraction of radioactive waste is suffers from several problems, described repeatedly in literature [1–5]. To overcome the major disadvantages of these hydro-metallurgical reprocessing methods, electro-transport and reductive extraction is applied to separate actinides and lanthanides from high-level radioactive waste. In this type of non-aqueous method liquid Cd is used to extract minor actinides from a liquid chloride salt solvent. The procedure is described in detail in [6–8].

The extraction behaviour of different elements between a molten chloride salt phase and a liquid metal strongly depends on the standard free energy of formation of the corresponding chlorides as well as on the activity coefficients of the extracted elements in the respective intermetallic compounds. Thus the separation factors are strongly influenced by the employed liquid metal which is preferentially Cd [9]. Therefore, a detailed knowledge of the respective Cd-RE phase diagrams as well as of the thermodynamic stabilities of the corresponding intermetallic compounds is of great importance. This was the reason for initiating a series of thermodynamic and phase diagram studies of different Cd-RE systems (cf. Refs. [10–11]).

Concerning the system Cd-Pr, only limited information about the phase diagram is available from literature. A compilation of structural data of the respective intermetallic compounds together with a partial phase diagram, determined by Johnson et al. [12], is given by Gschneidner and Calderwood [13]. Johnson et al. reported liquidus data in the composition range up to 1.83 at.% Pr, determined by chemical analysis of filtered samples of the corresponding equilibrium phases. The latter authors further applied differential thermal analysis and presented at least two invariant reactions. They argued for a degenerate eutectic reaction between Cd and $Cd_{11}Pr$ and a peritectic decomposition of $Cd_{11}Pr$ at 570°C, at which temperature 3.5 at.% Pr are soluble in liquid Cd. In a previous work Veleckis and Van Deventer [14] determined experimentally an invariant reaction temperature for a eutectic reaction between Pr and CdPr at 435°C.

On the basis of all available thermodynamic and phase diagram data Kurata and Sakamura [15] made a CALPHAD-type optimization and presented a partial Cd-Pr phase diagram between 0–25 at.% Pr.

Although the information on phase equilibria and invariant reactions in the Cd-Pr system is limited, an extensive survey of the occurring intermetallic compounds is given in literature. Table 1 compiles crystallographic data for the binary compounds together with their homogeneity ranges according to Reichmann and Ipser [11]. Related phase diagrams between Cd and lanthanides indicate that numerous intermetallic compounds are isotypic or

even isostructural. With the exception of the results of vapour pressure measurements given in Refs. [10,11], no significant homogeneity ranges of these phases are known. As mentioned in Table 1 some solubility was determined for at least five compounds whereas Cd_6Pr and $Cd_{11}Pr$ were described as line compounds. Noticeably, all compounds are located within the composition range 50–92 at.% Cd. The compound richest in Pr, CdPr, adopts the CsCl-structure type (*B*2). It was determined with energy-dispersive X-ray spectroscopy that CdPr dissolves around 3 at.% Pr whereas no significant solubility of Cd was found (cf. Table 1). The next compound richer in Cd is Cd_2Pr (structure type *C*6). Compounds with the respective composition ratios 1:1 and 2:1 were found in all phase diagrams between Cd and lanthanides. Compounds with the general formula Cd_2Ln, where Ln stands for lanthanides, were investigated extensively. They crystallize either in space-group *P*6/*mmm* or $P\bar{3}m1$ [19–24]. The only exception is Cd_2Eu for which space group *Imma* was found [25]. Compounds with space-group symmetry *P*6/*mmm* adopt the structure type AlB_2 (Pearson code *hP*3) with Wyckoff sequence *d a*; the site positions are (⅓ ⅔ ½) and (000). The compounds with space-group $P\bar{3}m1$ maintain the Pearson code and Wyckoff sequence, the site positions are (⅓ ⅔ *z*) and (000). However, the *z* parameter of the site 2(*d*) varies either between 0.042 and 0.080 or between 0.42 and 0.43. Phases adopting *z* parameters around 0.42 can be considered as having a distorted atomic arrangement from that found in space group *P*6/*mmm*. Curiously, both atomic arrangements with symmetry $P\bar{3}m1$ are currently known as the Cd_2Ce-type.

Single crystal X-ray diffraction was performed in the current study to determine an accurate *z* value for the Cd position in Cd_2Pr, as described in chapter 3. Although Iandelli and Palenzona [19] did not find evidence for any solid solubility of Cd_2Pr, Reichmann and Ipser [11] suggested a homogeneity range of around 1 at. %.

The compound Cd_3Pr was first described by Iandelli and Ferro [16] to crystallize in the BiF_3 structure type ($D0_3$). Compounds with the composition ratio 3:1 were found in most of the phase diagrams of Cd with lanthanides and appear with three different structure-types. In an early study of Bruzzone et al [18], who applied single crystal methods, the BiF_3 structure was confirmed as to be the structure-type of Cd_3Ce, Cd_3Pr and Cd_3Nd. This structure is coincident with a face centered cubic cell, formed by the respective rare earth element, where all cubic [8]-fold coordinated positions are occupied with Cd atoms [16].

In the very narrow composition range 79–82 at.% Cd, two intermetallic compounds are occurring: $Cd_{45}Pr_{11}$ (*cF*448) and $Cd_{58}Pr_{13}$ (*hP*142) [18]. Their unit cells are rather big, and compounds at these composition ratios appear irregularly in phase diagrams between Cd and lanthanides. $Cd_{45}Pr_{11}$ is isostructural with $Cd_{45}Sm_{11}$, which was investigated by single-crystal X-ray diffraction [26]. This structure type can be described by the so-called cluster concept originally adopted by Bradley and Jones [27]. $Cd_{45}Pr_{11}$ is thus an arrangement of 16 clusters of two types which are distributed along a NaTl-type unit cell. The two types of clusters which build up the $Cd_{45}Pr_{11}$ cell are related to clusters found in γ-brass phases and in α-Mn, respectively.

$Cd_{58}Pr_{13}$ forms a complex atomic arrangement that is isotypic to $Cd_{58}Ln_{13}$ where Ln stands for: La, Ce, Nd, Sm, Eu and Gd [18,24,28–30]. The basically hexagonal structure type contains various building blocks going along with extensive order-disorder phenomena resulting in distinct superstructures. Partly, an incommensurate behaviour is observed. Recently Piao et al. [31] discussed for the compound $Ce_{12.60}Cd_{58.68}$ a metrically commensurate representative which obviously represents a lock-in phase.

The compounds richest in Cd are Cd_6Pr and $Cd_{11}Pr$. Compounds with these composition ratios appear in all phase diagrams between Cd and lanthanides as line compounds, and Cd_6Pr and $Cd_{11}Pr$ are no exceptions, as determined by Reichmann and Ipser [11]. Johnson et al. [17] presented cell parameters for a number of compounds with the composition ratio 6:1. No additional information was given except that all homologues seem to be isomorphous. Subsequently, Larson and Cromer [32] investigated the crystal structure of Cd_6Y using single-crystal X-ray diffraction. They reported that the crystal structure is isotypic to Ru_3Be_{17} but with an additional Cd position in a 24-fold position and the site occupation factor of 0.33. Thus the structure-type of Cd_6Pr is considered to be YCd_6 (*cI*168). For the 1:11 stoichiometry two modifications are known, namely $BaCd_{11}$ (*tI*48) and $BaHg_{11}$ (*cP*36), where $Cd_{11}Pr$ is crystallizing in the latter structure type.

Due to the limited information about phase relations and invariant reaction temperatures, it was the aim of the present work to provide an experimental investigation of the Cd-Pr phase diagram. In addition, these data can serve as input into a CALPHAD-type optimization of the Cd-Pr system. This would allow a better understanding of the distribution behaviour of Pr in the electro-refining cell described above.

Table 1. Crystal structure data of binary compounds in the Cd-Pr system; phase boundaries at 550°C are given according to Reichmann and Ipser [11].

Phase	Lattice parameter (Å)	Phase boundaries (at.% Cd)	Structure type	Space group	References
$Cd_{11}Pr$	*a* = 9.287	91.67	$BaHg_{11}$	*Pm-3m*	[16]
Cd_6Pr	*a* = 15.689	85.71	Cd_6Y	*Im-3*	[17]
$Cd_{58}Pr_{13}$	*a* = 15.71	80.76–81.79	$Pu_{13}Zn_{58}$	*P6₃/mmc*	[18]
	c = 15.52				
$Cd_{45}Pr_{11}$	*a* = 21.842	79.98–80.36	$Cd_{45}Sm_{11}$	*F-43m*	[18]
Cd_3Pr	*a* = 7.186	75.00–76.19	BiF_3	*Fm-3m*	[16]
Cd_2Pr	*a* = 5.025	65.80–66.67	Cd_2Ce	*P-3m1*	[19]
	c = 3.459				
CdPr	*a* = 3.822	47.07–50.00	CsCl	*Pm-3m*	[16]

doi:10.1371/journal.pone.0094025.t001

Table 2. Experimental phase compositions and lattice parameters of selected Cd-Pr samples.

Sample		Phase analysis		SEM	
/nom. comp.	Heat treatment	Phase	Lattice parameter (Å)	Cd (at.%)	Pr (at.%)
(at.%)	T (°C); duration; T_{Max} (°C)[c]				
1	300; 3 months; 350	Cd	too ductile	100	0.0
$Cd_{98}Pr_2$		$Cd_{11}Pr$		91.5	8.5
2	300; 3 months; 350	Cd	too ductile	100	0.0
$Cd_{96}Pr_4$		$Cd_{11}Pr$		91.5	8.5
3a	300; 2 months; 700	Cd	a = 2.9788(2), c = 5.6134(5)	100	0.0
$Cd_{93}Pr_7$		$Cd_{11}Pr$	a = 9.3027(2)	91.4	8.6
3b	300; 3 months; 700	Cd	a = 2.9812(5), c = 5.6165(2)	100	0.0
$Cd_{93}Pr_7$		$Cd_{11}Pr$	a = 9.3076(4)	91.5	8.5
4a	540; 2 months; 900	$Cd_{11}Pr$	a = 9.3047(1)	91.5	8.5
$Cd_{88}Pr_{12}$		Cd_6Pr	a = 15.6904(2)	85.6	14.4
4b	540; 3 months; 700	$Cd_{11}Pr$	a = 9.3046(3)	91.5	8.5
$Cd_{88}Pr_{12}$		Cd_6Pr	a = 15.6919(4)	85.9	14.1
5a	600; 2 months; 1050	Cd_6Pr	a = 15.6933(2)	85.5	14.5
$Cd_{84}Pr_{16}$		$Cd_{58}Pr_{13}$	a = 15.6937(4), c = 15.5145(6)	81.8	18.2
5b	600; 3 months; 1050	Cd_6Pr	a = 15.6953(6)	85.5	14.5
$Cd_{84}Pr_{16}$		$Cd_{58}Pr_{13}$	a = 15.6934(1), c = 15.5189(2)	81.8	18.2
6a	600; 2 months; 1050	$Cd_{58}Pr_{13}$	a = 15.7032(4), c = 15.4759(6)	80.8	19.2
$Cd_{81}Pr_{19}$		$Cd_{45}Pr_{11}$	a = 21.8484(7)	80.3	19.7
6b	600; 3 months; 1050	$Cd_{58}Pr_{13}$	a = 15.6911(1), c = 15.4731(2)	80.9	19.1
$Cd_{81}Pr_{19}$		$Cd_{45}Pr_{11}$	a = 21.8428(2)	80.0	20.0
7	800; 2 months; 800	$Cd_{58}Pr_{13}$	a = 15.6894(1), c = 15.4660(2)	80.4	19.6
$Cd_{78.5}Pr_{21.5}$		Cd_3Pr	a = 7.1819(6)	76.3	23.7
8	650; 2 months; 1050	$Cd_{45}Pr_{11}$	a = 21.8424(3)	79.6	20.4
$Cd_{78}Pr_{22}$		Cd_3Pr	a = 7.1920(6)	76.2	23.8
9	700; 3 months; 1050	$Cd_{45}Pr_{11}$	a = 21.8448(6)	79.6	20.4
$Cd_{78}Pr_{22}$		Cd_3Pr	a = 7.1893(2)	76.3	23.7
10[a]	545; 6 weeks	Cd_3Pr	a = 7.2014(4)	75.3	24.7
$Cd_{74.9}Pr_{25.1}$		Cd_2Pr	a = 5.0463(2), c = 3.4447(3)	– [b]	– [b]
11[a]	680; 6 weeks	Cd_3Pr	–	75.7	24.3
$Cd_{74.7}Pr_{25.3}$		Cd_2Pr	–	– [b]	– [b]
12	650; 2 months; 1050	Cd_3Pr	a = 7.2029(9)	75.5	24.5
$Cd_{71}Pr_{29}$		Cd_2Pr	a = 5.0461(9), c = 3.4451(1)	66.3	33.7
13	700; 3 months; 1050	Cd_3Pr	a = 7.1979(4)	75.8	24.2
$Cd_{71}Pr_{29}$		Cd_2Pr	a = 5.0451(5), c = 3.4455(5)	66.6	33.4
14	800; 2 months; 1050	Cd_2Pr	a = 5.0446(3), c = 3.4452(3)	65.6	34.4
$Cd_{63}Pr_{37}$		CdPr	a = 3.8356(4)	50.1	49.9
15	650; 2 months; 1050	Cd_2Pr	a = 5.0439(5), c = 3.4453(5)	65.4	34.6
$Cd_{58}Pr_{42}$		CdPr	a = 3.8340(6)	50.0	50.0

Table 2. Cont.

Sample		Phase analysis		SEM	
/nom. comp.	Heat treatment	Phase	Lattice parameter (Å)	Cd (at.%)	Pr (at.%)
(at.%)	T (°C); duration; T_{Max} (°C)[c]				
16	700; 3 months; 1050	Cd_2Pr	$a = 5.0404(8)$, $c = 3.4434(6)$	65.6	34.4
$Cd_{58}Pr_{42}$		CdPr	$a = 3.8349(9)$	49.9	50.1
17	700; 3 months; 1050	CdPr	$a = 3.8498(8)$	47.1	52.9
$Cd_{46}Pr_{54}$		β-Pr	less intensity	22.1	77.9
18	600; 3 months; 1020	CdPr	too ductile	47.1	52.9
$Cd_{40}Pr_{60}$		β-Pr		20.0	80.0
19	400; 5 months; 1050	CdPr	too ductile	47.6	52.4
$Cd_{37}Pr_{63}$		α-Pr		_ [b]	_ [b]
20	530; 2 months; 1050	CdPr	too ductile	47.3	52.7
$Cd_{33}Pr_{67}$		β-Pr		18.7	81.3
21	700; 3 months; 1020	β-Pr	too ductile	14.9	85.1
$Cd_{15}Pr_{85}$					
22	500; 3 months; 1020	α-Pr	too ductile	3.5	96.5
$Cd_{10}Pr_{90}$		β-Pr		15.1	84.9
23	550; 3 months; 1020	α-Pr	too ductile	3.4	96.6
Cd_8Pr_{92}		β-Pr		12.2	87.8
24	600; 3 months; 1020	α-Pr	too ductile	3.1	96.9
Cd_6Pr_{94}		β-Pr		9.5	90.5
25	400; 5 months; 1050	CdPr	too ductile	_ [b]	_ [b]
Cd_3Pr_{97}		α-Pr		1.8	98.2

[a]Samples prepared with an isopiestic vapour pressure method, see Reichmann and Ipser [11].
[b]Microstructure of the respective phase was too fine to measure accurately with EDX.
[c]Highest temperature during sample preparation.
doi:10.1371/journal.pone.0094025.t002

Experimental

All samples were prepared from pure elements, using Cd shot (99.9999%, AlfaAesar, Johnson Matthey Chemicals, Karlsruhe, Germany) and Pr pieces (99.9%, Smart Elements, Vienna, Austria). The surface-oxide layer of the Pr pieces was removed with a file. The elements were weighed with a semi-micro balance to an accuracy of about ± 0.5 mg, resulting in an accuracy of ± 0.01 at.% in the nominal composition for a total sample mass of 1 g. To prevent Pr from oxidation, the whole sample preparation was carried out in a glove box under Ar atmosphere (oxygen level: <1 ppm, water level: <1 ppm). The metals were placed in Ta crucibles which were designed in our laboratory and subsequently enclosed by means of arc welding under an Ar atmosphere of 0.25 bar.

For equilibration, the crucibles were sealed into silica glass tubes under a dynamic vacuum of better than 10^{-2} mbar. Afterwards, melting and annealing procedures were performed in muffle furnaces. The corresponding heat treatments are listed in Table 2. Samples were slowly heated (0.5 K/min) to temperatures above the melting point of Cd; this allows that Cd reacted with Pr rather completely before reaching elevated temperatures. It was realized that the heating step had a decisive influence on the quality of the final samples. Since Cd has a high vapour pressure above its melting point [33] and boils at 767°C, it builds up a rather high pressure inside the closed crucibles when present as pure metal. It was observed several times that samples with rather high Cd contents, heated too fast, showed a drastic expansion of the Ta crucibles. Sometimes, condensed Cd was found at the inner top of the Ta crucibles, resulting in a large deviation of the corresponding sample compositions. This behaviour could be avoided by a slow heating rate. To reach a homogeneous distribution of the elements, all samples with a Pr content higher than 10 at.%, were heated above the overall melting point of the respective alloys or at least above the melting point of Pr. All other samples which contained high amounts of Cd were heated to temperatures below the boiling point of Cd, to prevent condensation of Cd at the inner top of the crucibles, and cooled quickly by removing them from the furnace. Annealing and maximum temperatures are listed in Table 2. Quick cooling was important to obtain as-cast alloys for further investigations of the crystallisation behaviour but it helped also to obtain small grains which guaranteed short diffusion paths during any following annealing step. Samples were annealed for at least five weeks and subsequently quenched in cold water.

Phase identification and precise lattice parameters of the different phases were obtained by means of powder X-ray diffraction (powder-XRD) using a Bruker D8 Discover Series 2 powder diffractometer in Bragg-Brentano pseudo-focusing geometry employing CuKα radiation. Data were collected by either a LynxEye silicon strip detector (exposure time: 2 h) or a solid state detector (exposure time: 4 h). Additional measurements were performed on a Guinier-Huber camera 670 operating with $CuK\alpha_1$

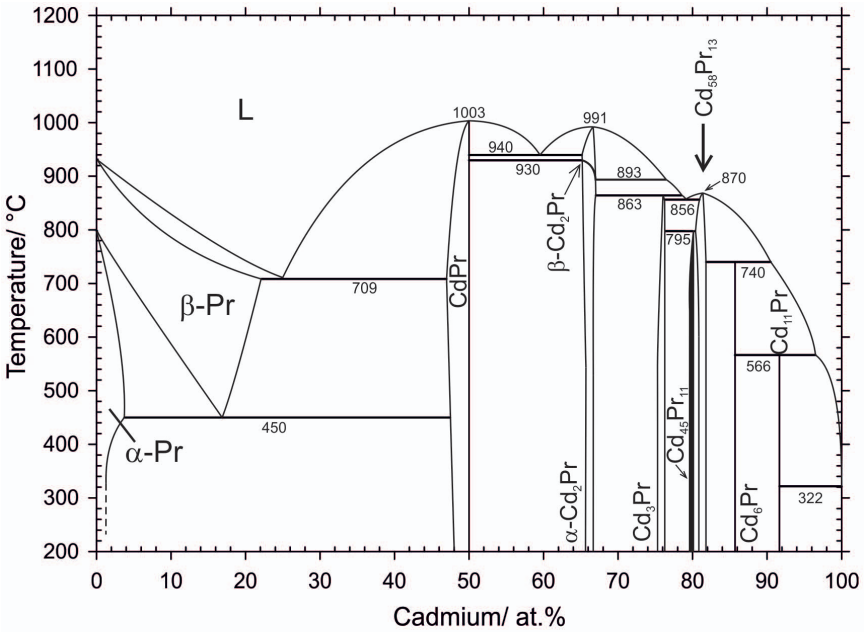

Figure 1. Cd-Pr phase diagram according to present results. The solubility of Pr in liquid Cd between 96.5–99.98 at.% Cd was taken from Johnson et al. [12].
doi:10.1371/journal.pone.0094025.g001

radiation and an image plate detector (measurement period: 2 h, 10 detection loops). For powder-XRD measurements small pieces of each sample were powdered in a tungsten carbide mortar. Special sample holders with X-ray transparent lids were used to prevent the sample powders from oxidation. The corresponding XRD patterns were analyzed and refined by means of the TOPAS 3 software, applying the fundamental parameter approach for peak profile modeling.

For single-crystal structure determination, a Nonius four-circle diffractometer equipped with a 300 μm capillary-optics collimator, graphite monochromatized MoKα radiation and a CCD detector, was used. Unit-cell parameters were obtained by least-square refinements of all 2θ values of the registered reflections. Corrections of Lorentz, polarization and adsorption effects were made and structure refinement was done with the software SHELXL-97 [34]. To prevent the present samples from oxidation during the experiments, they were coated with vaseline and measured under a dry nitrogen atmosphere. All further instrumental information is given in chapter 3.

For investigations of the microstructures, selected samples were embedded in phenolic hot mounting resin and then ground and polished. Grinding was carried out with silicon carbide abrasive paper (mesh size: 400, 600, 800, 1000 and 1200) using water as fluid. Although Pr containing alloys are essentially sensitive to water, it was sufficient to keep the grinding steps as short as possible to prevent oxidation. Grinded samples were intermediately stored in cyclohexane. For fine polishing of the surface a water-free diamond suspension was taken with kerosene as fluid.

Metallographic analyses were carried out on a binocular reflected-light microscope (Zeiss Axiotech 100) featured with a bi-refringent prism for differential interference contrast (DIC) imaging and equipment for operation under polarized light. Quantitative examinations of the microstructures were performed on a Zeiss Supra 55 VP environmental scanning electron microscope (SEM) using pure elements as standard materials and Co for the energy calibration of the energy-dispersive X-ray (EDX) detector signal. A 120 μm aperture was used and an acceleration voltage of 20 kV was applied. For imaging of the microstructures, a back-scatter detector was employed. Final compositions were calculated by conventional ZAF matrix correction from the measured X-ray intensities. The composition of each phase was measured at ten or more spots in order to minimize statistical errors and to obtain more reliable results. An estimated error of about ± 0.5 at.% was assumed for all measurements.

Differential thermal analysis (DTA) was carried out on a Netzsch DSC 404 F1 Pegasus using closed Ta crucibles with flat bottoms and a constant argon flow of 50 mL/min, respectively. Sapphire was used as the reference material. The temperature was measured with type-S (Pt/Pt10%Rh) thermocouples which were calibrated at the melting points of the high purity metals Sn, Zn, Ag and Cu. The samples weighed usually around 150–200 mg and were positioned in good thermal contact to the crucibles. Optionally, samples were powdered and pressed into pills to ensure good contact of the individual grains for better diffusion. Two heating- and cooling-curves were recorded for each sample using a heating rate of 5 $Kmin^{-1}$.

Results and Discussion

A total number of 29 samples were annealed and characterized by powder-XRD, SEM and DTA to obtain a complete description of the Cd-Pr phase diagram. Equilibrated samples and as-cast alloys were consulted to define homogeneity ranges, phase equilibria and crystallization behaviour. All relevant samples, examined with isothermal methods, are listed in Table 2. Heat treatments, identified phases and phase compositions are given. The corresponding results are discussed in detail in chapter 1. Samples studied by DTA are listed in Table 3, together with their thermal effects from two heating and cooling cycles, respectively. These thermal effects are discussed properly in chapter 2. On the basis of the combined results a complete version of the Cd-Pr phase diagram was drawn, which is given in Fig. 1.

Table 3. Thermal effects of selected samples determined with DTA.

Sample	Nominal comp. (at.%)	Annealing temperature (°C)	Heating (°C)					Cooling (°C)	
			Invariant effects		Other effects			Liquidus	Liquidus
1	$Cd_{98}Pr_2$	300	323					558	520
2	$Cd_{96}Pr_4$	300	321	569				606	567
3	$Cd_{93}Pr_7$	300	322	567				690	669
4	$Cd_{88}Pr_{12}$	540	742	563				795	791
5	$Cd_{84}Pr_{16}$	600	738					851	838
6	$Cd_{81}Pr_{19}$	600	858					867	830
7	$Cd_{78.5}Pr_{21.5}$	800	856					865	860
8+9	$Cd_{78}Pr_{22}$	650 and 700	799	857				867	855
12+13	$Cd_{71}Pr_{29}$	650 and 700	865					968	948
14	$Cd_{63}Pr_{37}$	800	931	941				982	968
15+16	$Cd_{58}Pr_{42}$	650 and 700	928	939				960	956
17	$Cd_{46}Pr_{54}$	700						996	991
18	$Cd_{40}Pr_{60}$	600	456	709				953	951
19	$Cd_{37}Pr_{63}$	400	451	710				934	925
20	$Cd_{33}Pr_{67}$	530	449	704				886	873
21	$Cd_{15}Pr_{85}$	700	448		496		746	784	782
22	$Cd_{10}Pr_{90}$	700						832	834
23	Cd_8Pr_{92}	550			806			848	855
24	Cd_6Pr_{94}	600	450		670		820	870	871
25	Cd_3Pr_{97}	400			595	731	871	897	899
26	$Cd_{91.7}Pr_{8.3}$	500	566					708	687
27	$Cd_{85.7}Pr_{14.3}$	500	741					836	803
28	$Cd_{81.7}Pr_{18.3}$	500						870	838
29[a]	$Cd_{81.2}Pr_{18.8}$	552						870	863
30[a]	$Cd_{81.1}Pr_{18.9}$	558	859					869	842
31	$Cd_{80.4}Pr_{19.6}$	500	796	855				867	842
32	$Cd_{79.9}Pr_{20.1}$	750	791	854				866	849
33	$Cd_{75}Pr_{25}$	500	864					909	894
34	$Cd_{68}Pr_{32}$	800	860					986	980
35	$Cd_{67}Pr_{33}$	800	893					988	983
36	$Cd_{66.7}Pr_{33.3}$	500			909			991	959
37[a]	$Cd_{66.5}Pr_{33.5}$	632			915			991	986
38[a]	$Cd_{65.8}Pr_{34.2}$	732			923			986	984

Table 3. Cont.

Sample	Nominal comp. (at.%)	Annealing temperature (°C)	Heating (°C)			Cooling (°C)	
			Invariant effects		Other effects	Liquidus	Liquidus
39	$Cd_{55}Pr_{45}$	800	930	940		991	977
40	$Cd_{41}Pr_{59}$	400	454	702		959	958
41	$Cd_{29}Pr_{71}$	400	449	715		–	817
42	$Cd_{25}Pr_{75}$	400	448	711		711	–
43	$Cd_{21}Pr_{79}$	400	448		720	733	738
44	$Cd_{18}Pr_{82}$	400	446	565		755	752
45	$Cd_{12}Pr_{88}$	400	447		549	766 812	813
46	Cd_9Pr_{91}	400	453		608	796 838	843

[a]Samples prepared with an isopiestic vapour pressure method, see Reichmann and Ipser [11].

doi:10.1371/journal.pone.0094025.t003

1. Results from Isothermal Methods

As can be seen in Table 2, several samples were prepared to determine the homogeneity ranges of the different intermetallic compounds at selected temperatures. All seven intermetallic compounds known from literature were confirmed with powder-XRD and SEM: $Cd_{11}Pr$, Cd_6Pr, $Cd_{58}Pr_{13}$, $Cd_{45}Pr_{11}$, Cd_3Pr, Cd_2Pr and CdPr. Estimated phase boundaries, defined at 550°C, fit quite well with values reported by Reichmann and Ipser [11] who applied an isopiestic vapour pressure method. Their values are included in Table 1 and indicate narrow but finite homogeneity ranges for all compounds except $Cd_{11}Pr$ and Cd_6Pr, which were identified as line compounds also in the present study.

As seen from Table 2, not all samples could be examined with both methods, *i.e.* SEM and powder-XRD. Samples containing large amounts of Cd or Pr, respectively, turned out to be rather ductile; consequently powder-XRD could not be applied. Trials to grind two-phase samples of CdPr together with α/β-Pr into powders failed: apart from the fact that they were very ductile, Pr has a high atomic number and thus absorption effects were found to be quite high when irradiating with X-rays. The resulting low intensities made it impossible to perform an accurate evaluation of the lattice parameters. With respect to their ductility, no powder-XRD was carried out for samples 1 and 2 as well. Indeed, these results were assumed to be similar to the results from samples 3a and 3b, respectively.

The overall composition of each sample determined by SEM was compared with its nominal composition to estimate possible weight losses due to volatile Cd. No significant deviation of the determined composition from the nominal composition was found in most of the samples (*e.g.* sample 21 in Table 2). Even for samples with high Cd contents only a very thin Cd film could be observed visually inside the crucibles indicating negligible deviation from the nominal composition.

From the present results it was possible to derive the homogeneity ranges of the seven intermetallic compounds and of the solid solutions based on Pr and Cd. They are listed in Table 4. The phase boundaries on either side of $Cd_{11}Pr$ and Cd_6Pr were found to deviate hardly at all from their corresponding stoichiometric compositions (*cf.* Table 2), *i.e.* the deviation was within the estimated error of the SEM measurements. Additionally, no significant variability of lattice parameters was observed, and thus $Cd_{11}Pr$ and Cd_6Pr were treated as line compounds at their stoichiometric compositions.

On the other hand, $Cd_{58}Pr_{13}$ exhibited clearly some solubility of Pr. As suggested by [11], the Pr solubility is temperature dependent. Its maximum solubility was predominantly described by sample 7 to be at around 80.4 at.% Cd at 800°C. Several single-phase samples of $Cd_{58}Pr_{13}$, taken from previous isopiestic vapour pressure experiments [11], were used to investigate lattice parameters. Although these samples were annealed at different temperatures between 480 and 600°C, phase compositions were plotted against cell parameters according to Vegard's rule (Fig. 2). As can be seen, there is no significant change of lattice parameter *a* along the homogeneity range of $Cd_{58}Pr_{13}$ but with increasing Cd content the cell expands in the *c* direction. Since the covalent radius of Pr is definitely higher than the covalent radius of Cd one would expect the opposite behaviour. A possible explanation might be that in $Cd_{58}Pr_{13}$ vacancies on Cd sites are responsible for the deviation from stoichiometry to the Pr side. Thus, the higher the Cd content the lower would be the vacancy concentration which would explain the observed expansion. Furthermore, the formation of complicated superstructures has to be taken into account as found in the related $Cd_{58}Ce_{13}$ phase [31]. From samples 5a and 5b it can be seen that phase compositions at the

Table 4. Maximum phase boundaries of Cd-Pr phases and of α–Pr and β–Pr (SEM) together with corresponding melting or decomposition temperatures averaged from DTA results.

Phase	Phase boundaries (at.% Cd)	Melting/decomposition temperatures (°C)
$Cd_{11}Pr$	91.7 (line compound)	566
Cd_6Pr	85.7 (line compound)	740
$Cd_{58}Pr_{13}$	80.4–81.8	870
$Cd_{45}Pr_{11}$	79.6–80.4	795
Cd_3Pr	75.0–76.3	863
Cd_2Pr	65.2–67.0	991
CdPr	47.0–50.1	1003
β–Pr	0–22.1	–
α–Pr	0–3.6	–

doi:10.1371/journal.pone.0094025.t004

Cd rich border of the homogeneity range of $Cd_{58}Pr_{13}$ were determined to be virtually identical to the stoichiometric composition, and thus the Cd solubility should be rather low.

$Cd_{58}Pr_{13}$ is in thermodynamic equilibrium with $Cd_{45}Pr_{11}$ within a very narrow two-phase field. In order to confirm this two-phase field, samples with the nominal composition $Cd_{81}Pr_{19}$ (samples 6a and 6b) were prepared and annealed at 600°C. Powder-XRD as well as SEM confirmed clearly the existence of the two-phase field $Cd_{58}Pr_{13}$+$Cd_{45}Pr_{11}$. The corresponding powder-XRD pattern of sample 6a is shown in Fig. 3. The latter sample was additionally used to determine the solubility of Cd in $Cd_{45}Pr_{11}$ at 600°C. The phase boundary was measured at 80.3 at.% Cd which corresponds exactly with the stoichiometric composition of $Cd_{45}Pr_{11}$. Three samples with the nominal compositions $Cd_{78}Pr_{22}$ (samples 8 and 9) and $Cd_{78.5}Pr_{21.5}$ (sample 7), respectively, were prepared and annealed at temperatures between 650 and 800°C to investigate a possible variation of the Pr-rich phase boundary of $Cd_{45}Pr_{11}$ with temperature. The phase boundary of $Cd_{45}Pr_{11}$ turned out to be the same at 650 and 700°C, both determined at 79.6 at.% Cd. However, when investigating sample 7, which had been annealed at 800°C, a two-phase equilibrium between $Cd_{58}Pr_{13}$ and Cd_3Pr was observed; the expected phase $Cd_{45}Pr_{11}$ was absent. Thus $Cd_{45}Pr_{11}$ must decompose at some temperature lower than 800°C. The corresponding DTA results are given in detail in section 2.

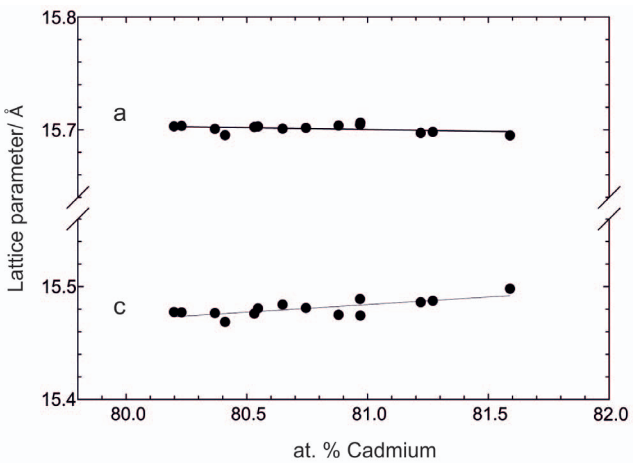

Figure 2. Lattice parameters *a* and *c* against at. % Cd within the homogeneity range of $Cd_{58}Pr_{13}$.
doi:10.1371/journal.pone.0094025.g002

Although [11] described that Cd_3Pr is only slightly more stable than a two-phase mixture of its neighbouring phases, in the present study it was found to form reliably as an intermediate compound between $Cd_{45}Pr_{11}$ and Cd_2Pr. Seven samples (7–13) were consulted to describe the phase boundaries of Cd_3Pr accurately between 545 and 800°C. As can be seen in Fig. 1 the homogeneity range is shifted towards compositions richer in Cd. Obviously, the homogeneity range does not include the stoichiometric composition at elevated temperatures. Nevertheless, the Pr-rich phase boundary of Cd_3Pr reaches 75.3 at.% Cd at 545°C. This value is indeed close to the stoichiometric composition, which would be reached by an extrapolation to lower temperatures.

This relatively broad homogeneity range suggested an investigation of the defect mechanism. Therefore, the lattice parameter *a* was plotted *vs.* the composition in Fig. 4. This plot is based on results from samples 8–11 and 13. A decrease of the lattice parameter *a* with increasing Cd content is indicated which is in agreement with the smaller covalent radius of Cd. Since interstitial Cd sites are unlikely within this close packed BiF_3-type structure, there are either mixed Cd/Pr positions or vacancies formed at the Pr site. To learn more about the defect mechanism, single-crystal X-ray diffraction was performed and the results are discussed in 3.

From the present results a homogeneity range of 65.4–66.7 at.% Cd could be estimated for Cd_2Pr at 550°C which is in good agreement with values given by [11]. No significant change of the lattice parameters was observed with varying composition. When grinding samples containing Cd_2Pr and CdPr, it appeared that these compounds are rather ductile. Vickers hardness measurements of single-phase Cd-Gd alloys were carried out by Bruzzone et al. [35]. When comparing the values of the different Cd-Gd compounds, one can recognize that especially the phases Cd_2Gd and CdGd show relatively small values. Since Cd_2Gd and CdGd are isotypic with the present phases Cd_2Pr and CdPr a similar mechanical behaviour was expected; in fact, it was extremely difficult to powder these samples. Consequently, the XRD-powder patterns of Cd_2Pr and CdPr showed rather broad peak shapes. Additionally, absorption phenomena of these Pr-rich phases lowered also the intensities and made it altogether difficult to derive accurate lattice parameters.

For structural investigations suitable single-crystals were obtained from an as-cast alloy with the stoichiometric composition Cd_2Pr. The corresponding sample was analysed with SEM to

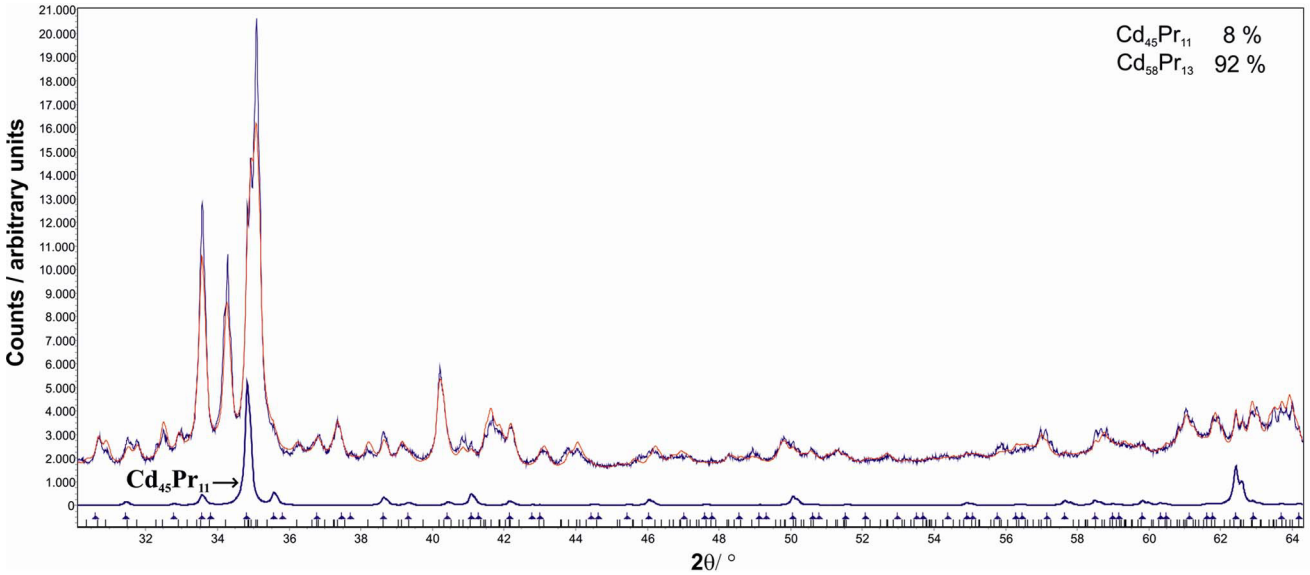

Figure 3. Powder-XRD pattern of an alloy with the nominal composition $Cd_{81}Pr_{19}$ (6a) which clearly contains both $Cd_{45}Pr_{11}$ and $Cd_{58}Pr_{13}$.; red curve: calculated pattern.
doi:10.1371/journal.pone.0094025.g003

consist of Cd_2Pr and Cd_3Pr grains. Phase compositions were found to be $Cd_{66.2}Pr_{33.8}$ (Cd_2Pr) and $Cd_{75.8}Pr_{24.2}$ (Cd_3Pr), respectively. Its microstructure exhibited clearly a primary crystallization of Cd_2Pr (*cf.* Fig. 5a). The results of a single crystal X-ray study of this phase can be found in chapter 3.

The compound richest in Pr is CdPr. It crystallizes in the CsCl-structure type and exhibits an ordered variety of the β-Pr structure which crystallizes in the *bcc* W-structure ($a = 4.1300$ Å [36]); half of the Pr sites in β-Pr are substituted by Cd atoms. Besides, a partial substitution of Pr by Cd according to $Cd_{1-x}Pr_{1+x}$, $x < 0.06$, was observed. The two-phase field β-Pr+CdPr can be considered as a large miscibility gap which cuts off a continuous solid solution (with a second-order phase transition) between these two phases. Samples with major amounts of $Cd_{1-x}Pr_{1+x}$, were used to show the correlation of the lattice parameter a with the composition (Fig. 6). The increasing Pr content goes along with an increase of the lattice parameter which is in perfect agreement with the relative atomic radii of Pr and Cd; the excellent linear fit (Fig. 6) corresponds with Vegard's rule.

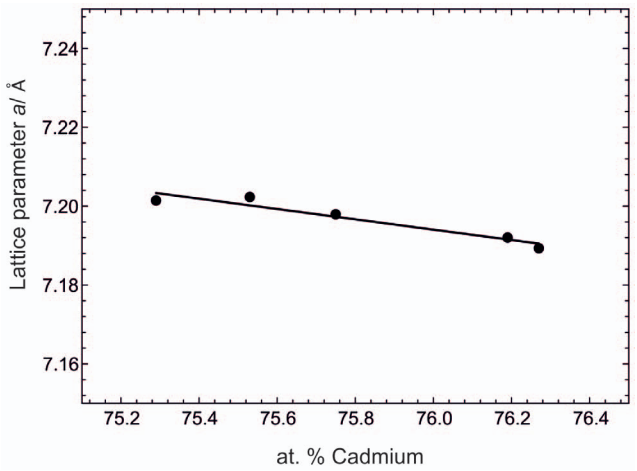

Figure 4. Lattice parameter *a* against at.% Cd within the homogeneity range of Cd_3Pr.
doi:10.1371/journal.pone.0094025.g004

2. Results of Thermal Analyses

Binary phase reactions were examined by means of DTA. For the description of the reaction scheme and the graphical representation of the phase diagram (Fig. 1) samples listed in Table 2 as well as additional equilibrated samples and such from isopiestic experiments [11] were used. Effects measured from samples with equal nominal compositions were averaged. The corresponding results of the DTA measurements are given in detail in Table 3. For each sample two heating and cooling cycles were performed at a heating rate of 5 K/min in order to check if equilibrium conditions can be restored after the first melting of the sample. It was found that most of the specimens were still in equilibrium after the first cycle. Nevertheless, for the graphical representation of the phase diagram all thermal effects, except the liquidus, were taken from the first heating curves. In case of the liquidus effect, usually an average value from the two heating curves was taken for the evaluation. Although most of the cooling curves exhibited considerable supercooling, their liquidus values were still considered to guide the construction of the liquidus curves shown in Figs. 1 and 7.

All invariant reactions, evaluated from the present results, are listed in Table 5 together with the respective reaction temperatures and types and the phase compositions. As can be seen, the intermetallic compounds $Cd_{11}Pr$, Cd_6Pr, $Cd_{45}Pr_{11}$ and Cd_3Pr are formed incongruently whereas $Cd_{58}Pr_{13}$, Cd_2Pr and CdPr show congruent melting behaviour. For measuring the melting or decomposition temperatures of these compounds pure samples were required. Therefore, alloys with stoichiometric compositions were subjected to special treatments. They were heated within 24 hours to a final temperature of 750°C, i.e., slightly below the boiling point of Cd, and held for 48 hours to reach a homogeneous distribution of the elements. Afterwards the temperature was slowly reduced to room temperature. All alloys were checked by powder-XRD to consist of single-phases only; the corresponding melting or decomposition temperatures are included in Table 4.

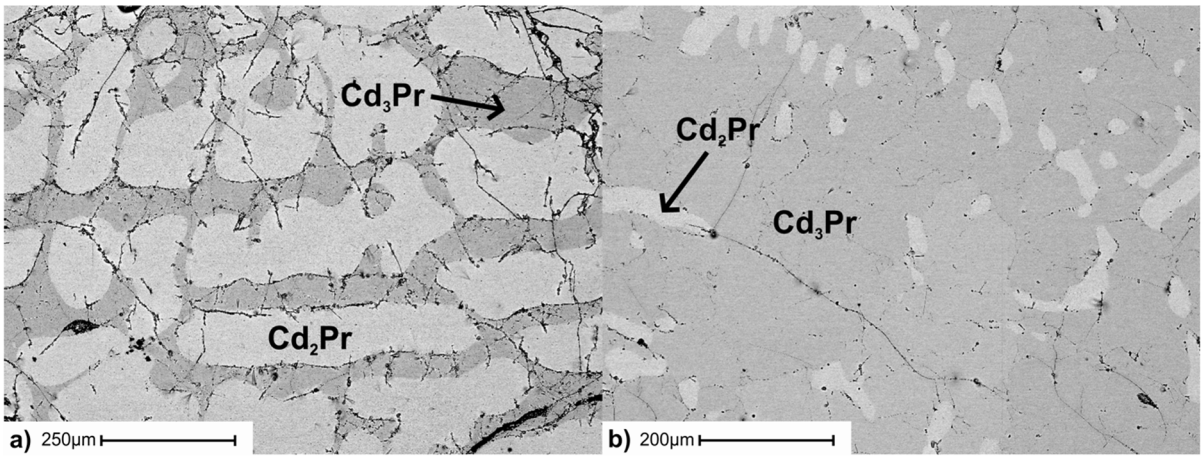

Figure 5. BSE image of an a) as-cast alloy with the stoichiometric composition of Cd_2Pr and b) as-cast alloy with the stoichiometric composition of Cd_3Pr.
doi:10.1371/journal.pone.0094025.g005

At the very Cd-rich side of the phase diagram a degenerate isothermal reaction takes place which could be either a eutectic or a peritectic reaction, respectively. Samples with nominal compositions within the two-phase field Cd+$Cd_{11}Pr$ were studied by DTA to define the reaction temperature. Unfortunately, no significant evidence could be obtained for either case because the melting point of Cd is very close to the reaction temperature. Therefore, a DTA investigation of a sample with the nominal composition $Cd_{96}Pr_4$ (sample 2, Table 3) was performed against pure Cd as a reference material. Assuming, that both sample and reference position are symmetrical within the furnace, one would expect an effect at first caused by the sample if the respective reaction exhibits a degenerate eutectic. Contrary, one would expect to observe first the melting point of Cd if a degenerate peritectic reaction takes place. Since Cd is used as the reference material, its melting effect is hypothetically exothermal and thus in the opposite direction in the DTA curve, compared to effects from the samples. From the present experiment it was clearly found that Cd melted first. Thus a degenerate peritectic reaction was considered for the formation of Cd.

The two line-compounds $Cd_{11}Pr$ and Cd_6Pr decompose peritectically at 566 and 740°C, respectively. The peritectic reaction temperature of $Cd_{11}Pr$ fits excellently with the value of 570°C, reported by Johnson et al [12]. Although there were no experimental data available, Kurata and Sakamura [15] calculated an isothermal reaction temperature of 678°C for the peritectic formation of Cd_6Pr. As can be seen this value is quite different from the presently obtained one at 740°C.

The liquidus between 100 and 96 at.% Cd is rising rather steeply (Fig. 1). Its shape was drawn according to results from Johnson et al. [12] which agree quite well with the present results. Johnson et al. [12] determined the solubility of Pr in liquid Cd by

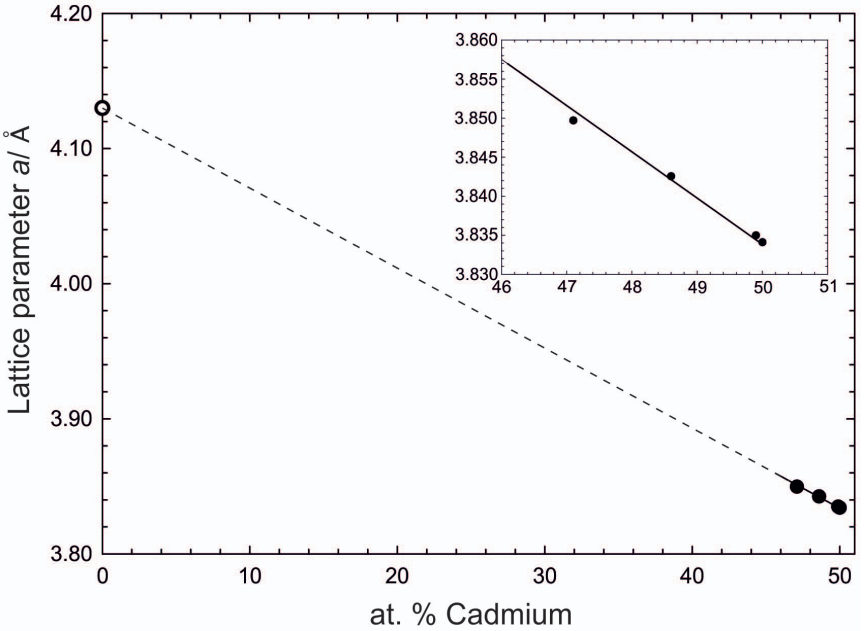

Figure 6. Lattice parameter *a* against at.% Cd for CdPr.; full circles: sample compositions defined by SEM (see text).
doi:10.1371/journal.pone.0094025.g006

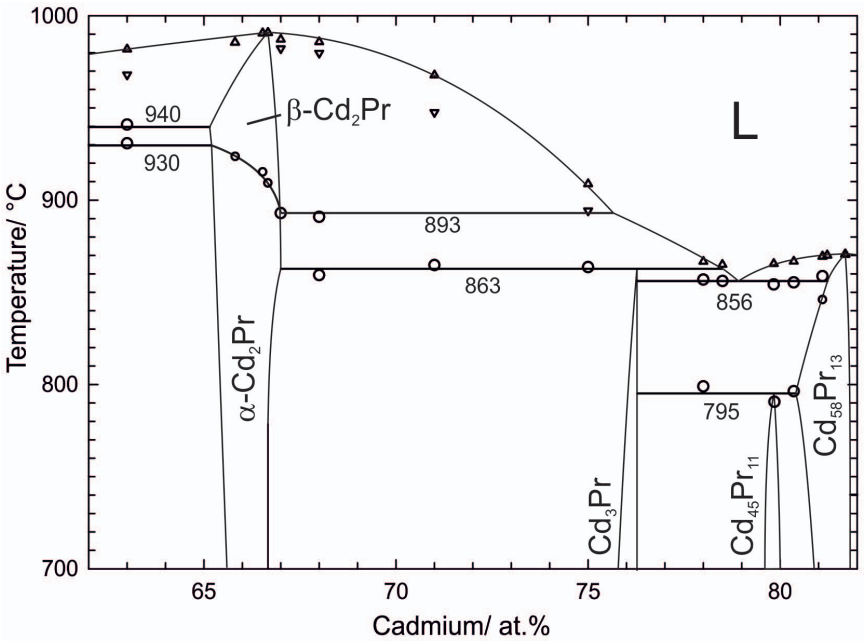

Figure 7. Partial phase diagram of Cd-Pr between 61 and 82 at.% Cd. Large circles: invariant thermal effects. Small circles: non-invariant effects. Triangles up: liquidus on heating. Triangles down: liquidus on cooling.
doi:10.1371/journal.pone.0094025.g007

chemical analysis of filtered samples. From an empirical fit of their solubility data the authors calculated that 3.5 at.% Pr are soluble in liquid Cd at 570°C. This solubility was considered in the present version of the phase diagram to be the liquidus composition at the peritectic formation temperature of $Cd_{11}Pr$.

In the narrow composition range 62 to 82 at.% Cd four intermetallic compounds are located and several invariant reactions take place (see Fig. 7). As described above, the two compounds $Cd_{58}Pr_{13}$ and $Cd_{45}Pr_{11}$ are in thermodynamic equilibrium within a very narrow two-phase field and the decomposition of $Cd_{45}Pr_{11}$ must occur at some temperature below 800°C. A rather weak effect was found in samples containing $Cd_{45}Pr_{11}$ and the corresponding average value was 795°C. Due to the fact that these effects were rather weak and that no $Cd_{45}Pr_{11}$ was found at 800°C it was reasonable to assume a solid-phase reaction, *i.e.* a peritectoid formation of $Cd_{45}Pr_{11}$.

To determine the primary crystallization behaviour of as-cast alloys at the stoichiometric compositions $Cd_{58}Pr_{13}$ and $Cd_{45}Pr_{11}$, their microstructures were investigated. The respective microstructure of an as-cast alloy with the stoichiometric composition of $Cd_{45}Pr_{11}$ is shown in Fig. 8a. As $Cd_{58}Pr_{13}$ is the primary crystallizing phase and Cd_3Pr forms the matrix, a eutectic reaction was assumed between these two phases; this was also indicated from the DTA experiments that provided an average eutectic

Table 5. Invariant reactions in the system Cd-Pr derived from a combination of all present results.

Reaction	*T*/°C	Phase compositions (at.% Cd)			Reaction type
L+$Cd_{11}Pr$ ⇄ Cd	322±2	~100	91.7	~100	degenerate peritectic
L+Cd_6Pr ⇄ $Cd_{11}Pr$	566±3	96.5[a]	85.7	91.7	peritectic
L+$Cd_{58}Pr_{13}$ ⇄ Cd_6Pr	740±3	90.5	81.8	85.7	peritectic
$Cd_{58}Pr_{13}$ ⇄ L	870±2		81.7		congruent melting
$Cd_{58}Pr_{13}$+ Cd_3Pr ⇄ $Cd_{45}Pr_{11}$	795±5	80.4	76.3	79.8	peritectoid
L ⇄ $Cd_{58}Pr_{13}$+ Cd_3Pr	856±3	78.9	81.3	76.3	eutectic
Cd_2Pr ⇄ L	991±2		66.7		congruent melting
L+α-Cd_2Pr ⇄ Cd_3Pr	863±3	78.5	67.0	76.3	peritectic
α-Cd_2Pr ⇄ β-Cd_2Pr	893±4		67.0		polymorphic transformation
	930±2		65.2		
CdPr ⇄ L	1003±2		50.0		congruent melting
L ⇄ β-Cd_2Pr+CdPr	940±2	59.1	65.2	50.1	eutectic
L ⇄ CdPr+β-Pr	709±5	25.0	47.0	22.1	eutectic
β-Pr ⇄ CdPr+α-Pr	450±5	16.8	47.1	4.0	eutectoid

[a]value was taken from Johnson et al. [12].
doi:10.1371/journal.pone.0094025.t005

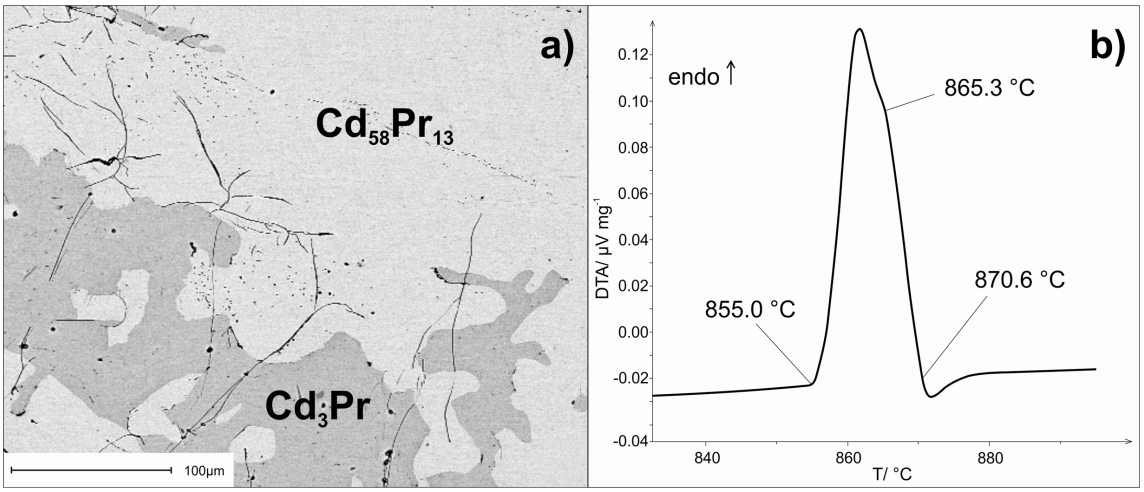

Figure 8. a) Microstructure of an as-cast alloy with the stoichiometric composition of $Cd_{45}Pr_{11}$; b) DTA curve of sample 7 against pure $Cd_{58}Pr_{13}$ as reference.
doi:10.1371/journal.pone.0094025.g008

temperature of 856°C. To confirm the congruent formation of $Cd_{58}Pr_{13}$, a sample with the nominal composition $Cd_{78.5}Pr_{21.5}$ was annealed at 800°C (sample 7); pure $Cd_{58}Pr_{13}$ served as the reference material for the DTA. The procedure was exactly the same as described above. The corresponding DTA curve is given in Fig. 8b. As expected, there was at first an endothermic effect in the sample, dedicated to the eutectic reaction, followed by the liquidus of the sample, measured at 865.3°C. Subsequently, the melting effect of $Cd_{58}Pr_{13}$ appeared at around 870.6°C in terms of a hypothetical exothermal effect. Thus, the congruent formation of $Cd_{58}Pr_{13}$ is apparent.

When investigating samples located in the two-phase field (CdPr+Cd_2Pr) two effects were found to occur at 930 and 940°C, respectively. Clearly, there is a eutectic reaction between the congruently melting compounds CdPr and Cd_2Pr at 940°C. The eutectic point could be located between 58.0 and 59.4 at.% Cd. As-cast alloys at these compositions showed primary crystallization of CdPr and Cd_2Pr, respectively. However, the effect at lower temperature was unexpected. Single-phase samples of Cd_2Pr exhibited small effects slightly below 930°C. Thus a structural transformation of Cd_2Pr was assumed similar to the situation reported for Cd_2Gd [35] or Cd_2Dy [19,20]. DTA results of samples, located in the homogeneity range as well as adjacent two-phase fields of Cd_2Pr, showed that the polymorphic transformation is temperature dependent and varies between 893°C on the Cd-rich side and 930°C on the Pr-rich side. Several attempts to quench the high temperature modification β-Cd_2Pr were not successful but attempts to clarify its structure are still continuing.

Several samples were investigated to clarify the homogeneity range of the high-temperature modification of Pr exactly.

Table 6. Details for single-crystal X-ray data collections and structure refinements for the compounds Cd_2Pr and Cd_3Pr.

Compound	Cd_2Pr	$Cd_{76.4}Pr_{23.6}$
Crystal system, space group	hexagonal, *P6/mmm*	cubic, $Fm\bar{3}m$
a/Å	5.043 (2)	7.204 (1)
c/Å	3.455 (1)	–
ρ_{calc}/g•cm^{-3}; μ(*MoKα*)/mm^{-1}	7.98; 29	8.49; 29
Z	1	4
Total reflections measured	1022[a,*]	1443[a,**]
Unique reflections (*n*); reflections with $F_o > 4\sigma(F_o)$	87; 82	63; 58
$R_{int} = \Sigma \lvert F_o^2 - F_o^2(\text{mean})\rvert / \Sigma F_o^2$	0.0459	0.0272
$R1 = \Sigma (\lvert\lvert F_o\rvert - \lvert F_c\rvert\rvert) / \Sigma \lvert F_o\rvert$ observed; all reflections	0.0299; 0.0319	0.0168; 0.0178
$wR^2 = [\Sigma w(F_o^2 - F_c^2)^2 / \Sigma wF_o^4]^{1/2}$	0.0720	0.0371
$GooF = [\Sigma w(F_o^2 - F_c^2)^2 / (n-p)]^{1/2}$	1.187	1.093
Extinction parameter	0.016(14)	0.0019(2)
Max Δ/σ; number of variable parameters (p)	<0.001; 6	<0.001; 9
Final difference Fourier map/eÅ^{-3}	−2.02 to +2.25	−0.71 to +0.97

[a]NONIUS four-circle diffractometer (equipped with a CCD detector and a 300 µm capillary-optics collimator, Mo tube, graphite monochromator; 30 mm crystal-detector distance; rotation angle 2° per image, φ-scans at 14 distinct ω-angles). Structure refinements were performed with program SHELXL (Sheldrick [34]).
*513 measured frames, exposure time of 145 seconds per degree.
**514 measured frames, exposure time of 165 seconds per degree.
doi:10.1371/journal.pone.0094025.t006

Table 7. Atomic coordinates and equivalent isotropic displacement parameters for Cd_2Pr and Cd_3Pr.

Atomic Position	Wykoff letter	Occupation factor	Atomic coordinates	U_{eq}
Cd_2Pr				
Pr	1(*a*)	1.0	(0 0 0)	0.0170(3)
Cd	2(*d*)	1.0	(⅔ ⅓ ½)	0.0199(3)
Cd_3Pr				
Pr	4*a*	0.93(1)	(0 0 0)	0.0151(4)
Cd1	4*b*	1	(½ ½ ½)	0.0173(5)
Cd2	32*f*	0.246(2)	(*x x x*) *x* = 0.2392(5)	0.0297(10)

doi:10.1371/journal.pone.0094025.t007

Respective DTA results fit excellently with phase compositions obtained from EDX measurements. Therefore, the maximum solubility of Cd in β-Pr could be determined reliably and is given as around 22.1 at.% Cd (*cf.* sample 17). From the determined liquidus temperatures of all samples located within 0–50 at.% Cd, the eutectic point L⇄CdPr+β-Pr was estimated to be around 25 at.% Cd. From DTA of twelve samples the eutectoid decomposition temperature of β-Pr was averaged and a value of 450°C was obtained. Veleckis and Van Deventer [14] listed isothermal reaction temperatures for eutectic reactions between lanthanides and the respective compound richest in lanthanide, which is, with the exception of Cd_5Eu_6, CsCl-structured CdLn (Ln = lanthanide). As indicated by Gschneidner and Calderwood [13] the eutectic temperatures do not fit well with subsequently reported values. The largest differences between values given by Veleckis and Van Deventer and those reported later occurred when the corresponding lanthanide undergoes an allotropic transformation. The present authors assume that Veleckis and Van Deventer did not consider the high-temperature allotropic modifications of the respective lanthanides. Indeed, their reported value for the eutectic formation of Pr and CdPr, given as 435°C, corresponds quite well with the present value for the eutectoid decomposition of β-Pr.

3. Single-crystal X-ray Study of Cd_3Pr and Cd_2Pr

Fig. 4 shows a decrease of the lattice parameter *a* with increasing Cd content in Cd_3Pr. This behaviour is following Vegard's rule and is expected when considering that the covalent radius of Cd is noticeably smaller. As described above the most probable defects are mixed positions or vacancies on the Pr site of the Cd_3Pr lattice.

Single-crystal X-ray diffraction experiments were performed in the present study to determine the defect mechanism in Cd_3Pr accurately. Suitable single crystals were found in an as-cast alloy with the stoichiometric composition of Cd_3Pr. The corresponding microstructure is shown in Fig. 5b. The atomic arrangement was refined from single-crystal X-ray diffraction data (see Table 6). Atomic coordinates, occupation factors and equivalent isotropic displacement parameters are listed in Table 7. The structure of Cd_3Pr consists of three atomic positions, all originally described as special positions. Pr atoms are located at the site 4(*a*) exhibiting minor vacancies. The Cd atoms are located at the fully occupied site 4(*b*) and the site 32(*f*), roughly occupied to a quarter. Attempts to refine the crystal structure in any subgroup of $Fm\bar{3}m$ to establish an ordered structure model failed. Considering vacancies at the Pr and Cd(2) sites reduced the R-values significantly.

Moreover, the vacancies observed at the Pr site are in agreement with the analytically observed homogeneity range of Cd_3Pr. The chemical composition calculated from the structure refinement ($Cd_{76.3}Pr_{23.7}$) is in excellent agreement with the composition detected by SEM investigations ($Cd_{75.9}Pr_{24.1}$).

Iandelli and Palenzona [19] as well as Mulokozi [22] described Cd_2Pr to crystallize in the Cd_2Ce-type, a deformed AlB_2-type structure type with space-group symmetry $P\bar{3}m1$, where Cd occupies the site 2(*d*) (⅓ ⅔ *z*) with z = 0.42. During the present work a suitable crystal of Cd_2Pr with the dimensions $0.02\times0.02\times0.10$ mm was used for single-crystal X-ray diffraction measurements. The corresponding data collection is given in Table 6. Atomic coordinates, occupation factors and equivalent isotropic displacement parameters are listed in Table 7. The structural refinement exhibited space-group symmetry $P6/mmm$ with the Cd atom located at (⅓ ⅔ ½). Any attempts to refine the crystal structure with a lower symmetry failed. Consequently, Cd_2Pr is also assumed to adopt the simple AlB_2-type.

Conclusion

The complete Cd-Pr phase diagram was investigated with a combination of powder-XRD, SEM and DTA; it is presented in Fig. 1. Based on the present results, the homogeneity ranges of the altogether seven intermetallic compounds and of the solid solution of Cd in Pr were derived (Table 4). The solubility ranges fit quite well with values reported previously by Reichmann and Ipser [11]. Additionally, melting or decomposition temperatures of all intermetallic compounds, derived from DTA measurements, are listed. It was found that the intermetallic compounds $Cd_{11}Pr$, Cd_6Pr, $Cd_{45}Pr_{11}$ and Cd_3Pr are formed incongruently whereas $Cd_{58}Pr_{13}$, Cd_2Pr and CdPr exhibit congruent formation behaviour. The invariant reaction temperature for the peritectic formation of $Cd_{11}Pr$ was comparable with values reported by Refs. [12] and [15]. The solid solubility of Cd in β-Pr could be determined reliably and is given as about 22.1 at.% Cd. The addition of Cd stabilizes the high-temperature modification β-Pr down to 450°C where it decomposes in terms of a eutectoid reaction.

A phase transformation of Cd_2Pr is suggested by the DTA results. Several attempts to synthesize and quench the high temperature modification β-Cd_2Pr were not successful but attempts are continuing to clarify its structure. The low-temperature modification of Cd_2Pr was examined by single-crystal XRD and determined to crystallize in the simple AlB_2-type. Furthermore, single-crystal X-ray diffraction was employed to explain the defect mechanism in Cd_3Pr. Due to reduction in symmetry of one Cd position and the resulting introduction of ordered vacancies the R-values could be decreased noticeable.

Acknowledgments

The authors want to thank the Faculty of Physics of the University of Vienna and especially Dr. Stephan Puchegger for help with the SEM measurements.

Author Contributions

Conceived and designed the experiments: TLR HSE HI. Performed the experiments: TLR HSE. Analyzed the data: TLR HSE. Contributed reagents/materials/analysis tools: HSE HI. Wrote the paper: TLR. Contributed research strategy: HI TLR.

References

1. Olander D (2009) Nuclear fuels - Present and future. J. Nuclear Mater. 389: 1–22.
2. Johnson I (1988) The Thermodynamics of Pyromchemical Processes for Liquid Metal Reactor Fuel Cycles. J. Nuclear Mater. 154: 169–180.
3. Ackerman JP (1991) Chemical Basis for Pyrochemical Reprocessing of Nuclear-Fuel. Ind. Eng. Chem. Res. 30: 141–145.
4. Laidler JJ, Battles JE, Miller WE, Ackerman JP, Carls EL (1997) Development of Pyroprocessing Technology. Progr. Nuclear Energy 31 no.1/2: 131–140.
5. Yamana H, Wakayama N, Souda N, Moriyama H (2000) Systematics of the thermodynamic properties of trivalent f-elements in a pyrometallurgical bi-phase extraction system. J. Nuclear Mater 278: 37–47.
6. Moriyama H, Seshimo S, Moritani K, Ito Y, Mitsugashira T (1994) Reductive Extraction Behavior of Actinide and Lanthanide Elements in Molten-Salt and Liquid-Metal Binary Phase Systems. J. Alloys Comp. 213: 354–359.
7. Moriyama H, Yamana H, Nishikawa S, Shibata S, Wakayama N, et al. (1998) Thermodynamics of reductive extraction of actinides and lanthanides from molten chloride salt into liquid metal. J. Alloys Comp. 271: 587–591.
8. Conocar O, Douyere N, Glatz J-P, Lacquement J, Malmbeck R, et al. (2006) Promising pyrochemical actinide/lanthanide separation processes using aluminum. Nuclear Sci. Eng. 153: 253–261.
9. Kurata M, Sakamura Y, Hijikata T, Kinoshita K (1995) Distribution behavior of uranium, neptunium, rare-earth elements (Y,La,Ce,Nd,Sm,Eu,Gd) and alkaline-earth metals (Sr,Ba) between molten LiCl-KCl eutectic salt and liquid cadmium or bismuth. J. Nuclear Mater. 227: 110–121.
10. Skołyszewska-Kühberger B, Reichmann TL, Ganesan R, Ipser H (2013) Thermodynamic study of the cerium-cadmium system. CALPHAD 10.1016/j.calphad.2013.07.005.
11. Reichmann TL, Ipser H (2013) Thermochemical Investigations in the System Cadmium-Praseodymium Relevant for Pyrometallurgical Fuel Reprocessing Metall. Mater. Trans. A DOI:10.1007/s11661-013-2065-4.
12. Johnson I, Anderson KE, Blomquist RA (1966) Partial Constitutional Diagrams for Cd-La, Cd-Ce, Cd-Pr, Cd-Nd and Cd-Sm Systems. Trans. ASM 59: 352–355.
13. Gschneidner KA Jr, Calderwood FW (1988) The Cd-Pr system. Bull. Alloy Phase Diag. 9: 130–132.
14. Veleckis E, Van Deventer E (1964) ANL-6925, Semi-Annual Report, Argone National Lab.
15. Kurata M, Sakamura Y (2001) Thermodynamic assessment of systems of actinide or rare earth with Cd. J. Phase Equilibria 22 no.3: 232–240.
16. Iandelli A, Ferro R (1954) Alloys of Cadmium with Lanthanum, Cerium and Praseodymium. Gazz. Chim. Ital. 84: 463–478.
17. Johnson I, Schablaske RV, Tani BS, Anderson K (1964) $CeCd_6$ -Type Rare Earth-Cadmium Alloys. Trans. Met. Soc. AIME 230: 1485–1487.
18. Bruzzone G, Fornasini ML, Merlo F (1973) Rare earth intermediate phases with cadmium. J. Less-Common Met. 30: 361–375.
19. Iandelli A, Palenzona A (1968) On Occurrence of MX_2 Phases of Rare Earths with Ib, IIb and IIIb Group Elements and Their Crystal Structures. J. Less-Common Met. 15: 273–284.
20. Laube E, Kusma JB (1964) Über einige Y- und Dy-haltige Legierungsphasen. Monatsh. Chem. 95: 1504–1513.
21. Kusma JB, Uhryn NS (1966) Crystal structures of some compounds of rare earth metals with cadmium. Dopovidi Akademii Nauk Ukrains'koi RSR: 1025–1027.
22. Mulokozi AM (1977) Nature of bonding in Rare-Earth compounds RX_2 with AlB_2-type or closely related structures I: Compounds RCd_2 with a deformed AlB_2 structure and influence of F-bonding. J. Less-Common Met. 53: 205–210.
23. Hoffmann RD, Pöttgen R (2001) AlB_2-related intermetallic compounds - a comprehensive view based on group-subgroup relations. Z. Kristallogr. 216: 127–145.
24. Tang J, Gschneidner KA Jr (1989) Searching for new heavy fermion materials in cerium intermetallic compounds. J. Less-Common Met. 149: 341–347.
25. Koester W, Meixner J (1965) The constitution of the systems of Europium with Silver, Cadmium and Indium and the Cadmium-Strontium system. Z. Metallkde. 56: 695–703.
26. Fornasini ML, Chabot B, Parthé E (1978) Crystal-Structure of $Sm_{11}cd_{45}$ with Gamma-Brass and Alpha-Mn Clusters. Acta. Cryst. B34: 2093–2099.
27. Bradley AJ, Jones P (1933) An X-ray investigation of the copper-aluminium alloys. J. Inst. Met. 51: 131–162.
28. Bruzzone G, Fornasini ML (1974) Contribution to System Samarium-Cadmium. J. Less-Common Met. 37: 289–292.
29. Bruzzone G, Merlo F (1973) Lanthanum-Cadmium System. J. Less-Common Met. 30: 303–305.
30. Piao SY, Gomez CP, Lidin S (2006) Complexity of hexagonal approximants in the $RE_{13}Zn{\sim}58$ system (RE = Ce, Pr, Nd, Sm, Gd, Tb and Dy). Z. Kristallogr., New Cryst. Struct. 221: 391–401.
31. Piao SY, Palatinus L, Lidin S (2008) All the disorder mechanisms in the 13:58 phases come together. Out of the modulated confusion rises the remarkable phase Ce12.60Cd58.68(2). Inorg. Chem. 47: 1079–1086.
32. Larson AC, Cromer DT (1971) Crystal Structure of YCd_6. Acta. Cryst. B27: 1875–1879.
33. Binnewies M, Milke E (1999) Thermodynamic Data of Elements and Compounds. WILEY-VCH, Weinheim. 295 p.
34. Sheldrick GM (2007) A short history of SHELX, Acta Crystallographica Section A: Foundations of Crystallography 64: 112–122.
35. Bruzzone G, Fornasini ML, Merlo F (1971) Gadolinium-Cadmium System. J. Less-Common Met. 25: 295–301.
36. Spedding FH, Hanak JJ, Daane AH (1961) High Temperature Allotropy and Thermal Expansion of the Rare-Earth Metals. J. Less-Common Met. 3 no.2: 110–124.

Publication 3

Thomas L. Reichmann, Klaus W. Richter, Simona Delsante, Gabriella Borzone and Herbert Ipser

Enthalpies of formation of Cd-Pr intermetallic compounds and thermodynamic assessment of the Cd-Pr system

CALPHAD (2014), 47: 56-62

Contributions to this paper:

T.L. Reichmann: sample preparation and calorimetric measurements, CALPHAD-type optimization, writing of the paper

K.W. Richter: introduction into CALPHAD, support with optimization and theoretical advice

S. Delsante: performance of calorimetric measurements

G. Borzone: performance of calorimetric measurements

H. Ipser: general advice and helpful comments, proofreading of the manuscript

Contribution of T. L. Reichmann to this paper: 60 %

CALPHAD: Computer Coupling of Phase Diagrams and Thermochemistry 47 (2014) 56–62

Contents lists available at ScienceDirect

CALPHAD: Computer Coupling of Phase Diagrams and Thermochemistry

journal homepage: www.elsevier.com/locate/calphad

Enthalpies of formation of Cd–Pr intermetallic compounds and thermodynamic assessment of the Cd–Pr system

Thomas L. Reichmann [a,*], Klaus W. Richter [a], Simona Delsante [b], Gabriella Borzone [b], Herbert Ipser [a]

[a] Department of Inorganic Chemistry (Materials Chemistry), University of Vienna, 1090 Wien, Austria
[b] Dipartimento di Chimica e Chimica Industriale, Università di Genova, 16146 Genova, Italy

ARTICLE INFO

Article history:
Received 3 February 2014
Received in revised form
17 June 2014
Accepted 20 June 2014
Available online 3 July 2014

Keywords:
CALPHAD
Phase diagram Cd–Pr
Enthalpy of formation
Alloys

ABSTRACT

In the present study standard enthalpies of formation were measured by reaction and solution calorimetry at stoichiometric compositions of Cd_2Pr, Cd_3Pr, $Cd_{58}Pr_{13}$ and Cd_6Pr. The corresponding values were determined to be −46.0, −38.8, −35.2 and −24.7 kJ/mol(at), respectively. These data together with thermodynamic data and phase diagram information from literature served as input data for a CALPHAD-type optimization of the Cd–Pr phase diagram. The complete composition range could be described precisely with the present models, both with respect to phase equilibria as well as to thermodynamic input data. The thermodynamic parameters of all intermetallic compounds were modelled following Neumann–Kopp rule. Temperature dependent contributions to the individual Gibbs energies were used for all compounds. Extended solid solubilities are well described for the low- and high-temperature modifications of Pr and also for the intermetallic compound CdPr. A quite good agreement with all viable data available from literature was found and is presented.

1. Introduction

In the last decades, the question of how to satisfy the ever increasing demand of energy has become most pressing for countries with high economic growth. The utilization of nuclear energy is sometimes inevitable for nations belonging to the group of developing and emerging countries. For an efficient use of nuclear energy, these countries have to establish strategies comprising an optimized reprocessing routine of spent nuclear fuels as well as an adequate waste management on the back-end of their nuclear fuel cycle. Indeed, low-level and intermediate-level radioactive waste is currently stored in interim storage facilities or deposited in geological repositories. Solutions for high-level waste are currently still in a planning stage and thus this type of waste is actually stored on-site.

Focusing onto reprocessing of nuclear waste, this is currently practiced by means of solvent extraction of actinides using tributyl phosphate (TBP), known as hydro-metallurgical technique or aqueous reprocessing (e.g., PUREX), respectively. Unfortunately, this technique deals with several problems like radiation and temperature instability of the various solvents used in the process. In addition, a huge amount of liquid waste is produced when applying PUREX or related processes. It is therefore reasonable to investigate an alternative type of reprocessing, called the pyro-metallurgical technique. The latter technique is not dealing with the major disadvantages of the aqueous methods, as outlined by Olander [1], and it is described repeatedly in literature, see e.g., Refs. [2–5].

In particular, electro-transport and reductive extraction is applied to separate actinides and lanthanides from high-level radioactive waste inside an “electro-transporter” cell. The respective electrochemical vessel contains a liquid metal pool at the bottom, covered by a molten salt solution serving as electrolyte. One basket anode, containing chopped nuclear fuels, and at least two cathodes are inserted into the liquid salt. During the process especially uranium, plutonium and minor actinides are transported whereas rare earth elements, alkaline and alkaline earth elements remain in the liquid salt. Additional reductive agents like Li are added to the salt which promotes the extractability of rare earth (RE) elements into the liquid metal pool at the bottom by forming intermetallic compounds. Moriyama et al. [6–7] determined that the separation factors, which are an indicator for extractability, are quite different between actinides and lanthanides. In principle, actinides have the higher affinity for extraction into a metal phase, a fact that is desirable, considering the chemical similarity to lanthanides. The extraction behaviour of different elements between a molten chloride salt phase and a liquid metal strongly depends on the standard free energy of formation of the corresponding chlorides as well as on the activity coefficients of the extracted elements in the

* Corresponding author.
E-mail address: thomas.reichmann@univie.ac.at (T.L. Reichmann).

http://dx.doi.org/10.1016/j.calphad.2014.06.005

respective intermetallic compounds. Thus the separation factors are strongly influenced by the employed liquid metal which is preferentially Cd [8]. Therefore, a detailed knowledge of the respective Cd–RE phase diagrams as well as of the thermodynamic stabilities of the corresponding intermetallic compounds is of great importance. This was the reason for initiating a series of thermodynamic and phase diagram studies of different Cd–RE systems (cf. Refs. [9–11]).

It was the aim of the present study to perform a CALPHAD-type optimization of the complete Cd–Pr system based on relevant literature data on phase equilibria and thermodynamic properties, and supported by additional experimental values for the enthalpy of formation of the intermetallic compounds Cd_2Pr, Cd_3Pr, $Cd_{58}Pr_{13}$ and Cd_6Pr.

2. Literature overview

The Cd–Pr phase diagram has been investigated in detail by Reichmann et al. [11] who applied conventional methods, i.e. powder X-ray diffraction (XRD), differential thermal analysis (DTA), and scanning electron microscopy (SEM), to clarify the phase relationships, including extent of solid solutions, homogeneity ranges and isothermal reaction temperatures in the whole composition range. In addition, a complete literature survey concerning the intermetallic compounds observed within this system was given there. All intermetallic compounds, i.e. CdPr, Cd_2Pr, Cd_3Pr, $Cd_{45}Pr_{11}$, $Cd_{58}Pr_{13}$, Cd_6Pr and $Cd_{11}Pr$, presented previously by Gschneidner and Calderwood [12], were confirmed. Additionally, an extended solid solubility of 22.1 at% Cd in the high-temperature allotropic modification of Pr was reported. Apparently, the addition of Cd stabilizes the high-temperature modification β-Pr down to 450 °C where it decomposes in a eutectoid reaction. All isothermal reactions as well as the corresponding reaction temperatures relevant for the present CALPHAD-type optimization are listed in Table 1. All intermetallic compounds except Cd_6Pr and $Cd_{11}Pr$ show noticeable homogeneity ranges in the order of ~1 at% which were defined by Reichmann et al. in their recent phase diagram study [11] in agreement with the results from vapour pressure measurements [10].

Besides the work of Reichmann et al. [11] only limited information concerning phase diagram data was available from literature. Johnson et al. [13] reported liquidus data in the composition range up to 1.83 at% Pr, determined by chemical analysis of filtered samples of the corresponding equilibrium phases. These data were considered in Ref. [11]. In addition, Johnson et al. applied DTA and presented at least two invariant reactions. They argued for a degenerate eutectic reaction between Cd and $Cd_{11}Pr$ and a peritectic decomposition of $Cd_{11}Pr$ at 570 °C, at which temperature 3.5 at% Pr are soluble in liquid Cd. In their DTA measurements Reichmann et al. could show that the degenerate reaction between Cd and $Cd_{11}Pr$ must actually be a peritectic reaction. However, the peritectic formation temperature of $Cd_{11}Pr$ agrees quite well with the results of Ref. [11] where it was re-determined as 566 °C.

In a previous paper Veleckis and Van Deventer [14] determined experimentally an invariant reaction temperature of 435 °C for a eutectic reaction between Pr and CdPr, a value which corresponds obviously to the eutectoid decomposition reaction of β-Pr (see above). It must be assumed that Veleckis and Van Deventer did not consider the high-temperature allotropic modification of Pr.

As far as thermodynamic information is concerned, Reichmann and Ipser [10] determined Cd vapour pressures as a function of composition and temperature, using an isopiestic vapour pressure method. From these data the authors derived activity values of Cd at 823 K. By using an activity value for Pr in the two-phase field $Cd_{11}Pr+L$, taken from Johnson and Yonco [15], as integration constant, a Gibbs–Duhem integration was performed to calculate Gibbs energies of formation at 823 K. In the study by Johnson and Yonco, the Gibbs energy of formation of the compound $Cd_{11}Pr$ had been determined by means of a Gibbs–Duhem integration based on thermodynamic activity values of Pr in $Cd_{11}Pr$ from own emf measurements. They showed that both, enthalpy and entropy of formation, of $Cd_{11}Pr$ were independent of temperature between 635 and 825 K.

In an early work by Castrillejo et al. [16], Gibbs energies of formation of the three intermetallic compounds $Cd_{11}Pr$, Cd_6Pr and $Cd_{58}Pr_{13}$ were measured by electrochemical techniques. The corresponding values at 823 K were determined to be -11.2 ± 0.1, -18.7 ± 0.1 and -22.9 ± 0.1 kJ mol(at)$^{-1}$. Comparing these values with Gibbs energies of formation given by Reichmann and Ipser [10] a quite good agreement can be observed. In addition, Castrillejo et al. listed partial Gibbs energies of Pr in the two-phase fields $Cd_{58}Pr_{13}+Cd_6Pr$, $Cd_6Pr+Cd_{11}Pr$, and $Cd_{11}Pr+L$, given as -107.6 ± 0.6, -127.4 ± 0.9 and -133.8 ± 1.2 kJ mol(at)$^{-1}$ for 823 K.

Based on the results of Johnson and co-workers [13,15], Kurata and Sakamura [17] made a CALPHAD-type optimization of the Cd–Pr system up to 25 at% Pr. They considered $Cd_{11}Pr$, Cd_6Pr and $Cd_{58}Pr_{13}$ as line-compounds in their calculations and defined temperature dependent Gibbs energies for two of these compounds. Moreover, Kurata and Sakamura presented activity values of Pr in liquid Cd derived from their calculations.

Recently, experimental heat capacities became available for the compound $Cd_{11}Pr$ [24]; they had been obtained for the temperature interval 300–550 K by differential scanning calorimetry (DSC).

Table 1
All invariant reactions and respective phase compositions determined experimentally by [11] together with the calculated reaction temperatures for comparison.

Reaction	T (°C)		Phase compositions (at% Cd)						Reaction type
	Calculated	Experimental	Calculated			Experimental			
[a]$L+Cd_{11}Pr\rightleftarrows Cd$	321	322	~100	~100	91.7	~100	91.7	~100	Degenerate peritectic
$L+Cd_6Pr\rightleftarrows Cd_{11}Pr$	570	566	97.2	85.7	91.7	96.5	85.7	91.7	Peritectic
$L+Cd_{58}Pr_{13}\rightleftarrows Cd_6Pr$	734	740	92.4	81.7	85.7	90.5	81.8	85.7	Peritectic
$L \rightleftarrows Cd_{58}Pr_{13}$	876	870		81.7			81.7		Congruent melting
$Cd_{58}Pr_{13}+Cd_3Pr\rightleftarrows Cd_{45}Pr_{11}$	800	795	81.7	75.0	80.4	80.4	76.3	79.8	Peritectoid
$L\rightleftarrows Cd_{58}Pr_{13}+Cd_3Pr$	867	856	78.8	81.7	75.0	78.9	81.3	76.3	Eutectic
$L\rightleftarrows Cd_2Pr$	984	991		66.7			66.7		Congruent melting
$L+\alpha\text{-}Cd_2Pr\rightleftarrows Cd_3Pr$	869	863	78.8	66.7	75.0	78.5	67.0	76.3	Peritectic
$L\rightleftarrows CdPr$	999	1003		50.0			50.0		Congruent melting
$L\rightleftarrows\beta\text{-}Cd_2Pr+CdPr$	947	940	59.2	66.7	50.0	59.1	65.2	50.1	Eutectic
$L\rightleftarrows CdPr+\beta\text{-}Pr$	712	709	23.0	47.1	20.3	25.0	47.0	22.1	Eutectic
$\beta\text{-}Pr\rightleftarrows CdPr+\alpha\text{-}Pr$	437	450	17.0	47.4	4.5	16.8	47.1	4.0	Eutectoid

[a] Reaction was modelled as degenerate eutectic $L\rightleftarrows Cd+Cd_{11}Pr$ (compare text).

Table 2
Standard enthalpies of formation measured by reaction and solution calorimetry; estimated error ±2 kJ/mol(at); reference state: Cd(s), α-Pr(s).

Phase	Solution calorimetry $\Delta_f H$/kJ mol $(at)^{-1}$	Reaction calorimetry $\Delta_f H$/kJ mol $(at)^{-1}$
Cd_6Pr	−24.7	–
$Cd_{58}Pr_{13}$	−34.3[a]	−36.0[a]
Cd_3Pr	−38.8	–
Cd_2Pr	−46.0	–

[a] Average of two measured values, see Section 3.

3. Experimental

To provide additional input data for the present CALPHAD-type optimization, calorimetric measurements were performed in two ways. Reaction calorimetric measurements were carried out in Genova to determine the enthalpy of formation of the intermetallic compound $Cd_{58}Pr_{13}$. In addition, solution calorimetry was used in Vienna to obtain enthalpies of formation of Cd_2Pr, Cd_3Pr, $Cd_{58}Pr_{13}$ and Cd_6Pr. The experimental setups of both methods are discussed in detail in Sections 3.1 and 3.2. All calorimetric results are listed in Table 2.

3.1. Reaction calorimetry

High purity Cd rods (5N, Koch-Light Laboratories LTD., Colnbrook, England) and Pr pieces (99.9%, Smart Elements, Vienna, Austria) were used for sample preparation. To lower diffusion paths and increase the reaction rate during the calorimetric synthesis, samples were prepared with Cd and Pr powders. The metals were filed inside a glove box under Ar atmosphere (oxygen level: <1 ppm, water level: <1 ppm) to prevent oxidation. The metal powders were then weighed according to calculated amounts, mixed homogeneously and pressed into compact pellets. For the calorimetric measurements, the pellets were enclosed in tight-sealed Ta crucibles to prevent oxidation and to avoid possible weigh-losses due to the rather high vapour pressure of Cd.

All calorimetric experiments were performed using a high temperature drop calorimeter described repeatedly in literature [18,19]. Heat effects were evaluated following a series of calibration runs by dropping specimens of known heat content, typically pure Ag, into the calorimeter. Each measurement involved two separate runs: a reaction run and a reference run; a detailed description is given by Ghosh et al. [20]. All runs were performed at a drop temperature of 298 K and a calorimeter temperature of 1048 K. In the first run, the so-called reaction run, the sample is dropped into the calorimeter, and the observed heat effect ΔH_1 is due to

$$Cd(s,\ 298\ K) + Pr(s,\ 298\ K) \rightarrow Cd_{58}Pr_{13}(s,\ 1048\ K) \quad (1)$$

After retrieving the reacted sample from the calorimeter, it is dropped once more into the calorimeter where the following heat effect ΔH_2 is observed:

$$Cd_{58}Pr_{13}(s,\ 298\ K) \rightarrow Cd_{58}Pr_{13}(s,\ 1048\ K) \quad (2)$$

By taking the difference $\Delta H_1 - \Delta H_2$, crucible effects are cancelled out and the enthalpy of formation of $Cd_{58}Pr_{13}$ is observed at 298 K

$$\Delta H_1 - \Delta H_2 = \Delta_f H^0_{Cd_{58}Pr_{13}}(s,\ 298\ K) \quad (3)$$

The equilibrium state of every sample after the reaction run was checked by standard phase analysis methods (LOM, SEM, X-ray powder diffraction, EPMA). The respective uncertainty of the enthalpy of mixing values is estimated to be around ±2 kJ/mol (at). The accuracy of the measurement and the evaluation of the error are discussed in detail in Refs. [18–20].

3.2. Solution calorimetry

Solution calorimetry in liquid Sn was performed using a Calvet-type twin calorimeter with two thermopiles with more than 200 thermocouples each. Enthalpies of formation were measured indirectly by dropping pure Cd (99.9999% Alfa AESAR, Karlsruhe, Germany), Pr (99.9%, Smart Elements, Vienna, Austria) and corresponding pieces of the intermetallic compounds into molten Sn at 823 °C. The intermetallic compounds were synthesized in their stoichiometric ratios using an isothermal isopiestic method according to Ref. [10]. All samples were determined to be pure single-phase by powder-XRD. An automated drop device was used and drops were performed under an Ar atmosphere. Ten sample pieces (between 30 and 50 mg each) and additional five pieces of NIST standard sapphire, for the calibration of the heat signal, were dropped at each calorimetric run. Graphite was used as crucible material. No reaction between the metals and the crucible material was observed in any measurement. Limiting heats of solution $\Delta_{sol}\overline{H}^0_i$ were derived by extrapolation for Cd, Pr and the respective compounds and enthalpies of formation were evaluated according to

$$\Delta_f H^{T_d}_{Cd_xPr_y} = x\Delta_{sol}\overline{H}^0_{Cd} + y\Delta_{sol}\overline{H}^0_{Pr} - \Delta_{sol}\overline{H}^0_{Cd_xPr_y} \quad (4)$$

where T_d is the drop temperature (298 K). The furnace temperature and the drop temperature were recorded for each drop; the calculations were made using mean values over all drops. The scattering of the temperature signals were low and did not influence the measurements significantly.

Besides all instrumental errors, systematic errors were estimated to be mainly due to incomplete mixing of the samples with the solvent as well as due to evaporation of Cd. In general it was observed that some Cd condensed at the colder part of the silica glass tubes during the calorimetric runs. Therefore, the intervals between individual drops were reduced to 40 min. Although the effect was still present it was clearly less significant. According to the evaluation of the results of these measurements (compare chapter 4), the overall error for the enthalpies of formation is estimated to be ±2 kJ/mol(at).

4. Thermodynamic modelling

The aim of the present work was to derive a set of thermodynamic model parameters, describing Gibbs energies of all phases in the system, which can be used as input data for a CALPHAD-type calculation. The optimization, described in detail by Lukas et al. [21], is based on obtaining the minimum total Gibbs energy of the system at constant temperature and pressure, yielding the composition and the amount of phases in equilibrium. For the calculations themselves the ThermoCalc® Classic software package (version S) [25] was used.

4.1. Pure elements

The Gibbs energy function ${}^0G^\theta_i = G^\theta_i - H_i^{SER}$ for element i (i=Cd, Pr) in the phase θ (θ=α-Pr, β-Pr, Cd, or liquid) is described by a power series as defined by Dinsdale [26]. The corresponding parameters were taken from the SGTE 5.1 database included in the software package.

4.2. Modelling of liquid and solid solution phases

The solid solutions based on α-Pr and β-Pr as well as the liquid phase were modelled in terms of a standard substitutional model with one sublattice. The molar Gibbs energy of a solution phase θ is described as follows:

$$G_m^\theta = G_{ref}^\theta + G_{id}^\theta + G_E^\theta + G_{other}^\theta + \ldots \quad (5)$$

where G_{ref}^θ is the molar Gibbs energy of the weighted sum of the system constituents i in the crystallographic structure corresponding to the phase θ relative to the chosen reference state (typically the stable element reference state, SER)

$$G_{ref}^\theta = \sum_{i=1}^{n} x_i {}^0G_i^\theta \quad (6)$$

and its temperature dependence is given by

$$G(T) = a + bT + cT\ln(T) + \sum_n d_n T^n \quad (7)$$

where $a - d_i$ are adjustable coefficients.

The contribution to the Gibbs energy from ideal random mixing of the constituents in the crystal lattice or in the liquid, denoted G_{id}^θ, is defined as ideal mixing

$$G_{id}^\theta = RT \sum_{i=1}^{n} x_i \ln(x_i) \quad (8)$$

for a system consisting of n components.

The Gibbs energy which describes the effect of non-ideal mixing behaviour on the thermodynamic properties of a solution phase is given by the usual Redlich–Kister formalism [22]

$$G_E^\theta = x_i x_j ({}^0L_{ij} + {}^1L_{ij}(x_i - x_j) + {}^2L_{ij}(x_i - x_j)^2 + \ldots) \quad (9)$$

where the temperature-dependent interaction parameters, describing the mutual interaction between constituents i and j, are denoted ${}^\nu L$ (ν=0, 1, 2, …). The temperature dependence of the interaction parameters is usually defined as

$${}^\nu L_{ij} = {}^\nu a + {}^\nu bT \quad (10)$$

4.3. Modelling of intermetallic phases

The intermetallic phase CdPr with CsCl-(B2-) structure was modelled with a two-sublattice model $(Pr)_{0.5}(Cd,Pr)_{0.5}$; since the experimental results indicate a homogeneity range to the Pr-rich side only, it was assumed that the Pr-sublattice remains fully occupied whereas on the Cd-sublattice a small amount of Cd-atoms can be substituted by Pr-atoms. This was discussed in detail in Ref. [11]. The G_{ref}^θ for such a model is given by

$$G_{ref}^\theta = \sum {}^1y_i {}^2y_j {}^0G_{(i:j)} \quad i,j = \mathrm{Cd},\ \mathrm{Pr} \quad (11)$$

where the y terms are the site fractions of each constituent in the relevant sublattices, 1 and 2. The term ${}^0G_{(i:j)}$ is the Gibbs energy of formation of the "virtual compound" (or "end member") ij.

All other phases were treated as stoichiometric compounds, i.e. no variability concerning the composition was considered. The Gibbs energy is modelled relative to the surface of reference

$${}^{srf}G_m^\theta = \sum_{i=1}^{n} b_i G_i^{SER} \quad (12)$$

with G_i^{SER} as the Gibbs energy of component i in the stable element form and b_i as the stoichiometric coefficient for i in the phase θ.

5. Results and discussion

5.1. Calorimetric measurements

The enthalpies of formation at the stoichiometric compositions of Cd_2Pr, Cd_3Pr, $Cd_{58}Pr_{13}$ and Cd_6Pr, derived from the present calorimetric measurements, are listed in Table 2. All values are referred to the standard reference states of Cd and Pr and are given at 298 K.

Reaction calorimetric measurements were done by dropping samples with the stoichimetric composition $Cd_{58}Pr_{13}$ into the calorimeter. Additionally, samples with compositions close to $Cd_{58}Pr_{13}$ were dropped to obtain the trend of $\Delta_f H^0$ vs. composition, and to evaluate the most reliable value. From these experiments, two values were derived at the stoichiometric composition of $Cd_{58}Pr_{13}$, namely −35.0 kJ/mol(at) and −37.0 kJ/mol(at), and the corresponding accuracy was calculated to be within ±1.4 kJ/mol (at). Thus, an average value of −36.0 kJ/mol(at) is given in Table 2. Considering all possible statistical and systematic errors, as outlined in detail by Delsante and Borzone [23], the resulting error should not exceed ±2 kJ/mol(at).

From solution calorimetry, enthalpies of formation could be derived for Cd_2Pr, Cd_3Pr, $Cd_{58}Pr_{13}$ and Cd_6Pr. The rather Cd-rich compound $Cd_{58}Pr_{13}$ was measured twice which allowed the estimation of an internal error for the present measurements. The two values, i.e. −35.1 kJ/mol(at) and −33.4 kJ/mol(at) with an error of ±2 kJ/mol(at), were found to be in good agreement with each other. Again, an average value of 34.4 kJ/mol(at) is listed in Table 2. Comparing the results of the two different calorimetric methods, a value of −35 ± 2 kJ/mol(at) is suggested for the standard enthalpy of formation of $Cd_{58}Pr_{13}$.

The accuracy of the enthalpy of formation for Cd_2Pr, Cd_3Pr and Cd_6Pr was assumed to be similar and is given likewise with ±2 kJ/mol(at). The corresponding enthalpy values, together with the results of the CALPHAD optimization, are presented in Fig. 1. As it was indicated already earlier by Reichmann and Ipser [10], an exothermic behaviour is observed within the composition range 40–100 at% Cd.

5.2. Thermodynamic optimization

The present optimization is based on thermodynamic data and phase diagram information collected for this system. Gibbs energies of formation and activity values of Cd at 823 K were taken from Reichmann and Ipser [10]. Additionally, enthalpies of formation

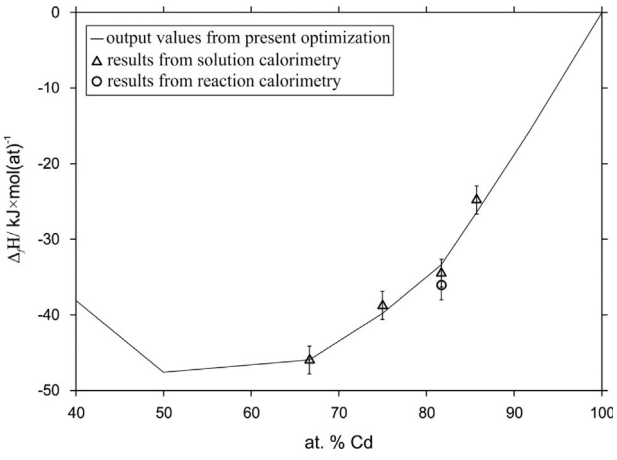

Fig. 1. Comparison of enthalpies of formation from calorimetric measurements with output values from the present calculation; reference state: Cd(s) and α-Pr(s); error bars are given according to chapter 3.

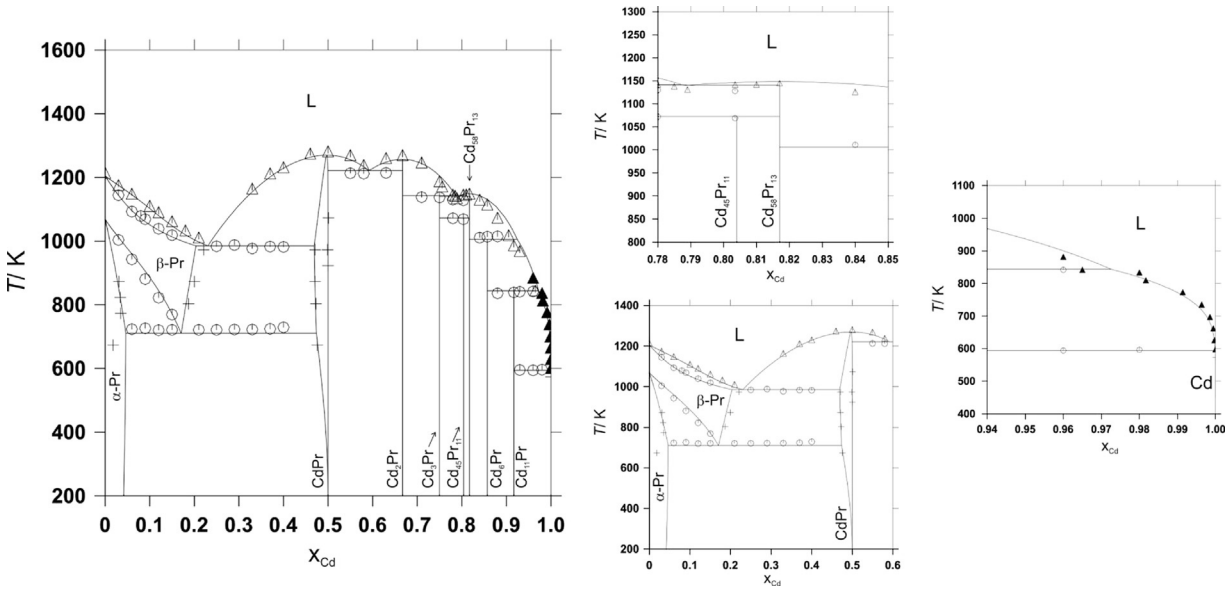

Fig. 2. Comparison of the calculated Cd–Pr phase diagram with data available from literature; open triangles and circles: DTA values, plus signs: SEM data, both from Reichman et al. [11]; filled triangles: Johnson et al. [13].

from the present study were used as input values. The phase diagram was optimized according to the experimentally determined version published by Reichmann et al. [11] and liquidus values from Johnson et al. [13]. All additional data were taken for comparison.

The calculated phase diagram is shown in Fig. 2 together with experimental results. A comparison between calculated and experimentally determined invariant reaction temperatures is listed in Table 1. The entire composition range could be well described with the present model. Considering the rather small homogeneity ranges of the compounds (compare Refs. [10,11]) only CdPr was introduced with some solubility into the model while all other compounds were treated as line compounds. According to the results by Reichmann et al. [11], CdPr dissolves apparently around 3 at% Pr by substituting Cd sites. The corresponding model parameters are given in Table 3.

A temperature dependent phase transformation of Cd_2Pr, suggested in Ref. [11], was not considered in the calculations but the two modifications of Cd_2Pr were treated as one single phase. In Ref. [11] there were strong experimental indications for a degenerate peritectic formation reaction of (Cd) at 322 °C. To simplify the calculations this was considered as a degenerate eutectic reaction in the present study. Treating the reaction as a peritectic would be only possible when assuming some solubility of Pr in Cd. Since no experimental information on solubility is available, this was avoided here.

All line-compounds were modelled using temperature dependent contributions to the total Gibbs energies. The respective thermodynamic parameters are listed in Table 3. Experimental Gibbs energies of formation at 823 K served as starting points for the modelling and the parameters *a* and *b* for all stoichiometric phases were subsequently optimized according to experimental thermodynamic data. Since no thermodynamic information was available for the liquid, the parameters for the liquid were subsequently adapted to reproduce the experimental phase diagram data. Calculated Gibbs energies of formation at 823 K are shown together with values from literature in Fig. 3; it can be seen that the overall agreement is quite good. Similar as for the Gibbs energies of formation, it was possible to adjust Cd activities to the values determined experimentally by Reichmann and Ipser [10]. Again, the comparison presented in Fig. 4 shows very good agreement. Nevertheless, some deviations between calculated and experimentally determined Cd activities occurred in the two-phase fields adjacent to $Cd_{45}Pr_{11}$. Considering that the stoichiometric compositions of $Cd_{45}Pr_{11}$ and $Cd_{58}Pr_{13}$ are very close to each other, it was reasonable to model them with a similar temperature dependence of the energy contribution. Only in this way it was possible to model both compounds stable in the whole

Table 3
All parameters of the thermodynamic assessment of the Cd–Pr phase diagram are given for the temperature interval 298–1600 K in Joules.

DHCP (α-Pr):
${}^0G_{Cd} = GHSERCD + 5000$
${}^0L_{Cd,Pr} = -108290 + 60T$
BCC (β-Pr):
${}^0L_{Cd,Pr:Va} = -152571 + 68T$
${}^1L_{Cd,Pr:Va} = -54630 + 23T$
LIQ:
${}^0L_{Cd,Pr} = -132020 + 52T$
${}^1L_{Cd,Pr} = -27000 + 1T$
${}^2L_{Cd,Pr} = -2000 + 1T$
$Cd_{11}Pr$
${}^0G_{Cd:Pr} = 0.917 \cdot GHSERCD + 0.083 \cdot GHSERPR - 15900 + 3T$
Cd_6Pr
${}^0G_{Cd:Pr} = 0.857 \cdot GHSERCD + 0.143 \cdot GHSERPR - 26502.7 + 6.6T$
$Cd_{58}Pr_{13}$
${}^0G_{Cd:Pr} = 0.817 \cdot GHSERCD + 0.183 \cdot GHSERPR - 33366.4 + 9.5T$
$Cd_{45}Pr_{11}$
${}^0G_{Cd:Pr} = 0.804 \cdot GHSERCD + 0.196 \cdot GHSERPR - 34708.7 + 10.126T$
Cd_3Pr
${}^0G_{Cd:Pr} = 0.75 \cdot GHSERCD + 0.25 \cdot GHSERPR - 39827.2 + 12.3T$
Cd_2Pr
${}^0G_{Cd:Pr} = 0.667 \cdot GHSERCD + 0.333 \cdot GHSERPR - 45989.7 + 14.2T$
CdPr
${}^0G_{Cd:Pr} = 0.5 \cdot GHSERCD + 0.5 \cdot GHSERPR - 47613.2 + 15.7T$
${}^0G_{Pr:Pr} = GHSERPR + 6180.5 + 3T$

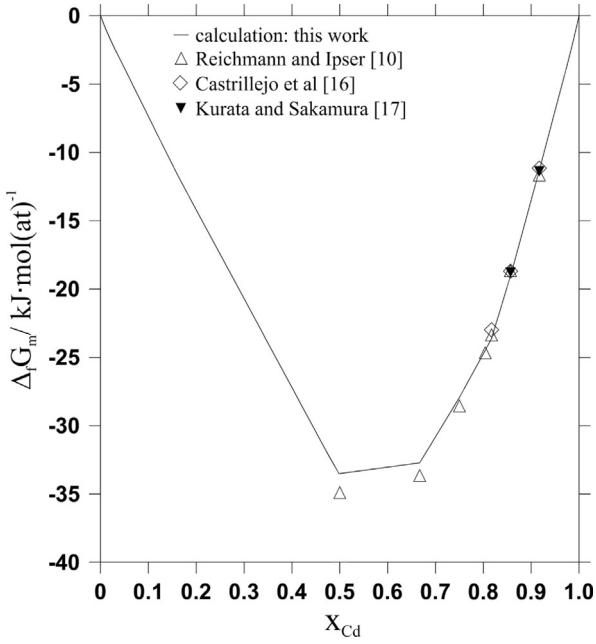

Fig. 3. Comparison of calculated Gibbs energies of formation at 823 K with values from literature; reference states: Cd(l) and α-Pr(s).

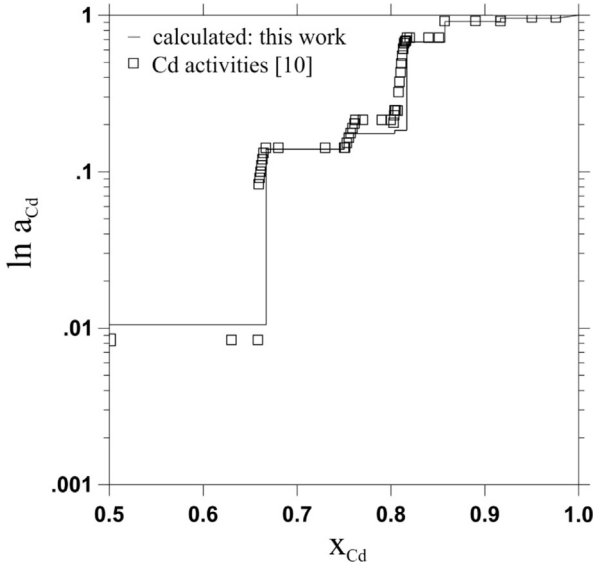

Fig. 4. Comparison of calculated Cd activities with values from literature; 823 K, and reference state: Cd(l).

temperature range. The values shown in Fig. 4 lead to the best consistency of all input data.

As described above, the modelled Gibbs energies of formation for Cd_6Pr, $Cd_{58}Pr_{13}$, Cd_3Pr and Cd_2Pr are based on the enthalpy values from the present calorimetric measurements, compare Table 2. The respective calculated enthalpies of formation were compared with those determined experimentally (Fig. 1). Considering the accuracy of ± 2 kJ/mol(at) of the calorimetric measurements, the respective calculated enthalpies of formation are within the error limit.

As can be observed in Table 3, only the parameters *a* and *b* were modelled for the individual Gibbs energies of the intermetallic compounds, following the Neumann–Kopp rule. C_p data of $Cd_{11}Pr$ were measured by DSC by Kumar et al. [24] between 300 and 550 K. The comparison with the calculated values, shown in Fig. 5, indicates that the deviation of the heat capacity of $Cd_{11}Pr$ from

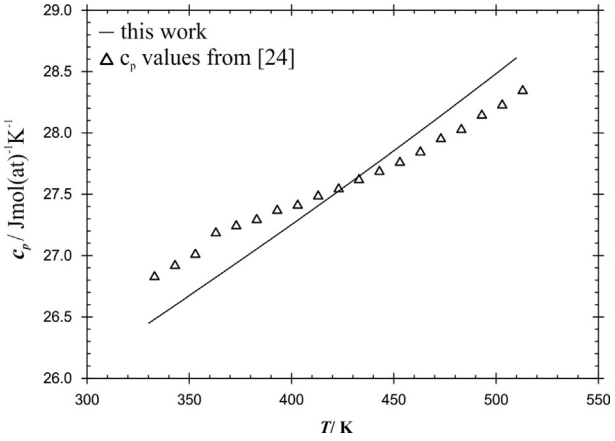

Fig. 5. Heat capacity of $Cd_{11}Pr$ between 300 and 550 K; line: values according Neumann–Kopp from the present calculation, triangles: data determined with DSC [24].

Neumann–Kopp's rule is minimal (within the experimental error) and does not require the introduction of higher order terms to the Gibbs energy description.

The intermetallic compound CdPr was modelled with an ideal two-sublattice model. By modelling of the hypothetical end member $^0G_{Pr:Pr}$, using a temperature dependent contribution, the homogeneity range of CdPr was optimized according to the experimental data.

The solid solutions of Cd in the low- (*DHCP*, α-Pr) and high-temperature (*BCC*, β-Pr) modifications of Pr were modelled according to the Redlich–Kister formalism using one (^0L) and two (^0L, ^1L) interaction parameters, respectively. In order to describe the experimentally determined liquidus along the whole composition range with the present model, three interaction parameters ^0L, ^1L and ^2L were required for the liquid phase.

It should be pointed out that the present thermodynamic optimization is exclusively valid for the temperature range between 298 and 3200 K and does not include temperatures above and below.

6. Summary

Standard enthalpies of formation of the four intermetallic compounds Cd_6Pr, $Cd_{58}Pr_{13}$, Cd_3Pr and Cd_2Pr were measured by calorimetry. Solution calorimetry was employed for all four compounds and the enthalpy of formation of stoichiometric $Cd_{58}Pr_{13}$ was also measured by direct reaction calorimetry. The experimental values for $Cd_{58}Pr_{13}$ from the two different methods were in good agreement with each other, and an average value of -35 ± 2 kJ/mol(at) is suggested. All present calorimetric data together with thermodynamic data from literature served as input data for a thermodynamic assessment of the Cd–Pr phase diagram. The complete composition range including all invariant reactions could be calculated, and the agreement with phase diagram data presented by Refs. [11,13] is very good. A comparison of calculated and experimentally determined phase diagram is given in Fig. 2 and Table 1. A temperature dependent contribution to the individual Gibbs energy was introduced for all phases to guarantee a consistent description of all input data.

Acknowledgements

The authors want to thank the Austrian Science Fund (FWF) for financial support of this study under Project no. P 23270-N19, and

the Scientific-Technical Cooperation between Austria and India (Project no. IN 05/2011). They are also grateful to Dr. R. Ganesan, from the Indira Gandhi Centre for Atomic Research (Kalpakkam, India), for providing experimental C_p values for $Cd_{11}Pr$ prior to publication.

Appendix A. Supporting information

Supplementary data associated with this article can be found in the online version at http://dx.doi.org/10.1016/j.calphad.2014.06.005.

References

[1] D. Olander, Nuclear fuels – present and future, J. Nucl. Mater. 389 (2009) 1–22.
[2] I. Johnson, The thermodynamics of pyrochemical processes for liquid metal reactor fuel cycles, J. Nucl. Mater. 154 (1988) 169–180.
[3] J.P. Ackerman, Chemical basis for pyrochemical reprocessing of nuclear-fuel, Ind. Eng. Chem. Res. 30 (1991) 141–145.
[4] J.J. Laidler, J.E. Battles, W.E. Miller, J.P. Ackerman, E.L. Carls, Development of pyroprocessing technology, Progr. Nucl. Energy 31 (1/2) (1997) 131–140.
[5] H. Yamana, N. Wakayama, N. Souda, H. Moriyama, Systematics of the thermodynamic properties of trivalent f-elements in a pyrometallurgical bi-phase extraction system, J. Nucl. Mater. 278 (2000) 37–47.
[6] H. Moriyama, S. Seshimo, K. Moritani, Y. Ito, T. Mitsugashira, Reductive extraction behavior of actinide and lanthanide elements in molten-salt and liquid-metal binary phase systems, J. Alloys Compd. 213 (1994) 354–359.
[7] H. Moriyama, H. Yamana, S. Nishikawa, S. Shibata, N. Wakayama, Y. Miyashita, K. Moritani, T. Mitsugashira, Thermodynamics of reductive extraction of actinides and lanthanides from molten chloride salt into liquid metal, J. Alloys Compd. 271 (1998) 587–591.
[8] M. Kurata, Y. Sakamura, T. Hijikata, K. Kinoshita, Distribution behavior of uranium, neptunium, rare-earth elements (Y,La,Ce,Nd,Sm,Eu,Gd) and alkaline-earth metals (Sr,Ba) between molten LiCl–KCl eutectic salt and liquid cadmium or bismuth, J. Nucl. Mater. 227 (1995) 110–121.
[9] B. Skołyszewska-Kühberger, T.L. Reichmann, R. Ganesan, H. Ipser, Thermodynamic study of the cerium–cadmium system, CALPHAD 44 (2014) 14–20.
[10] T.L. Reichmann, H. Ipser, Thermochemical Investigations in the system cadmium–praseodymium relevant for pyrometallurgical fuel reprocessing, Metall. Mater. Trans. A 45 (no. 3) (2014) 1171–1180.
[11] T.L. Reichmann, H.S. Effenberger, H. Ipser, Experimental investigation of the Cd–Pr phase diagram, Plos One 9 (4) (2014) 1–14.
[12] K.A. Gschneidner Jr, F.W. Calderwood, The Cd–Pr system, Bull. Alloy Phase Diagr. 9 (1988) 130–132.
[13] I. Johnson, K.E. Anderson, R.A. Blomquist, Partial constitutional diagrams for Cd–La Cd–Ce Cd–Pr Cd–Nd and Cd–Sm systems, Trans. ASM, 59, 1966352–355.
[14] E.Veleckis, E. Van Deventer, ANL-6925, Semi-Annual Report, Argonne National Lab, 1964.
[15] I. Johnson, R.M. Yonco, Thermodynamics of cadmium- and zinc-rich alloys in the Cd–La, Cd–Ce, Cd–Pr, Zn–La, Zn–Ce and Zn–Pr systems, Metall. Trans. 1 (1970) 905–910.
[16] Y. Castrillejo, M.R. Bermejo, P.D. Arocas, A.M. Martínez, E. Barrado, The electrochemical behaviour of the Pr(III)/Pr redox system at Bi and Cd liquid electrodes in molten eutectic LiCl–KCl, J. Electroanal. Chem. 579 (2005) 343–358.
[17] M. Kurata, Y. Sakamura, Thermodynamic assessment of systems of actinide or rare earth with Cd, J. Phase Equilib. 22 (2001) 232–240.
[18] G. Cacciamani, G. Borzone, R. Ferro, On a simple high-temperature direct reaction calorimeter, J. Alloys Compd. 220 (1995) 106–110.
[19] G. Borzone, R. Raggio, R. Ferro, Remarks on the role of thermochemical data in intermetallic crystallochemistry, J. Alloys Compd. 367 (2004) 89–102.
[20] G. Ghosh, S. Delsante, M. Borzone, Phase stability and cohesive properties of Ti–Zn intermetallics: first-principles calculations and experimental results, Acta Mater. 54 (2006) 4977–4997.
[21] H.L. Lukas, S.G. Fries, B. Sundman, Computational Thermodynamics – The CALPHAD Method, Cambridge University Press, Cambridge, 2007.
[22] O. Redlich, A.T. Kister, Algebraic representation of thermodynamic properties and the classification of solutions, Ind. Eng. Chem. 2 (1948) 345.
[23] S. Delsante, G. Borzone, Thermochemical investigation of Sm–Mg alloys, CALPHAD 44 (2013) 10–13.
[24] S. Shyam Kumar, R. Ganesan, R. Sridharan, Indira Gandhi Centre for Atomic Research, Kalpakkam, India, Private communication, 2013.
[25] J.-O. Andersson, T. Helander, L. Höglund, P. Shi, B. Sundman, Thermo-Calc & DICTRA, computational tools for materials science, CALPHAD 26 (2002) 273–312.
[26] A. Dinsdale, SGTE data for pure elements, CALPHAD 15 (1991) 317–425.

Publication 4

Thomas L. Reichmann, Rajesh Ganesan and Herbert Ipser

Thermochemical investigations in the system Cd-Gd

J. Alloys Comp. (2014), 610: 676-683

Contributions to this paper:

T.L. Reichmann:	performance of experiments, analysis and evaluation, writing of the paper
R. Ganesan:	design of experimental method, first exploratory experiments, helpful comments
H. Ipser:	general advice and helpful comments, proofreading of the manuscript

Contribution of T. L. Reichmann to this paper: 70 %

Journal of Alloys and Compounds 610 (2014) 676–683

Contents lists available at ScienceDirect

Journal of Alloys and Compounds

journal homepage: www.elsevier.com/locate/jalcom

Thermochemical investigations in the system Cd–Gd

Thomas L. Reichmann [a,*], Rajesh Ganesan [b], Herbert Ipser [a]

[a] Department of Inorganic Chemistry (Materials Chemistry), University of Vienna, 1090 Vienna, Austria
[b] Indira Gandhi Centre for Atomic Research, Kalpakkam, Tamil Nadu, India

ARTICLE INFO

Article history:
Received 2 April 2014
Received in revised form 8 May 2014
Accepted 9 May 2014
Available online 17 May 2014

Keywords:
Cd–Gd alloys
Isopiestic measurements
Vapour pressure method
Thermodynamic properties

ABSTRACT

Vapour pressure measurements were performed in terms of a non-isothermal isopiestic method to determine vapour pressures of Cd in the system Cd–Gd between 693 and 1045 K. From these results thermodynamic activities of Cd were derived as a function of temperature for the composition range 52–86 at.% Cd. By employing an adapted Gibbs–Helmholtz equation, partial molar enthalpies of mixing of Cd were obtained for the corresponding composition range, which were used to convert the activity values of Cd to a common average sample temperature of 773 K. The relatively large variation of the activity across the homogeneity ranges of the phases Cd_2Gd and $Cd_{45}Gd_{11}$ indicates that they probably belong to the most stable intermetallic compounds in this system.

An activity value of Gd for the two phase field Cd_6Gd+L was available from literature and served as an integration constant for a Gibbs–Duhem integration. Integral Gibbs energies are presented between 51 and 100 at.% Cd at 773 K, referred to Cd(l) and α-Gd(s) as standard states. Gibbs energies of formation for the exact stoichiometric compositions of the phases $Cd_{58}Gd_{13}$, $Cd_{45}Gd_{11}$, Cd_3Gd and Cd_2Gd were obtained at 773 K as about −19.9, −21.1, −24.8, and −30.0 kJ g atom^{-1}, respectively.

1. Introduction

In the last decades, the question of how to satisfy the ever increasing demand of energy has become most pressing for countries with high economic growth. The utilization of nuclear energy is sometimes inevitable for nations belonging to the group of developing and emerging countries. For an efficient use of nuclear energy, these countries have to establish strategies comprising an optimized reprocessing routine of spent nuclear fuels as well as an adequate waste management on the back-end of their nuclear fuel cycle. Indeed, low-level and intermediate-level radioactive waste is currently stored in interim storage facilities or deposited in geological repositories. Solutions for high-level waste are currently still in a planning stage and thus this type of waste is actually stored on-site.

Focusing onto reprocessing of nuclear waste, electro-transport and reductive extraction is applied to separate actinides and lanthanides from high-level radioactive waste (cf. Refs. [1–5]). Moriyama et al. [6] determined that the separation factors, which are an indicator for extractability, are quite different between actinides and lanthanides and are predominantly dependent on the employed liquid metal which is preferentially Cd [7]. Therefore, a detailed knowledge of the respective Cd-RE phase diagrams as well as of the thermodynamic stabilities of the corresponding intermetallic compounds is of great importance. This was the reason for initiating a series of thermodynamic and phase diagram studies of different Cd-RE systems (cf. Refs. [8–10]).

Concerning the Cd–Gd phase diagram, a rather complete description was given by Bruzzone et al. [11], who applied conventional methods, i.e. differential thermal analysis and chemical-, metallographic- and X-ray analyses. Six intermetallic compounds in total were determined, i.e. CdGd, Cd_2Gd, Cd_3Gd, $Cd_{45}Gd_{11}$, $Cd_{58}Gd_{13}$ and Cd_6Gd, where for Cd_2Gd a polymorphic transformation into a high temperature modification was indicated at 995 °C. All intermetallic compounds were shown to be line compounds, i.e. no significant solid solubility of either Cd or Gd is indicated.

Besides the work of Bruzzone et al. [11], only limited information concerning phase equilibria was available from literature. Johnson [12] reported liquidus data in the temperature range 324–500 °C, determined by chemical analysis of filtered samples of corresponding equilibrium phases. Tang and Gschneidner [13] prepared single-phase samples located within the homogeneity range of the Cd stabilized high temperature modification of Gd (β-Gd). Using differential thermal analyses (DTA) these authors could determine that the eutectoid decomposition of β-Gd takes place at 738 °C whereas Bruzzone et al [11] reported a value given as 725 °C.

* Corresponding author.
E-mail address: thomas.reichmann@univie.ac.at (T.L. Reichmann).

http://dx.doi.org/10.1016/j.jallcom.2014.05.062
0925-8388/

Although a rather complete description of the phase diagram was available, less information was found in literature regarding thermodynamic data. In an early work Roshchina and Bayanov [14] employed an electrochemical technique to determine activities of Gd in liquid Cd between 390 and 530 °C. By means of a Gibbs–Duhem integration, the authors were able to calculate the standard Gibbs energy of formation of Cd_6Gd, given as -20.8 ± 0.6 kJ mol(at)$^{-1}$, referred to the elements in their standard states.

In another early study Kurata et al. [15] presented an activity coefficient of Gd in liquid Cd at 500 K, given as −6.20. It was stated that this value was derived from an evaluation of electrochemical studies of Sakamura et al. [16]. These latter authors listed activity coefficients of rare earth elements in liquid Cd at 450 °C. Their corresponding activity coefficient of Gd in liquid Cd at 450 °C was −6.60.

Based on the results of Refs. [11,12,16], Kurata and Sakamura [17] made a CALPHAD-type optimization of the complete Cd–Gd system. All intermetallic compounds were modelled as stoichiometric line compounds, and temperature dependent Gibbs energies were listed which could be used for comparison in the present study.

2. Experimental

A non-isothermal isopiestic method was applied to determine Cd vapour pressures in Cd–Gd alloys. This method was previously described by Ipser et al. [18]. The corresponding experimental arrangement is shown schematically in Fig. 1. The entire setup is made of fused silica glass and consists of four parts. A silica glass crucible, where the volatile metal is held (the reservoir), is placed at the bottom of the outer tube. On top of this crucible a glass spacer is located, connected to a sample holder tube, in which tantalum crucibles are stacked one on top of the other. The defined distance from the bottom of the reservoir to the uppermost crucible is around 350 mm. Another inner tube with its upper end widened is used as a thermocouple well. This widened part is sealed with the outer tube under dynamic vacuum.

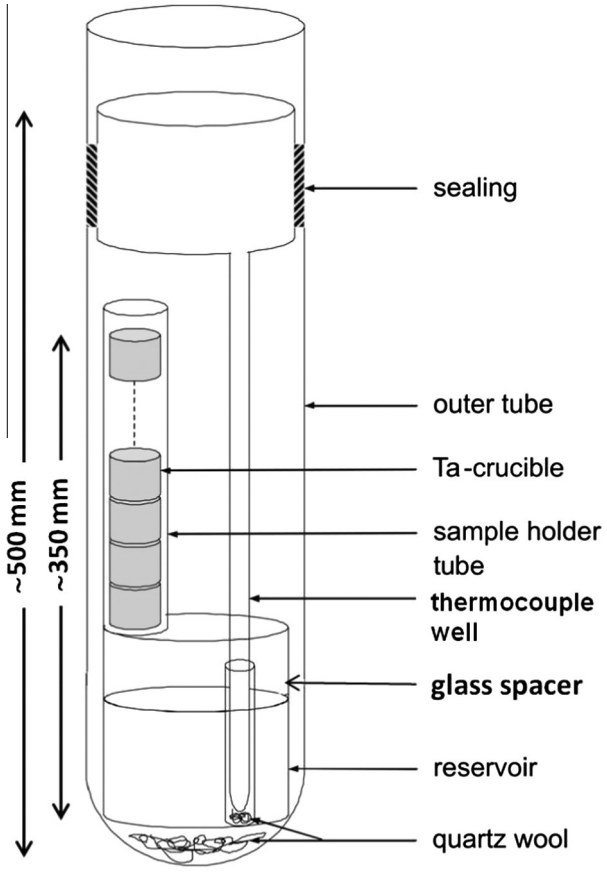

Fig. 1. Isopiestic quartz glass apparatus used in the present study.

Before use, the entire apparatus was cleaned with an acid mixture ($HF/HNO_3/H_2O$), rinsed with distilled water and dried. Afterwards the completely assembled setup, including the empty Ta crucibles (approximately 20), was degassed under dynamic vacuum (10^{-3} mbar) at 900 °C for 5 h. Depending on the experimental temperatures, the reservoir was filled with 25–35 g Cd (99.9999% Alfa AESAR, Karlsruhe, Germany). All further handling was carried out in a glove box, filled with Ar (oxygen level: <1 ppm, water level: <1 ppm), to protect the Gd samples from oxidation.

At the beginning, several experiments were carried out using tiny pieces of pure Gd (99.9 %, Smart Elements, Vienna, Austria) as sample material, but it became obvious that during equilibration of Gd with Cd vapour the diffusion is rather low, i.e. no intermetallic compounds were formed within the samples. Although samples were equilibrated at different temperatures, it was not possible to reach equilibrium states within any reasonable time. In a second series of experiments Gd powder (99.9% Alfa AESAR, Karlsruhe, Germany) was employed as sample material. Although first results appeared to be encouraging it was observed that powder X-ray diffraction (XRD) patterns, obtained from the pure Gd powder, showed predominantly the presence of Gd_2O_3 together with traces of $Gd(OH)_3$ whereas the expected reflections from Gd itself were not obtained. It must be assumed that the Gd particles in the powder are coated with a rather dense oxide/hydroxide layer. Obviously, this layer and relevant absorption effects due to the high atomic number of Gd are the reason for the almost undetectable intensity of Gd reflections.

Therefore it was finally decided to use a master alloy as sample material for the vapour pressure measurements, which was produced from Cd and Gd bulk material (99.9999% Alfa AESAR, Karlsruhe, Germany; 99.9%, Smart Elements, Vienna, Austria). Several attempts were carried out to synthesize single-phase alloys from different Cd–Gd intermetallic compounds. The best results were achieved for the compound $Cd_{45}Gd_{11}$. Stoichiometric amounts of Cd and Gd were weighed into a Mo crucible to a total amount of 12 g which was sufficient for two isopiestic runs. The crucible was covered with a Mo lid and enclosed into a silica glass tube under dynamic vacuum. The arrangement was slowly heated to 750 °C, a temperature below the boiling point of Cd, and held for two days. Afterwards, the alloy was cooled within four days to 525 °C, held for three more days and then cooled to ambient temperature. The rather low cooling rate was selected to guarantee a continuous reduction of the Cd vapour pressure within the crucible and to prevent condensation of Cd on the crucible wall. The master compound was powdered and characterized by XRD to be phase pure. About 200–350 mg of the $Cd_{45}Gd_{11}$ master alloy was weighed into each Ta crucible (10 mm o.d., 12 mm height) with an accuracy of ±0.1 mg.

After loading the arrangement (Fig. 1), it was securely closed with a glass stopper and shuttled out of the glove box. It was connected to a vacuum pump, evacuated and sealed under a dynamic vacuum of better than 10^{-4} mbar.

In the following, the isopiestic experiments were heated in different temperature gradients using two-zone furnaces. A total number of seven runs were performed at different reservoir (T_R) and sample temperatures (T_S). The respective temperature gradients were recorded by raising a Pt/Pt10%Rh thermocouple inside the thermocouple well. Each experiment lasted for about four to six weeks, depending on the reservoir temperature. After equilibration, the isopiestic apparatus was quenched in cold water and cut open by a diamond saw. The Cd–Gd alloys which had been formed within the Ta crucibles during equilibration with the Cd vapour were weighed back and their compositions calculated from the difference in weight, which was attributed to the uptake of Cd.

Representative samples were characterized by powder XRD with Cu Kα radiation using a Bruker D8 Advance Diffractometer with Bragg-Brentano geometry. To protect the powdered alloys from oxidation, a special XRD sample holder with an X-ray transparent lid was used. The corresponding XRD patterns were analyzed and refined by means of TOPAS 3 software (provided by Bruker), applying the fundamental parameter approach for peak profile modelling.

In an attempt to determine accurate sample compositions, selected alloys were dissolved in nitric acid and analysed spectroscopically. For the determination of the Cd content a PerkinElmer AAS with flame atomizer (AAnalyst 200) was used with an accuracy of about ±0.01 mg/L. The Gd content was measured with an ICP-MS (Agilent Technologies 7500ce) and an accuracy of ±0.01 μg/L. Unfortunately, the derived compositions showed a considerable scatter with a very slight tendency to be somewhat richer in Cd. Based on this scatter, it had to be concluded that the overall error for the results from AAS and ICP-MS was in the range of ±1 at.% Cd. This rather high error is probably due to the number of dilution steps of the aqueous solutions of the alloys which were necessary to achieve concentrations within the dynamic ranges of AAS and ICP-MS measurements. Considering this significant error, it was decided to use the alloy compositions as derived from weighing. Nevertheless, it is possible that the actual compositions during equilibration of the alloys are indeed slightly richer in Cd and that, due to the finite quenching rate, some of the Cd re-evaporates. This behaviour is outlined in detail in Ref. [8]. Considering all this, the resulting error in compositions was estimated not to exceed ±0.5 at.%. This was kept in mind when empirically fitting our isopiestic data in terms of the equilibrium curves which are shown in Fig. 2.

3. Results and discussion

3.1. Isopiestic experiment

On the basis of seven isopiestic runs which were carried out at different temperature conditions, thermodynamic activities were derived as a function of temperature and composition in the range between 51 and 86 at.% Cd. The reservoir temperatures which were set between 678 and 888 K correspond to Cd vapour pressures between 2 and 137 mbar, respectively. All samples were placed within a temperature interval of 693–1045 K. The vapour pressure of pure Cd at different temperatures was calculated according to the equation of Binnewies and Milke [19]:

$$\log\left(\frac{p^0_{Cd}}{bar}\right) = 8.7 - 5690 \cdot \frac{K}{T} - 1.07 \cdot \log\frac{T}{K} \quad (1)$$

Since the melting point of Cd is rather low and it has indeed a much higher vapour pressure compared to Gd at the respective experimental temperatures, the total pressure in the system is determined only by the temperature of the Cd reservoir (T_R). Equilibrium within the system is reached when the Cd vapour pressure over each sample, at its corresponding sample temperature T_S, is equal to the vapour pressure of pure Cd at the reservoir temperature T_R:

$$p_{Cd}(T_S) = p^0_{Cd}(T_R) \quad (2)$$

Thus the thermodynamic activity of Cd for each sample can be obtained combining Eqs. (1) and (2), based on the conventional definition for the activity:

$$a_{Cd}(T_S) = \frac{p_{Cd}(T_S)}{p^0_{Cd}(T_S)} = \frac{p^0_{Cd}(T_R)}{p^0_{Cd}(T_S)} \quad (3)$$

All results, including sample temperatures and compositions, sample identifications, Cd activities and partial enthalpy values, are listed in Table 1. The compositions were calculated from the mass change during the experiment as described above. All samples were ascribed to one- or two-phase fields in the phase diagram which was confirmed by powder XRD.

The relative uncertainty in the compositions due to experimental errors should not exceed 0.5 at.% as outlined in Section 2 and the measured temperatures are assumed to be accurate within ±2 K. (A more detailed discussion on possible error sources in this type of isopiestic experiments can be found in Ref. [18].)

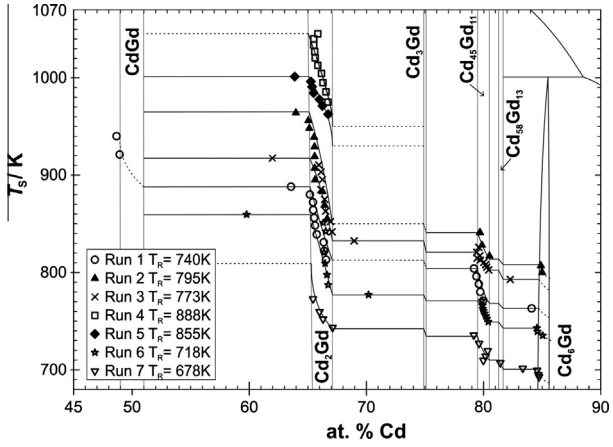

Fig. 2. Sample temperature against sample composition superimposed on the partial Cd–Gd phase diagram [11]. Assumed trends of the equilibrium curves are drawn with dotted lines.

From the derived sample compositions homogeneity ranges were estimated for all phases at 773 K (see Table 2). Except for $Cd_{58}Gd_{13}$ and Cd_3Gd, all other compounds show significant homogeneity ranges. As indicated above, phase equilibria of all samples were identified by powder XRD and agree excellently with the defined homogeneity ranges.

By plotting sample compositions against sample temperatures T_S for one particular run, a so-called equilibrium curve can be drawn connecting the individual data points in terms of an isobar. Fig. 2 shows these equilibrium curves for all runs, superimposed on the Cd–Gd phase diagram version from Ref. [11] but corrected with the estimated homogeneity ranges from the present study. As can be seen, most of the samples are concentrated within the homogeneity ranges of the two phases Cd_2Gd and $Cd_{45}Gd_{11}$, suggesting that these phases are among the most stable ones in the Cd–Gd system. Besides, no samples were obtained in the phase Cd_3Gd suggesting that Cd_3Gd is only slightly more stable than a two-phase mixture of its neighbouring compounds. This phenomenon was actually observed already earlier in the systems Cd–Pr and Cd–Ce where similarly no single-phase samples of the corresponding phases Cd_3Pr and Cd_3Ce were formed [8,9]. Nevertheless, it should be mentioned that Cd_3Gd crystallizes in a different crystal structure compared to Cd_3Pr and Cd_3Ce [20], a fact that makes the comparability regarding stability of these phases more surprising.

As can be seen in Fig. 2, some of the samples formed in the isopiestic runs were obtained in various two-phase fields after equilibration. This is probably caused by slight variations of the sample temperatures. Nevertheless, these samples allow the calculation of Cd activities for the respective two-phase fields at the corresponding sample temperatures T_S (cf. Section 3.2).

3.2. Partial enthalpy of mixing of Cd in two-phase fields

From the Cd vapour pressures of samples located within two-phase fields, Cd activities were calculated at the respective sample temperatures T_S (see Table 1). Natural logarithms of these activity values were plotted against reciprocal sample temperatures for almost all two-phase fields, i.e.: CdGd + Cd_2Gd, Cd_2Gd + Cd_3Gd, Cd_3Gd + $Cd_{45}Gd_{11}$, $Cd_{45}Gd_{11}$ + $Cd_{58}Gd_{13}$ and $Cd_{58}Gd_{13}$ + Cd_6Gd (see Fig. 3). According to an adapted Gibbs–Helmholtz equation (4), partial enthalpy values of mixing of Cd were directly calculated from the slopes:

$$\frac{\partial \ln a_{Cd}}{\partial(1/T)} = \frac{\Delta \bar{H}_{Cd}}{R} \quad (4)$$

where the temperature is in K, R is the gas constant in J (mol K)$^{-1}$, and the partial enthalpy of Cd is in J mol(Cd)$^{-1}$. For this approach straight phase boundaries, i.e. no variation of solid solubilities with temperature, of the different compounds were assumed. Although it is obvious that the solubilities will be temperature dependent in the examined temperature ranges, this is still a useful approximation to obtain information on the corresponding partial enthalpy values in a certain temperature range within two-phase fields (cf. Table 1). By comparing the slopes in Fig. 3, an exothermic behaviour is observed in the corresponding composition range 50–86 at.% Cd. Obviously, the partial molar enthalpy of mixing of Cd becomes more negative with decreasing Cd content of the alloys. The relatively high difference of the Cd activities between two-phase fields adjacent to Cd_2Gd and $Cd_{45}Gd_{11}$ indicate once more that these phases have to be much more stable than a mixture of their neighbouring phases.

3.3. Partial enthalpy of mixing of Cd in single-phase fields

Partial enthalpies of mixing of Cd were determined in the homogeneity ranges of Cd_2Gd and $Cd_{45}Gd_{11}$ in the same manner

Table 1
Experimental results of isopiestic experiments, standard state: Cd(l).

Sample no.	Cd (at.%)	T_S (K)	ln a_{Cd} (T_S)	Phases	$\Delta\overline{H}_{Cd}$/kJ g-atom^{-1}	ln a_{Cd} (773 K)
Run 1: T_R = 740 K, 40 days						
1	84.11	763	−0.50	$Cd_{58}Gd_{13}$ + Cd_6Gd	−15.5	−0.47
2	79.96	771	−0.67	$Cd_{45}Gd_{11}$	−15.5	−0.66
3	79.73	780	−0.85	$Cd_{45}Gd_{11}$	−21.1	−0.88
4	79.60	788	−1.01	$Cd_{45}Gd_{11}$	−25.7	−1.09
5	79.40	796	−1.17	Cd_3Gd + $Cd_{45}Gd_{11}$	−26.2	−1.29
6	79.19	804	−1.32	Cd_3Gd + $Cd_{45}Gd_{11}$	−26.2	−1.48
7	66.56	813	−1.49	Cd_2Gd	−11.9	−1.58
8	66.40	822	−1.65	Cd_2Gd	−14.7	−1.79
9	66.36	831	−1.81	Cd_2Gd	−15.3	−1.98
10	65.76	839	−1.95	Cd_2Gd	−24.9	−2.26
11	65.62	848	−2.11	Cd_2Gd	−27.0	−2.48
12	65.54	856	−2.24	Cd_2Gd	−28.2	−2.67
13	65.46	864	−2.38	Cd_2Gd	−29.3	−2.85
14	65.44	872	−2.50	Cd_2Gd	−29.6	−3.02
15	65.18	880	−2.63	Cd_2Gd	−33.0	−3.09
16	63.57	888	−2.76	CdGd + Cd_2Gd	−30.4	−3.37
17	48.94	921	−3.25	CdGd	–	–
18	48.67	940	−3.51	CdGd	–	–
Run 2: T_R = 795 K, 28 days						
1	85.00	800	−0.10	Cd_6Gd	–	−0.34[a]
2	84.89	807	−0.23	Cd_6Gd	–	−0.38[a]
3	80.50	817	−0.41	$Cd_{45}Gd_{11}$	−14.7	−0.97
4	79.86	828	−0.61	$Cd_{45}Gd_{11}$	−17.6	−1.23
5	79.69	841	−0.84	$Cd_{45}Gd_{11}$	−22.5	−1.56
6	66.65	855	−1.08	Cd_2Gd	−10.3	−1.23
7	66.42	869	−1.31	Cd_2Gd	−14.3	−1.55
8	66.26	883	−1.53	Cd_2Gd	−17.1	−1.86
9	65.62	895	−1.71	Cd_2Gd	−27.0	−2.29
10	65.60	907	−1.89	Cd_2Gd	−27.3	−2.52
11	65.58	919	−2.07	Cd_2Gd	−27.6	−2.75
12	65.57	929	−2.21	Cd_2Gd	−27.7	−2.93
13	65.53	939	−2.35	Cd_2Gd	−28.3	−3.13
14	65.12	948	−2.47	Cd_2Gd	−33.8	−3.44
15	65.04	956	−2.58	Cd_2Gd	−34.8	−3.62
16	63.98	964	−2.68	CdGd + Cd_2Gd	−30.4	−3.62
Run 3: T_R = 773 K, 28 days						
1	82.28	793	−0.40	$Cd_{58}Gd_{13}$ + Cd_6Gd	−15.5	−0.46
2	80.44	803	−0.59	$Cd_{45}Gd_{11}$	−13.9	−0.67
3	80.27	805	−0.64	$Cd_{45}Gd_{11}$	−12.9	−0.72
4	80.18	808	−0.69	$Cd_{45}Gd_{11}$	−13.1	−0.78
5	80.03	811	−0.73	$Cd_{45}Gd_{11}$	−14.5	−0.84
6	79.72	813	−0.78	$Cd_{45}Gd_{11}$	−21.6	−0.94
7	79.45	815	−0.81	$Cd_{45}Gd_{11}$	−32.3	−1.07
8	79.69	817	−0.86	$Cd_{45}Gd_{11}$	−22.6	−1.05
9	79.41	821	−0.92	$Cd_{45}Gd_{11}$	−34.1	−1.23
10	79.59	826	−1.01	$Cd_{45}Gd_{11}$	−26.3	−1.27
11	68.96	833	−1.13	Cd_2Gd + Cd_3Gd	−26.4	−1.43
12	67.07	842	−1.29	Cd_2Gd	−2.5	−1.32
13	66.93	852	−1.47	Cd_2Gd	−5.1	−1.54
14	66.52	863	−1.65	Cd_2Gd	−12.6	−1.85
15	66.44	875	−1.84	Cd_2Gd	−14.0	−2.10
16	66.11	885	−2.00	Cd_2Gd	−19.5	−2.39
17	66.24	895	−2.16	Cd_2Gd	−17.3	−2.52
18	66.13	903	−2.28	Cd_2Gd	−19.2	−2.71
19	65.94	910	−2.38	Cd_2Gd	−22.2	−2.91
20	61.97	917	−2.48	CdGd + Cd_2Gd	−30.4	−3.23
Run 4: T_R = 888 K, 55 days						
1	66.72	975	−1.22	Cd_2Gd	−9.1	−1.51
2	66.55	986	−1.35	Cd_2Gd	−12.0	−1.76
3	66.30	995	−1.46	Cd_2Gd	−16.4	−2.04
4	66.16	1004	−1.58	Cd_2Gd	−18.7	−2.25
5	65.86	1013	−1.68	Cd_2Gd	−23.5	−2.54
6	65.63	1021	−1.77	Cd_2Gd	−26.9	−2.78
7	65.58	1027	−1.84	Cd_2Gd	−27.5	−2.90
8	65.49	1034	−1.92	Cd_2Gd	−28.8	−3.05
9	65.51	1040	−1.99	Cd_2Gd	−28.6	−3.13
10	65.85	1045	−2.05	Cd_2Gd	−23.6	−3.00
Run 5: T_R = 855 K, 55 days						
1	66.73	963	−1.59	Cd_2Gd	−8.9	−1.86
2	66.24	971	−1.70	Cd_2Gd	−17.3	−2.25
3	65.99	978	−1.78	Cd_2Gd	−21.3	−2.48

(*continued on next page*)

Table 1 (*continued*)

Sample no.	Cd (at.%)	T_S (K)	ln a_{Cd} (T_S)	Phases	$\Delta\bar{H}_{Cd}$/kJ g-atom^{-1}	ln a_{Cd} (773 K)
4	65.49	984	−1.86	Cd_2Gd	−28.9	−2.83
5	65.36	991	−1.94	Cd_2Gd	−30.7	−2.99
6	65.26	996	−2.01	Cd_2Gd	−32.0	−3.12
7	63.88	1001	−2.07	CdGd + Cd_2Gd	−30.4	−3.14
Run 6: T_R = 718 K, 58 days						
1	85.04	735	−0.40	Cd_6Gd	–	−0.32[a]
2	84.59	739	−0.50	$Cd_{58}Gd_{13}$ + Cd_6Gd	−15.5	−0.38
3	84.54	743	−0.57	$Cd_{58}Gd_{13}$ + Cd_6Gd	−15.5	−0.48
4	80.40	749	−0.72	$Cd_{45}Gd_{11}$	−13.5	−0.65
5	80.28	752	−0.79	$Cd_{45}Gd_{11}$	−12.9	−0.73
6	80.19	755	−0.84	$Cd_{45}Gd_{11}$	−13.0	−0.80
7	80.09	758	−0.90	$Cd_{45}Gd_{11}$	−13.7	−0.86
8	79.99	760	−0.96	$Cd_{45}Gd_{11}$	−15.0	−0.92
9	79.93	763	−1.01	$Cd_{45}Gd_{11}$	−16.0	−0.98
10	79.90	766	−1.07	$Cd_{45}Gd_{11}$	−16.6	−1.05
11	79.87	771	−1.18	$Cd_{45}Gd_{11}$	−17.3	−1.17
12	70.18	777	−1.30	Cd_2Gd + Cd_3Gd	−26.4	−1.32
13	66.73	787	−1.51	Cd_2Gd	−8.8	−1.50
14	66.63	798	−1.71	Cd_2Gd	−10.6	−1.71
15	66.48	809	−1.93	Cd_2Gd	−13.3	−2.02
16	66.38	821	−2.14	Cd_2Gd	−15.0	−2.28
17	66.53	842	−2.52	Cd_2Gd	−12.5	−2.68
18	66.32	851	−2.67	Cd_2Gd	−16.1	−2.90
19	59.77	859	−2.81	CdGd + Cd_2Gd	−30.4	−3.29
Run 7: T_R = 678 K, 58 days						
1	84.74	693	−0.39	Cd_6Gd	–	–[b]
2	84.67	695	−0.45	Cd_6Gd	–	–[b]
3	84.58	699	−0.56	$Cd_{58}Gd_{13}$ + Cd_6Gd	−15.5	−0.28
4	83.35	702	−0.61	$Cd_{58}Gd_{13}$ + Cd_6Gd	−15.5	−0.36
5	81.43	707	−0.76	$Cd_{58}Gd_{13}$	−15.8[a]	−0.53
6	79.98	710	−0.81	$Cd_{45}Gd_{11}$	−15.2	−0.60
7	80.18	714	−0.92	$Cd_{45}Gd_{11}$	−13.1	−0.75
8	80.36	720	−1.05	$Cd_{45}Gd_{11}$	−13.2	−0.90
9	79.62	727	−1.23	$Cd_{45}Gd_{11}$	−25.0	−0.99
10	79.17	736	−1.43	Cd_3Gd + $Cd_{45}Gd_{11}$	−26.2	−1.22
11	67.10	743	−1.60	Cd_2Gd	−1.9	−1.78
12	66.30	752	−1.79	Cd_2Gd	−16.4	−1.88
13	66.00	760	−1.96	Cd_2Gd	−21.3	−2.17
14	65.44	773	−2.23	Cd_2Gd	−29.5	−2.23

[a] Value was estimated by linear interpolation of the partial enthalpies/activity values of Cd in the adjacent two-phase fields.
[b] Samples are single-phase at T_S but two-phase (Cd_6Gd + $Cd_{58}Gd_{13}$) at 773 K.

Table 2
Homogeneity ranges of the intermetallic compounds at 773 K estimated from the equilibrium curves; the phase boundary of the liquid was taken from Johnson [12].

Phase	Phase boundaries (at.% Cd)	Reference
CdGd	49.0–51.0	
Cd_2Gd	65.3–67.1	
Cd_3Gd	74.9–75.1	
$Cd_{45}Gd_{11}$	79.5–80.5	
$Cd_{58}Gd_{13}$	81.3–81.7	
Cd_6Gd	84.8–85.7	
L	96.7–100	[12]

as described above. For instance, for the evaluation of Cd_2Gd, sample temperatures for selected compositions were obtained along the entire homogeneity range by interpolation from the equilibrium curves in Fig. 2. For these hypothetical samples, Cd activities were calculated according to Eqs. (1) and (3). Natural logarithms of these activities were plotted as a function of reciprocal temperature in Fig. 4. Applying the adapted Gibbs–Helmholtz equation (4), a linear regression was applied for data points of each selected composition in the entire homogeneity range of Cd_2Gd. Although these data show some scatter it should be kept in mind that the data points are spaced in very narrow composition steps, and that small errors in composition and/or temperature in the equilibrium

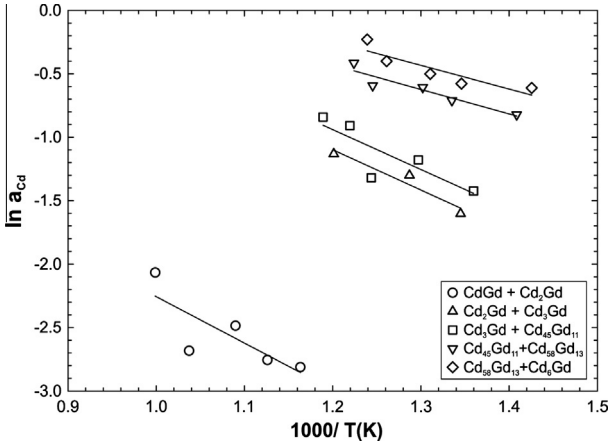

Fig. 3. Natural logarithm of the Cd activity against reciprocal sample temperature for different two-phase fields.

curves in Fig. 2 may lead to a noticeable shift in the ln a_{Cd} vs. $1/T$ data points.

Values of $\Delta\bar{H}_{Cd}$ were directly calculated from the slopes of the straight lines in Fig. 4 and plotted against composition in Fig. 5. As can be seen, the partial enthalpy values vary over an extended

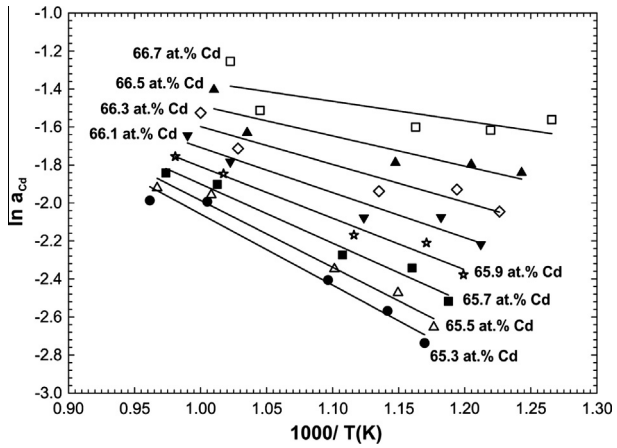

Fig. 4. Natural logarithm of the Cd activity against reciprocal sample temperature for selected compositions in the homogeneity range of Cd_2Gd.

range from −8 at the Cd-rich side to −32 kJ mol(Cd)$^{-1}$ at the Gd-rich border of the homogeneity range, indicating once more the stability of this phase.

An analogous evaluation as given for Cd_2Gd was carried out for the $Cd_{45}Gd_{11}$ phase. The corresponding values are included in Table 1. As discussed in detail in Ref. [18], the error in the partial enthalpies should be within ±5 kJ mol(at)$^{-1}$ which was confirmed by an error analysis of the present data.

Partial enthalpy values within the homogeneity range of $Cd_{58}Gd_{13}$ could not be derived in the described way because of a limited number of samples, but were estimated from the neighbouring two-phase fields assuming a linear behaviour with composition between the values of the two-phase fields. The same procedure was employed for the Cd_3Gd phase where no samples at all were available from the experiment (cf. Table 1).

3.4. Thermodynamic activity of Cd at 773 K

Thermodynamic activities of Cd for single- and two-phase fields were obtained at one particular temperature using an integrated form of the adapted Gibbs–Helmholtz equation:

$$\ln a_{Cd}(773K) - \ln a_{Cd}(T_S) = \frac{\Delta\bar{H}_{Cd}}{R} \cdot \left(\frac{1}{773} - \frac{1}{T_S}\right) \quad (5)$$

with the temperature in K and the partial enthalpy of Cd in J mol(Cd)$^{-1}$. Accordingly, the activity values of all samples were converted to 773 K which represents a mean temperature of all sample temperatures T_S. The required enthalpy values in the respective single- and two-phase fields were obtained according to Sections 3.2 and 3.3. As indicated in the previous chapter, the error in the partial enthalpies should be within ±5 kJ mol(at)$^{-1}$ resulting in an error of at most ±0.15 in the value of ln a_{Cd}. A detailed discussion concerning error sources and error limits in this isopiestic method was previously given by Ipser et al. [18].

As an example, ln a_{Cd} for Cd_2Gd is shown in Fig. 6 as a function of composition at 773 K. The corresponding phase boundaries at this temperature were taken from Table 2. The data points were fitted with a polynomial function, leading to the best compatibility with the activity values in the adjacent two-phase fields.

As mentioned previously, numerous samples were located in the homogeneity range of $Cd_{45}Gd_{11}$, allowing a similar evaluation as it was done for Cd_2Gd. The homogeneity range was estimated between 79.5 and 80.5 at.% Cd at 773 K and corresponding activity values of samples located within $Cd_{45}Gd_{11}$ were converted to 773 K. For the conversion of activity values to one particular temperature, enthalpy values of Cd as a function of composition were empirically fitted as described in 3.3. All enthalpy and activity values of Cd of single-phase samples of $Cd_{45}Gd_{11}$ are included in Table 1.

Thermodynamic activities of Cd at 773 K for the phases Cd_3Gd and $Cd_{58}Gd_{13}$, given in Table 1, had to be converted from their corresponding sample temperatures with enthalpy values estimated by a linear interpolation between the values in the neighbouring two-phase fields, as discussed above.

The Cd activity at 773 K in the two-phase field Cd_6Gd + L could not be obtained from the present measurements but was calculated from the results of Roshchina and Bayanov [14]. For this two-phase field a value of ln a_{Cd} = −0.04 was determined. The corresponding evaluation is described in detail in Section 3.5.

3.5. Integral Gibbs energy

As outlined above, Roshchina and Bayanov [14] determined thermodynamic activities of Gd in the liquid phase and the two-phase field Cd_6Gd + L between 663 and 801 K. By means of a Gibbs–Duhem integration, the authors calculated the standard Gibbs energy of formation at the stoichiometric composition of Cd_6Gd, given as −20.8 ± 0.6 kJ mol(at)$^{-1}$, referred to Cd(s) and α-Gd(s) as standard states. The standard Gibbs energy of formation of Cd_6Gd was re-calculated at 773 K to be about −16.1 kJ mol(at)$^{-1}$, referred to Cd(l) and α-Gd(s). From the emf data at 775.15 K [14] a value for the thermodynamic activity of Gd could be obtained for

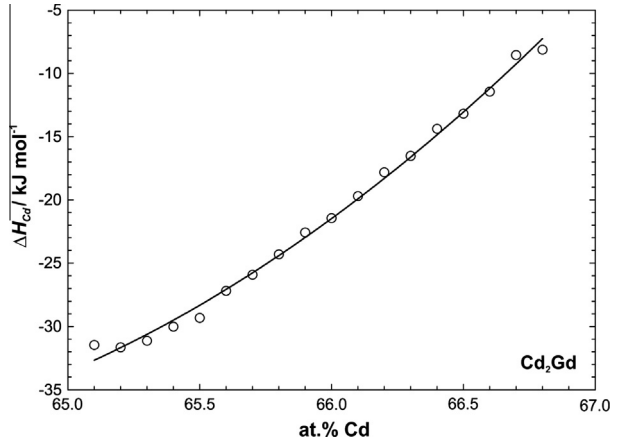

Fig. 5. Partial molar enthalpy of Cd in the homogeneity range of Cd_2Gd; standard state: Cd(l).

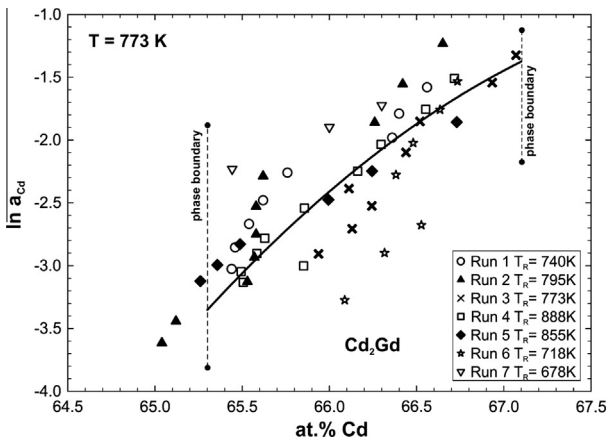

Fig. 6. Natural logarithm of the Cd activity for Cd_2Gd at 773 K; standard state: Cd(l). The symbols are the same as in Fig. 2.

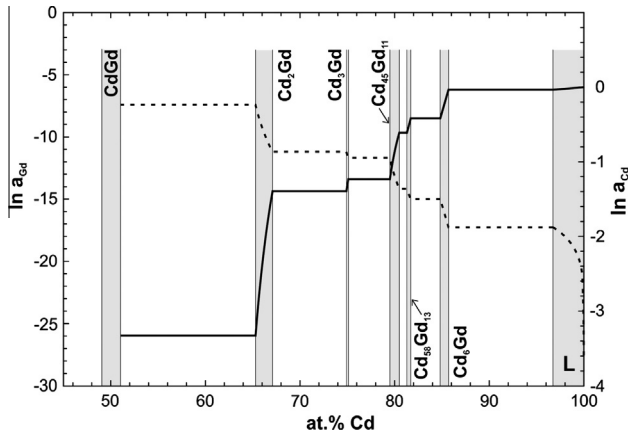

Fig. 7. Natural logarithm of Cd and Gd activities against composition at 773 K, referred to Cd(l) and α-Gd(s) as standard states.

the two-phase field Cd_6Gd + L, namely ln $a_{Gd} = -17.27$. The corresponding solubility of Gd in liquid Cd obtained from the kink of the emf curve is given as 3.3 at.%. Assuming that the phase boundary Cd_6Gd/Cd_6Gd + L corresponds to the stoichiometric composition of Cd_6Gd, i.e. there is no solid solubility of Cd within Cd_6Gd at 773 K, an activity value of ln $a_{Cd} = -0.04$ was obtained for the two-phase field Cd_6Gd + L.

The activity value ln $a_{Gd} = -17.27$ served as an integration constant for a Gibbs–Duhem integration in the present study. The corresponding activity values of Cd and Gd in the composition range 51–100 at.% Cd are plotted as natural logarithms in Fig. 7. Once more it is indicated that the intermetallic compounds Cd_2Gd and $Cd_{45}Gd_{11}$ have to be very stable, due to the marked variation of the activities across their homogeneity ranges.

From the activity data for Cd and Gd, integral Gibbs energies were calculated for the respective composition range at 773 K and plotted in Fig. 8, referred to Cd(l) and α-Gd(s) as standard states. Gibbs energies of formation at the exact stoichiometric compositions of the phases $Cd_{58}Gd_{13}$, $Cd_{45}Gd_{11}$, Cd_3Gd and Cd_2Gd were obtained to be about −19.9, −21.1, −24.8, and −30.0 kJ g atom^{-1} at 773 K, respectively. Assuming an error of ±0.15 in the value of ln a_{Cd} at 773 K (as discussed above) and relying on the error limit given by Roshchina and Bayanov [14], the error in the integral Gibbs energy can be estimated to be in the range of ±1 kJ mol(at)$^{-1}$ at about 85 at.% Cd, increasing to at most ±5 kJ mol(at)$^{-1}$ around 50 at.% Cd.

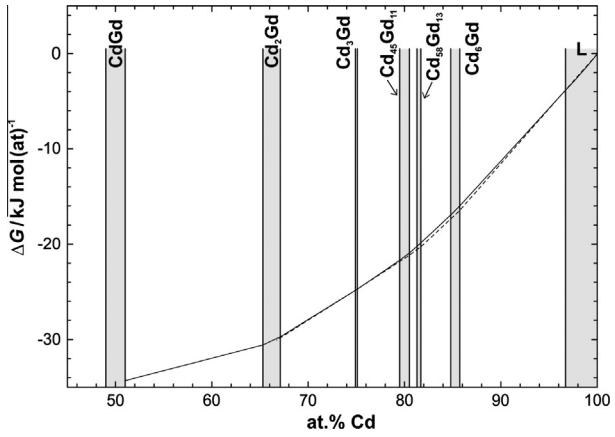

Fig. 8. Integral Gibbs energy of formation against composition at 773 K, referred to Cd(l) and α-Gd(s) as standard states; dashed line refers to Kurata and Sakamura [17].

The integral Gibbs energies of all intermetallic compounds were compared with those listed by Kurata and Sakamura [17] who made a CALPHAD-type optimization. The very good agreement in Fig. 8 proves that the assumptions that were used in the present Gibbs–Duhem integration are actually quite reasonable.

4. Summary

Seven isopiestic runs in total were carried out to measure vapour pressures of Cd in the system Cd–Gd between 693 and 1045 K. For this purpose, the intermetallic compound $Cd_{45}Gd_{11}$ was used as a master compound and equilibrated with Cd vapour at constant Cd vapour pressures between 2 and 137 mbar, respectively. Plotting sample temperatures against sample compositions, equilibrium curves were drawn (Fig. 2) and thermodynamic activity values of Cd were calculated for the composition range 51–86 at.% Cd. By employing an adapted Gibbs–Helmholtz equation partial molar enthalpies of mixing of Cd were obtained for the corresponding composition range, which were used to convert the activity values of Cd to a common average temperature of 773 K. With additional information from literature concerning a value for the activity of Gd in the two-phase field Cd_6Gd + L [14], a Gibbs–Duhem integration was performed. The corresponding activity values of Cd and Gd are reported for the composition range 50–100 at.% Cd, see Fig. 7. From these data integral Gibbs energies were calculated and presented as a function of composition in Fig. 8. Gibbs energies of formation at the exact stoichiometric compositions of the phases $Cd_{58}Gd_{13}$, $Cd_{45}Gd_{11}$, Cd_3Gd and Cd_2Gd were obtained to be about −19.9, −21.1, −24.8, and −30.0 kJ g atom^{-1} at 773 K, respectively.

Acknowledgements

The authors want to thank the Austrian Science Fund (FWF) for financial support of this study under Project No. P 23270-N19, and the Scientific-Technical Cooperation between Austria and India (Project No. IN 05/2011). Moreover, Dr. Franz Jirsa and Mag. Sarah Theiner of the University of Vienna are gratefully acknowledged for their assistance in carrying out AAS and ICP-MS measurements.

References

[1] D. Olander, Nuclear fuels – present and future, J. Nucl. Mater. 389 (2009) 1–22.
[2] I. Johnson, The Thermodynamics of pyrochemical processes for liquid metal reactor fuel cycles, J. Nucl. Mater. 154 (1988) 169–180.
[3] J.P. Ackerman, Chemical basis for pyrochemical reprocessing of nuclear–fuel, Ind. Eng. Chem. Res. 30 (1991) 141–145.
[4] J.J. Laidler, J.E. Battles, W.E. Miller, J.P. Ackerman, E.L. Carls, Development of pyroprocessing technology, Progr. Nucl. Energy 31 (1/2) (1997) 131–140.
[5] H. Yamana, N. Wakayama, N. Souda, H. Moriyama, Systematics of the thermodynamic properties of trivalent f-elements in a pyrometallurgical bi-phase extraction system, J. Nucl. Mater 278 (2000) 37–47.
[6] H. Moriyama, H. Yamana, S. Nishikawa, S. Shibata, N. Wakayama, Y. Miyashita, K. Moritani, T. Mitsugashira, Thermodynamics of reductive extraction of actinides and lanthanides from molten chloride salt into liquid metal, J. Alloys Comp. 271 (1998) 587–591.
[7] M. Kurata, Y. Sakamura, T. Hijikata, K. Kinoshita, Distribution behavior of uranium, neptunium, rare-earth elements (Y, La, Ce, Nd, Sm, Eu, Gd) and alkaline-earth metals (Sr, Ba) between molten LiCl–KCl eutectic salt and liquid cadmium or bismuth, J. Nucl. Mater. 227 (1995) 110–121.
[8] T.L. Reichmann, H. Ipser, Thermochemical investigations in the system cadmium–praseodymium relevant for pyrometallurgical fuel reprocessing metall, Mater. Trans. A 45 (3) (2014) 1171–1180.
[9] B. Skołyszewska-Kühberger, T.L. Reichmann, R. Ganesan, H. Ipser, Thermodynamic study of the cerium–cadmium system, CALPHAD 44 (2014) 14–20.
[10] T.L. Reichmann, H.S. Effenberger, H. Ipser, Experimental investigation of the Cd–Pr phase diagram, Plos One 9 (4) (2014) 1–14.
[11] G. Bruzzone, M.L. Fornasini, F. Merlo, The gadolinium–cadmium system, J. Less-Common. Met. 25 (1971) 295–301.
[12] I. Johnson, Rare Earth Research, Gordon and Breach, 1962, pp. 125–131.
[13] J. Tang, K.A. Gschneidner Jr., Physical metallurgy and magnetic behaviour of Cd-stabilized b.c.c. β-Gd alloys, J. Alloys Comp. 234 (1996) 26–33.

[14] V.R. Roshchina, A.P. Bayanov, Thermochemistry of gadolinium–cadmium alloy formation, J. Phys. Chem. 55 (12) (1981) 3017–3020.
[15] M. Kurata, Y. Sakamura, T. Matsui, Thermodynamic quantities of actinides and rare earth elements in liquid bismuth and cadmium, J. Alloys Comp. 234 (1996) 83–92.
[16] Y. Sakamura, T. Inoue, T.S. Storvick, L.F. Grantham, Characterizations of Rare Earths and Actinides in a Molten Salt/Liquid Cadmium System, in: 26th Symp. on Molten Salt Chem., Sapporo, 1995, p. 101.
[17] M. Kurata, Y. Sakamura, Thermodynamic assessment of systems of actinide or rare earth with Cd, J. Phase Equilib. 22 (3) (2001) 232–240.
[18] H. Ipser, R. Krachler, K.L. Komarek, in: H. Brodowsky, H.-J. Schaller (Eds.), Thermochemistry of Alloys, Springer, Kluwer Academic Publishers, Dordrecht, 1989, pp. 293–306.
[19] M. Binnewies, E. Milke, Thermochemical Data of Elements and Compounds, WILEY-VCH, Weinheim, 1999, p. 295.
[20] G. Bruzzone, M.L. Fornasini, F. Merlo, Rare earth intermediate phases with cadmium, J. Less-Common Met. 30 (1973) 361–375.

Publication 5

Thomas L. Reichmann and Herbert Ipser

Reinvestigation of the Cd-Gd phase diagram

J. Alloys Comp. (2014), accepted

Contributions to this paper:

T.L. Reichmann: sample preparation, SEM-, powder XRD-, and DTA-measurements, analysis and interpretation, writing of the paper

H. Ipser: general advice and helpful comments, proofreading of the manuscript

Contribution of T. L. Reichmann to this paper: 75 %

Reinvestigation of the Cd-Gd phase diagram

Thomas L. Reichmann* and Herbert Ipser

Department of Inorganic Chemistry (Materials Chemistry), University of Vienna, 1090 Wien Austria

Abstract

The complete Cd-Gd equilibrium phase diagram was investigated by a combination of powder-XRD, SEM and DTA. All previously reported phases, i.e. CdGd, Cd_2Gd, Cd_3Gd, $Cd_{45}Gd_{11}$, $Cd_{58}Gd_{13}$, and Cd_6Gd, could be confirmed. In addition, a new intermetallic compound with a stoichiometric composition corresponding to "Cd_8Gd" was found to exist. It was obtained that "Cd_8Gd" decomposes peritectically at 465 °C. Homogeneity ranges of all intermetallic compounds were determined at distinct temperatures. In addition, the maximum solubilities of Cd in the low- and high-temperature modifications of Gd were determined precisely as 4.6 and 22.6 at.%, respectively. All invariant reaction temperatures (with the exception of the formation of $Cd_{58}Gd_{13}$) as well as liquidus temperatures were determined, Most probably, $Cd_{58}Gd_{13}$ is formed in a peritectoid reaction from $Cd_{45}Gd_{11}$ and Cd_6Gd at a temperature below 700 °C.

Keywords: Intermetallics, phase transformation, heat treatment, microstructure, diffraction (X–ray), differential thermal analysis.

*Corresponding author.

E-mail address: thomas.reichmann@univie.ac.at (Thomas L. Reichmann)

1. Introduction

For an efficient use of nuclear energy, reprocessing of nuclear waste should be balanced with an adequate waste management. Actually, low-level and intermediate-level radioactive waste is mostly stored in interim storage facilities or deposited in geological repositories. The situation concerning disposal of high-level nuclear waste is more serious. In fact, deposition of this waste in e.g. geological repositories does not solve the problem but defers it to further generations. Hence, disposal of nuclear waste turned more and more into a question of sustainability. In fact, no geological repository for high-level waste is presently available and thus it is actually stored on-site.

To lower the amount of radioactive waste, separation techniques are currently employed to selectively reprocess spent nuclear fuels. Reprocessing is mostly performed by means of solvent extraction of actinides using tributyl phosphate (TBP), known as hydro-metallurgical technique or aqueous reprocessing [1]. To evade some of the key problems of these aqueous methods, pyro-metallurgical techniques have been developed [2]. The central part of pyro-metallurgical reprocessing is the electro-refining step where a liquid Cd cathode is used to selectively extract minor actinides from the irradiated metallic fuel. The theoretical feasibility was described repeatedly in literature, see e.g. Refs. [3-5]. One of the key problems of this method is the clean separation of actinides from a salt molten solution which also contains a considerable amount of lanthanides. Moriyama et al. [6] determined that the separation factors, which are an indicator for extractability, are quite different between actinides and lanthanides and are predominantly dependent on the employed liquid metal which is preferentially Cd [7]. Therefore, a detailed knowledge of the respective Cd-RE (RE...rare earth element) phase diagrams as well as of the thermodynamic stabilities of the corresponding intermetallic compounds is of great importance. This was the reason for initiating a series of thermodynamic and phase diagram studies of different Cd-RE systems in our laboratory (*cf.* Refs. [8-13]).

Concerning the system Cd-Gd, a complete version of the phase diagram was available from literature, given by Bruzzone et al. [14]. The authors presented phase equilibria and melting behaviour in the complete composition range and showed the occurrence of altogether six intermetallic compounds. They identified three new phases, i.e. Cd_3Gd, $Cd_{4-x}Gd$ and $Cd_{4.5-x}Gd$, of which the latter two were reported to be isomorphous with Pt_5Zn_{21} [15] and $Gd_{13}Zn_{58}$ [16], respectively. In addition, they confirmed the existence of CdGd, Cd_2Gd and Cd_6Gd which had already been reported previously [25, 27, 29]. Moreover, a polymorphic

transformation of Cd_2Gd into a high temperature modification (β-Cd_2Gd) at 995 °C was indicated by Bruzzone et al. [14], but no information on the corresponding crystal structure was given since quenching of this high temperature phase (β-Cd_2Gd) was not possible. It was further stated that no detectable range of solid solubility was observed for any of the phases except for the high temperature allotropic modification of Gd. By addition of Cd, β-Gd could be stabilized down to 725 °C where it decomposes in a eutectoid reaction at 16 at.% Cd. It was shown that β-Gd forms a eutectic reaction with CdGd at 27 at.% Cd and 920 °C, a temperature where 22 at.% Cd are dissolved. The only congruently melting phase in this system is CdGd with a melting point of 1170 °C at the stoichiometric composition. All other compounds are formed incongruently: β-Cd_2Gd (1010 °C), Cd_3Gd (815 °C), $Cd_{4\sim}Gd$ (*i.e.* $Cd_{45}Gd_{11}$, 806 °C), $Cd_{4.5\sim}Gd$ (*i.e.* $Cd_{58}Gd_{13}$, 803 °C), and Cd_6Gd (716 °C). Hence, the liquidus curve continuously decreases from 1170 to 316 °C, which corresponds to the eutectic formed between Cd and Cd_6Gd at 97.5 at.% Cd.

The solubility of Gd in liquid Cd was extrapolated from DTA results but does not correspond to data presented earlier by Johnson [17] who had determined the solubility of Gd in liquid Cd by chemical analysis of filtered samples between 324 and 500 °C. From these results Johnson derived much lower solubility limits within this temperature range, *i.e.* 0.17-1.45 at.% Gd. In a subsequent study, Roshchina and Bayanov [18] employed an emf method to determine activities of Gd in liquid Cd. From their emf signals the solubility of Gd in liquid Cd was estimated between 390 and 528 °C. The values were given within 2.4 and 3.5 at.% Gd which agrees with the data of Bruzzone et al. [14].

Based on a combination of all available data, Gschneidner and Calderwood [19] presented an assessment of the Cd-Gd phase diagram which corresponds to the version of Bruzzone et al. [14]. Gschneidner and Calderwood described the phases $Cd_{4\sim}Gd$ and $Cd_{4.5\sim}Gd$ as $Cd_{45}Gd_{11}$ and $Cd_{58}Gd_{13}$, respectively, which is a consistent notation for these compounds also in other Cd-RE systems. Moreover, they raised the isothermal reaction temperature of the eutectic reaction L⇄CdGd+β-Gd to 937 °C which is 17 °C higher than the value given by Bruzzone et al. [14]. Obviously, the latter authors used for sample preparation Gd metal with a melting point exactly 17 °C lower than the accepted value from Gschneidner and Calderwood [20]. In a subsequent study, Tang and Gschneidner [21] performed DTA measurements of rapidly quenched as-cast alloys and determined the eutectoid transformation from low to high temperature Gd at 738 °C which is 13 °C higher than the value given by Bruzzone et al. [14]. Tang and Gschneidner even obtained lattice parameters of solid solutions of Cd in β-Gd. Through a linear extrapolation they determined the lattice parameter of pure β-Gd, given as

3.99±0.04 Å. Based on the results of Refs. [14,17,22], Kurata and Sakamura [23] made a CALPHAD-type optimization between 0 and 60 at.% Cd. All intermetallic compounds were modelled as stoichiometric line compounds.

Since all intermetallic Cd-Gd compounds have isomorphous homologues in other Cd-RE systems as already mentioned by Gschneidner and Calderwood [24], their crystal structures are sufficiently well known. A list of crystallographic data concerning all binary compounds relevant for the current work is shown in Table 1 together with phase boundaries at 500 °C from Reichmann et al. [13] and corresponding references [14,44]. No significant homogeneity ranges of these phases were given in literature up to now. Concerning the Cd-Gd phases, vapour pressure measurements have been carried out by Reichmann et al. [13] and phase boundaries were derived at 500 °C, see Table 1. Significant solubility limits were determined for at least five compounds whereas Cd_3Gd was described as a line compound.

Compounds with the respective composition ratio 1:1 were found in most systems between Cd and RE elements, and the system Cd-Gd is no exception [26-28]. As all other homologues, CdGd is crystallizing in the CsCl structure (*B2*) which is an ordered variety of the *bcc* W-structure of β-Gd. As it was recently described in the Cd-Pr phase diagram, CdPr can be built up by substituting Pr sites in β-Pr with Cd atoms [10]. Actually, the two-phase field β-Pr+CdPr can be treated as a miscibility gap which breaks off a continuous solid solution between both phases, a situation which seems to be quite similar in the Cd-Gd phase diagram (see section 3.3. below).

The next compound richer in Cd is Cd_2Gd (*i.e.* α-Cd_2Gd, structure type *C*6). Compounds with the general formula Cd_2RE were investigated extensively. They crystallize either in space-group *P*6/*mmm* or $P\bar{3}m1$ [29-33]. The only exceptions are Cd_2Eu and Cd_2Yb for which space group *Imma* [34] and $P6_3/mmc$ [35] were found. Compounds with space-group symmetry *P*6/*mmm* adopt the simple AlB_2 structure type (Pearson code *hP*3) with Wyckoff sequence *d a*; the site positions are (⅓⅔½) and (000). The compounds with space-group $P\bar{3}m1$ maintain the Pearson code and Wyckoff sequence, the site positions are (⅓⅔ *z*) and (000). However, the *z* parameter of the site 2(*d*) varies either between 0.042 and 0.080 or between 0.42 and 0.43. Phases adopting *z* parameters around 0.42 can be considered as having a distorted atomic arrangement from that found in space group *P*6/*mmm*. Curiously, both atomic arrangements with symmetry $P\bar{3}m1$ are currently known as the Cd_2Ce-type.

Iandelli and Palenzona [29] described Cd_2Gd to crystallize in the Cd_2Ce-type where Cd occupies the site 2(*d*) (⅓⅔ *z*) with z = 0.42. The authors outlined that this atomic arrangement corresponds to a completely disordered mixture of the simple AlB_2-type and the CdI_2-type

structures. From a single-crystal investigation of the Cd_2Pr compound [10], it was obtained that this phase crystallizes in the simple AlB_2-type with space group *P*6/*mmm* and the site positions (⅓⅔½) and (000). It was even found in the present study, that Cd_2Gd (*i.e.* α-Cd_2Gd) should crystallize in the simple AlB_2-type, compare 3.1.

The compound Cd_3Gd was first described by Bruzzone et al. [14] to crystallize in the Ni_3Sn structure ($D0_{19}$). Subsequent single-crystal measurements were performed by Bruzzone et al. [36] to determine crystal structure data in detail. Compounds with the composition ratio 3:1 were found in most of the phase diagrams of Cd with rare earth elements and appear with three different structure-types *i.e.* BiF_3, Ni_3Sn and $ErCd_3$ [24]. With the exception of Cd_3Tb, which either crystallizes in the hexagonal Ni_3Sn or orthorhombic $ErCd_3$ structure [36], Cd_3Gd is the only compound preferring the hexagonal cell ($P6_3/mmc$).

In the very narrow composition range 79-82 at.% Cd, two intermetallic compounds with rather big unit cells are occurring: $Cd_{45}Gd_{11}$ (*cF*448) and $Cd_{58}Gd_{13}$ (*hP*142) [14]. $Cd_{45}Gd_{11}$ is isostructural with $Cd_{45}Sm_{11}$, which was investigated by single-crystal X-ray diffraction [37]. This structure type can be described by the so-called cluster concept originally adopted by Bradley and Jones [38]. $Cd_{45}Gd_{11}$ is thus an arrangement of 16 clusters of two types which are distributed along a NaTl-type unit cell. The two types of clusters which build up the $Cd_{45}Gd_{11}$ cell are related to clusters found in γ-brass phases and in α-Mn, respectively.

$Cd_{58}Gd_{13}$ forms a complex atomic arrangement that is isotypic to $Cd_{58}RE_{13}$ where RE stands for: Y, La, Ce, Pr, Nd, Sm and Eu [33, 36, 39-40]. Recently, Piao et al. [41] have synthesised also $Cd_{58}Dy_{13}$ and $Cd_{58}Tb_{13}$ but observed differences to the archetype structure. The basically hexagonal structure type contains various building blocks going along with extensive order-disorder phenomena resulting in distinct superstructures. Partly, an incommensurate behaviour is observed. More recently, Piao et al. [42] discussed for the compound $Ce_{12.60}Cd_{58.68}$ a metrically commensurate representative which obviously represents a lock-in phase.

The compound richest in Cd is Cd_6Gd. Johnson et al. [25] presented cell parameters for a number of compounds with the composition ratio 6:1. No additional information was given except that all homologues seem to be isomorphous. Subsequently, Larson and Cromer [43] investigated the crystal structure of Cd_6Y using single-crystal X-ray diffraction. They reported that the crystal structure is isotypic to Ru_3Be_{17} but with an additional Cd position in a 24-fold position and the site occupation factor of 0.33. More recently, Gomez and Lidin [44] employed single-crystal X-ray diffraction to investigate disorder phenomena in MCd_6 (M = Pr, Nd, Sm, Eu, Gd, Dy, Yb, Y and Ca). In the course of their study they could compare the

different types of disorder of the central Cd_4 tetrahedra, which belong to the additional Cd position introduced by Larson and Cromer. According to Gomez and Lidin, the respective Cd position is somehow split and manifests itself as smeared out electron density. Their corresponding structural data were taken for the present refinements.

Due to some discrepancies concerning the published phase diagram data, it was the aim of the present work to provide an experimental re-investigation of the Cd-Gd phase diagram. In addition, these data can serve as input into a CALPHAD-type optimization of the Cd-Gd system. This would contribute to a better understanding of the distribution behaviour of Gd in the electro-refining cell described above.

2. Experimental

All samples were prepared from pure elements, using cadmium shot (99.9999 %, AlfaAesar, Johnson Matthey Chemicals, Karlsruhe, Germany) and gadolinium pieces (99.9 %, Smart Elements, Vienna, Austria; 99.9 %, Goodfellow, Cambridge, UK). The surface of the Gd pieces was filed to remove the corresponding oxide layer. The elements were weighed with a semi-micro balance to an accuracy of about ± 0.5 mg which corresponds to an actual accuracy of ± 0.01 at.%. Typically, samples with a total mass of 1 g were produced. To prevent Gd from oxidation, the whole sample preparation was carried out in a glove box, filled with Ar (oxygen and water level: < 1ppm each). The metals were placed in Ta crucibles which were designed in our laboratory and subsequently enclosed by means of arc welding under an Ar atmosphere of 0.28 bar.

For equilibration, the crucibles were sealed into silica glass tubes under dynamic vacuum of better than 10^{-2} mbar. Afterwards, sample preparation was done according to different heating procedures to achieve optimal homogenisation. Whereas the melting points of these elements differ noticeably, Cd has a rather high vapour pressure and a low boiling point, *i.e.* 767 °C [45]. This can cause a severe Cd pressure inside the crucibles, when heating the samples too fast to temperatures above 767 °C. Thus, all samples were slowly heated (0.5 K/ min) to temperatures above the melting point of Cd and held for one day, which allowed a more or less complete reaction of Cd with Gd before reaching elevated temperatures. All heat treatments are listed in Table 2. It was observed that this pre-heating step had a decisive influence on the quality of the final samples: several times it was observed that samples with rather high Cd contents, heated too fast, showed a drastic expansion of the Ta crucibles. Sometimes, condensed Cd was found at the inner top of the Ta crucibles, resulting in a large deviation of the corresponding sample compositions. This behaviour could be avoided by a slow heating rate.

After pre-heating of the samples to a temperature just above the melting point of Cd, they were homogenized at elevated temperatures, specified as T_{max} in Table 2, and further annealed. Samples with a Cd content less than 22 at.% were homogenized at 1400 °C using an induction furnace. At this temperature Cd is already gaseous which could cause a violent pressure increase inside the crucibles. Thus a reliable homogenization was only expected when Cd had already completely reacted with Gd during the pre-heating step. It turned out that samples with higher amounts of Cd than 22 at.% led to severe expansion of the crucibles when heated above 1200 °C. Hence, these samples were slowly heated (0.5 K/ min) to

temperatures were the corresponding alloy was completely or partially melted. After pre-heating and homogenization at elevated temperatures, the samples were annealed for at least five weeks at different temperatures (Tab. 2) and subsequently quenched in cold water.

Phase identification and precise lattice parameters of the different phases were obtained by means of powder X-ray diffraction (powder-XRD) using a Bruker D8 Discover Series 2 powder diffractometer in Bragg-Brentano pseudo-focusing geometry and employing CuKα radiation. Data were collected by a LynxEye silicon strip detector (exposure time: 2h). Additional measurements were performed on a Guinier-Huber camera 670 operating with $CuK\alpha_1$ radiation and an image plate detector (measurement period: 2h, 10 detection loops). Special sample holders with X-ray transparent lids were used to prevent the sample powders from oxidation. The corresponding powder-XRD patterns were analyzed and refined by means of the TOPAS 3 software, applying the fundamental parameter approach for peak profile modelling.

For investigation of the microstructures, selected samples were embedded in phenolic hot mounting resin and then ground and polished. Grinding was carried out with silicon carbide abrasive paper (mesh size: 400, 600, 800, 1000 and 1200) using water as fluid. Although Gd containing alloys are essentially sensitive to water, it was sufficient to keep the grinding steps as short as possible to prevent oxidation. Grinded samples were intermediately stored in cyclohexane. For fine polishing of the surface a water-free diamond suspension was taken with kerosene as fluid.

Metallographic analyses were carried out on a binocular reflected-light microscope (Zeiss Axiotech 100) featured with a bi-refringent prism for differential interference contrast (DIC) imaging and equipment for operation under polarized light. Quantitative examinations of the microstructures were performed on a Zeiss Supra 55 VP environmental scanning electron microscope (SEM) using pure elements as standard materials and Co for the energy calibration of the energy-dispersive X-ray (EDX) detector signal. A 120 µm aperture was used and an acceleration voltage of 20 kV was applied. For imaging of the microstructures, a back-scatter detector was employed. Final compositions were calculated by conventional ZAF matrix correction from the measured X-ray intensities. The composition of each phase was measured at ten or more spots in order to minimize statistical errors and to obtain more reliable results.

Differential thermal analysis (DTA) was carried out on a Netzsch DSC 404 F1 Pegasus using closed Ta crucibles with flat bottoms and a constant Ar flow of 50 mL/min, respectively. Sapphire was used as the reference material. The temperature was measured

with type-S (Pt/Pt10%Rh) thermocouples which were calibrated at the melting points of the high purity metals Sn, Al, Ag and Cu. The samples weighed usually around 150-200 mg and were positioned in good thermal contact to the crucibles. Optionally, samples were powdered and pressed into pills to ensure good contact of the individual grains for better diffusion. Two heating- and cooling-curves were recorded for each sample using a heating rate of 5 $Kmin^{-1}$.

3. Results and discussion

A number of samples were annealed and characterised by powder-XRD, SEM and DTA, to reinvestigate the equilibrium phase diagram of Cd-Gd, presented first by Bruzzone et al. [14]. In particular, it was of interest to verify the homogeneity ranges of the intermetallic compounds (see below) which were recently derived from isopiestic vapour pressure measurements [13]. Moreover, all phase equilibria and the complete reaction scheme were re-examined and discussed. A selection of relevant samples, examined with isothermal methods, is listed in Table 2. Heat treatments, identified phases and phase compositions are given.

All samples which were studied by DTA are listed in Table 3, together with their thermal effects from two heating and cooling cycles, respectively. On the basis of the combined results a complete version of the Cd-Gd phase diagram was drawn, which is shown in Fig. 1.

3.1. Phase equilibria, reaction scheme and a new compound "Cd_8Gd"

As can be seen in Table 2, several samples were annealed at different temperatures to accurately determine the homogeneity ranges of the corresponding intermetallic compounds. Unfortunately, it was not possible to examine all samples with both methods, *i.e.* SEM and powder-XRD. Samples containing large amounts of Cd or Gd, respectively, turned out to be rather ductile; consequently powdering of these samples was virtually impossible. Attempts to grind samples with a Gd content higher than 60 at.% into powders failed: apart from the fact that they were very ductile, Gd has a high atomic number and thus absorption effects were found to be quite high when irradiated by X-rays. The resulting low intensities made it impossible to perform an accurate evaluation of the lattice parameters of α- and β-Gd. With respect to its ductility, no powder-XRD was carried out for sample 1 as well. Indeed, the lattice parameters of Cd were assumed to be similar to those from sample 2, which was annealed at 300 °C.

The overall composition of each sample, obtained by EDX, was compared with its nominal composition to estimate possible weight losses due to volatile Cd. No significant deviation of the determined composition from the nominal composition was found in most of the samples; *e.g.* nominal compositions of the single-phase samples 6 and 25 (Tab. 2) are in excellent agreement with EDX results. Even for samples with high Cd contents only a very thin Cd film could be observed visually inside the crucibles indicating negligible deviation from the nominal composition. As all homogeneity ranges were derived from several samples

and most of them were prepared twice, an experimental error of about ± 0.5 at.% for EDX measurements could be estimated. From the comparison of the EDX results of the stoichiometric compound Cd_3Gd it can be clearly seen that all values lie within the estimated error limit, see Table 4.

EDX measurements of samples 1 and 2 indicated a new intermetallic compound with the stoichiometric composition $Cd_{88.7}Gd_{11.3}$. Corresponding powder-XRD results as well as the formation behaviour of this new compound, which corresponds to the empirical formula "Cd_8Gd", are described below. Unfortunately, it was not possible to obtain structural data of "Cd_8Gd" in the present study. Work is still going on to produce suitable single crystals for a proper structure determination.

As pointed out, homogeneity ranges of all intermetallic compounds were defined at 500 °C and are listed in Table 4. Apparently, these values agree quite well with phase boundaries reported recently [13] and listed in Table 1. The present data indicate narrow but finite homogeneity ranges for all compounds except Cd_3Gd and "Cd_8Gd", which were identified as line compound, *i.e.* no significant solid solubility of either Cd or Gd was determined. The largest deviation of the solubility limits was observed for the Gd-rich boundary of CdGd. The homogeneity ranges given in Ref. [13] are based on powder-XRD results of equilibrated CdGd alloys. It is possible that, due to the discussed absorption effects of Gd, samples were misinterpreted to be phase-pure CdGd although they might actually have been located already in the two-phase field α-Gd+CdGd. Thus, the solubility of Gd within CdGd at 500 °C is probably less than indicated in Ref. [13] and much closer to the value obtained here.

All binary phase reactions were examined by means of DTA. For the description of the reaction scheme and the graphical representation of the phase diagram (Fig. 1), samples listed in Table 2 as well as additional equilibrated samples were taken. Effects measured from samples with identical nominal compositions were usually averaged. The corresponding results of the DTA measurements of all samples are listed in Table 3. For each sample two heating and cooling cycles were performed at a heating rate of 5 K/min in order to check if equilibrium conditions can be restored after the first melting of the sample. It was found that most of the alloys were still in equilibrium after the first cycle but, for the graphical representation of the phase diagram, all thermal effects, except the liquidus, were taken from the first heating curves. In case of the liquidus effect, usually an average value from the two heating curves was taken for the evaluation. Although most of the cooling curves exhibited

considerable supercooling, their liquidus values were still considered to guide the construction of the liquidus curves.

In addition to the new compound "Cd_8Gd", all six intermetallic compounds, which were already described by Bruzzone et al. [14], were confirmed in the current study. All invariant reactions, evaluated from the present results, are listed in Table 5 together with the respective reaction temperatures and types and the phase compositions. As can be seen, all compounds except CdGd are formed through a cascade of incongruent reactions which was also obtained by Bruzzone et al. Although the reaction scheme is in agreement with that of the latter authors, there are some discrepancies with regard to the isothermal reaction temperatures and the liquidus shape. In addition, the homogeneity ranges of the low- and high-temperature modifications of Gd seem to be narrower than indicated by [14]. Distinct differences are discussed below in section 3.3. To clarify the formation reactions of the two intermetallic compounds $Cd_{45}Gd_{11}$ and $Cd_{58}Gd_{13}$, with compositions rather close to each other, the composition range between 78 and 82 at.% Cd was extensively investigated (see section 3.2.).

In the very Cd-rich part of the phase diagram, Bruzzone et al. described a eutectic reaction $L \rightleftarrows Cd_6Gd+Cd$ at 97.5 at.% Cd. The rather extended solubility of Gd in liquid Cd was extrapolated from DTA results but does not correspond to data presented earlier by Johnson [17]. Johnson determined much smaller solubilities, i.e. varying from 0.17 to 1.45 at.% Gd between 324 and 500 °C. These values are in excellent agreement with the present DTA data of samples with nominal compositions between 90 and 98 at.% Cd (Table 3). Thus the liquidus curve between 98 and 100 at.% Cd (Fig. 1) was fitted according to Johnson's solubility data which result apparently in a degenerate eutectic reaction, *i.e.* $L \rightleftarrows Cd_8Gd+Cd$.

Several alloys were prepared to produce an almost single phase sample of "Cd_8Gd". It turned out that this phase forms rather slowly, especially when heating the respective alloy above its overall melting point. An alloy with the nominal composition $Cd_{90}Gd_{10}$ (No. 2, Table 2) was homogenized at 800 °C before it was annealed for about 2 month at 300 °C. Its corresponding BSE image is shown in Figure 2. Only a small amount of "Cd_8Gd" was found to be present, exclusively occurring at the boundaries between Cd and Cd_6Gd grains. This typical microstructure argues for a peritectic formation of "Cd_8Gd". Samples produced in the same way as sample 2 but with higher Cd contents *i.e.* 92, 96 and 98 at.%, were produced in order to achieve equilibrium alloys within the two-phase field Cd+"Cd_8Gd". It turned out that with increasing Cd contents of the alloys and a corresponding lower melting point, the amounts of Cd_6Gd could be decreased and an equilibrium sample within the two-phase field

Cd+"Cd_8Gd" could be prepared (No. 1, Tab.2). This is probably related to shorter diffusion paths due to smaller primary crystals of Cd_6Gd. It seems that the peritectic formation of "Cd_8Gd" is rather determined kinetically than thermodynamically. As a consequence, all attempts to produce a single-phase sample of "Cd_8Gd" by annealing an as-cast alloy failed.

Therefore, a sample with the nominal composition $Cd_{88.7}Gd_{11.3}$, was slowly heated to 350 °C and held at this temperature for 2 months without prior homogenization at elevated temperatures. In this case, Gd powder was used to achieve a better mixing of the metals. The corresponding BSE image showed that this alloy was phase-pure "Cd_8Gd" with the measured composition $Cd_{88.6}Gd_{11.4}$. The respective powder-XRD pattern, given in Figure 3, shows likewise that this alloy is phase-pure and no additional reflections belonging to Cd and/or Cd_6Gd were obtained. It is assumed that after the melting point of Cd was reached, initially the phase richest in Cd ("Cd_8Gd") was formed at the surface boundaries of the Gd particles. Probably, these surface layers acted as nuclei which actually promoted the formation of "Cd_8Gd".

As already observed by Bruzzone et al. [14], the present DTA results indicated a polymorphic transformation of Cd_2Gd into a high-temperature modification β-Cd_2Gd. Its corresponding transition temperature as well as the peritectic decomposition temperature of β-Cd_2Gd were slightly lower than given in Ref. [14], *i.e.* 986 and 998 °C instead of 995 and 1010 °C, see Fig. 4. Although these two invariant reactions were clearly indicated in all DTA curves of corresponding samples, it was often not possible to evaluate the peritectic decomposition temperature precisely, especially when both effects strongly overlapped. Several attempts were carried out to quench the high-temperature modification of β-Cd_2Gd but were not successful. Efforts are still going on to clarify its structure.

Iandelli and Palenzona [29] as well as Mulokozi [32] described α-Cd_2Gd to crystallize in the Cd_2Ce-type, a deformed AlB_2-type structure with space group symmetry $P\bar{3}m1$, where Cd occupies the site 2(*d*) (⅓⅔ *z*) with z = 0.42. The respective unit cell is shown in Figure 5. More recently, a single-crystal investigation of iso-structural α-Cd_2Pr [10] showed that this phase crystallizes with space group *P6/mmm* and the corresponding site positions were determined at (⅓⅔½) and (000). The latter structure is currently known as the simple AlB_2-type (Fig. 5.). Compared to the Cd_2Ce-type, there is a planar arrangement of Cd atoms with equidistant spacing to all neighbouring Gd atoms. This ordering effect leads to an increase of the cell symmetry and a change from space group $P\bar{3}m1$ to its supergroup *P6/mmm* according to the group/subgroup relation. As a consequence, the calculated powder-XRD patterns of Cd_2Ce and AlB_2 look slightly different. It was observed that especially the reflexes (012) and

(212) seem to be systematically extinguished in the AlB_2-type, a fact that corresponds to the present observed powder-patterns of α-Cd_2Gd. Therefore, it is assumed that α-Cd_2Gd is also crystallizing with space group *P*6/*mmm* and the corresponding Cd position (⅓⅔½) as listed in Table 1.

3.2. The formation behaviour of $Cd_{45}Gd_{11}$ and $Cd_{58}Gd_{13}$

As previously indicated by Bruzzone et al. [14], two compounds are located in the rather narrow composition range 80-82 at.% Cd, namely $Cd_{58}Gd_{13}$ and $Cd_{45}Gd_{11}$. Compounds with this stoichiometry were found to be in thermodynamic equilibrium in a number of Cd-RE phase diagrams but Cd-Gd is the only system were both phases decompose within a rather close temperature interval, *i.e.* 803 and 806 °C [14]. Hence, these phases should be quite similar with respect to their relative stability. The existence of a narrow but definite two-phase field along the entire temperature interval indicates that they are truly separate phases and not just parts of a solid solution. Actually, this was not to be expected because there is no structural relation between the crystal structures of $Cd_{58}Gd_{13}$ and $Cd_{45}Gd_{11}$. In order to elucidate the temperatures and the sequence of the corresponding formation reactions it was tried to prepare a two-phase alloy of $Cd_{58}Gd_{13}$ and $Cd_{45}Gd_{11}$.

Initially, a sample, with a nominal composition located within the two-phase field of $Cd_{58}Gd_{13}$ and $Cd_{45}Gd_{11}$ (No. 6, Table 2), was annealed at 700 °C. As can be seen from the EDX and powder-XRD results in Table 2, this sample was a single-phase alloy of $Cd_{45}Gd_{11}$. Next, a sample with the nominal composition $Cd_{83.5}Gd_{16.5}$ (No. 3) was annealed at 700 °C. Differently than expected from the phase diagram [14], a two-phase equilibrium between Cd_6Gd and $Cd_{45}Gd_{11}$ was obtained for this alloy. All further attempts to produce an alloy, which contains $Cd_{58}Gd_{13}$ at temperatures above 700 °C failed. In fact, all respective samples were observed to be two-phase alloys of Cd_6Gd and $Cd_{45}Gd_{11}$. Based on the EDX results of sample No. 3, the homogeneity range of $Cd_{45}Gd_{11}$ could be limited at a composition of 81.3 at.% Cd at 700 °C (Fig. 4). This relatively high solubility of Cd within $Cd_{45}Gd_{11}$ at 700 °C explained why sample 6 was just single-phase.

Since there was no doubt that $Cd_{58}Gd_{13}$ is an equilibrium phase, which was recently found in isopiestic samples between 430 and 530 °C [13], it was assumed that it decomposes at some temperature below 700 °C. Therefore, a sample (No. 4), with the nominal composition equal to sample No. 3, was annealed at 600 °C without prior homogenisation at elevated temperatures. The corresponding powder-XRD pattern clearly showed presence of $Cd_{58}Gd_{13}$

with comparable amounts of its neighbouring phases Cd_6Gd and $Cd_{45}Gd_{11}$, respectively. Although this sample was not in equilibrium, it indicated that $Cd_{58}Gd_{13}$ is an equilibrium phase. Nevertheless, all attempts to prepare an equilibrium sample, which contains $Cd_{58}Gd_{13}$ only, were not successful.

Therefore, seven well equilibrated samples from the isopiestic vapour pressure measurements (see Ref. [13]; run/sample: 1/1, 3/1, 6/2, 6/3, 7/3-7/5), which contained considerable amounts of $Cd_{58}Gd_{13}$, were powdered and pressed into pills, which allowed for rather short diffusion paths. It was assumed that initially present $Cd_{58}Gd_{13}$ crystals would promote its further growth. The overall composition of the respective pills was $Cd_{82.3}Gd_{17.7}$, which is rather close to the stoichiometric composition of $Cd_{58}Gd_{13}$. The pills were annealed for 3 months at 500 and 700 °C and the corresponding powder-XRD patterns before as well as after annealing are shown in Figure 6. Before annealing, the alloy contained comparable amounts of Cd_6Gd, $Cd_{58}Gd_{13}$ and $Cd_{45}Gd_{11}$. It was observed that after annealing at 500 °C, the amount of $Cd_{45}Gd_{11}$ had considerably decreased by forming Cd_6Gd and $Cd_{58}Gd_{13}$. On the contrary, the alloy which was annealed at 700 °C showed a noticeable increase of $Cd_{45}Gd_{11}$ whereas $Cd_{58}Gd_{13}$ had completely disappeared. This behaviour agrees well with the results described above. In addition, all samples, which contained $Cd_{58}Gd_{13}$, were investigated by DTA in order to obtain the decomposition temperature of this compound. Unfortunately, no additional effect, apart from the effects dedicated to the decomposition reactions of Cd_6Gd and $Cd_{45}Gd_{11}$, was observed in the respective heating curves. However, some of the cooling curves comprised an additional peak just below the melting effect. Thus, powder-XRD measurements were performed from DTA samples after the final cooling run, in order to see if $Cd_{58}Gd_{13}$ was formed. Unfortunately, no $Cd_{58}Gd_{13}$ was in any of these alloys.

As a conclusion, it has to be assumed that $Cd_{58}Gd_{13}$ is not stable at temperatures above 700 °C. Obviously, this phase is formed through a peritectoidic reaction between Cd_6Gd and $Cd_{45}Gd_{11}$, *cf.* Table 5. Attempts are still going on to clarify the range which is currently labelled with a question mark in Fig. 4.

To confirm the incongruent formation of $Cd_{45}Gd_{11}$, an alloy with the respective stoichiometric composition was prepared by equilibration with Cd vapour as in the isopiestic vapour pressure measurements [13]; powder-XRD confirmed that this alloy was phase-pure $Cd_{45}Gd_{11}$. Since the liquidus temperature of this alloy seems to be rather close to the peritectic decomposition temperature of $Cd_{45}Gd_{11}$ [14], no clear proof for an incongruent melting behaviour could be obtained by DTA. Actually, the DTA curve looked quite similar to that of a congruently melting phase. Hence, a sample with the nominal composition $Cd_{79}Gd_{21}$ (No. 7)

was measured in DTA against pure $Cd_{45}Gd_{11}$ as the reference material. It was assumed that both sample and reference position are symmetrical within the furnace. If $Cd_{45}Gd_{11}$ were a congruently melting phase, one would first expect a eutectic effect caused by the two-phase sample, followed by the congruent melting effect of the $Cd_{45}Gd_{11}$ reference. Contrary, if $Cd_{45}Gd_{11}$ is an incongruently melting phase, the trend of the resulting DTA curve would be strongly determined from the difference in mass of the sample and the reference. The corresponding DTA curve is shown in Fig. 7, superimposed onto the DTA curves from sample No. 7 and $Cd_{45}Gd_{11}$ against NIST[1] standard sapphire as reference material. It can be seen, that there is an initial hypothetically exothermal effect which belongs to a reaction within the reference material, *i.e.* $Cd_{45}Gd_{11}$. Apparently, $Cd_{45}Gd_{11}$ has to be an incongruently melting phase because otherwise one would definitely expect an endothermic effect at first. It can even be observed, that this effect follows the peak which was observed in the DTA curve from pure $Cd_{45}Gd_{11}$ against NIST sapphire. The evaluation of the onset of the "exothermal" effect resulted in a value of 806.0 °C which is taken as the peritectic reaction temperature of $Cd_{45}Gd_{11}$. The onset of sample No. 7 also corresponds to the peritectic formation of $Cd_{45}Gd_{11}$ but since it is more distinct, the temperature value is much closer to the average reaction temperature of 808±2 °C (*cf.* Table 5).

3.3. The composition range 0-52 at.% Cd

The partial equilibrium phase diagram between 0 and 52 at.% Cd is shown in Fig. 8 together with the experimental data points from DTA and EDX measurements (Tables 2 and 3). Although the reaction scheme of Bruzzone et al. [14] could be confirmed, isothermal reaction temperatures as well as homogeneity ranges of the low- and high-temperature modifications of Gd differ noticeably. The melting point of CdGd was determined to be about 23 °C lower, namely 1147 °C (Table 3). The isothermal reaction temperature of the eutectic reaction L⇄CdGd+β-Gd was obtained to be 895±5 °C. Actually, this value is about 25 °C lower than given in Ref. [14] and clearly disagrees from the estimation by Gschneidner and Calderwood [20], see *Introduction*. However, the corresponding eutectic point was found to be quite similar to that given earlier, *i.e.* 26.5 instead of 27.0 at.% Cd [14].

Veleckis and Van Deventer [46] listed isothermal reaction temperatures for eutectic reactions between RE elements and the respective compound richest in RE, which is, with the exception of Cd_5Eu_6, CsCl-structured CdRE. As indicated by Gschneidner and Calderwood

[1] National Institute of Standards and Technology, Gaithersburg, MD, USA

[24] the eutectic temperatures do not fit well with subsequently reported values. The largest differences between values given by Veleckis and Van Deventer and those reported later occurred when the corresponding RE undergoes an allotropic transformation. It has to be assumed that Veleckis and Van Deventer did not consider the high-temperature allotropic modifications of the respective RE elements. Indeed, their reported value for the eutectic reaction at 719 °C corresponds reasonably well with the present value for the eutectoid decomposition of β-Gd, namely 745±4 °C. This latter value was averaged from DTA data of nine samples, see Fig. 8. Actually, the eutectoid reaction temperature was altered a few times in literature. First given as 725 °C by Bruzzone et al., it was more recently determined by Tang and Gschneidner [21] to be about 738 °C. Tang and Gschneidner performed DTA measurements with a heating rate of 2 K/min whereas in the present study 5 K/min was used. According to the deviation of the measured transition temperatures, it has to be assumed that the transformation from α- to β-Gd is kinetically determined. In fact, β-Gd was sometimes found in samples annealed below the eutectoid temperature. By extrapolation of the heating rate to 0 K/min, the eutectoid reaction temperature is obtained to be 734 °C, a temperature which is probably closer to the equilibrium transformation temperature.

The respective DTA results fit excellently with phase compositions obtained from EDX measurements. Hence, the homogeneity ranges of α- and β-Gd could be determined rather accurately. The maximum solubility of Cd in β-Gd was determined as 22.6 at.% (*cf.* sample No. 20). This corresponds reasonably with data from Bruzzone et al. [14] whereas the shape of the phase boundaries of β-Gd is somewhat different from those in Ref. [14]. Since the eutectoid decomposition point could be defined reliably by EDX at $Cd_{19.1}Gd_{80.9}$, this unusual phase boundary is apparent.

The compound richest in Gd is CdGd. It crystallizes in the CsCl-structure type and exhibits an ordered variety of the β-Gd structure which crystallizes in the *bcc* W-structure (a = 3.99±0.04 Å [21]); half of the Gd sites in β-Gd are substituted by Cd atoms. Besides, a partial substitution of Cd by Gd according to $Cd_{1-x}Gd_{1+x}$, $x < 0.02$, was observed. The two-phase field β-Gd+CdGd can be considered as a large miscibility gap which cuts off a continuous solid solution (with a second-order phase transition) between these two phases. Samples with major amounts of $Cd_{1-x}Gd_{1+x}$, were used to show the correlation of the lattice parameter a with the composition. The increasing Gd content goes along with an increase of the lattice parameter which is in perfect agreement with the relative atomic radii of Gd and Cd; the excellent linear fit (Fig. 9) corresponds with Vegard's rule.

Conclusions

The complete Cd-Gd phase diagram was reinvestigated by a combination of powder-XRD, SEM and DTA; it is presented in Fig. 1. Based on the present results, the homogeneity ranges of the altogether seven intermetallic compounds were determined and listed in Table 4. Moreover, the extended solid solubility limits of Cd in the low- and high temperature modification of Gd were determined at 4.6 and 22.6 at.%, respectively. The addition of Cd stabilizes the high-temperature modification β-Gd down to 745 °C where it decomposes in terms of a eutectoid reaction.

Moreover, a new compound was found with a stoichiometry of "Cd_8Gd", decomposing peritectically at 465 °C. Its corresponding powder-XRD pattern is given in Figure 3. The peritectic decomposition of $Cd_{58}Gd_{13}$ could not be determined as given by [14] but is assumed that this phase forms through a peritectoidic reaction below 700 °C. It was obtained that the solubility of Cd in $Cd_{45}Gd_{11}$ increases rather extensively before the phase decomposes at 808 °C. A phase transformation of Cd_2Gd was previously indicated by Bruzzone et al. [14] and confirmed according to the present DTA results. However, attempts to quench the high temperature modification β-Cd_2Gd were not successful although attempts are continuing to clarify its structure. It was observed that the corresponding low-temperature modification α-Cd_2Gd crystallizes in the simple AlB_2-type, a fact that was previously discussed for isomorphous α-Cd_2Pr [10]. A partial substitution of Cd by Gd according to $Cd_{1-x}Gd_{1+x}$, $x < 0.02$, was observed in CdGd with CsCl-structure. Actually, it was described that the defect mechanism corresponds to Vegard's rule (Fig. 9).

Acknowledgements

The authors want to thank the Austrian Science Fund (FWF) for financial support of this study under Project No. P 23270-N19, and the Scientific-Technical Cooperation between Austria and India (Project No. IN 05/2011). Additionally the authors want to thank Victoria Dostal, Sunil Kavunga and Raphael Krausl for their help in sample preparation as well as Dr. Stephan Puchegger from the Department of Dynamic of Condensed Systems at the University of Vienna for his assistance with the SEM measurements.

References

[1] Olander D (2009) Nuclear fuels - Present and future. *J. Nucl. Mater.* 389: 1-22.

[2] Battles JE, Laidler JJ, McPheeters CC, Miller WE (1994) Pyrometallurgical processes for recovery of actinide elements. Actinide Process. *Proc. Int. Symp. 123rd Annu. Meet. Miner.*, Met., Mater. Soc. 135-151.

[3] Ackerman JP (1991) Chemical Basis for Pyrochemical Reprocessing of Nuclear Fuel. *Ind. Eng. Chem. Res.* 30: 141-145.

[4] Johnson I (1988) The Thermodynamics of Pyrochemical Processes for Liquid Metal Reactor Fuel Cycles. *J. Nuclear Mater.* 154: 169-180.

[5] Laidler JJ, Battles JE, Miller WE, Ackerman JP, Carls EL (1997) Development of Pyroprocessing Technology. *Progr. Nucl. Energy* 31 no. 1/2: 131-140.

[6] Moriyama H, Yamana H, Nishikawa S, Shibata S, Wakayama N, Miyashita Y, Moritani K, Mitsugashira T (1998) Thermodynamics of reductive extraction of actinides and lanthanides from molten chloride salt into liquid metal. *J. Alloys Comp*. 271: 587-591.

[7] Kurata M, Sakamura Y, Hijikata T, Kinoshita K (1995) Distribution behavior of uranium, neptunium, rare-earth elements (Y,La,Ce,Nd,Sm,Eu,Gd) and alkaline-earth metals (Sr,Ba) between molten LiCl-KCl eutectic salt and liquid cadmium or bismuth. *J. Nuclear Mater.* 227: 110-121.

[8] Reichmann TL, Ipser H (2014) Thermochemical Investigations in the System Cadmium-Praseodymium Relevant for Pyrometallurgical Fuel Reprocessing. *Metall. Mater. Trans. A*. 45 no. 3: 1171-1180.

[9] Skołyszewska-Kühberger B, Reichmann TL, Ganesan R, Ipser H (2014) Thermodynamic study of the cerium-cadmium system. *CALPHAD* 44: 14-20.

[10] Reichmann TL, Effenberger HS, Ipser H (2014) Experimental investigation of the Cd-Pr phase diagram. *PlosOne* 9 no. 4: 1-14.

[11] Reichmann TL, Richter KW, Ipser H (2014) Enthalpies of formation of Cd-Pr intermetallic compounds and thermodynamic assessment of the Cd-Pr system. *CALPHAD* 47: 56-62.

[12] Skołyszewska-Kühberger B, Reichmann TL, Ipser H (2014) Phase equilibria in the neodymium-cadmium binary system. *J. Alloys Comp.* 606: 242-248.

[13] T. L. Reichmann, R. Ganesan, H. Ipser. Thermochemical investigations in the system Cd-Gd. *J. Alloys Comp.* (2014), 610: 676-683.

[14] Bruzzone G, Fornasini ML, Merlo F (1971) The Gadolinium-Cadmium System. *J. Less-Common Met.* 25: 295-301.

[15] Berndt AF(1966) A γ-phase in the plutonium-mercury system. *J. Less-Common Met.* 11: 216-219.

[16] Wang FE (1967) The crystal structure of $Gd_{13}Zn_{58}$. *Acta Cryst.* 22: 579-584.

[17] Johnson I (1962) Solubility of the Rare-Earth Metals in Liquid Cadmium. *2nd Proc. Conf. Rare Earth Res.*: 125-131.

[18] Roshchina VR, Bayanov AP (1981) Thermochemistry of gadolinium-cadmium alloy formation. *J. Phys. Chem.* 55 no. 12: 3017-3020.

[19] Gschneidner Jr KA, Calderwood FW (1988) The Cd-Gd (Cadmium-Gadolinium) System. *Bull. Alloy Ph. Diagr.* 9 no. 1: 29-30.

[20] Gschneidner Jr KA, Calderwood FW (1986) Intra Rare Earth Binary Alloys: Phase Relationships, Lattice Parameters and Systematics. *Handb. Phys. Chem. Rare Earths* 8: 1-161.

[21] Tang J, Gschneidner Jr KA (1996) Physical metallurgy and magnetic behaviour of Cd-stabilized b.c.c. β-Gd alloys. *J. Alloys Comp.* 234: 26-33.

[22] Sakamura Y, Inoue T, Storvick TS, Grantham LF (1995) Characterizations of Rare Earths and Actinides in a Molten Salt/Liquid Cadmium System. *26th Symp. on Molten Salt Chem.*, Sapporo: 101.

[23] Kurata M, Sakamura Y (2001) Thermodynamic assessment of systems of actinide or rare earth with Cd. *J. Phase Equilibria* 22 no. 3: 232-240.

[24] Gschneidner Jr KA, Calderwood FW (1988) The Cadmium-Rare Earth Systems. *Bull. Alloy Ph. Diagr.* 9 no. 1: 16-20.

[25] Johnson I, Schablaske RV, Tani BS, Anderson K (1964) $CeCd_6$ -Type Rare Earth-Cadmium Alloys. *Trans. Met. Soc. AIME* 230: 1485-1487.

[26] Iandelli A (1960) Intermetallic and Metalloid Gadolinium Compounds. *Mat. Natur. Rend.* 29: 62-69.

[27] Iandelli A, Palenzona A (1965) Atomic size of rare earths in intermetallic compounds. MX compounds of CsCl type. *J. Less-common Met.* 9: 1-6.

[28] Chao CC, Duwez P (1966) New CsCl Type Intermediate Phases in Binary Alloys Involving Rare-Earth Elements. *J. Appl. Phys.* 37: 2631.

[29] Iandelli A, Palenzona A (1968) On Occurrence of MX_2 Phases of Rare Earths with Ib, IIb and IIIb Group Elements and Their Crystal Structures. *J. Less-Common Met.* 15: 273-284.

[30] Laube E, Kusma JB (1964) Über einige Y- und Dy-haltige Legierungsphasen. *Monatsh. Chem.* 95: 1504-1513.

[31] Kusma JB, Uhryn NS (1966) Crystal structures of some compounds of rare earth metals with cadmium. *Dopovidi Akademii Nauk Ukrains'koi RSR*: pp. 1025-1027.

[32] Mulokozi AM (1977) Nature of bonding in Rare-Earth compounds RX_2 with AlB_2-type or closely related structures I: Compounds RCd_2 with a deformed AlB_2 structure and influence of F-bonding. *J. Less-Common Met.* 53: 205-210.

[33] Tang J, Gschneidner KA Jr (1989) Searching for new heavy fermion materials in cerium intermetallic compounds. *J. Less-Common Met.* 149: 341-347.

[34] Koester W, Meixner J (1965) The constitution of the systems of Europium with Silver, Cadmium and Indium and the Cadmium-Strontium system. *Z. Metallkde.* 56: 695-703.

[35] Palenzona A (1971) The Ytterbium- Cadmium system. *J. Less-Common Met.* 25: 367-372.

[36] Bruzzone G, Fornasini ML, Merlo F (1973) Rare earth intermediate phases with Cd. *J. Less-Common Met.* 30: 361-375.

[37] Fornasini ML, Chabot B, Parthé E (1978) Crystal-Structure of $Sm_{11}cd_{45}$ with Gamma-Brass and Alpha-Mn Clusters. *Acta. Cryst.* B34: 2093-2099.

[38] Bradley AJ, Jones P (1933) An X-ray investigation of the copper-aluminium alloys. *J. Inst. Met.* 51: 131-162.

[39] Bruzzone G, Fornasini ML (1974) Contribution to System Samarium-Cadmium. *J. Less-Common Met.* 37: 289-292.

[40] Bruzzone G, Merlo F (1973) Lanthanum-Cadmium System. *J. Less-Common Met.* 30: 303-305.

[41] Piao SY, Gomez CP, Lidin S (2006) Complexity of hexagonal approximants in the $RE_{13}Zn$~58 system (RE = Ce, Pr, Nd, Sm, Gd, Tb and Dy). *Z. Kristallogr.*, New Cryst. Struct. 221: 391-401.

[42] Piao SY, Palatinus L, Lidin S (2008) All the disorder mechanisms in the 13:58 phases come together. Out of the modulated confusion rises the remarkable phase Ce12.60Cd58.68(2). *Inorg. Chem.* 47: 1079-1086.

[43] Larson AC, Cromer DT (1971) Crystal Structure of YCd_6. *Acta. Cryst.* B27: 1875-1879.

[44] Gomez CP, Lidin S (2003) Comparative structural study of the disordered MCd_6 quasicrystal approximants. *Phys. Rev. B* 68: 1-9.

[45] Binnewies M, Milke E (1999) Thermodynamic Data of Elements and Compounds. *WILEY-VCH*, Weinheim: 295-296.

[46] Veleckis E, Van Deventer E (1964) ANL-6925, *Semi-Annual Report*, Argone National Lab.

Table 1: Crystal structure data of binary compounds in the Cd-Gd system; phase boundaries at 500 °C are given according to [13]

Phase	Lattice parameter (Å)	Phase boundaries (at.% Cd)	Structure type	Space group	References
"Cd_8Gd"	-	-	-	-	this work
Cd_6Gd	a = 15.441	84.8 – 85.7	Cd_6Y	$Im\bar{3}$	[44]
$Cd_{58}Gd_{13}$	a = 15.40 c = 15.28	81.3 – 81.7	$Pu_{13}Zn_{58}$	$P6_3/mmc$	[14]
$Cd_{45}Gd_{11}$	a = 21.603	79.5 – 80.5	$Cd_{45}Sm_{11}$	$F\bar{4}3m$	[14]
Cd_3Gd	a = 6.621 c = 4.933	74.9 – 75.1	Ni_3Sn	$P6_3/mmc$	[14]
α-Cd_2Gd	a = 4.941 c = 3.467	65.3 – 67.1	AlB_2 [a]	$P6/mmm$ [a]	[14]
β-Cd_2Gd [b]	-	-	-	-	[14]
CdGd	a = 3.750	49.0 – 51.0	CsCl	$Pm\bar{3}m$	[14]

[a] Actually described with space group $P\bar{3}m1$ ($CeCd_2$-type) by [14] but modified according to the results of the present study.

[b] High temperature modification formed at 995 °C [14]

Table 2: Experimental phase compositions and lattice parameters of selected Cd-Gd samples

Sample / nom. comp. (at.%)	Phase analysis			SEM (EDX)	
	Heat treatment T (°C); duration; T_{max} (°C)	Phase	Lattice parameter (Å)	Cd (at.%)	Gd (at.%)
1 $Cd_{98}Gd_2$	300; 3 months; 800	Cd "Cd_8Gd"	*too ductile*	100 88.7	0.0 11.3
2 $Cd_{90}Gd_{10}$	300; 2 months; 800	Cd "Cd_8Gd" Cd_6Gd	a = 2.9792 (1), c = 5.6130(4) *no structure data available* a = 15.5263(4)	100 88.7 85.5	0.0 11.3 14.5
3 $Cd_{83.5}Gd_{16.5}$	700; 3 months; 950	Cd_6Gd $Cd_{45}Gd_{11}$	a = 15.5226(3) a = 21.6003(3)	85.2 81.3	14.8 18.7
4 $Cd_{83.5}Gd_{16.5}$	600; 2 months; 600	Cd_6Gd $Cd_{45}Gd_{11}$ $Cd_{58}Gd_{13}$	a = 15.5253(6) a = 21.6076(9) a = 15.3963(6), c = 15.2661(1)	85.4 -[a]	14.6 -[a]
5 $Cd_{82.3}Gd_{17.7}$	500; 3 months; 500	Cd_6Gd $Cd_{58}Gd_{13}$	a = 15.5265(3) a = 15.3969(4), c = 15.2659(7)	-[b]	-[b]
6 $Cd_{80.6}Gd_{19.4}$	700; 3 months; 900	$Cd_{45}Gd_{11}$	a = 21.5964(1)	80.9	19.1
7 $Cd_{79}Gd_{21}$	750; 3 months; 950	$Cd_{45}Gd_{11}$ Cd_3Gd	a = 21.6058(3) a = 6.6272(4), c = 4.9359(6)	79.8 74.9	20.2 25.1
8 $Cd_{78}Gd_{22}$	700; 3 months; 950	$Cd_{45}Gd_{11}$ Cd_3Gd	a = 21.6091(2) a = 6.6228(4), c = 4.9329(6)	79.9 75.0	20.1 25.0
9 $Cd_{73}Gd_{27}$	750; 4 months; 950	Cd_3Gd α-Cd_2Gd	a = 6.6194(6), c = 4.9337(8) a = 4.9404(6), c = 3.4711(5)	74.9 67.2	25.1 32.8
10 $Cd_{71.2}Gd_{28.8}$	700; 3 months; 1100	Cd_3Gd α-Cd_2Gd	a = 6.6220(4), c = 4.9342(6) a = 4.9403(2), c = 3.4673(2)	74.8 67.1	25.2 32.9
11 $Cd_{69}Gd_{31}$	750; 3 months; 900	Cd_3Gd α-Cd_2Gd	a = 6.6090(1), c = 4.9389(2) a = 4.9407(3), c = 3.4669(3)	74.8 67.5	25.2 32.5

Journal of Alloys and Compounds (2014), in print

12 $Cd_{63}Gd_{37}$	750; 4 months; 1050	α-Cd_2Gd CdGd	a = 4.9432(2), c = 3.4698(2) a = 3.7501(8)	-[c] 50.8	-[c] 49.2
13 $Cd_{63}Gd_{37}$	950; 4 months; 1050	α-Cd_2Gd CdGd	a = 4.9406(2), c = 3.4702(3) a = 3.7487(1)	66.9 51.0	33.1 49.0
14 $Cd_{58.8}Gd_{41.2}$	900; 2 months; 1200	α-Cd_2Gd CdGd	a = 4.9406(2), c = 3.4657(2) a = 3.7482(3)	66.6 51.1	33.4 48.9
15 $Cd_{58.8}Gd_{41.2}$	1003; 2 months; 1200	α-Cd_2Gd CdGd	a = 4.9432(3), c = 3.4667(3) a = 3.7470(3)	66.4 51.3	33.6 48.7
16 $Cd_{54}Gd_{46}$	950; 3 months; 1200	α-Cd_2Gd CdGd	a = 4.9410(2), c = 3.4715(3) a = 3.7470(5)	66.8 51.3	33.2 48.7
17 $Cd_{45}Gd_{55}$	850; 3 months; 1200	CdGd β-Gd	a = 3.7573(5) -	49.3 21.2	50.7 78.8
18 $Cd_{40}Gd_{60}$	700; 2 months; 1200	CdGd α-Gd	a = 3.7596(3) a = 3.642(3), c = 5.7602(8)	49.5 3.0	50.5 97.0
19 $Cd_{40}Gd_{60}$	800; 3 months; 1200	CdGd β-Gd	a = 3.7561(4) -	49.5 20.5	50.5 79.5
20 $Cd_{40}Gd_{60}$	900; 2 months; 1200	CdGd β-Gd	a = 3.7554(3) -	49.1 22.6	50.9 77.4
21 $Cd_{35}Gd_{65}$	650; 3 months; 1200	CdGd α-Gd	*too ductile*	49.5 2.8	50.5 97.2
22 $Cd_{30}Gd_{70}$	600; 3 months; 1200	CdGd α-Gd	*too ductile*	49.8 1.9	50.2 98.1
23 $Cd_{25}Gd_{75}$	850; 3 months; 1200	CdGd β-Gd	*too ductile*	49.5 21.2	50.5 78.8
24 $Cd_{22}Gd_{78}$	750; 3 months; 1200	CdGd β-Gd	*too ductile*	49.8 19.1	50.2 80.9
25 $Cd_{17}Gd_{83}$	900; 3 months; 1200	β-Gd	*too ductile*	17.3	82.7

26 $Cd_{10}Gd_{90}$	800; 2 months; 1200	β-Gd α-Gd	*too ductile*	16.9 4.3	83.1 95.7
27 $Cd_{10}Gd_{90}$	900; 2 months; 1200	β-Gd α-Gd	*too ductile*	-[c] 4.4	-[c] 95.6

[a] Sample not in equilibrium; EDX data of $Cd_{45}Gd_{11}$ and $Cd_{58}Gd_{13}$ could not be separated, see 3.2.

[b] Sample, taken from isopiestic measurements [13], was too brittle to prepare for EDX

[c] Microstructure of the respective phase was too fine to measure accurately with EDX

Table 3: Thermal effects of selected samples determined with DTA

Sample	Nominal comp. (at.%)	Annealing temperature (°C)	Heating (°C)				Cooling (°C)
			Invariant effects	Other effects		Liquidus	Liquidus
1	$Cd_{98}Gd_2$	300	319			-	526
2	$Cd_{90}Gd_{10}$	300	321			723	700
3	$Cd_{83.5}Gd_{16.7}$	700	730			798	789
6	$Cd_{80.6}Gd_{19.4}$	700	808			813	806
7	$Cd_{79}Gd_{21}$	750	808			814	807
8	$Cd_{78}Gd_{22}$	700	808	822		841	831
9	$Cd_{73}Gd_{27}$	750	819			990	945
10	$Cd_{71.2}Gd_{28.8}$	700	821			986	969
11	$Cd_{69}Gd_{31}$	750	816	[a]		991	988
12,13	$Cd_{63}Gd_{37}$	750, 950	985			1055	-
14,15	$Cd_{58.8}Gd_{41.2}$	900, 1003	988	998		1093	1068
16	$Cd_{54}Gd_{46}$	950	984	[b]		1128	1036
17	$Cd_{45}Gd_{55}$	850	887			1133	1125
18,19,20	$Cd_{40}Gd_{60}$	700, 800, 900	746	900		1097	1096
21	$Cd_{35}Gd_{65}$	650	746	[b]		1047	1042
22	$Cd_{30}Gd_{70}$	600	745	898		967	966
23	$Cd_{25}Gd_{75}$	850	[b]			936	913
24	$Cd_{22}Gd_{78}$	750	742			976	976
25	$Cd_{17}Gd_{83}$	900	746		782 931	1071	1062
26,27	$Cd_{10}Gd_{90}$	800, 900	746		942 1057	1202	1202
28	$Cd_{96}Gd_4$	300	320			639	578
29	$Cd_{95}Gd_5$	300	320			660	658
30	$Cd_{92}Gd_8$	300	318			707	686

31	$Cd_{88.7}Gd_{11.3}$	350	465				727		727
32	$Cd_{77.6}Gd_{22.4}$	700	810	821			840		811
33	$Cd_{50}Gd_{50}$	750					1147		1132
34	$Cd_{16}Gd_{84}$	900	745		795	942	1080		1080
35	$Cd_{15}Gd_{85}$	700	746		784	945	1081		1081
36	Cd_6Gd_{94}	700	743				1233		1233
37	Cd_3Gd_{97}	700					1282		1280

[a] DTA curve shows an invariant effect in the cooling curve probably caused by the polymorphic transformation of Cd_2Gd

[b] The onset could not be evaluated due to an abnormal peak shape; invariant effects can be clearly seen in the cooling curves

Tab. 4: Estimated phase boundaries of Cd-Gd phases at 500 °C (EDX) together with corresponding melting or decomposition temperatures averaged from DTA results

Phase	Phase boundaries (at.% Cd)	Melting or decomposition temperatures (°C)
"Cd_8Gd"	88.7 (line compound)	465
Cd_6Gd	84.8 – 85.7	730
$Cd_{58}Gd_{13}$	see text	
$Cd_{45}Gd_{11}$	79.6 – 80.8	808
Cd_3Gd	75.0 (line compound)	819
Cd_2Gd	65.8 – 67.1	998 *
CdGd	49.8 – 50.9	1147

* Cd_2Gd transforms into a high-temperature modification at 986 °C

Table 5: Invariant reactions in the system Cd-Gd derived from a combination of all present results

Reaction	*T* / °C	Phase compositions (at.% Cd)			Reaction type
$L \rightleftarrows Cd + Cd_8Gd$	320 ± 2	99.8 [a]	~100	88.7	degenerate eutectic
$L + Cd_6Gd \rightleftarrows Cd_8Gd$	465 ± 2	99.0 [a]	85.7	88.7	peritectic
$L + Cd_{45}Gd_{11} \rightleftarrows Cd_6Gd$	730 ± 2	88.2	81.7	85.7	peritectic
$Cd_6Gd + Cd_{45}Gd_{11} \rightleftarrows Cd_{58}Gd_{13}$	[b]				probably peritectoid
$L + Cd_3Gd \rightleftarrows Cd_{45}Gd_{11}$	808 ± 2	81.5	75.0	80.2	peritectic
$L + \alpha\text{-}Cd_2Gd \rightleftarrows Cd_3Gd$	819 ± 3	79.0	67.1	75.0	peritectic
$L + CdGd \rightleftarrows \beta\text{-}Cd_2Gd$	998 ± 4	68.3	51.2	66.1	peritectic
$\alpha\text{-}Cd_2Gd \rightleftarrows \beta\text{-}Cd_2Gd$	986 ± 3				polymorphic transformation
$CdGd \rightleftarrows L$	1147 ± 5		50.0		congruent melting
$L \rightleftarrows CdGd + \beta\text{-}Gd$	895 ± 5	26.5	49.0	22.6	eutectic
$\beta\text{-}Gd \rightleftarrows CdGd + \alpha\text{-}Gd$	745 ± 4	19.1	49.6	4.6	eutectoid

[a] Solubility values were taken from Johnson et al. [17]

[b] Isothermal reaction temperature could not be defined according to the present results, compare 3.2.

Journal of Alloys and Compounds (2014), in print

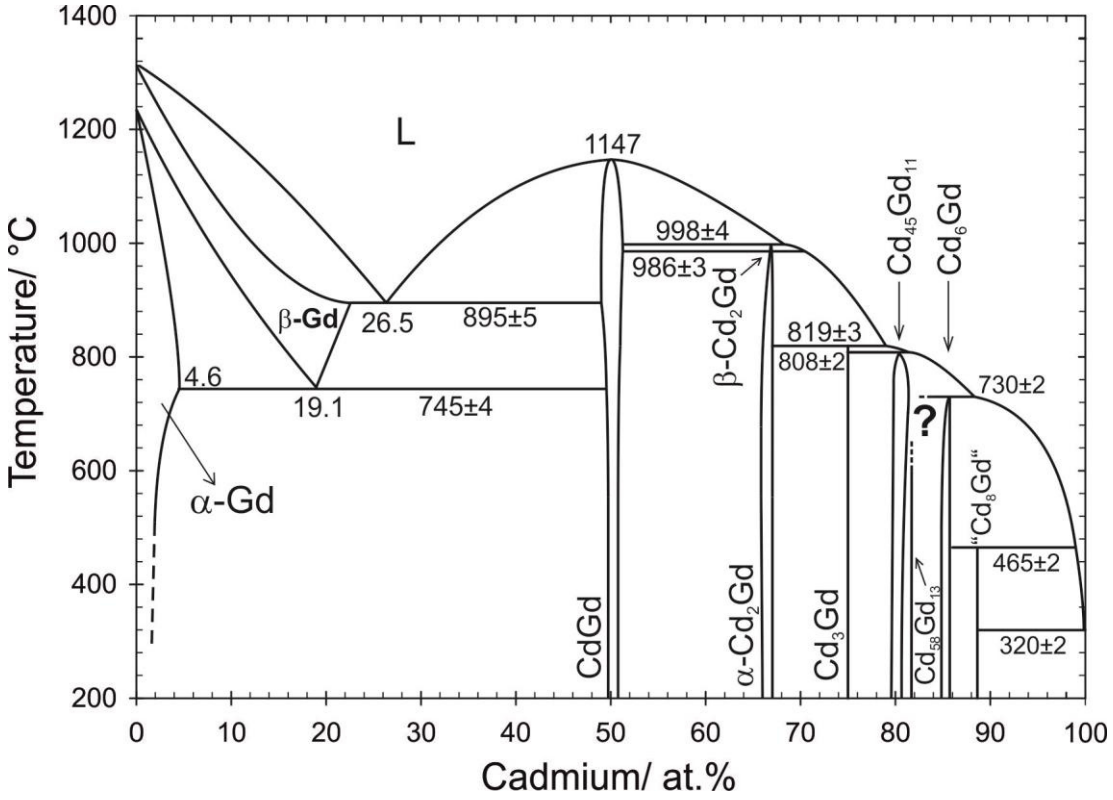

Fig.1: Cd-Gd phase diagram according to the present results. The solubility of Gd in liquid Cd between 324 and 500 °C was taken from Johnson [17]

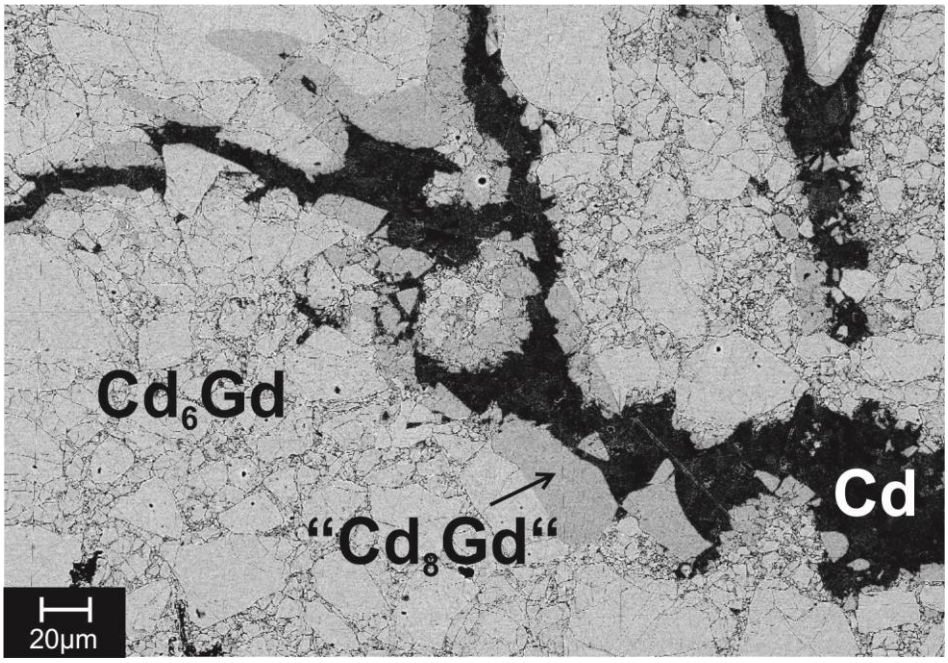

Fig.2: Microstructure (BSE image) of an alloy with the nominal composition $Cd_{90}Gd_{10}$ (No. 2, Table 2)

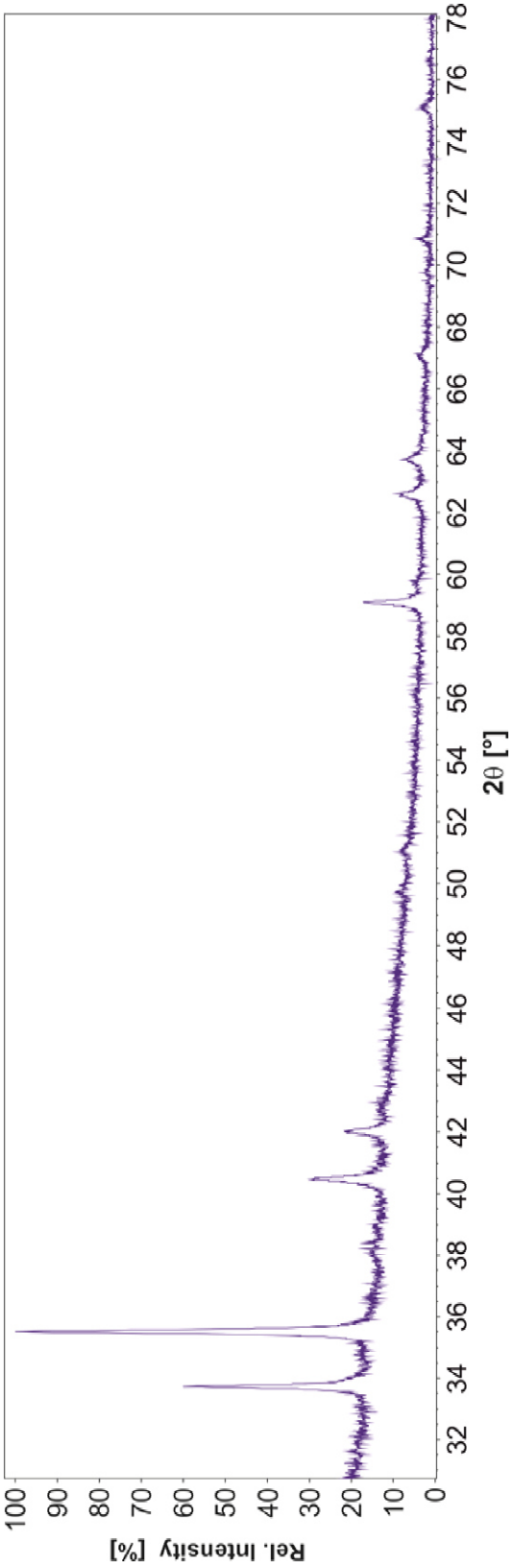

Fig.3: Powder-XRD pattern of a single-phase alloy with the nominal composition $Cd_{88.7}Gd_{11.3}$ which corresponds to "Cd_8Gd"

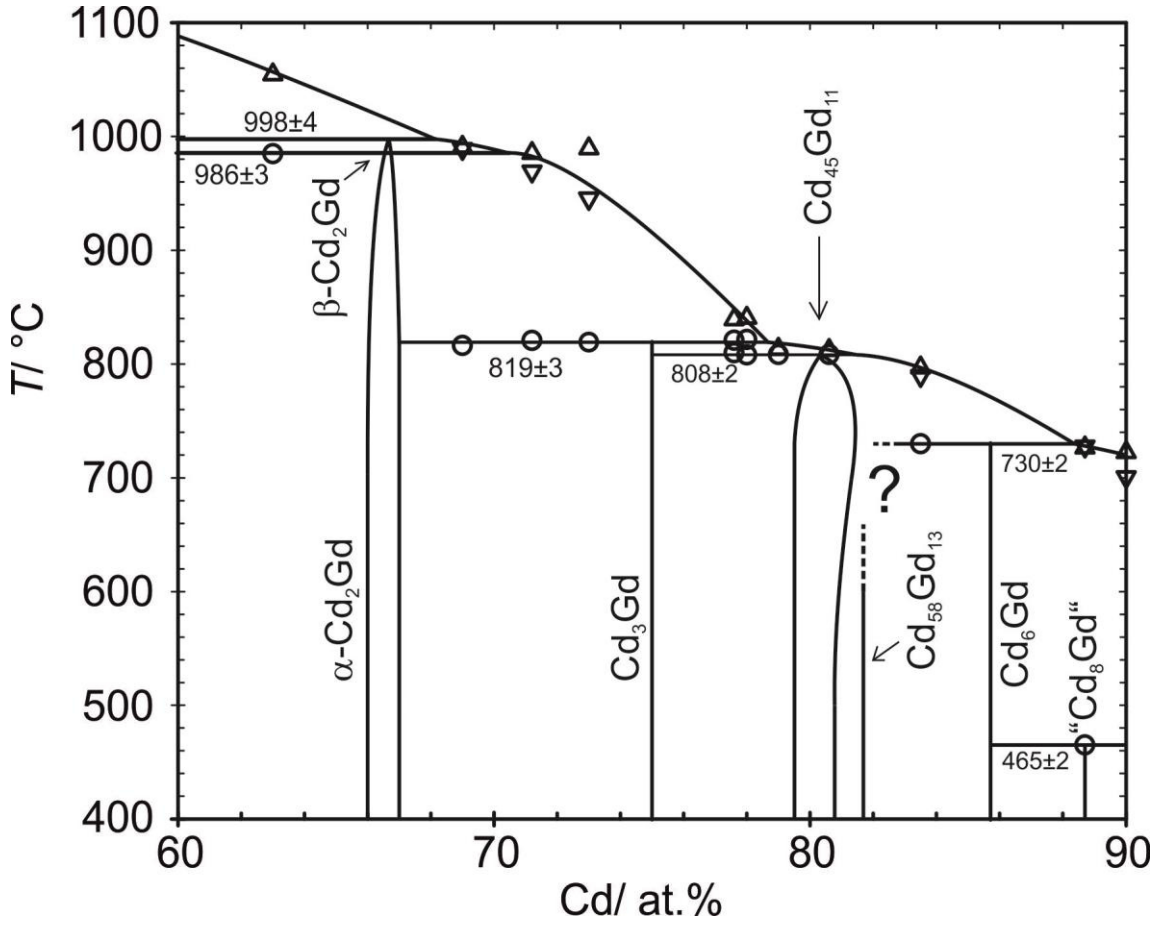

Fig.4: Partial phase diagram of Cd-Gd between 60 and 90 at.% Cd. Large circles: invariant thermal effects. Triangles up: liquidus on heating. Triangles down: liquidus on cooling

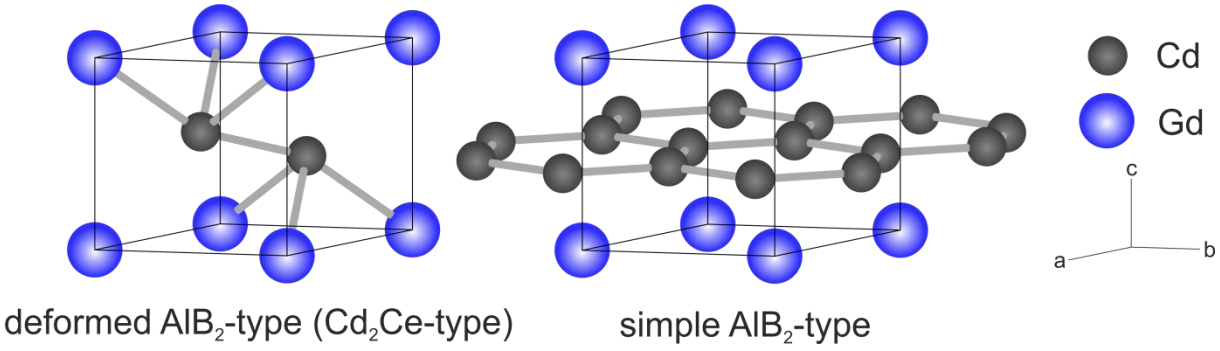

Fig.5: Comparison of the deformed (Cd_2Ce-type, $P\bar{3}m1$) and the simple AlB_2-type (*P6/mmm*) structure

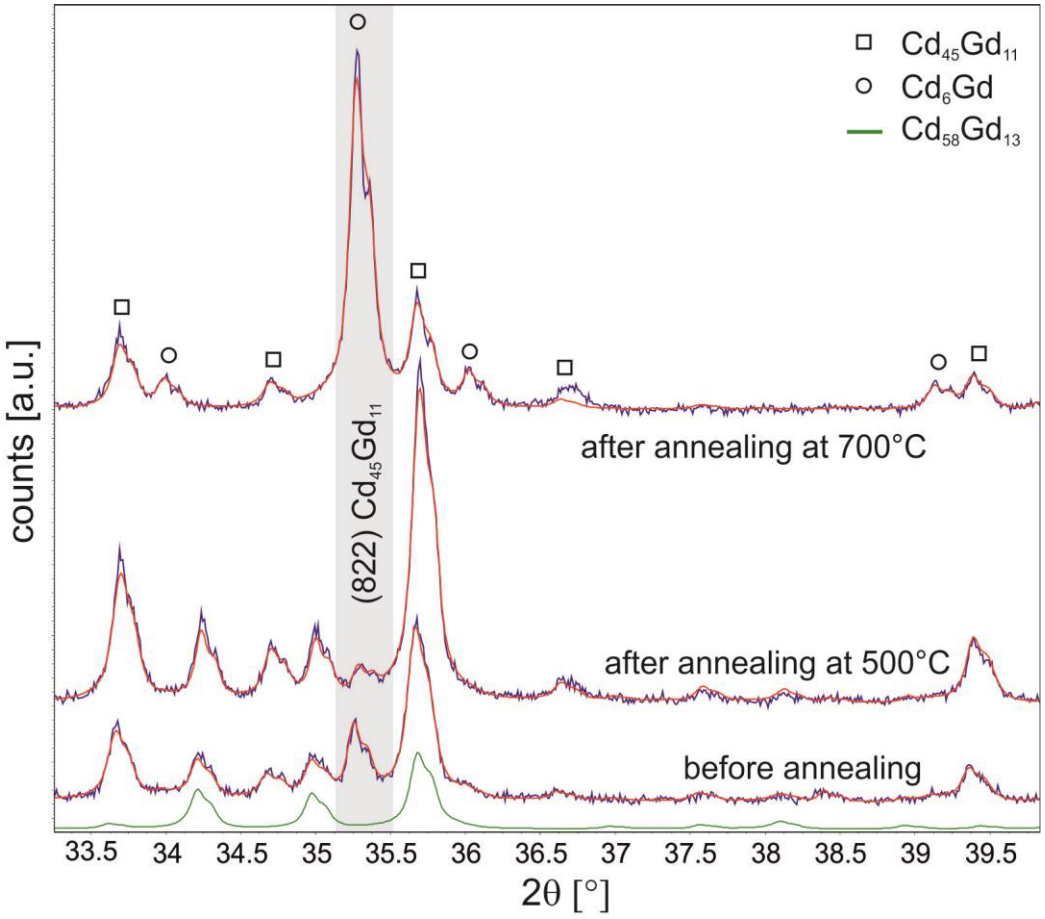

Fig.6: Powder-XRD patterns of alloys, with the nominal composition $Cd_{82.3}Gd_{17.7}$, before as well as after annealing at 500 and 700 °C. Reflex (822) indicates the relative increase and decrease of $Cd_{45}Gd_{11}$

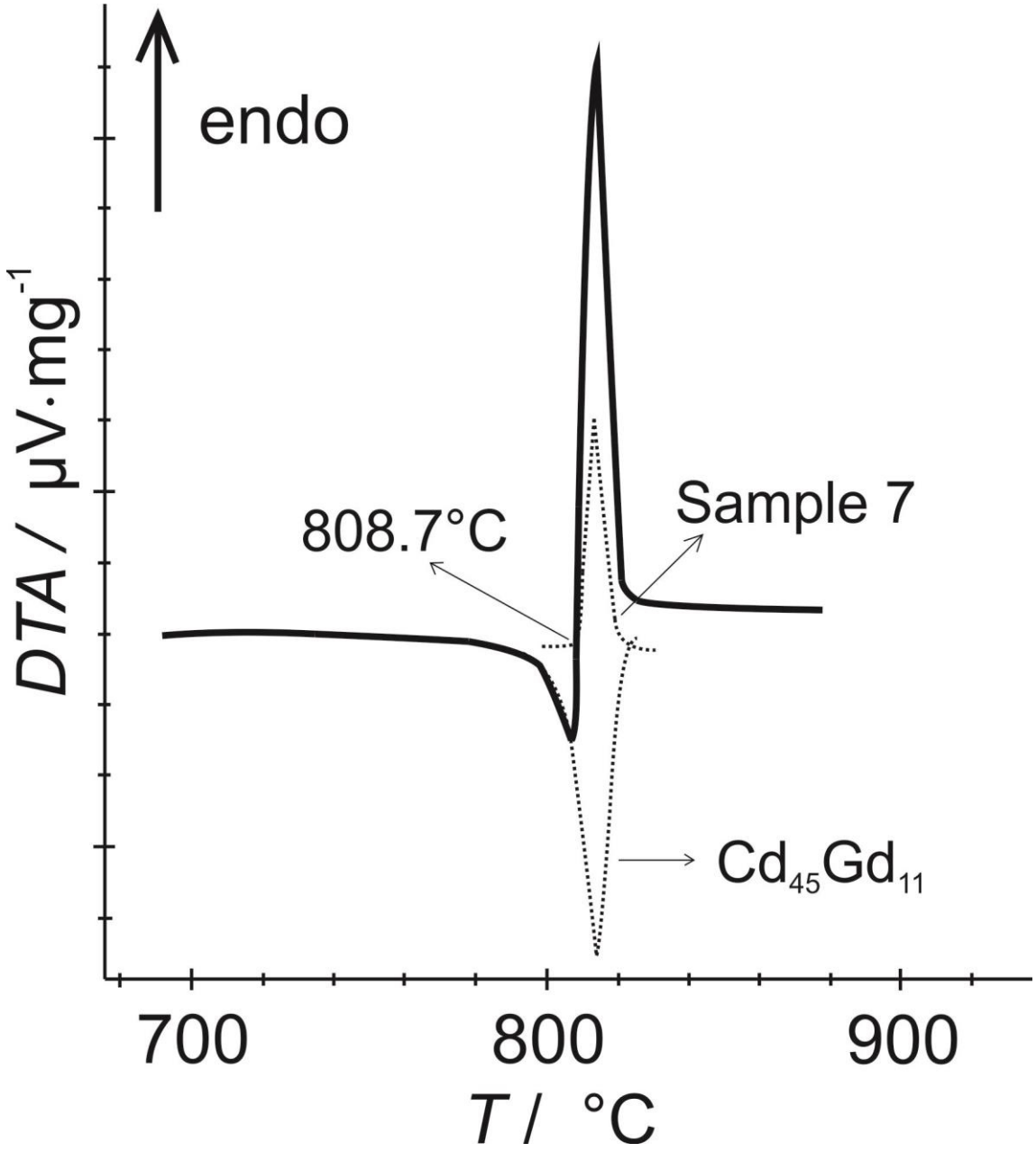

Fig.7: DTA curve of sample 7 against pure $Cd_{45}Gd_{11}$ as reference. Corresponding DTA results from sample 7 and $Cd_{45}Gd_{11}$ against NIST standard sapphire as reference are shown as dotted curves for comparison

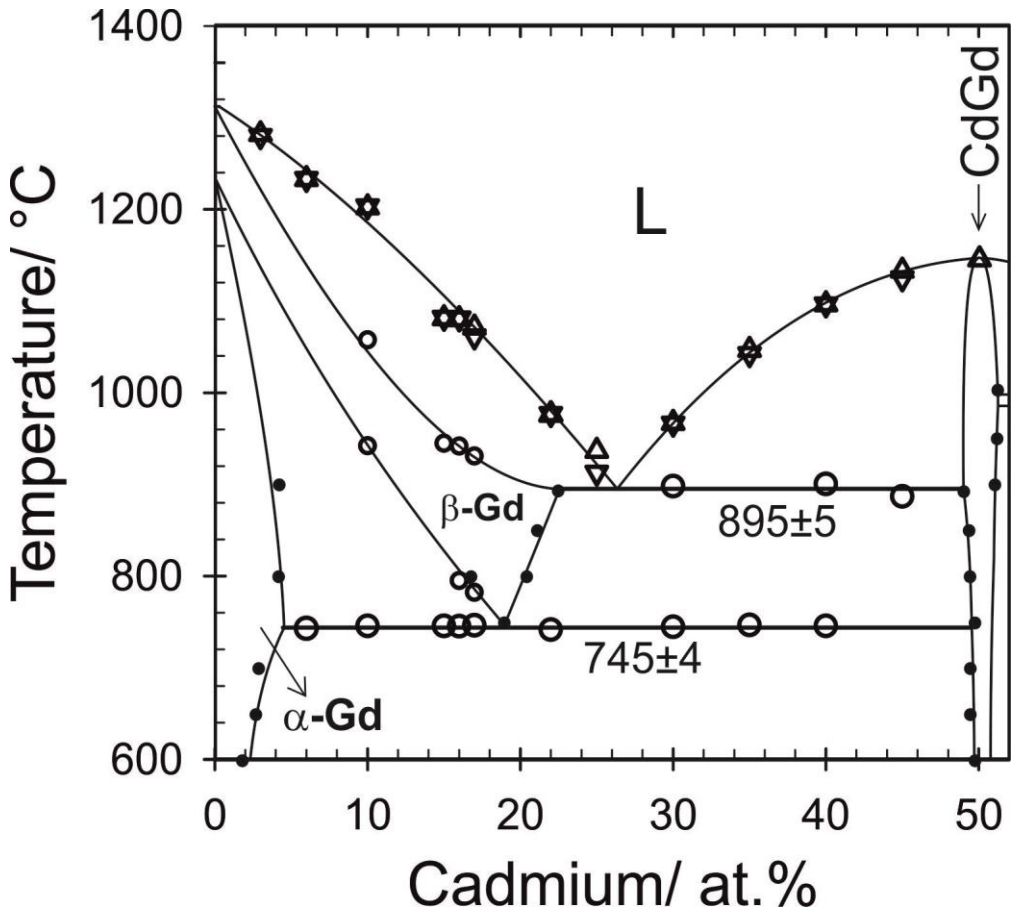

Fig.8: Partial phase diagram of Cd-Gd between 0 and 52 at.% Cd. Large circles: invariant thermal effects. Small open circles: non-invariant effects. Triangles up: liquidus on heating. Triangles down: liquidus on cooling. Small filled circles: EDX data

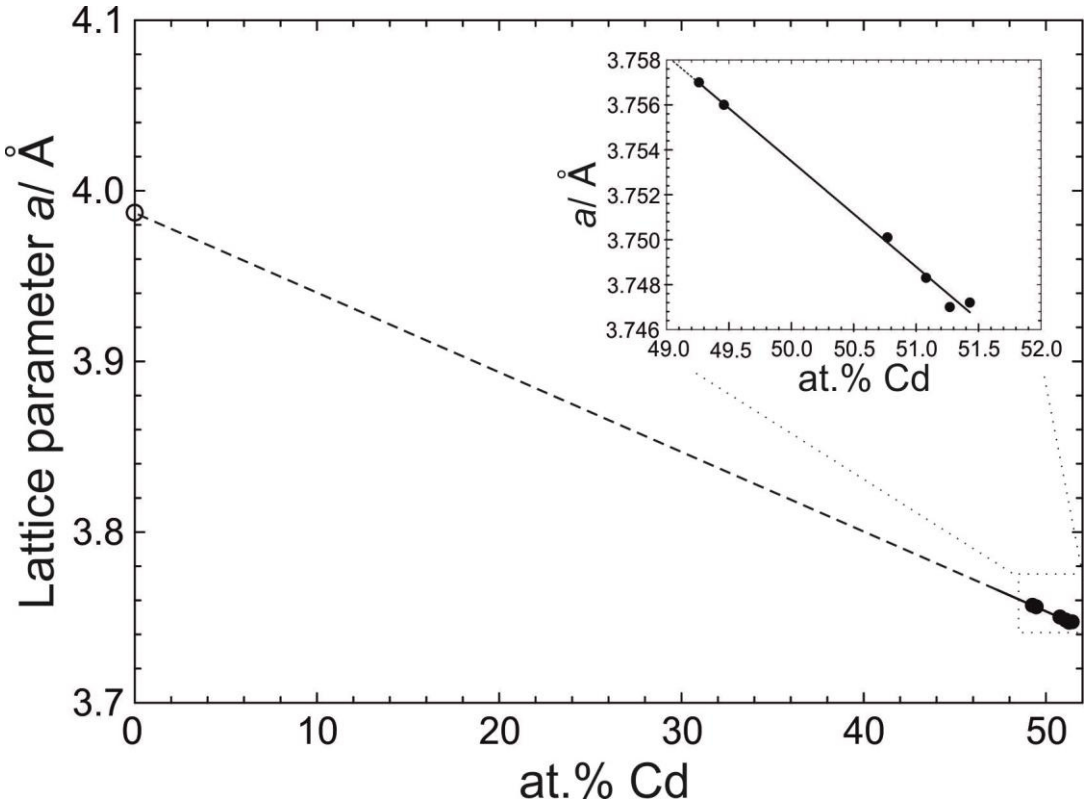

Fig. 9: Lattice parameter *a* against at.% Cd for CdGd; filled circles: sample compositions defined by EDX, see section 3.3

IV. Conclusive discussion

The present study was performed in the course of a stand-alone project supported by the Austrian Science Fund (FWF) under the project No. P 23270-N19. It was also part of the Scientific-Technical Cooperation program between Austria and India which was provided by the Austrian Agency for International Cooperation in Education and Research (Project No. IN 05/2011).

It was the aim of the project to provide a detailed knowledge of thermodynamic properties as well as phase diagrams of Cd-RE (RE...Ce, Pr, Nd, Gd) systems. Corresponding phase diagram data and thermodynamic descriptions of all systems have been published in peer reviewed journals; *cf.* [1-7]. Another two publications are currently in preparation [8,9].

All phase diagrams were studied in detail using conventional isothermal and dynamic methods. Concerning the systems Cd-Ce and Cd-Gd, complete versions of the phase diagrams were previously reported by Canepa et al. [10] and Bruzzone et al. [11]. Nevertheless, a lack of information was found in both studies and re-investigations were deemed necessary. In contrast, the phase diagram information available for Cd-Nd and Cd-Pr were rather limited and only rudimentary versions were found in literature [12,13].

Concerning the Cd-Ce phase diagram, Canepa et al. [10] exclusively used DTA for the determination of homogeneity ranges and the corresponding reaction scheme. For their evaluation the authors used thermal effects which were observed on cooling. As long as cooling experiments can be affected by supercooling effects, these data are usually not reliable. Especially, in the equilibrium range of the high-temperature compound $Cd_{17}Ce_2$, the reaction sequence could not be clearly determined. In the present study [8], the complete composition and temperature range of the Cd-Ce phase diagram was re-investigated using well equilibrated samples. EDX measurements indicated significant solid solubility in most compounds. Based on the EDS and DTA results, the homogeneity ranges of the solid solutions of Cd in the low- and high-temperature modifications of Ce could be well determined. In comparison to Canepa et al. [10], transition reaction temperatures were found to be systematically higher. Furthermore a single-phase sample of $Cd_{17}Ce_2$ was prepared in order to clarify formation and decomposition temperatures of this phase. In addition, a suitable single crystal served for a structural analysis of $Cd_{17}Ce_2$.

The previous evaluation of the Cd-Gd phase diagram was based on a detailed investigation of equilibrated samples [11]. However, discrepancies were found in some parts of the diagram. The solubility of Gd in liquid Cd did not correspond to the results obtained previously by Johnson [14]. Moreover, it was observed that all intermetallic compounds except CdGd are formed through a cascade of incongruent reactions. It is indicated that especially $Cd_{58}Gd_{13}$ and $Cd_{45}Gd_{11}$ decompose within a rather small temperature interval. Compounds with this stoichiometry were found to be in thermodynamic equilibrium in a number of Cd-RE phase diagrams but Cd-Gd is the only system were these phases are rather similar in respect to their relative stability. A distinct investigation of the reaction sequence in the corresponding temperature range is missing. According to the present results [2], $Cd_{58}Gd_{13}$ is most probably decomposing in terms of a peritectoid reaction and not peritectically as indicated by Bruzzone et al. [11]. In addition, homogeneity ranges were determined for all phases and significant solid solubility was obtained for several compounds. In the very Cd-rich part of the phase diagram a new compound with a stoichiometry close to "Cd_8Gd" was found to exist and characterised by EDS, powder-XRD and DTA. Attempts are still continuing to synthesise a suitable single crystal for a structural analysis.

The previously known phase diagram versions of Cd-Nd and Cd-Pr were mainly based on the work of Johnson et al. [15]. Although less information was available about phase equilibria and transition reactions, all equilibrium compounds were still determined and discussed extensively in literature. In the current studies [1,3], homogeneity ranges of all phases were determined at various temperatures and complete reaction schemes were derived. The solid solubility of Cd in the low- and high-temperature modifications of Nd and Pr was extensively investigated by EDS and DTA. In addition, dilatometric measurements were performed in case of Cd-Nd which fit well with the latter results. Structural analyses were employed for a few compounds in order to clarify open questions. A structural transformation of Cd_2RE was obtained in both systems similar to the situation reported for Cd_2Gd [11]. However, several attempts to quench the high-temperature modification β-Cd_2RE (RE...Pr, Nd, Gd) were not successful.

Non-isothermal isopiestic vapour pressure measurements were carried out in all systems. From the respective equilibrium curves, phase boundaries could be derived for most phases.

With no exception, these data agreed well with data obtained from EDS. Respective Cd vapour pressures were used to calculate thermodynamic activities of Cd as a function of temperature and composition. Using these results, partial molar enthalpies of mixing of Cd were derived and Cd activities were converted to a well defined temperature. From the Cd activities as a function of composition at one well defined temperature, relative stabilities of several phases could be estimated. Usually, there is a marked difference in the activity values of adjacent two-phase fields of a phase which is relatively stable. Especially, strong variations of the activity values were found within the homogeneity ranges of $Cd_{58}Ce_{13}$ [6] and $Cd_{58}Pr_{13}$ [4], and as expected these phases show congruent formation behaviour [1,8]. As described in [2], the formation reaction of $Cd_{58}Gd_{13}$ could not be exactly determined but a decomposition temperature much lower than that of $Cd_{45}Gd_{11}$ was indicated according to the results. In this case it would be expected that a distinct difference in stability of both phases should be also indicated by the corresponding activity data. In fact, thermodynamic activities vary strongly within the homogeneity range of $Cd_{45}Gd_{11}$ and only very little in $Cd_{58}Gd_{13}$ [5].

Moreover, Gibbs-Duhem integrations were employed using RE activity values, which were taken from literature, as starting values. Integral Gibbs energies as a function of composition could be derived for all systems and Gibbs energies of formation at the exact stoichiometric compositions of respective compounds were listed. The corresponding values were in perfect agreement with data found in literature.

Table 2: Gibbs energies of formation in kJ/mol(at) of various CdRE intermetallic compounds, referred to Cd(l) and RE(s)

	CdRE compound						
RE	CdRE	Cd_2RE	Cd_3RE	$Cd_{45}RE_{11}$	$Cd_{58}RE_{13}$	Cd_6RE	T/ K
La	-	-	-	-	-27.0	-	800
Ce	-36.9	-34.9	-29.6	-	-24.7	-19.9	823
Pr	-35.0	-33.8	-28.7	-24.8	-23.5	-18.8	823
Gd	-34.6	-30.0	-24.8*	-21.1	-19.9	-	773

*crystal structure is different compared to the others

The mutual comparison of Gibbs energies of formation of isomorphous Cd-RE (RE...La, Ce, Pr, Gd [4-6,16]) compounds exhibits systematically lower absolute (less negative) values

for compounds containing REs with high atomic numbers, *cf.* Table 2. According to the well known “lanthanide contraction”, the cell volume of isomorphous Cd-RE compounds steadily decreases with an increase of the atomic number of the respective REs.

In an early study, Tao et al. [17] calculated enthalpies of formation of 344 Mg-RE compounds using first-principle calculations. Similarly, it was observed that the stability of isomorphous Mg-RE compounds decreases steadily with an increase of the atomic number of the respective RE. No further discussion was given on that behaviour. However, the authors explained that within the three different structure families MgRE, Mg_2RE and Mg_3RE, the cell volume has a decisive influence onto phase stability. Accordingly, among the same stoichiometric compounds within a structure family, small cell volumes go along with stronger bonding in the system and hence higher stability. Right now, the reason why Gibbs energies of formation within a certain structure family, as it can be observed from the present results, become absolutely lower (less negative) with an increase of the ionic radii of the respective RE is not clear.

In the course of a CALPHAD-type optimisation of the Cd-Pr system respective data obtained from isopiestic vapour pressure measurements and standard enthalpies of formation, determined by calorimetry, were consulted to reproduce the experimentally determined phase diagram [7]. A quite good agreement between the optimised data and all viable data from literature was observed. It was pointed out that especially data from non-isothermal isopiestic vapour pressure measurements can serve as a reliable source of thermodynamic data suitable for thermodynamic modelling. Consistent descriptions of all systems according to the CALPHAD approach, would certainly contribute to a reliable Cd-RE database which provides fundamental thermodynamic and phase diagram data required for pyrometallurgical reprocessing of spent nuclear fuels.

References

[1] T. L. Reichmann, H. S. Effenberger, H. Ipser. Experimental investigation of the Cd-Pr phase diagram. *PlosOne* (2014), 9(4): 1-14.

[2] T. L. Reichmann, H. Ipser. Reinvestigation of the Cd-Gd phase diagram. *J. Alloys Comp.* (2014), in print.

[3] B. Skołyszewska-Kühberger, T. L. Reichmann, H. Ipser. Phase equilibria in the neodymium-cadmium binary system. *J. Alloys Comp.* (2014), 606: 242-248.

[4] T. L. Reichmann, H. Ipser. Thermochemical Investigations in the System Cadmium-Praseodymium Relevant for Pyrometallurgical Fuel Reprocessing. *Metall. Mater. Trans. A* (2014), 45(3): 1171-1180.

[5] T. L. Reichmann, R. Ganesan, H. Ipser. Thermochemical investigations in the system Cd-Gd. *J. Alloys Comp.* (2014), 610: 676-683.

[6] B. Skołyszewska-Kühberger, T. L. Reichmann, R. Ganesan, H. Ipser. Thermodynamic study of the cerium-cadmium system. *CALPHAD* (2014), 44: 14-20.

[7] T. L. Reichmann, K. W. Richter, H. Ipser. Enthalpies of formation of Cd-Pr intermetallic compounds and thermodynamic assessment of the Cd-Pr system. *CALPHAD* (2014), 47: 56-62.

[8] B. Skołyszewska-Kühberger, T. L. Reichmann, H. S. Effenberger H. Ipser. A re-investigation of the cerium-cadmium phase diagram and a structural analysis of the high-temperature phase Ce_2Cd_{17}. *Publication in preparation*.

[9] B. Skołyszewska-Kühberger, H. Ipser. Thermodynamic study of the neodymium-cadmium system. *Publication in preparation*.

[10] F. Canepa, G. A. Costa, E. A. Franceschi. The phase diagram of the cerium-cadmium system. *Lan. and Act. Res.* (1985), 1(1): 41-47.

[11] G. Bruzzone, M. L. Fornasini, F. Merlo. The Gadolinium-Cadmium System. *J. Less-Common Met*. (1971), 25: 295-301.

[12] K. A. Gschneidner Jr, F. W. Calderwood. The Cd-Nd system. *Bull. Alloy Phase Diag.* (1988), 9: 130-132.

[13] K. A. Gschneidner Jr, F. W. Calderwood. The Cd-Pr system. *Bull. Alloy Phase Diag.* (1988), 9: 128-130.

[14] I. Johnson. Solubility of the Rare-Earth Metals in Liquid Cadmium. *2nd Proc. Conf. Rare Earth Res.* (1962), 125-131.

[15] I. Johnson, K. E. Anderson, R. A. Blomquist. Partial Constitutional Diagrams for Cd-La, Cd-Ce, Cd-Pr, Cd-Nd and Cd-Sm Systems. *Trans. ASM* (1966), 59: 352-355.

[16] K. W. Richter, S. Besana, G. Borzone, H. Ipser. Thermodynamic investigations in the lanthanum-cadmium system. *J. Alloys Comp.* (2004), 365: 181-187.

[17] X. Tao, Y. Ouyang, H. Liu, Y. Feng, Y. Du, Y. He, Z. Jin. Phase stability of magnesium-rare earth binary systems from first-principles calculations. *J. Alloys Comp.* (2011), 509: 6899-6907.

V. Summary

The current study provides a complete investigation of the Cd-Gd and Cd-Pr phase diagram as well as structural analysis of several intermetallic compounds. For the evaluation of phase equlibria and transition reaction temperatures, a combination of powder-XRD, EDS and DTA was used. In addition, an isopiestic vapour pressure method was applied to obtain thermodynamic activities in both systems. Standard enthalpies of formation of several Cd-Pr alloys were measured with solution and reaction calorimetry. Based on the data obtained from thermodynamic measurements, a CALPHAD-type (Computer Coupling of Phase Diagrams and Thermochemistry) optimisation was made for the system Cd-Pr.

Actually, phase diagram and thermodynamic data of Cd-RE systems are of crucial importance for pyrochemical reprocessing of spent nuclear fuels. Accordingly, electro-transport and reductive extraction is applied to separate actinides and REs from high-level radioactive waste. In this type of non-aqueous method, liquid Cd is used as extractant. In fact, the extraction behaviour of REs strongly depends on the thermodynamic stability of the respective Cd-RE compounds. Therefore, a detailed knowledge of the respective Cd-RE phase diagrams as well as thermodynamic properties is necessary.

Concerning the Cd-Pr system, the homogeneity ranges of the altogether seven intermetallic compounds and of the solid solution of Cd in Pr were derived. The solid solubility of Cd in β-Pr could be determined reliably and was given as 22.1 at.% Cd. The addition of Cd stabilised the high-temperature modification β-Pr down to 450 °C where it decomposed in terms of an eutectoid reaction. Moreover, the DTA results indicated a phase transformation of Cd_2Pr into a high-temperature modification between 893 and 930 °C. The low-temperature modification of Cd_2Pr was examined by single crystal X-ray diffraction and determined to crystallise in the simple AlB_2-type. Furthermore, single crystal XRD was employed to explain the defect mechanism in Cd_3Pr. Due to reduction in symmetry of one Cd position and the resulting introduction of ordered vacancies the R-values could be decreased noticeable.

The complete Cd-Gd phase diagram was reinvestigated. Based on the present results, the homogeneity ranges of the altogether seven intermetallic compounds were determined and the limited solid solubility of Cd in the low- and high-temperature modification of Gd were

determined as 4.6 and 22.6 at.%, respectively. Moreover, a new compound was found with a stoichiometry close to Cd_8Gd, decomposing peritectically at 465 °C. It was obtained that the solubility of Cd in $Cd_{45}Gd_{11}$ increases rather extensively before the phase decomposes at 808 °C. The compound $Cd_{58}Gd_{13}$ is apparently decomposing at any temperature below 700 °C. A partial substitution of Cd by Gd according to $Cd_{1-x}Gd_{1+x}$, $x < 0.02$, was observed in CdGd which adopts the CsCl-structure.

Seven isopiestic runs were carried out in each system to measure vapour pressures of Cd in Cd-Gd and Cd-Pr. Concerning Cd-Gd, $Cd_{45}Gd_{11}$ was used as a master compound and equilibrated with Cd vapour at constant Cd vapour pressures between 2 and 137 mbar, respectively. In the case of Cd-Pr, pure Pr was equilibrated with Cd vapour pressures between 7 and 101 mbar. From the primary results, equilibrium curves were drawn and thermodynamic activity values of Cd were calculated as a function of composition and temperature. An adapted Gibbs-Helmholtz equation was applied to convert thermodynamic activity values of Cd to a common average sample temperature of 773 (Cd-Gd) and 823 K (Cd-Pr), respectively. RE activity values from literature were taken as starting values for Gibbs-Duhem integrations. From these data integral Gibbs energies were calculated as a function of composition and Gibbs energies of formation at exact stoichiometric compositions of several intermetallic compounds were listed.

Furthermore, standard enthalpies of formation of the four intermetallic compounds Cd_6Pr, $Cd_{58}Pr_{13}$, Cd_3Pr and Cd_2Pr were measured by calorimetry. Solution calorimetry was employed for all four compounds and the enthalpy of formation of stoichiometric $Cd_{58}Pr_{13}$ was also measured by direct reaction calorimetry. The experimental values for $Cd_{58}Pr_{13}$ from the two different methods were in good agreement with each other, and an average value of -35±2 $kJ \cdot mol(at)^{-1}$ was calculated. All present thermodynamic data from calorimetric and isopiestic measurements served as input data for a thermodynamic assessment of the Cd-Pr phase diagram. The complete composition range including all invariant reactions could be calculated. A temperature dependent contribution to the individual Gibbs energy was introduced for all phases to guarantee a consistent description of all data.

Zusammenfassung

Im Zuge dieser Arbeit wurden die Phasendiagramme Cd-Gd und Cd-Pr detailliert untersucht und sämtliche intermetallische Phasen strukturell charakterisiert. Phasengleichgewichte und Reaktionstemperaturen wurden mittels einer Kombination aus Röntgenpulverdiffraktometrie (Pulver-XRD), energiedispersiver Röntgenspektroskopie (EDS) und Differenzthermoanalyse (DTA) bestimmt und ausgewertet. Zusätzlich wurde eine isopiestische Dampfdruckmethode verwendet und aus den gemessenen Dampfdrücken thermodynamische Aktivitäten bestimmt. Desweiteren wurden Standardbildungsenthalpien mithilfe von Lösungskalorimetrie bzw. Reaktionskalorimetrie bestimmt. Auf der Basis aller erhaltenen thermodynamischen Daten wurde anhand der CALPHAD-Methode (Computer Coupling of Phase Diagrams and Thermochemistry) das Phasendiagram Cd-Pr berechnet und sämtliche Daten in Konsistenz gebracht.

Die entsprechenden Phasendiagramme sowie die thermodynamischen Eigenschaften der Cd-SE (SE...Seltene Erden) Systeme sind von größtem Nutzen für die pyro-metallurgische Aufarbeitung von abgebrannten Kernbrennstoffen. Demzufolge werden Actinoide und SE Elemente elektrochemisch mittels Cd aus hoch-radioaktivem Atommüll extrahiert. Das Extraktionsverhalten hängt dabei maßgeblich von der thermodynamischen Stabilität der Cd-SE Verbindungen ab. Die genaue Kenntnis der entsprechenden Phasendiagramme sowie der thermodynamischen Eigenschaften der jeweiligen Verbindungen ist notwendig um bestimmte Prozessparameter adäquat steuern zu können.

Das Cd-Pr Phasendiagramm wurde im gesamten Konzentrations- und Temperaturebereich anhand von Gleichgewichtsproben untersucht. Die Homogenitätsbereiche sämtlicher Phasen wurden mittels EDS und DTA bestimmt. Es konnte festgestellt werden, dass sich bis zu 22.1 at.% Cd in festem β-Pr lösen. Dadurch wird die Hochtemperaturphase bis zu einer Temperatur von 450 °C stabilisiert bei der sie eutektoidisch zerfällt. Desweiteren haben DTA Ergebnisse angedeutet, dass Cd_2Pr bei Temperaturen zwischen 893 und 930 °C in eine Hochtemperatur-Modifikation übergeht. Einkristallmessungen der Tieftemperaturphase Cd_2Pr ergaben, dass diese Phase im einfachen AlB_2-Typ kristallisiert. Der Defektmechanismus in Cd_3Pr wurde ebenfalls mittels Einkristallmessungen untersucht. Strukturverfeinerungen

ergaben, dass Cd_3Pr in einer unsymmetrischeren Raumgruppe kristallisiert als bisher angenommen.

In gleicher Weise wurde das Cd-Gd Phasendiagramm neu untersucht und mit bereits bekannten Daten verglichen. EDX Messungen ergaben für sämtliche intermetallische Phasen signifikante Phasenbreiten. Die maximalen Löslichkeiten von Cd in der Tief- und Hochtempermodifikation von Gd wurde anhand von DTA und EDS Daten abgeschätzt und betragen 4.6 bzw. 22.6 at.%. Im Cd-reichen Teil des Cd-Gd Phasendiagramms wurde eine neue intermetallische Verbindung mit der stöchiometrischen Zusammensetzung Cd_8Gd gefunden. Anhand von DTA-Ergebnissen konnte eine inkongruente Zersetzungstemperatur von 465 °C bestimmt werden. Die intermetallische Verbindung $Cd_{58}Gd_{13}$ zersetzt sich offenbar unter 700 °C. Eine lineare Abhängigkeit des Gitterparameters mit der Zusammensetzung wurde in CdGd (CsCl-Struktur) festgestellt. Die maximale Löslichkeit von Gd auf dem Cd-Untergitter konnte gemäß $Cd_{1-x}Gd_{1+x}$, $x < 0.02$ verifiziert werden.

Jeweils sieben isopiestische Experimente wurden in den beiden Systemen Cd-Gd und Cd-Pr durchgeführt. Für die Gleichgewichtsmessungen im System Cd-Gd wurde reines $Cd_{45}Gd_{11}$ als Probenmaterial vorgelegt und entsprechend Cd-Dampfdrücke zwischen 2 und 137 mbar eingestellt. Reines Pr wurde für die Dampfdruckmessungen im Cd-Pr System verwendet. Anhand der erhaltenen Daten wurden sogenannte Gleichgewichtskurven, d.h. Isobaren, gezeichnet und die thermodynamischen Aktivitäten als Funktion der Zusammensetzung bzw. der Temperatur berechnet. Mithilfe einer integrierten Form der Gibbs-Helmholtz Gleichung, konnten die thermodynamischen Aktivitäten bei einer durchschnittlichen Probentemperatur von 773 (Cd-Gd) bzw. 823 K (Cd-Pr) berechnet werden. Als Startwerte für Gibbs-Duhem Integrationen dienten SE-Aktivitäten aus der Literatur. Es konnten integrale Gibbs Energien als Funktion der Zusammensetzung bei bestimmten Temperaturen berechnet werden.

Mithilfe von Lösungs- bzw. Reaktionskalorimetrie wurden Standardbildungsenthalpien der vier intermetallischen Verbindungen Cd_6Pr, $Cd_{58}Pr_{13}$, Cd_3Pr and Cd_2Pr bestimmt. Die experimentell gefundenen Werte für die Phase $Cd_{58}Pr_{13}$ passten perfekt überein und ergaben einen Mittelwert von -35±2 $kJ \cdot mol(at)^{-1}$. Auf der Basis aller generierten thermodynamischen Daten, konnte anhand der CALPHAD-Methode das Phasendiagram Cd-Pr reproduziert werden. Temperaturabhängige Beiträge zu den individuellen Gibbs Energien wurden dafür herangezogen.

VI. Appendices

Appendix A: Supplementary material

Enthalpies of formation of Cd-Pr intermetallic compounds and thermodynamic assessment of the Cd-Pr system

T. L. Reichmann, K. W. Richter, S. Delsante, G. Borzone and H. Ipser, *CALPHAD* (2014), 47: 56-62

ThermoCalc data base:

```
$ Database file written 2013-8-21
$ From database: PURE5
ELEMENT /-      ELECTRON_GAS      0.0000E+00  0.0000E+00  0.0000E+00!
ELEMENT VA      VACUUM            0.0000E+00  0.0000E+00  0.0000E+00!
ELEMENT CD      HCP_A3            1.1241E+02  6.2509E+03  5.1798E+01!
ELEMENT PR      DHCP              1.4091E+02  0.0000E+00  0.0000E+00!

FUNCTION GLIQCD         2.98150E+02 -955.025+89.209282*T-22.0442408*T*LN(T)
    -.006273908*T**2-6966*T**(-1); 4.00000E+02 Y
    +21716.884-371.046869*T+53.1313898*T*LN(T)-.115159917*T**2
    +2.8899781E-05*T**3-1271815*T**(-1); 5.94220E+02  Y
    -3252.303+138.251107*T-29.7064*T*LN(T); 1.60000E+03  N !
FUNCTION GFCCCD         2.98150E+02 +GHSERCD#+892.3-.92*T;  1.60000E+03  N !
FUNCTION GBCCCD         2.98150E+02 +GHSERCD#+1000;  1.60000E+03  N !
FUNCTION GHSERCD        2.98150E+02 -7083.469+99.506198*T-22.0442408*T*LN(T)
    -.006273908*T**2-6966*T**(-1);  5.94220E+02  Y
    -20064.971+256.812233*T-45.1611543*T*LN(T)+.008832011*T**2
    -8.99604E-07*T**3+1241290*T**(-1);  1.50000E+03  Y
    -9027.489+148.20548*T-29.7064*T*LN(T);  1.60000E+03  N !
FUNCTION GLIQPR         2.98150E+02  +3848.961-29.099465*T-4.7344931*T*LN(T)
    -.035119723*T**2+5.427467E-06*T**3-207406*T**(-1);  1.06800E+03  Y
    -10539.574+219.508805*T-42.9697*T*LN(T);  3.80000E+03  N !
FUNCTION GBCCPR         2.98150E+02  -2863.651+28.274853*T-13.7470527*T*LN(T)
    -.02284377*T**2+3.542468E-06*T**3-87486*T**(-1);  1.06800E+03  Y
    -11985.919+188.657121*T-38.451*T*LN(T);  1.20400E+03  Y
    +953.224+100.826281*T-26.6824313*T*LN(T)-.004106833*T**2
    +1.76214E-07*T**3-2473024*T**(-1);  3.80000E+03  N !
FUNCTION GHSERPR        2.98150E+02  -18803.379+356.587384*T-68.9176*T*LN(T)
    +.072929*T**2-2.5184333E-05*T**3+507385*T**(-1);  5.00000E+02  Y
    -7246.848+82.427384*T-22.8909*T*LN(T)-.00497126*T**2-1.22951E-06*T**3;
    8.00000E+02  Y
    +95411.023-1073.55111*T+146.764*T*LN(T)-.1288205*T**2
```

```
    +1.5592233E-05*T**3-11588800*T**(-1);  1.06800E+03  Y
    -481663.131+4234.33311*T-606.120311*T*LN(T)+.305181506*T**2
    -3.0994702E-05*T**3+70926840*T**(-1);  1.20400E+03  Y
    -20014.678+227.685155*T-42.9697*T*LN(T);  3.80000E+03  N !
FUNCTION UN_ASS 298.15 0; 300 N !

TYPE_DEFINITION % SEQ *!
DEFINE_SYSTEM_DEFAULT ELEMENT 2 !
DEFAULT_COMMAND DEF_SYS_ELEMENT VA /- !

PHASE LIQUID  %  1  1.0  !
    CONSTITUENT LIQUID  :CD,PR :  !
PARAMETER G(LIQUID,CD;0)  2.98150E+02  +GLIQCD#;  1.60000E+03  N REF3 !
PARAMETER G(LIQUID,PR;0)  2.98150E+02  +GLIQPR#;  3.80000E+03  N REF3 !
PARAMETER G(LIQUID,CD,PR;0) 2.98150E+02  -132020+52*T;  1.60000E+03 N!
PARAMETER G(LIQUID,CD,PR;1) 2.98150E+02  -27000+1*T;  1.60000E+03 N!
PARAMETER G(LIQUID,CD,PR;2) 2.98150E+02 -2000+1*T;  1.60000E+03 N!

TYPE_DEFINITION & GES A_P_D BCC_A2 MAGNETIC  -1.0    4.00000E-01 !
PHASE BCC_A2  %&  2 1   3 !
    CONSTITUENT BCC_A2  :CD,PR : VA :  !
PARAMETER G(BCC_A2,CD:VA;0)  2.98150E+02  +GBCCCD#;  1.60000E+03  N REF5 !
PARAMETER G(BCC_A2,PR:VA;0)  2.98150E+02  +GBCCPR#;  3.80000E+03  N REF3 !
PARAMETER G(BCC_A2,Cd,PR:VA;0)  2.98150E+02  -152571+68*T;  1.60000E+03 N!
PARAMETER G(BCC_A2,Cd,PR:VA;1)  2.98150E+02  -54630+23*T;  1.60000E+03 N!

PHASE BCT_A5  %  1  1.0  !
    CONSTITUENT BCT_A5  :CD :  !
PARAMETER G(BCT_A5,CD;0)  2.98150E+02  +GHSERCD#+5000;  1.60000E+03  N REF4 !

PHASE DHCP  %  1  1.0  !
    CONSTITUENT DHCP  :CD,PR :  !
PARAMETER G(DHCP,PR;0)  2.98150E+02  +GHSERPR#;  3.80000E+03  N REF1 !
PARAMETER G(DHCP,CD;0)  2.98150E+02  5000+GHSERCD#;  1.60000E+03  N!
PARAMETER G(DHCP,CD,PR;0)  2.98150E+02  -108290+60*T;  1.60000E+03  N!

TYPE_DEFINITION ' GES A_P_D FCC_A1 MAGNETIC  -3.0    2.80000E-01 !
PHASE FCC_A1  %'  2 1   1 !
    CONSTITUENT FCC_A1  :CD : VA :  !
PARAMETER G(FCC_A1,CD:VA;0)  2.98150E+02  +GFCCCD#;  1.60000E+03  N REF3 !

TYPE_DEFINITION ( GES A_P_D HCP_A3 MAGNETIC  -3.0    2.80000E-01 !
PHASE HCP_A3  %(  2 1   .5 !
    CONSTITUENT HCP_A3  :CD : VA :  !
PARAMETER G(HCP_A3,CD:VA;0)  2.98150E+02  +GHSERCD#;  1.60000E+03  N REF1 !

PHASE RHOMBOHEDRAL_A10  %  1  1.0  !
    CONSTITUENT RHOMBOHEDRAL_A10  :CD :  !
```

```
PARAMETER G(RHOMBOHEDRAL_A10,CD;0)  2.98150E+02  +GHSERCD#+800
.62*T; 1.60000E+03  N REF4 !
PHASE TETRAGONAL_A6  %  1  1.0  !
    CONSTITUENT TETRAGONAL_A6  :CD :  !
PARAMETER G(TETRAGONAL_A6,CD;0)  2.98150E+02  +GHSERCD#+892.3-
92*T; 1.60000E+03  N REF3 !

PHASE CD11PR %&  2 .917   .083 !
    CONSTITUENT CD11PR  :CD : PR :  !
PARAMETER G(CD11PR,CD:PR;0)  2.98150E+02 -15900 +3*T
+.917*GHSERCD# +.083*GHSERPR#; 1.60000E+03   N!

PHASE CD6PR %&  2 .857   .143 !
    CONSTITUENT CD6PR  :CD : PR :  !
PARAMETER G(CD6PR,CD:PR;0)  2.98150E+02 -26502.7+6.6*T
+.857*GHSERCD# +.143*GHSERPR#; 1.60000E+03   N!

PHASE CD58PR13 %&  2 .817   .183 !
    CONSTITUENT CD58PR13  :CD : PR :  !
PARAMETER G(CD58PR13,CD:PR;0)  2.98150E+02 -33366.4 +9.5*T
+.817*GHSERCD# +.183*GHSERPR#; 1.60000E+03   N!

PHASE CD45PR11 %&  2 .804   .196 !
    CONSTITUENT CD45PR11  :CD : PR :  !
PARAMETER G(CD45PR11,CD:PR;0)  2.98150E+02 -34708.698 +10.126*T
+.804*GHSERCD# +.196*GHSERPR#; 1.60000E+03   N!

PHASE CD3PR %&  2 .75    .25 !
    CONSTITUENT CD3PR  :CD : PR :  !
PARAMETER G(CD3PR,CD:PR;0)  2.98150E+02 -39827.2 +12.3*T
+.75*GHSERCD# +.25*GHSERPR#; 1.60000E+03   N!

PHASE CD2PR %&  2 .667   .333 !
    CONSTITUENT CD2PR  :CD : PR :  !
PARAMETER G(CD2PR,CD:PR;0)  2.98150E+02  -45989.7 +14.2*T
+.667*GHSERCD# +.333*GHSERPR#; 1.60000E+03   N!

PHASE CDPR %&  2 .5   .5 !
    CONSTITUENT CDPR  :CD, PR : PR :  !
PARAMETER G(CDPR,CD:PR;0)  2.98150E+02 -47613.19 +15.7*T
+.5*GHSERCD# +.5*GHSERPR#; 1.60000E+03   N!
PARAMETER G(CDPR,PR:PR;0)  2.98150E+02 6180.5 +3*T
+GHSERPR#; 1.60000E+03   N!

LIST_OF_REFERENCES
NUMBER  SOURCE
REF3        'PURE3 - SGTE Pure Elements (Unary) Database (Version 3.0),
            developed by SGTE (Scientific Group Thermodata Europe), 1991-1996,
```

and provided by TCSAB (Aug. 1996). '

REF5 'PURE5 - SGTE Pure Elements (Unary) Database (Version 5.1), developed by SGTE (Scientific Group Thermodata Europe), 1991-2010, and provided by TCSAB (Jun. 2010). '

REF1 'PURE1 - SGTE Pure Elements (Unary) Database (Version 1.0), developed by SGTE (Scientific Group Thermodata Europe), 1991-1992, and provided by TCSAB (Jan. 1991). Also in: Dinsdale A. (1991): SGTE data for pure elements, Calphad, 15, 317-425.'

REF4 'PURE4 - SGTE Pure Elements (Unary) Database (Version 4.6), developed by SGTE (Scientific Group Thermodata Europe), 1991-2008, and provided by TCSAB (Jan. 2008). ' !

Appendix B: Curriculum vitae

Name, degree	Thomas Ludwig Reichmann, Mag. rer. nat.
Date of birth; place	Apr. 20th, 1986; Klagenfurt
Citizenship	Austria

Education

1992-1996	Elementary school in Maria Elend/ Rosental, Carinthia
1996-2004	Secondary school BG/ BRG Mössingerstraße with emphasis on science, Klagenfurt
2004-2010	Diploma study chemistry, Department of Chemistry/ University of Vienna
2010-2011	Diploma thesis at the Department of Inorganic Chemistry (Materials Chemistry), University of Vienna: „Investigation of the Al-Ge-Ni phase diagram with a view to joining application for Nickel Aluminides"
11/ 2010	Research stay at the Eidgenössischen Materialprüfungs- und Forschungsanstalt (EMPA), Zürich
07/ 2011-12/2013	Project collaborator, University of Vienna
Since 01/2014	Employed as assistant on the University of Vienna
Since 07/ 2011	Doctoral study at the Department of Inorganic Chemistry (Materials Chemistry), University of Vienna: „The interaction of Rare Earth Elements with Cadmium: The systems Cd-Gd and Cd-Pr"

Additional qualifications:

Languages:

German	native speaker
English	very experienced

Teaching activity at the University of Vienna:

Assistant:

Basic Chemistry Laboratory Course I – Introductory Lab Course

Basic Chemistry Laboratory Course I – Introductory Seminar

Demonstrator:

KinderUni on Tour, 2011 and 2012, demonstration of chemical experiments

Appendix C:

List of publications

(1) T. L. Reichmann, L. I. Duarte, H. S. Effenberger, C. Leinenbach, K. W. Richter. Phase equilibria and structural investigations in the Ni-poor part of the system Al-Ge-Ni. *Intermetallics* (2012), 28: 84-91.

(2) I. Jandl, T. L. Reichmann, K. W. Richter. The Ni-rich part of the Al-Ge-Ni phase diagram. *Intermetallics* (2013), 32: 200-208.

(3) B. Skołyszewska-Kühberger, T. L. Reichmann, R. Ganesan, H. Ipser. Thermodynamic study of the cerium-cadmium system. *CALPHAD* (2014), 44: 14-20.

(4) T. L. Reichmann, H. Ipser. Thermochemical Investigations in the System Cadmium-Praseodymium Relevant for Pyrometallurgical Fuel Reprocessing. *Metall. Mater. Trans. A* (2014), 45(3): 1171-1180.

(5) T. L. Reichmann, H. S. Effenberger, H. Ipser. Experimental investigation of the Cd-Pr phase diagram. *PlosOne* (2014), 9(4): 1-14.

(6) B. Skołyszewska-Kühberger, T. L. Reichmann, H. Ipser. Phase equilibria in the neodymium-cadmium binary system. *J. Alloys Comp.* (2014), 606: 242-248.

(7) T. L. Reichmann, K. W. Richter, H. Ipser. Enthalpies of formation of Cd-Pr intermetallic compounds and thermodynamic assessment of the Cd-Pr system. *CALPHAD* (2014), 47: 56-62.

(8) T. L. Reichmann, R. Ganesan, H. Ipser. Thermochemical investigations in the system Cd-Gd. *J. Alloys Comp.* (2014), 610: 676-683.

(9) T. L. Reichmann, H. Ipser. Reinvestigation of the Cd-Gd phase diagram. *J. Alloys Comp.* (2014), submitted.

(10) T. L. Reichmann, I. Jandl, H. S. Effenberger, P. Herzig, K. W. Richter. $Al_{15}Ge_4Ni_3$: A new intergrowth structure with Cu_3Au- and CaF_2-type building blocks. *Sol. St. Chem.* (2014), submitted.

Books:

- Investigation of the Al-Ge-Ni phase diagram, ISBN 978-3-639-40031-1, *Akademikerverlag*
- Handout: “Basic thermodynamics”, from Lecture: Synthesis and thermodynamic characterisation, *No. 270153 - University of Vienna*

Appendix D: Conference contributions

- EUROMAT 2011, “Phase equilibria and structural investigations in the Ni-poor part of the system Al-Ge-Ni”, *T. L. Reichmann, L. I. Duarte, C. Leinenbach, K. W. Richter*. Poster, Montpellier, France, Sept. 2011

- Chemietage 2011, “Phase equilibria and structural investigations in the Ni-poor part of the system Al-Ge-Ni”, *T. L. Reichmann, L. I. Duarte, C. Leinenbach, K. W. Richter*. Poster, Linz, Austria, Sept. 2011

- HTMC 2012, “Thermochemistry and phase equilibria in the systems Cd-Pr and Cd-Gd”, *T. L. Reichmann and H. Ipser*. Oral presentation, Bejing, China, Sept. 2012

- WACÖ 2012, “Phasengleichgewichte in Al-Ge-Ni: ein System mit Relevanz für das Diffusionslöten von Nickel-Aluminiden”, *T. L. Reichmann, K. W. Richter*. Oral presentation, Innsbruck, Austria, Apr. 2012

- TMS 2013, “Thermochemistry and phase equilibria in the systems Cd-Pr and Cd-Gd”, *T. L. Reichmann and H. Ipser*. Oral presentation, San Antonio, USA, Feb. 2013

- Chemietage 2013, “Thermochemical investigations in Cadmium-RE (RE=Ce,Gd,Nd,Pr) systems”, *T. L. Reichmann*. Oral presentation, Graz, Austria, Sept. 2013

- IGCAR, “Thermochemical investigations in Cadmium-RE (RE=Ce,Gd,Nd,Pr) systems”, *T. L. Reichmann and H. Ipser*. Oral presentation, Kalpakkam, India, Feb. 2013

- GDCh-Wissenschaftsforum Chemie 2013, “Lanthanoid-Cadmium-Systeme: Phasengleichgewichte und Thermochemie”, *T. L. Reichmann, B. Skolyszewska-Kühberger, R. Ganesan, S. Ghosh, H. Ipser*. Poster, Darmstadt, Germany, Sept. 2013

- TMS 2014, “The Cd-Pr system: phase equilibria, thermodynamic investigations and CALPHAD optimization”, *T. L. Reichmann*. Oral presentation, San Diego, USA, Mar. 2014